Universität Potsdam

Doctoral thesis

Gone with the breeze: A subsonic model for describing the Fermi bubbles features

A thesis submitted in fulfilment of the requirements for the
degree of "Doctor rerum naturalium" (Dr. rer. nat.)
in the
Institut für Physik und Astronomie
Mathematisch-Naturwissenschaftliche Fakultät

Author:
Olivier Asin

Supervisor
Dr. Andrew Taylor
Prof. Martin Pohl

Declaration

I, Olivier Asin, declare that this thesis titled, 'Gone with the breeze: A subsonic model for describing the Fermi bubbles features' and the work presented in it are my own in collaboration with my supervisor, Andrew Taylor and collaborator, Donna Rodgers-Lee.

I confirm that:

- No part of this work was or will be submitted for any degree or diploma or certificate or other qualification at this University or elsewhere.
- This thesis is the result of my own work.
- Any published work that has been consulted has been accurately referenced.
- The work in Chapter 2 and Chapter 3 has been published collectively in Monthly notices of Royal Astronomical Society, under my scientific author name, Olivier Tourmente (Tourmente, Rodgers-Lee and Taylor 2023).
- The work in Chapter 4 and 5 will be published in a peer-reviewed journal in the future.

Abstract

More than a decade ago, two Galactic bubbles lobes were detected by the Fermi-LAT instruments in a range of 10 GeV to 500 GeV, i.e., in the γ-ray energy band. Their emissions reach a latitude of $\sim 50°$ and a longitude of $\sim 40°$, corresponding to a height of $\sim$ 10 kpc and a width of 7 kpc for an observer at 8 kpc from the Galactic Center. The brightness intensity of the emissions appears to be constant within the lobes. Moreover, sharp edges are observed at the boundaries.

The Fermi bubbles could be a counterpart of the Microwave haze as they both exhibit a hard spectra and a matching width at their bases. More recently, the eROSITA bubbles have been observed in the X-ray band. They extend to a height of 14 kpc, enshrouding the Fermi bubbles and are likely connected to them.

To date, there is no clear consensus about the mechanism responsible for the formation of this bubble structure. Such a mechanism must be able to provide an explanation for the emission mechanism and the origin of the event giving rise to the bubbles. The emission of the Fermi bubbles could be explained by some hadronic or leptonic cosmic rays energy losses.

The majority of the models proposed for describing the Fermi bubbles assume a supersonic velocity profile with a velocity ranging from 500 to 1000 km s^{-1}. The observations of the UV absorption lines provided by cold clouds are able to establish a velocity profile for the Fermi bubbles. The velocities range from 100 to 300 km s^{-1}. A maximal velocity of $\sim$ 300 km s^{-1} at a height of $\sim$ 1 kpc from the Galactic Center has been observed. Moreover, beyond this height, the velocity decelerates continuously. Those observations seem to contradict the supersonic velocity models proposed so far.

In this thesis, a subsonic model is proposed for explaining the velocity profile and the emission of the Fermi bubbles. This model, called a Galactic breeze, exhibits a deceleration that could be in agreement with the observations. A hydrodynamic analytic model has been first explored. The Galactic breeze is considered to be thermally-driven in an isothermal hot Galactic halo. The first step is to define a Galactic gravitational potential. For the model, three components have been set up, a bulge, a disc and a dark matter halo. At a distance called the critical radius, the subsonic profile reaches its maximum velocity. The value of this critical radius depends on the gravitational potential and the thermal velocity. In order to have a subsonic velocity as close as possible to 300 km s^{-1} at the critical radius, the largest possible thermal velocity for the hot Galactic halo must be considered. Based on the observations of the Gaia mission, a fitting-range for the Galactic gravitational potential has been provided. For the Galactic breeze model, the gravitational potential has been normalised to reach the upper limit of this fitting range. Considering a critical radius at a height of 1 kpc from the Galactic Center the corresponding thermal velocity for the hot Galactic halo is 250 km s^{-1} corresponding to $\sim$ 400 eV.

Following these results, a numerical code has been used for solving the hydrodynamic equations and to provide a spatial distribution for the subsonic velocity profile. A Galactic breeze profile exhibiting a deceleration similar to the observations has been obtained. However, the maximal velocity reachable with this model is lower than the observations.

The next step has been to use the velocity profile provided by the numerical simulation to numerically solve a transport code for the propagation of cosmic rays. An isotropic and homogeneous diffusion has been considered and the gamma-rays emission finds its origin in the *pp* interactions. For an injected luminosity of $L_{\mathrm{inj}} = 1.4 \times 10^{40}$ erg s^{-1}, the Galactic breeze model is able to form a bubble structure that matches approximately with the observations. However, the bubbles formed are too wide when compared with the Fermi bubbles as the sharpness of the edges is not obtained.

Following these results, the Galactic breeze model has been extended to include the spatial distribution of a magnetic field. An analytic study of the influence of a magnetic field distribution on a subsonic profile has been done. This revealed that an azimuthal magnetic field distribution can have an effect on the position of the critical radius. Depending on the profile of the magnetic field, the critical radius can be shifted farther from the Galactic Center implying that the thermal velocity can be increased. However, it is extremely difficult to find a magnetic field distribution able to provide a maximal velocity of 300 km s^{-1} for the Galactic breeze and keep the critical radius at 1 kpc. As a first step, the model has been explored by considering values of just a few μG in order to conserve the Galactic breeze profile obtained with hydrodynamic simulations. A MHD numerical code has been used and the magnetic field has been injected with the velocity, allowing to study their mutual influence. Several configurations have been considered that have demonstrated the effect of a compression induced by the velocity profile on the azimuthal magnetic field. This compression leads to a magnetic tension effect that slightly disrupts the velocity profile.

In the same way as for the hydrodynamic model, both the velocity and the magnetic field distribution have been used to numerically solve the transport of cosmic rays. However, the diffusion is this time inhomogeneous. In order to compare the results with the hydrodynamic model and ensure the consistency of the results, an isotropic diffusion coefficient has been considered. For each configuration, a different coherent length has been fixed to have a diffusion length of ~ 0.1 pc inside the bubble structure, similar to the hydrodynamic model and the observations. The next step has been to consider an anisotropic diffusion coefficient. For this, a perpendicular diffusion coefficient ten times less than the parallel diffusion coefficient has been considered. With such anisotropy, the Galactic breeze model is able to provide γ-ray emissions, reproducing the sharpness observed for the Fermi bubbles.

Allgemeine Zusammenfassung

Die Fermi-Blasen sind eine Struktur von galaktischem Ausmaß, die sich über und unter dem galaktischen Zentrum der Milchstraße erstreckt. Diese Blasen emittieren im Gammastrahlen-Energiebereich. Diese Emissionen haben Aufschluss über die Eigenschaften der Fermi-Blasen gegeben. Sie haben ein kontinuierliches Spektrum und scharfe Kanten. Außerdem werden kalte Wolken durch den Ausfluss, der die Blasen formt, vorwärts bewegt. Durch Beobachtung der Emission dieser kalten Wolken wurde ein Geschwindigkeitsprofil ermittelt. Die Geschwindigkeit erreicht ein Maximum in einer Höhe von 1 kpc vom galaktischen Zentrum und eine kontinuierliche Verlangsamung über diesen Punkt hinaus. Es wurden mehrere Modelle zur Erklärung der Fermi-Blasen vorgeschlagen. Alle diese Modelle gehen jedoch von Überschallgeschwindigkeiten aus, die die beobachtete Verlangsamung nicht wiedergeben.

In dieser Arbeit wird ein alternatives Modell vorgeschlagen. Das Geschwindigkeitsprofil wird durch ein Unterschallmodell beschrieben, das als galaktische Brise bezeichnet wird und die Abbremsung auf natürliche Weise erklären kann. Dieses Modell der galaktischen Brise wird zunächst anhand eines hydrodynamischen Modells untersucht, bei dem die Diffusion der kosmischen Strahlung isotrop und homogen ist. Die Ergebnisse zeigen, dass ein solches hydrodynamisches Modell in der Lage ist, eine Blase von der Größe der Fermi-Blasen zu erzeugen, aber nicht in der Lage ist, die Schärfe der Kanten zu reproduzieren.

Das Modell wurde dann erweitert, um den Einfluss einer Magnetfeldverteilung zu berücksichtigen, die mit dem Ausfluss injiziert wird. Die Einbeziehung einer Magnetfeldverteilung ermöglicht die Berücksichtigung einer anisotropen und inhomogenen Diffusion für die kosmische Strahlung. Bei diesem Modell wurde die Schärfe der Kanten reproduziert.

Die in dieser Arbeit geleistete Arbeit zeigt also, dass ein galaktisches Brise-Modell in Kombination mit einem anisotropen Diffuson in der Lage ist, sowohl das Geschwindigkeitsprofil als auch die Schärfe der Kanten zu reproduzieren.

Acknowledgements

I would like to thank my supervisors, Andrew Taylor and Martin Pohl, who gave me the opportunity to do this thesis. I thank Donna Rodgers-Lee for her help and guidance. Prof. Christophe Sauty for accepting to be a reviewer. Prof. Achim Feldmeier, Prof. Tim Dietrich and Prof. Carsten Henkel for accepting to be on the committee.

I thank Vasundhara Shaw for discussions and companionship at work and Mahmoud Alawashra and Xin-Yue Shi for their advice about the corrections to bring.

I also thank Veronica who gave me the feeling that it was not for nothing.

Finally, I thank the one who had the only goal of seeing the accomplishment of this thesis and will not.

Les sanglots longs des violons d'automne

Bercent mon cœur d'une langueur monotone

Contents

List of Figures

List of Tables

Chapter 1

Introduction

The Milky Way halo is an active environment where an ensemble of phenomena takes place. Among these is the apparent ejection of outflows into the circumgalactic medium (CGM). This has the effect of advecting gas in which cosmic rays (CR) are embedded, resulting in the formation of bubble-like structures, multi-kiloparsec in size. The precise origin of these bubbles and the mechanism leading to their formation are still open questions. To try to answer these questions, the properties of the Galactic halo in which the bubbles propagate must be taken into account. Figure 1.1 shows a representation of the interaction of a galaxy with its CGM.

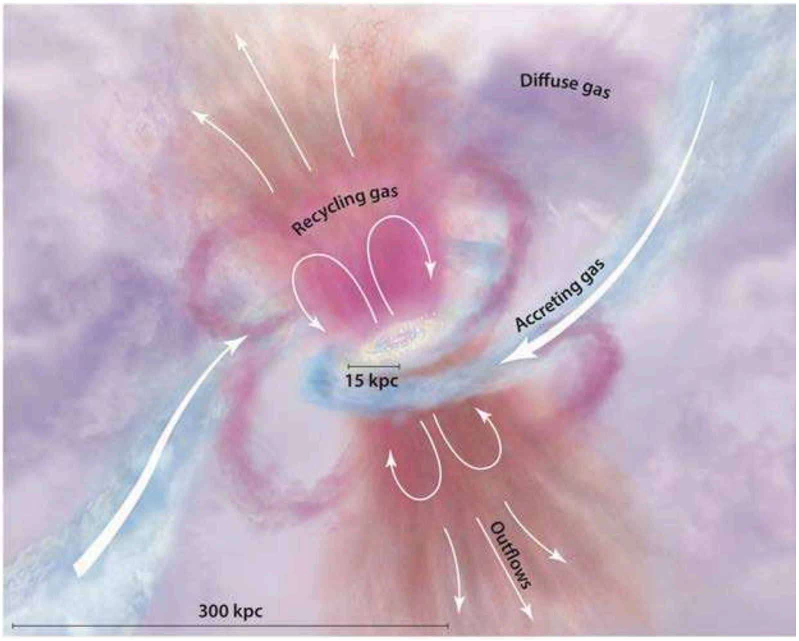

Figure 1.1: A cartoon representing the CGM. In red and brown, outflows travel from the Galactic Center to the CGM in purple. The outflow can enrich and heat the CGM or form a Galactic fountain, i.e., an inflow that will fall back, recycling material. This figure has been obtained from (Tumlinson, Peeples and Werk 2017).

1.1 Temperature and density distribution for the hot Galactic halo

The CGM presents a multiphase structure (Tumlinson, Peeples and Werk 2017; Dutta et al. 2023), composed of a cold ($\sim 10^4$ K), a warm ($\sim 10^5$ K) and a hot ($\sim 10^6$ K) gas. Soft X-ray emission (Anderson and Bregman 2010; Anderson, Bregman and Dai 2013) and absorption lines from quasi-stellar objects (Williams et al. 2005; Gupta et al. 2012) provide direct evidence for the presence of a hot gas component. Highly ionised metals and their interactions with high-velocity cold clouds provide indirect evidence (Brüns et al. 2000; Sembach et al. 2003; Fox, Savage and Wakker 2006; Lehner et al. 2009; Wakker et al. 2012). The mixture of cool, warm and hot gas is also predicted by hydrodynamic simulations (Stinson et al. 2012; Ford et al. 2013; Shen et al. 2013; Suresh et al. 2017). In addition to the three phases, another hotter phase of ~ 1 keV has been observed (Das et al. 2019b; Das et al. 2019a; Das et al. 2021b; Gupta et al. 2021; Ramesh, Nelson and Pillepich 2023). So far, this hotter phase has not been localised in some specific parts of the halo and seems to permeate the entire gas.

The hot Galactic halo

The existence of a hot halo surrounding the Galactic disc has been highlighted by the observations of $\mathrm{H_I}$ clouds that should be confined by an external medium (Spitzer 1956). Its extension and its proximity to the Galactic plane are still unclear. The presence of this hot halo gas is supported by numerical simulations (Nuza et al. 2014), for which a uniform temperature profile ($\mathrm{T} \gtrsim 10^5$ K) for each galaxy simulated is in good agreement with the observed profiles (Miller and Bregman 2015). The observations are also performed through bright Active Galactic Nucleus (AGN) sight lines with detection of $\mathrm{O_{VII}}$ and $\mathrm{O_{VIII}}$ in absorption, ram-pressure stripping of gas and high-resolution X-ray spectra with energies between 0.1 - 1 keV, implying temperatures between 10^{6-7} K (Blitz and Robishaw 2000; Stanimirović et al. 2002; Paerels and Kahn 2003; Sembach et al. 2003; Bregman and Lloyd-Davies 2007; Gatto et al. 2013; Miller and Bregman 2015; Salem et al. 2015).

The early models used X-ray observations, assuming an isothermal distribution and a constant density (Bregman and Lloyd-Davies 2007; Gupta et al. 2012). However, those models found different density distributions. One with $n = 9 \times 10^{-4}$ cm^{-3} at $r = 19$ kpc and the other with $n \geq 2 \times 10^{-4}$ cm^{-3} at $r \geq 139$ kpc. Another model for which the hot halo is composed of an adiabatic gas in hydrostatic equilibrium with the Galactic gravitational potential has been proposed (Fang, Bullock and Boylan-Kolchin 2013). It must be noted that observations tend to show that the Galactic halo does not have a constant entropy profile (Crain et al. 2010; Miller and Bregman 2015). At the present day, the hot halo temperature, inferred from X-ray observations, seems to be fairly uniform, around a value of $\sim 2 \times 10^6$ K but this feature does not imply strictly an isothermal profile (Henley et al. 2010).

More recent observations of $\mathrm{O_{VII}}$ and $\mathrm{O_{VIII}}$ emission lines have been studied (Henley and Shelton 2012; Miller and Bregman 2013; Miller and Bregman 2015), in combination with X-ray measurements to determine a hot halo density of 10^{-4} cm^{-3} to 10^{-5} cm^{-3} for 10 kpc $\leq r \leq$ 100 kpc. The hot halo gas mass has been approximated to be $\sim 10^{10}\ M_\odot$ within 250 kpc. To obtain this result, three assumptions have been made. First, the density profile for the hot halo is described by a spherically symmetric β-model taking the form $n(r) \propto r^{-\beta/2}$. Second, the hot halo is isothermal with a temperature of $T = 2 \times 10^6$ K. Third, it is in collisional ionisation equilibrium. Following those works, a physically plausible corona consistent with the observed halo dynamic and with the UV/X-ray measurements has been proposed (Tepper-Garcia, Bland-Hawthorn and Sutherland 2015). The dark matter halo is normalised to the density profile and the total mass inferred from the observations of the kinematics of halo stars (Kafle et al. 2012). For an isothermal dark matter halo, the core radius is $r_c \approx 0.5$ kpc. The study of the halo dispersion implies a gas temperature of $T \approx 10^6$ K. The total baryonic mass range for the hot halo gas, within the virial radius, is then $\sim 8.8 \pm 1.2 \times 10^{10}\ M_\odot$.

Figure 1.2 shows the temperature distribution of the hot Galactic halo as a function of the Galactic latitude.

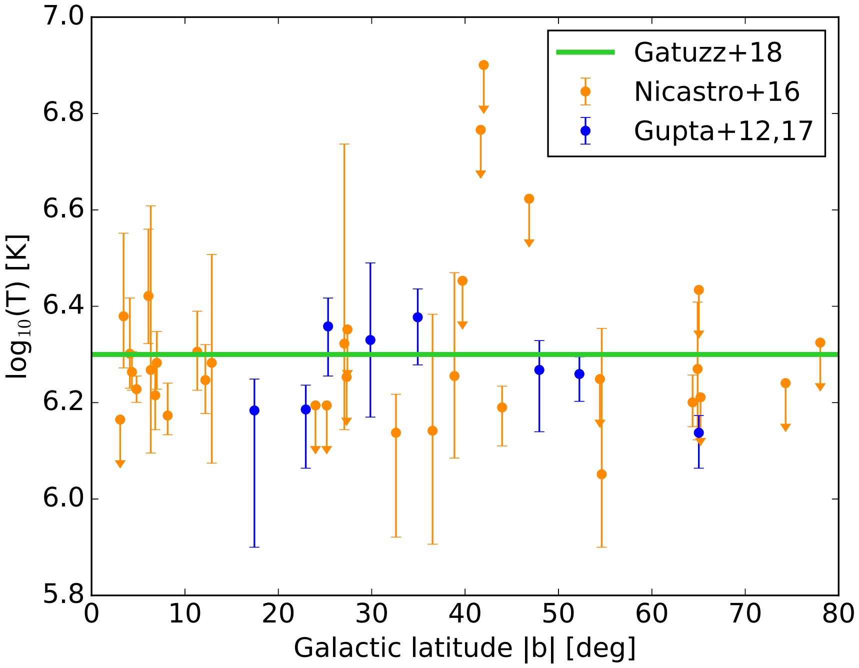

Figure 1.2: The figure presents the temperature distribution for the hot Galactic halo as a function of the Galactic latitude. The orange, blue and green dots and lines are observational data outputs provided by several different works. The median temperature has been estimated at $T = 2 \times 10^6$ K ($kT \approx 200$ eV). This figure has been obtained from (Das et al. 2021a).

1.2 Bubbles structures in the Galactic halo

Several bubble structures spread across the Galactic halo, finding their origin in the Galactic Center. Those are the Fermi bubbles (see section 1.2.1), the Microwave haze (see section 1.2.2) and the eROSITA bubbles (see section 1.2.3). They exhibit different emission mechanisms that have yet to be explained. Studying these structures allows for a better understanding of the mechanisms leading to the creation and propagation of a Galactic wind.

1.2.1 The Fermi bubbles

The Fermi bubbles have been observed by the Large Area Telescope (LAT) (Atwood et al. 2009), an instrument present onboard of the Fermi Gamma-ray Space Telescope, in the γ-ray energy range. The satellite was launched on 11th of June 2008, renamed in honour of Pr. Enrico Fermi.

The Fermi bubbles are composed of two lobes extending above and under the Galactic Center. They reach an angle of $\sim 50°$ in latitude, corresponding to a height from the Galactic Center of ~ 10 kpc. Their longitudinal width is $\sim 40°$, corresponding to ~ 7 kpc. Their γ-ray emission is in correlation with the microwave haze, which is centred around the Galactic Center and reaches a height of ~ 6 kpc (Dobler and Finkbeiner 2008; Planck Collaboration 2016b). They could even be related to the polarised giant radio lobes (Carretti et al. 2013).

The Fermi bubbles exhibit a harder spectrum than other emissions, making them easily visible for a photo-energy range above 2 eV. It must be noted that the spectrum of the Fermi bubbles is obtained after a complex and careful analysis. Different radiations must be considered when mapping a structure like this. Those radiations include the extragalactic background, the bremsstrahlung, the inverse Compton and the hadronic emissions. They have been modelled using the GALPROP CR propagation code (Moskalenko and Strong 1998; Moskalenko, Strong and Reimer 2004; Strong, Moskalenko and Reimer 2004; Ptuskin et al. 2006; Strong, Moskalenko and Ptuskin 2007; Strong et al. 2009; Vladimirov et al. 2011).

The observations in energy range from 100 MeV to 500 GeV above 10° in Galactic latitude. The γ-ray spectrum can be well described by a power-law with an exponential cutoff with an index of 1.9 ± 0.2 and a cutoff energy of 110 ± 50 GeV. The γ-ray luminosity is estimated to be $4.4^{+2.4}_{-0.9} \times 10^{37}$ erg s^{-1}. There are no significant variations in the spectrum across the bubbles. This smooth and extended distribution suggests that this γ-ray emission has been produced by a continuous process rather than individual discrete events. Moreover, they exhibit sharp edges (Ackermann et al. 2014). It is interesting to note that there is a significant enhancement of γ-ray emission in the southeastern part of the bubbles, but the origin of this phenomenon is still unknown (Atwood et al. 2009).

Recently, the HAWC observatory (Abeysekara et al. 2013) put constraints on the Fermi bubbles γ-ray flux in the energy range of 1.2 - 126 TeV. The spectrum at low latitude, that is, a latitude inferior to 10°, does not show a sign of cutoff at energies up to ~ 1 TeV (Yang and Razzaque 2019). The Fermi bubbles at low-latitudes are then not constraint, leaving the way clear for future observations for CTA (Cherenkov Telescope Array Consortium et al. 2019) and LHAASO (di Sciascio and Lhaaso Collaboration 2016) that will cover an energy range from 20 GeV to 300 TeV.

Figure 1.3 shows an illustration of the Fermi bubbles. The bottom figure on figure 1.4, shows an observation of the Fermi bubbles (in blue) in combination with the observations of the Microwave haze (in red).

1.2.2 The Microwave haze

In 2003, the Wilkinson Microwave Anisotropy Probe (WMAP) (Bennett et al. 2003) discovered some anomalously hard spectrum microwave emission, between 23 and 60 GHz, in the vicinity of the Galactic Center (Finkbeiner 2004; Dobler and

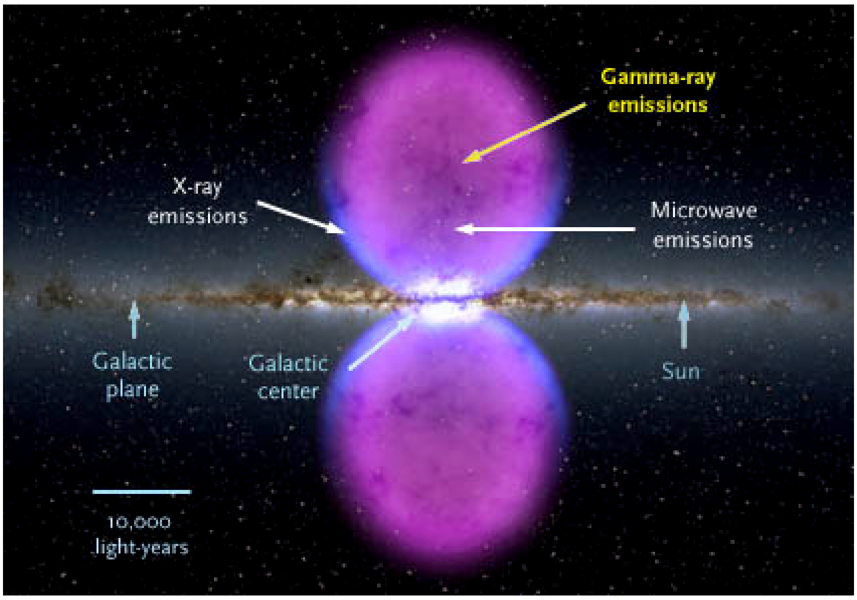

Figure 1.3: The figure is an illustration of the Fermi bubbles in the γ-ray emission. Both X-ray and microwave emissions at the base of the bubbles are also presented. **Source:** NASA / Goddard Space Flight Center.

Finkbeiner 2008; Dobler 2012; Pietrobon et al. 2012; Planck Collaboration 2013). This structure drew attention because its spectrum was too soft for a free-free emission and too hard for a synchrotron emission generated by electrons finding their origin in supernova remnant (Dobler and Finkbeiner 2008). It exhibits an elliptically symmetric shape and extends above the Galactic Center, towards the north and south directions, reaching a latitude of $\sim 35°$ (~ 6 kpc). In the south region, at low latitude, the morphology of the microwave haze is very similar to the Fermi bubbles as both haze and bubbles exhibit an electron spectrum of $dN/dE_e \propto E_e^{-2}$ (Dobler et al. 2010; Su, Slatyer and Finkbeiner 2010). In the north region, the observations are more complicated due to dusty regions (Dobler 2012). The correlation between the morphology and the spectrum provides a strong evidence that the Microwave haze and the Fermi bubbles are a same phenomenon observed at multiple wavelengths. At high latitude, i.e., for $b < -35°$, the microwave emission falls off quickly. The intensity, as a function of the latitude, does not have an edge, unlike the Fermi bubbles. The synchrotron emission maps and WMAP polarisation seem to indicate that the dominant component for the production of the synchrotron emission is the field present within the haze and the Fermi bubbles rather than the Galactic magnetic field (Dobler 2012). Figure 1.4 presents the observations obtained by the Planck mission (Planck Collaboration 2013). On top, both maps for 30 GHz (in red) and 44 GHz (in yellow) are shown. On bottom, the 2-5 GeV map for the Fermi bubbles (Dobler et al. 2010) is compared with the spatial distribution of the Microwave haze. The two bubble structures show an excellent correspondence suggesting they share a same physical mechanism.

1.2.3 The eROSITA bubbles

The observations performed by the eROSITA X-ray telescope (Predehl et al. 2020) have revealed in 2020 another bubble-shaped structure surrounding the Fermi bub-

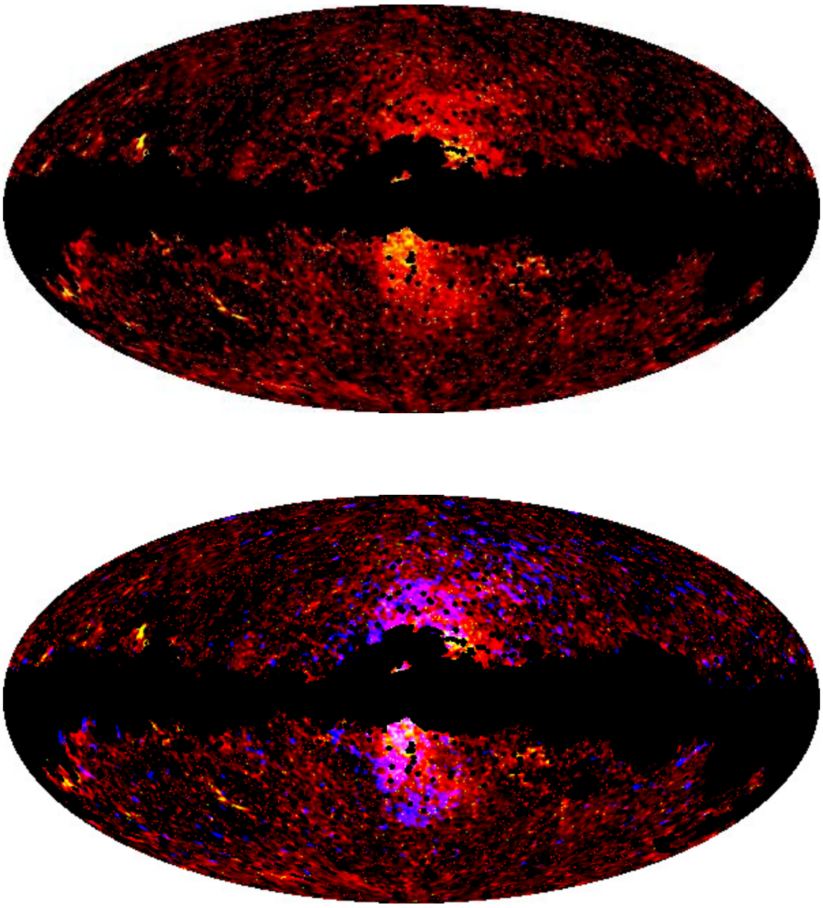

Figure 1.4: On top, the figure presents the observation obtained with Planck for 30 GHz in red and 44 GHz in yellow. On bottom, the figure presents the spatial correspondence between the MIcrowave haze and the Fermi bubbles for 2-5 GeV (in blue). This figure has been obtained from (Planck Collaboration 2013).

bles, called the eROSITA bubbles. Figure 1.5 presents the RGB map provided by observations by the eROSITA mission and figure 1.6 presents a schematic of the eROSITA bubbles. From their morphological similarities, they seem to be the counterparts in the X-ray energy range, from 0.6 to 1 keV, of the γ-ray Fermi bubbles. They are however more energetic and extend to $\sim 80^\circ$ in longitude and $\sim 85^\circ$ in latitude (Predehl et al. 2020). Their full vertical extent is estimated to be roughly 14 kpc.

It is assumed that the eROSITA bubbles have been produced by a shock structure propagating through the Galactic halo that has a temperature of 2×10^6 K. The Mach number for the propagation of the shock is estimated at $M = 1.5$. The temperature for the X-ray emitting shells has been measured to be $\sim$0.3 keV (Kataoka et al. 2013; Kataoka et al. 2015; Tahara et al. 2015; Akita et al. 2018; Kataoka et al. 2018; Predehl et al. 2020; Kataoka et al. 2021). However, recent studies have shown that the X-ray spectral model is more complex than previously assumed and the shell seems to be best described by a two temperature model. It is the same for the gas around the shell (Gupta et al. 2023). There is then a warm-hot phase at the Galactic virial temperature of $\sim$0.2 keV and a hotter phase at a super-virial

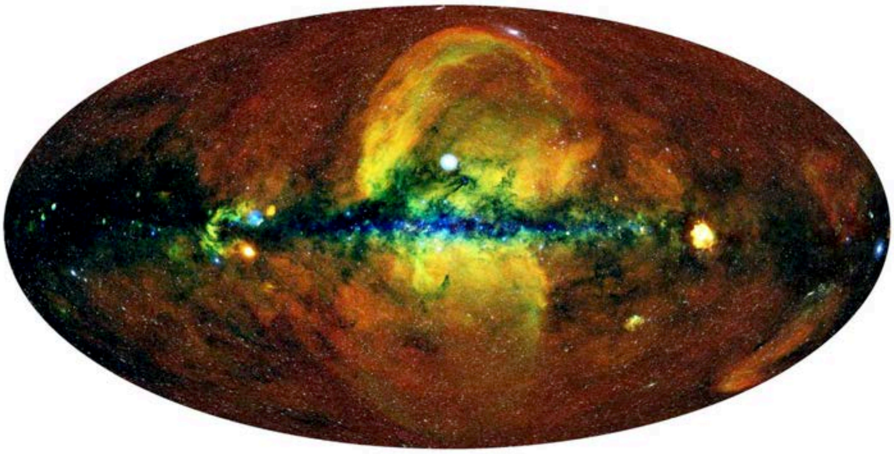

Figure 1.5: The figure presents the all-sky map in Galactic coordinates provided by the eROSTIA mission. The red color corresponds to 0.3-0.6 keV. The green color corresponds to 0.6-1.0 keV. The blue color corresponds 1.0-2.3 keV. This figure has been obtained from (Predehl et al. 2020).

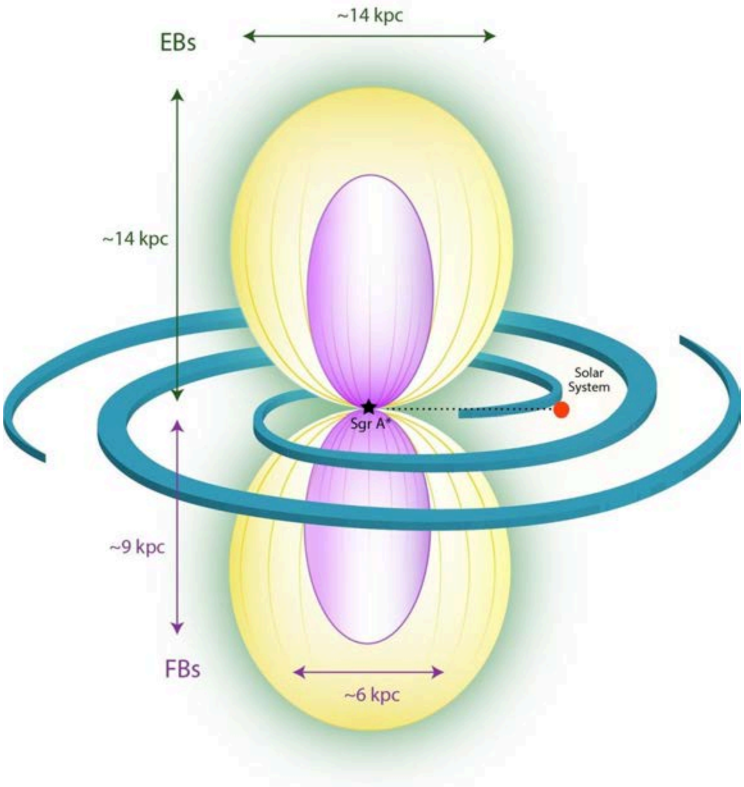

Figure 1.6: The figure is a schematic of the eROSITA bubbles (in yellow) and the Fermi bubbles contained inside (in purple). This figure has been obtained from (Predehl et al. 2020).

temperature ranging between 0.4 and 1.1 keV (Das et al. 2019b; Das et al. 2019a; Das et al. 2021b; Gupta et al. 2021).

Figure 1.7 shows a schematic of the different bubbles in interaction with a CGM wind.

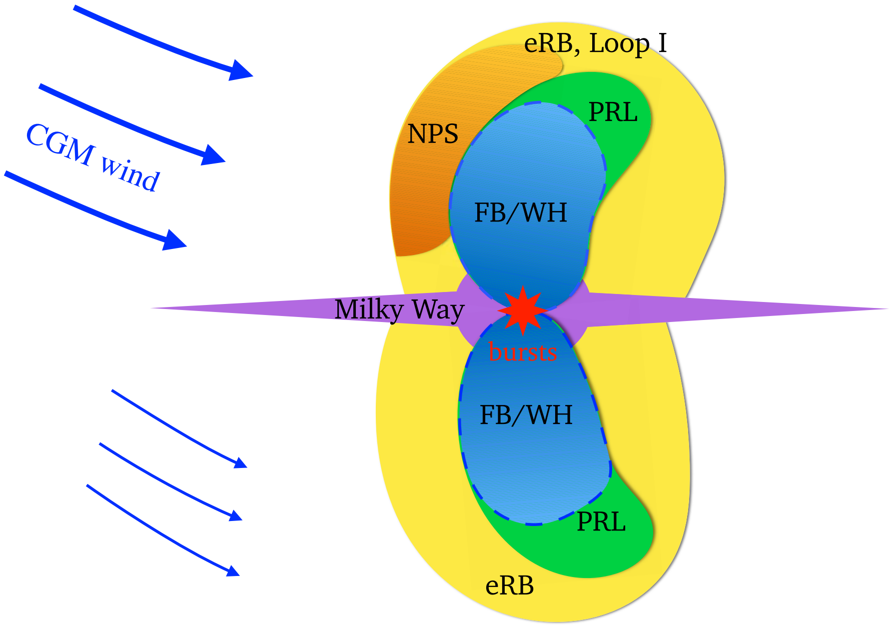

Figure 1.7: The figure shows a schematic of the different bubbles bended by a CGM wind model. The blue zones represent the Microwave haze and the Fermi bubbles. The green zones are the polarised radio lobes. The yellow zones represent the eROSITA bubbles and the Loop I in the northern part of the Galactic halo. The orange zones represent the North Polar Spur. This figure has been obtained from (Mou et al. 2023)

1.3 Origins of the Fermi bubbles

To be able to explain the origin of the Fermi bubbles, the source of their emission mechanism must be understood. Their γ-ray emission can be explained by a hadronic model or a leptonic model.

1.3.1 Hadronic model

For a hadronic model, CR protons interact with an ambient gas also composed of protons. This interaction produces pions that decay into γ-rays (see section 1.5.2). The energy loss time scale is the rate at which the CRs lose their energy. For a *pp* collision, it depends on the cross-section representing such a collision and the density of the ambient gas. For an ambient gas with a density of 3×10^{-3} cm^{-3}, the energy loss time scale is $\sim$ 20 Gyr (Gabici, Aharonian and Blasi 2007). The hadronic model then allows an age for the Fermi bubbles that ranges from multi Myr to a Gyr scale depending on the surrounding density. This means that a slow velocity outflow can be considered for describing the Fermi bubbles as well as a fast velocity outflow. In addition to γ-ray, hadronic interactions can produce secondary electrons (Patrignani et al. 2016). However, the synchrotron emission provided by those secondary electrons do not seem to be able to explain the spectrum observed for the Microwave haze bubbles (Ackermann et al. 2014; Crocker et al. 2015).

1.3.2 Leptonic model

For a leptonic model, γ-ray are produced by an inverse Compton scattering of high energy electrons and low energy photons (Blumenthal and Gould 1970; Rybicki and

Lightman 1979). The energy loss time scale for such an interaction is only a few Myr. For example, for an electron producing a 1 GeV energy photon is 1 Myr (Sarkar 2024). If the observed spectrum of the Fermi bubbles has a leptonic origin, this would imply that the bubbles are quite young. Also, for reaching a height of $\sim 8 - 10$ kpc with such a short energy loss time scale, the outflow velocity must be very high. A height of 10 kpc, reached in 1 Myr, requires a velocity of 10^4 km s^{-1}. Such a value matches with violent events such as supernovae (Shu 1992) or jet models (Mondal et al. 2022).

1.3.3 Velocity profile

Due to the Fermi bubbles being observed through their emission, it is impossible to make a direct detection of their velocity profile. It is however possible to observe the shifted spectrum of high-velocity cold clouds that propagate with the Fermi bubbles outflow. For this, a background source is necessary. Emission from this source is absorbed by the cold clouds. Their absorption spectra will be blue-shifted or red-shifted depending on their direction of propagation based on the position of the observer, allowing to know the direction of propagation and the magnitude of the velocity. Figure 1.8 shows an illustration of the way the velocity profile of the Fermi bubbles is observed.

A population of ~ 200 high-velocity $\mathrm{H_I}$ cold clouds have been detected within the 1.5 kpc of the Galactic plane (McClure-Griffiths et al. 2013; Di Teodoro et al. 2018; Lockman, Di Teodoro and McClure-Griffiths 2020; Sofue 2022). The kinematics of those clouds do not appear to follow the Galactic rotation but a Galactic centred biconical outflow. From those observations, the radial velocity has been estimated as a constant one, reaching ~ 330 km s^{-1}. The fitting-model provided a mass outflow rate of $\sim 0.1\ M_\odot$ yr^{-1} and a luminosity injection of $\sim 5 \times 10^{39}$ erg s^{-1} for the past 10 Myr. The luminosity is then less energetic than what could be expected from an active Galactic nucleus episode (Lacy and Sajina 2020), leading to the assumption that a past starburst episode could be at the origin of the outflow.

High Galactic latitude stars and UV-bright background AGN located behind or near the Fermi bubbles have been used to provide more information on the large-scale outflow in a range between ~ 1 kpc and 10 kpc (Keeney et al. 2006; Bowen et al. 2008; Zech et al. 2008; Fang and Jiang 2014; Fox et al. 2015; Bordoloi et al. 2017; Savage et al. 2017; Karim et al. 2018; Ashley et al. 2020; Cashman et al. 2021; Ashley et al. 2022). All those observations have shown that the blueshifted and redshifted high-velocity clouds exhibit maximum absolute local standard of rest (LSR) velocities that decrease when the Galactic latitude increases. The model considered by most is then a decelerating multi-phase outflow with an initial velocity of ~ 1000 - 1300 km s^{-1}. The total kinetic energy associated with such an outflow would be $\sim 6 \times 10^{55}$ erg, leading to a luminosity injection of $\sim 2 \times 10^{41}$ erg s^{-1}.

Figure 1.9 shows an illustration of the velocity profile of the cold clouds along the Galactic latitude based on observations.

1.4 Galactic magnetic field

Magnetic fields are present everywhere in the Universe and impregnate all the objects and their media. A magnetic field cannot be measured directly but the radiations

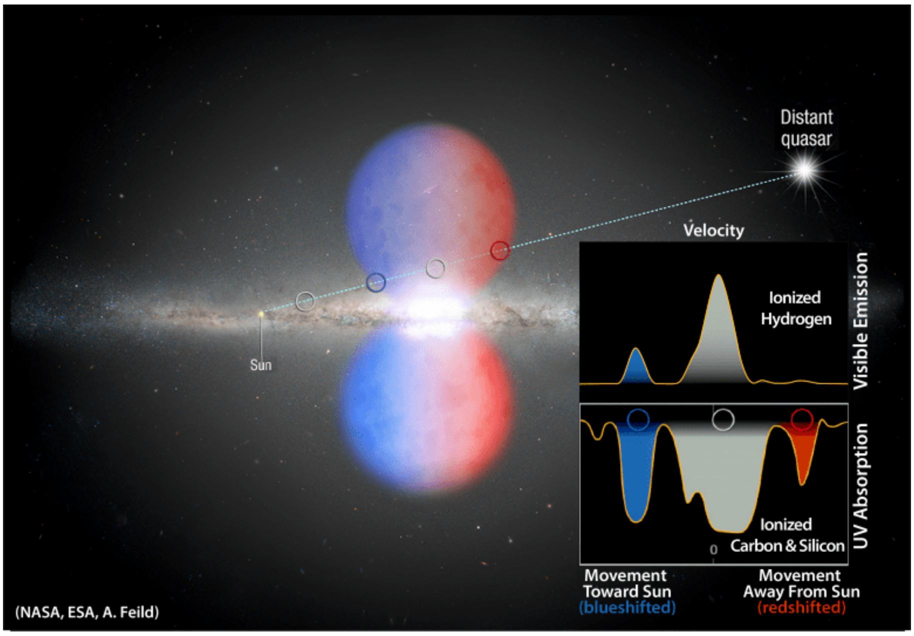

Figure 1.8: The figure shows the way the velocity profile of the Fermi bubbles is observed. For this, a light source is needed for the line-of-sight to pass through the bubbles. Depending on the shifting of the spectrum for UV absorption lines and visible emission, the velocity and its direction can be determined. **Source**: NASA, ESA.

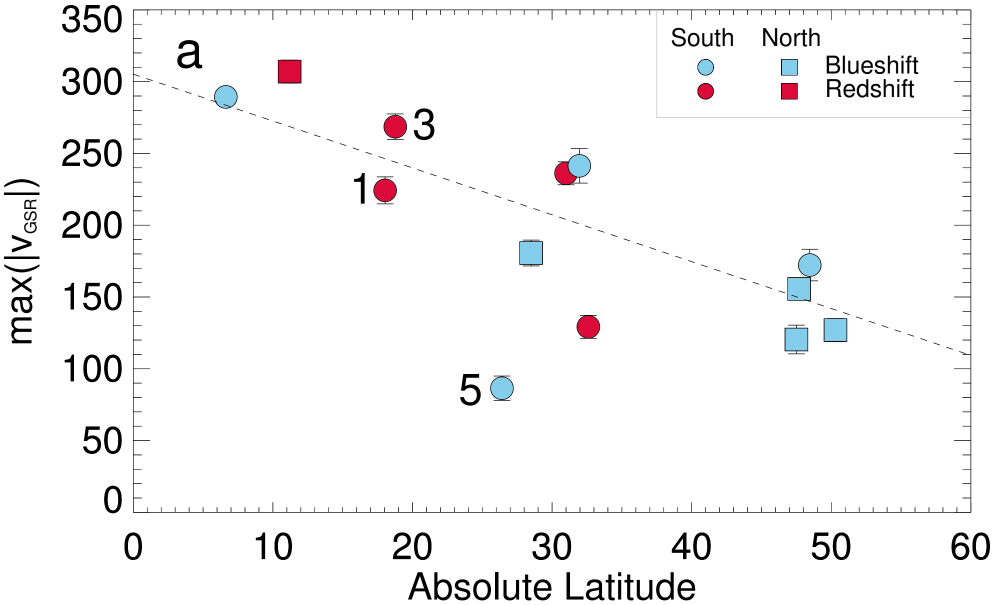

Figure 1.9: The figure presents the maximum velocity of some cold clouds along the Galactic latitude inside the south and north Fermi bubbles. The squares and circles represent clouds for the north and south bubbles respectively. The red colour represents the redshifted clouds and the blue colour the blueshifted clouds. This figure has been obtained from (Ashley et al. 2020).

due to the effects it has on particles are observable. However, they are very weak in diffuse media. For the interstellar medium (ISM), the magnitude of the magnetic fields reaches only a few μG (Beck and Wielebinski 2013). Due to the improvement of instruments for observations, in particular polarisation measurements, progress has been made during the last two decades for mapping the distribution of Galactic magnetic fields. A polarisation is defined as an alignment of electromagnetic wave oscillations. This polarisation is generally due to the influence of a magnetic field on the propagation of electromagnetic waves.

Observations of magnetic fields are very important for a theoretical work, as they play a role, passive or active, in the dynamic of different stellar objects. Every new detection of a magnetic field raises the question of its origin. A question that appears early after the discovery of a sunspot magnetic field through a Zeeman splitting of spectral lines (Hale 1908). Followed decades later by the observations of a magnetic field in the Milky Way inferred by the isotropy of CR and the polarisation of starlight (Fermi 1949; Hall 1949; Hiltner 1949). Stars and planets are formed in molecular clouds that are permeated by magnetic fields (Girart et al. 2009; Rao et al. 2014; Cox et al. 2015). Those clouds are formed by the contraction of interstellar gas itself, which is permeated by weak magnetic fields. Which raises the question of the origin of the magnetic fields in the interstellar medium and the intergalactic medium. Answering this question is important since the magnetic field in the Milky Way contributes to the containment of the charged CR and their transportation. To understand the origin and propagation of CR, it is then necessary to understand the Galactic magnetic field distribution (Letessier-Selvon and Stanev 2011).

Several methods can be used for determining the interstellar or intergalactic magnetic field. Some are based on the magnetic effects of the radiation processes, polarised thermal emission from aligned dust grains and diffuse radio synchrotron emission from charged particles in magnetic fields (Crutcher, Heiles and Troland 2003).

The observations of Zeeman-split emission lines can be used to measure the magnetic field vector, i.e., the total field strength can be measured from the separation of emission lines . The starlight polarisation, the polarised thermal dust emission and the synchrotron emission reveal the orientation of the transverse magnetic field component. Starlight becomes polarised due to the selective extinction of nonspherical dust grains that are aligned by a magnetic field. The major axis being perpendicular to the magnetic field implies that the polarisation angle of the starlight is parallel to the orientation of the transverse magnetic field component. A depolarisation may happen because of a different field orientation. The aligned dust grains have a temperature of ∼100 K producing a thermal emission observable in the millimetre, submillimetre and infrared (IR) spectrum (Han 2017). The thermal emission is linearly polarised with the E-vector along the axis of the dust grain. The observed polarisation is then perpendicular to the transverse magnetic field component (Han 2017).

The synchrotron emission originates from charged CR interactions with a magnetic field. This radiation is linearly polarised perpendicularly to the magnetic field and thus, the observed polarisation gives the orientation of the transverse magnetic field component. However, in most emission regions, the magnetic fields are not well ordered. They are composed of numerous small-scale irregular fields and a larger-scale ordered field. Such small-scale irregular magnetic fields produce a completely depolarised emission. The observed radiation can be partially polarised if the emission region possesses a sufficiently large organised magnetic field (Han 2017; Hu et al. 2024).

1.4.1 Magnetic fields on small scales

The magnetic fields in the interstellar medium are subject to several constraints, such as outflows created by newborn stars, shocks from stellar winds or supernova explosions.

The most prominent feature known to imply a magnetic field is the North Polar Spur, running from the disc to the north Galactic part. This is considered a local feature standing within a hundred parsec from the Sun (Das et al. 2020; Panopoulou et al. 2021). However, some past arguments consider that the NPS could find its origin in the Galactic Center (Sofue et al. 2016) in the same way that the Fermi bubbles (Su, Slatyer and Finkbeiner 2010; Ackermann et al. 2014) or even as a shell from the inner part of the Galaxy (Sun et al. 2015). The loops outside the Galactic plane possess a well-ordered magnetic field (Vidal et al. 2015) that has been observed through synchrotron emission (Planck Collaboration 2016b). The radio emission from supernova remnants originates mainly from synchrotron emission. The magnetic fields, in a shell formed by a shock structure, are always tangential to the shock front. The fields for young remnants are oriented radially from the remnant center (*The Magnetized Interstellar Medium* 2004). By considering the synchrotron emission, an estimation can be made for the magnetic field strength. For this, an equipartition between the energy density of the magnetic fields and relativistic particles is approximated (Govoni 2003; Beck and Krause 2005), leading to a value of a few ten of μG in shock shells and a few hundred of μG to a mG for young remnants (Xiao et al. 2008).

1.4.2 The magnetic field in the Galactic halo

Due to our presence in the Milky Way, the observations of the magnetic fields are of greater importance than for the other galaxies. The galactic magnetic fields are fundamental for understanding the propagation of CR (Prouza and Šmída 2003; Letessier-Selvon and Stanev 2011) and for the evolution of molecular clouds and star formation (Heiles and Crutcher 2005). Moreover, the polarisation of thermal dust emission and diffuse radio emission, which are the result of the presence of a Galactic magnetic field, pollute the observations and must therefore be deducted (Page et al. 2007; Planck Collaboration 2016b).

Synchrotron emission is produced by electrons gyrating around magnetic field lines. Such emission can be observed in the Galactic halo (Haslam et al. 1982; Reich 1982; Reich and Reich 1986; Reich, Testori and Reich 2001; Bennett et al. 2013; Planck Collaboration 2016b). But the synchrotron emission of the Galactic halo is buried by the strong emission of local sources. To be able to have a clear mapping of the halo magnetic field, those local emissions must be separated from the diffuse halo. Such a work has not yet been done. Also, radio synchrotron emission is polarised but at distant regions, polarised emission is mostly depolarised. The main polarised diffuse emission observed comes from the local region, which is within a few hundred parsecs around the Sun. Significant polarisations are detected in the outer part of the Galaxy. So far, the best polarisation maps available for synchrotron emission have been provided by the WMAP and Planck measurements (Page et al. 2007; Bennett et al. 2013; Planck Collaboration 2016b). Those polarisation maps have shown a well-ordered distribution of the E-vectors.

The Galactic halo therefore possesses radio synchrotron emission that contributes to the polarisations and intensities observed. But this emission cannot be easily distinguished from the local emission (Han 2017).

Our location at the edge of the Galactic disc allows us to observe a large number of extragalactic backgrounds and radio sources, as well as pulsars inside the Milky Way. Those can be used to probe the magnetic field in the Galactic halo. To probe the magnetised medium between the source and our position, the Faraday rotation can be used. The polarisation angle of a radio source, in intergalactic space, follows a random walk because of the intervening magnetised medium, implying that its rotation measure has a zero-mean Gaussian distribution. The observed rotation measures of radio sources are correlated, at low Galactic latitudes, with an angular scale of a few degrees and at high latitudes with an angular scale of a few tens of degrees (Simard-Normandin and Kronberg 1980; Oren and Wolfe 1995).

In the mid-latitude region, where $10° < b < 45°$, for the inner Galaxy, where $l < 90°$, the rotation measures show an antisymmetry to Galactic coordinates. Above the Galactic plane, a positive rotation measure dominates, while a negative one dominates under the Galactic plane. The antisymmetry of the magnetic field distribution in the Galactic halo has been confirmed by several observations (Taylor, Stil and Sunstrum 2009; Stil, Taylor and Sunstrum 2011; Xu and Han 2014; Oppermann et al. 2015). From those observations, it has been deduced that the asymmetry in the rotation measures is due to a toroidal magnetic field with reversed field directions above and below the Galactic plane (Han et al. 1997; Han, Manchester and Qiao 1999).

It has been estimated that the magnetic field has a magnitude of 0.2-0.3 μG for a distance between 700 pc and 1 kpc and with a direction going from the south to the north Galactic pole (Han and Qiao 1994; Taylor, Stil and Sunstrum 2009; Mao et al. 2010).

The toroidal and poloidal fields describe two distinct components of a magnetic field. They are defined based on their orientation within an axisymmetric system. The toroidal field lies on an azimuthal direction around a central axis. The poloidal field lies in the plane defined by the radial and polar directions. It forms a loop that connects the axis and moves around the cross-section of the torus. The results of those different observations, concerning the toroidal and poloidal magnetic fields, have been used as parameters for different numerical models that have so far successfully simulated the radio Galactic sky and its polarisations (Prouza and Šmída 2003; Sun et al. 2008; Pshirkov et al. 2011; Jansson and Farrar 2012).

Figure 1.10 shows an illustration of the magnetic field structure in the Galactic halo. The toroidal field is shown by the red arrows above and under the Galactic plane. The poloidal field is shown by the blue arrows looping from the Galactic center.

1.4.3 The magnetic field in the Galactic central region

It is extremely difficult to measure the magnetic fields in the central region. First, because of the possible confusion between the diffuse emission from the Galactic disc and secondly, because the toroidal and poloidal magnetic fields are almost perpendicular to the line of sight. Highly polarised non-thermal radio filaments have been observed close to the Galactic Center and are mostly perpendicular to the Galactic plane (Yusef-Zadeh, Morris and Chance 1984; Yusef-Zadeh, Hewitt and Cotton

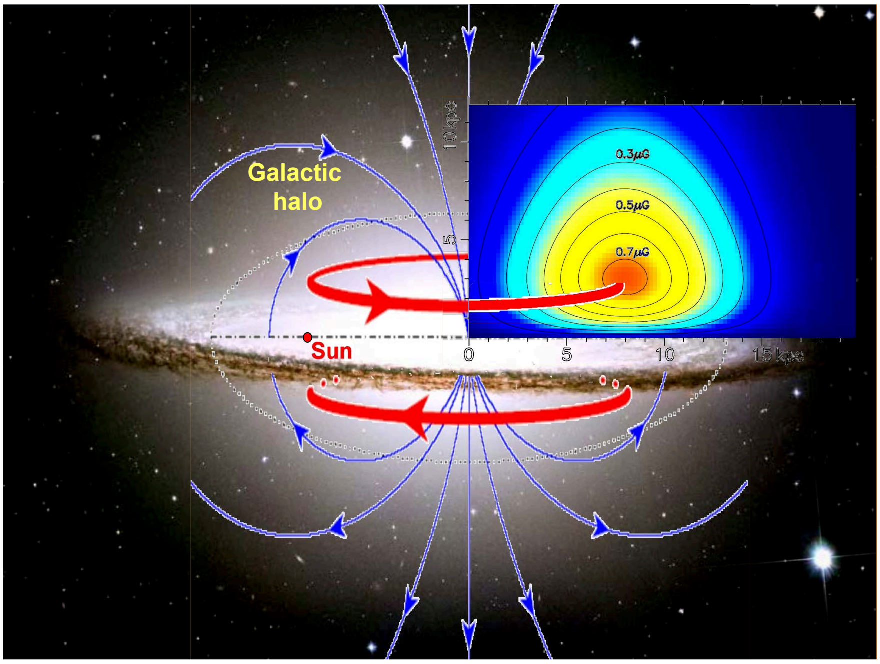

Figure 1.10: The figure is an illustration of the magnetic field structure in the Galactic halo. The blue lines correspond to the dipolar magnetic field. The red lines correspond to the toroidal magnetic field. On the top right, a recent model of the magnetic toroidal distribution has been added, based on data fitting. This figure has been obtained from (Xu and Han 2024).

2004; LaRosa et al. 2004). Those observations support the existence of magnetic flux tubes of poloidal fields within a few hundred parsecs of the Galactic Center and show that the magnetic fields are aligned with the filaments (Lang, Morris and Echevarria 1999) but the field direction cannot be determined. Assuming a hot gas of $\sim 10^8$ K and an electron density of $n_e \sim 0.04$ cm^{-3}, the rigidity of those filaments and the interaction with turbulent molecular gas lead to a magnetic field strength in the tube as strong as 1 mG (Morris and Serabyn 1996). However, more recent observations contradict this value as diffuse radio emission at low frequency within $\sim$ 400 pc from the Galactic Center for which a weak pervasive magnetic field of a few tens of μG exists, assuming an energy equipartition (LaRosa et al. 2005; Yusef-Zadeh et al. 2013). Moreover, the poloidal magnetic fields are frozen into the ionised ISM that dynamically rotates around the Galactic Center (Hodges-Kluck, Miller and Bregman 2016). In the inner disc, magnetic fields are possibly anchored to molecular clouds and are then stretched by their movement in the central molecular zone. This effect leads the magnetic field to be toroidal and parallel to the Galactic plane. Observations of thermal dust emission tend to confirm this hypothesis, as the orientation seems to align with the toroidal fields (Novak et al. 2003; Nishiyama et al. 2010; Planck Collaboration 2016a). The observations of the rotation measures of the background radio sources allow to measure the magnetic field along the line of sight passing through the Milky Way. Those background sources have a positive rotation measure indicating that, on average and along the Galactic bar, the magnetic fields point to the Sun (Roy, Pramesh Rao and Subrahmanyan 2008). The major contribution for the rotation measures comes from regions close to the Galactic Center (Lang, Morris and Echevarria 1999; Law, Brentjens and Novak 2011). In the central region, the antisymmetry present in the rotation measures is similar to the one observed in the Galactic halo. This indicates toroidal magnetic fields for the central region similar to the ones present in the Galactic halo (Novak et al. 2003; Law, Brentjens and Novak 2011). This could imply that the poloidal fields, near the Galactic Center, i.e., the central molecular zone and the disc region, should have directions from the south to the north. With such fields, the Fermi bubbles (Dobler et al. 2010; Su, Slatyer and Finkbeiner 2010; Ackermann et al. 2014) could be produced by the propagating CR, finding their origin in the Galactic Center, from massive star-forming regions like the central molecular zone or from an accretion zone around the central black hole of the Milky Way.

1.5 Cosmic rays origins and interactions

The CR are responsible for most of the emissions that can be observed all around us. Finding their possible origins and their emission mechanisms is then of great importance to understand the observations of the Fermi bubbles and propose a satisfactory model.

1.5.1 Cosmic rays origins in the Milky Way

CR find their origins through violent events across the Galaxy. However, only a few of those are able to provide an environment able to accelerate them to energies comparable with what has been observed. In this section, two possible origins for high-energy CR are reviewed.

Supernova and supernova remnant

It has been often considered that CR find their origins mostly among the supernovae (SNe) and their remnants (SNR) (Bykov et al. 2018; Liu et al. 2022) as only a few sources can provide the energy flux for the observed CR in the Galaxy (Berezinskii et al. 1984; Lingenfelter 2013). There is however a doubt as to whether the SNR can supply the observed CR flux for the highest energies (Cristofari 2021). Other possible sources have been considered as star clusters and star-forming regions (Bykov et al. 2020).

The violent event that represents SNe and SNR accelerates CR allowing them to reach higher energies. However, if SNe and SNR are considered as the only possible sources of CR in the Galaxy, they must convert ∼10 percent of their total energy to the CR to match the observations (Lingenfelter 2018). Such a high efficiency is possible for a strong diffusive shock (Liu et al. 2022). The maximal energy that can reach CR in an expanding SN shell can be estimated through the size of the shell, $r_{\rm sh}$, the shock velocity, $v_{\rm sh}$ and the strength of the magnetic field, B (Hillas 1984; Li et al. 2011; Marcowith et al. 2018; Cristofari 2021; Owen et al. 2023)

$$E_{\rm max} \approx 1 \left(\frac{r_{\rm sh}}{\rm pc}\right) \left(\frac{v_{\rm sh}}{10^4 \ {\rm km\ s^{-1}}}\right) \left(\frac{B}{\mu G}\right) \ {\rm TeV}. \tag{1.1}$$

The CR can then be accelerated to reach energies of ~ 1 TeV. To be able to reach energies beyond the TeV ranges, particular conditions must be met, such as a dense circumstellar medium in which the shock propagates and a larger magnetic field built-up by instabilities (Bell et al. 2013; Schure and Bell 2013; Schure and Bell

2014). Those conditions could be met in SNe of type II (Petropoulou et al. 2017; Marcowith et al. 2018).

The gas swept-up by a shock forms a shell, which forms a dense gas that acts as a target for pp-collisions. Moreover, pp-interactions also produce secondary leptons that radiate synchrotron emission (Reynolds 2008; Murase, Thompson and Ofek 2014).

Star-forming regions

The difference between the observed CR spectrum on Earth and the spectra of accelerated particles at SNR shocks motivated new studies about looking for other sources for the acceleration of CR (Tatischeff and Gabici 2018; Bykov et al. 2020). Those sources are star-forming regions, composed of young massive stellar clusters and the associated superbubbles. Through massive stars, star-forming regions can host large powerful winds. Those stars can also produce SNe (Owen et al. 2023). γ-ray observations of the Cygnus region support a hadronic CR acceleration in stellar clusters (Ackermann et al. 2011; Bartoli et al. 2014; Abeysekara et al. 2021; Cao et al. 2021). The presence of strong winds and shocks has its importance for the acceleration of CR (Voelk and Forman 1982; Cesarsky and Montmerle 1983). For clusters composed of young stars, the acceleration of CR happens at a termination shock. If the cluster is not compact, each star will develop its own stellar wind and therefore, its own termination shock. For compact clusters, the stellar wind of each star will merge to form one termination shock. Older clusters are located inside superbubbles (Owen et al. 2023) composed of hot gas and a low density region and surrounded by a dense shell (Mac Low and McCray 1988). For those structures, the mechanism related to the acceleration of CR is more complex. Acceleration can happen in the turbulent medium inside the bubbles or at the boundary (Bykov and Fleishman 1992; Parizot et al. 2004; Higdon and Lingenfelter 2005; Reimer, Pohl and Reimer 2006; Bykov 2014). The termination shock for the superbubbles has an important effect since it can accelerate CR up to PeV energy range (Bykov 2014; Gupta et al. 2018; Morlino et al. 2021).

1.5.2 pp interactions

The CR are numerous and interact with each other to produce different particles. The CR can be of different types, baryons, mesons, leptons, neutrinos or atomic nuclei. Considering the subject of this thesis, the focus is going to be on hadronic interactions.

Those hadronic CR are predominantly represented by protons. At low energies, ionisations and collisions are the main mechanisms for the exchange of energy. At higher energies, around GeV energy range and above, proton-proton, pp, and proton-photon $p\gamma$ interactions become predominant. For those two mechanisms, high energy photons are produced through pion formation for the pp interactions as well as electrons and neutrinos for the $p\gamma$ interaction. This can play an important role in the evolution of a system as non-thermal hadronic CR thermalise the surrounding medium by the formation of secondary CR electrons (Owen et al. 2018; Simpson et al. 2023).

The dominant pion production channel for pp interactions is (Owen et al. 2018)

$$
\mathrm{p} + \mathrm{p} \rightarrow \begin{cases} \mathrm{p}\Delta^{+} & \rightarrow \begin{cases} \mathrm{pp}\pi^{0} \\ \mathrm{pp}\pi^{+}\pi^{-} \\ \mathrm{pn}\pi^{+} \end{cases} \\ \mathrm{n}\Delta^{++} & \rightarrow \begin{cases} \mathrm{np}\pi^{+} \\ \mathrm{nn}2\pi^{+} \end{cases} \end{cases} . \tag{1.2}
$$

where Δ^+ and Δ^{++} are the delta baryons. Δ^+ is composed of three quarks u and Δ^{++} is composed of two quarks u and one quark d (Anderson et al. 1952; Hahn et al. 1952; Ashkin et al. 1956; Almeida et al. 1968; Skorodko et al. 2008). This interaction happens for a threshold energy above ~ 0.28 GeV which is the proton energy needed for the production of a neutral pion through the interaction $pp \rightarrow pp\pi^0$. Around 30 percent of the total interaction energy is transferred to neutral pions and the rest goes to charged pion production. A neutral pion, π^0, decays mostly into two photons through an electromagnetic process (Particle Data Group et al. 2020) giving

$$
\pi^0 \rightarrow 2\gamma. \tag{1.3}
$$

The branching ratio is 98.8 percent and occurs with a timescale of 8.5×10^{-17} s (Patrignani et al. 2016). As for the charged pions, they decay into electrons and neutrino through weak interactions, giving then

$$
\pi^+ \rightarrow \mu^+\nu_\mu \rightarrow e^+\nu_e\overline{\nu}_\mu\nu_\mu \tag{1.4}
$$

$$
\pi^- \rightarrow \mu^-\overline{\nu}_\mu \rightarrow e^-\overline{\nu}_e\nu_\mu\overline{\nu}_\mu \tag{1.5}
$$

where μ^+ and μ^- are muons, ν_μ is a muon neutrino, $\overline{\nu}_\mu$ is a muon antineutrino, e^- is an electron, e^+ is a positron, ν_e is an electron neutrino and $\overline{\nu}_e$ is an electron antineutrino. The branching ratio is 99.9 percent for each of these decays and occurs over a timescale of 2.6×10^{-8} s (Patrignani et al. 2016). The neutrinos get three quarters of the total energy and the rest is transferred to the electrons. The pp interactions and their secondary products have been extensively studied with Monte-Carlo simulations by simulating high-energy collisions (Engel et al. 1992; Fletcher et al. 1994; Engel, Ranft and Roesler 1995; Agostinelli et al. 2003; Ostapchenko 2006; Bopp et al. 2008; Bähr et al. 2008; Gleisberg et al. 2009; Bierlich et al. 2022) that have shown good agreement with experimental data (Amenomori et al. 2019).

1.6 Focus of this thesis

The purpose of this thesis is to explore an alternative to the different supersonic outflow models proposed so far to explain the observed spectrum of the Fermi bubbles (Crocker and Aharonian 2011; Guo and Mathews 2012; Yang et al. 2012; Mou et al. 2014; Crocker et al. 2015; Mou et al. 2015; Guo 2016; Yang and Ruszkowski 2017; Sarkar, Nath and Sharma 2017). For this, a subsonic model has been considered.

This model was first proposed in a free divergence form for the velocity field and showed promising results (Taylor and Giacinti 2017). In this thesis, the model has been extended to a non divergent form and the outflow propagates in an isothermal hot gas. The influence of a magnetic field distribution on the diffusion of CR has also been considered.

The thesis has been divided into two main parts. The first part, composed of chapters 2 and 3, introduces the hydrodynamic model and the second part, composed of chapters 4 and 5, the MHD model.

In chapter 2, the thermally-driven outflow model is introduced as well as the different parts needed for determining a subsonic solution. Those parts are the total Galactic gravitational potential, the density distribution and an isothermal temperature for the hot Galactic halo based on the provided fitting-range. A numerical simulation is then performed and the results are discussed and compared with existing observations.

In chapter 3, the velocity profile, numerically simulated, is used for solving a CR transport equation with a CR transport code. The CR transport equation is composed of a diffusive spatial current and an advective spatial current. A term representing an energy loss time scale for pp interactions is included and also a source term. As the velocity profile is non free divergent, a term about momentum advection, i.e., adiabatic losses, is also considered. For the hydrodynamic model, an isotropic and homogeneous diffusion coefficient has been implemented. The CR density map provided by the code is used to produce a γ-ray energy flux distribution for the subsonic velocity profile and is compared with data provided by the Fermi-LAT instruments.

In chapter 4, a magnetic field term is included for the momentum equation. Its effect on the subsonic solution is studied and compared with observations and simulations of the magnetic field distribution for the hot Galactic halo. MHD simulations are performed for several configurations with different values for the initial radial and azimuthal magnetic field and velocity components. The different velocity maps obtained are discussed.

In chapter 5, both the velocity and the magnetic field profiles are used for solving a CR transport equation. For this, two diffusion coefficients are considered, i.e., an isotropic one and an anisotropic one. For the isotropic case, the γ-ray energy flux emission of each configuration that has been introduced in chapter 4, is compared with the hydrodynamic model. Following this, the anisotropic diffusion coefficient is introduced and the necessary modifications for the CR transport code are discussed. Some configurations are processed and the resulting CR distribution and their γ-ray emission are presented.

Chapter 2

Thermally-driven subsonic outflow for a hydrodynamic model

As highlighted by observations, the Fermi bubbles exhibit a velocity profile that decelerates, passing a Galactic height of 1 kpc (Fox et al. 2015; Bordoloi et al. 2017; Karim et al. 2018; Lockman, Di Teodoro and McClure-Griffiths 2020; Ashley et al. 2020; Cashman et al. 2021). However, since their discovery, every model attempting to explain their emission has used supersonic velocity profiles mostly ranging from 500 km s^{-1} to 1000 km s^{-1} whether in the form of a wind (Crocker and Aharonian 2011; Mou et al. 2014; Crocker et al. 2015; Mou et al. 2015; Sarkar, Nath and Sharma 2017) or a jet (Guo and Mathews 2012; Yang et al. 2012; Yang, Ruszkowski and Zweibel 2013; Guo 2016; Yang and Ruszkowski 2017) . An alternative model is possible, based on a thermally-driven subsonic outflow (Taylor and Giacinti 2017). In this chapter, within the framework of a hydrodynamic model, the theoretical basis of such a subsonic outflow is described and developed for a Galactic halo model, through a Galactic gravitational potential and a density distribution in accordance with the observations. Using a hydrodynamic code for performing simulations, some initial conditions that are suitable for a subsonic solution are setup. Section 2.1, presents the conservation form of hydrodynamic equations. In section 2.2, the thermally-driven outflow model that will serve to define a subsonic solution is presented. In section 2.3, the different components that have been used for describing the total Galactic gravitational potential are introduced. In section 2.4, the analytic subsonic solution, obtained from a description of the Galactic halo introduced in the previous sections, is compared with the observations of high-velocity cold clouds that have provided a velocity profile for the Fermi bubbles. The velocities ranging from $\sim$ 300 km s^{-1} to $\sim$ 150 km s^{-1}. In section 2.5, a thermal distribution for the Galactic halo is discussed and a hydrostatic density distribution is described and compared with observations. Finally, in section 2.6, the numerical setup that has been used for the hydrodynamic simulations is introduced, followed by a description of the numerical results that have been obtained.

2.1 Conservation equations

The conservation equations for a hydrodynamic model describe the motion of fluid elements. The mass and momentum conservation equations are the fundamental principles of fluid motion. Solving those equations is a task that often requires numerical integration due to their non-linear nature. In this section, the mass and momentum equations are presented in their conservative form. As it will be seen, those equations are essential to describe the propagation of an outflow through an ambient gas. For the numerical simulations, this gas will take the form of a hot Galactic halo. It is assumed to be isothermal, i.e., it is described by a constant temperature. As the hot Galactic halo is isothermal, the energy conservation equation can then be omitted.

2.1.1 Mass conservation equation

The mass conservation equation states that the mass of a closed system remains constant over time. A change of mass within a defined volume is equal to the net mass that flows out of that volume. This equation is expressed as the following continuity equation

$$\frac{\partial \rho}{\partial t} + \nabla \cdot (\rho \mathbf{v}) = 0, \tag{2.1}$$

where ρ is the mass density and $\mathbf{v}$ the velocity vector of the fluid element.

2.1.2 Momentum conservation equation

The momentum conservation equation is an application of Newton's second law of motion for a fluid element. It describes the change in velocity of a fluid over time and space when different forces are applied to it. Its expression in a conservative form is given by

$$\frac{\partial \rho \mathbf{v}}{\partial t} + \nabla \cdot \left(\underbrace{\rho \mathbf{v} \mathbf{v}^T}_{\text{Ram pressure}} + \underbrace{P_{\text{th}} \mathbf{I}}_{\text{Thermal pressure}} \right) = 0, \tag{2.2}$$

where $\mathbf{I}$ is the unity tensor and P_{th} the thermal pressure. By further developing this equation, the equation of momentum conservation is obtained. For this, the following equality $\nabla \cdot \left(\rho \mathbf{v} \mathbf{v}^T\right) = (\rho \mathbf{v} \cdot \nabla) \mathbf{v}^T + \mathbf{v}^T \nabla \cdot (\rho \mathbf{v})$ has been used. This gives

$$\underbrace{\mathbf{v} \left[\frac{\partial \rho}{\partial t} + \nabla \cdot (\rho \mathbf{v}) \right]}_{\text{Mass equation } = \, 0} + \left[\rho \frac{\partial \mathbf{v}}{\partial t} + \rho \left(\mathbf{v} \cdot \nabla\right) \mathbf{v} + \nabla P_{\text{th}} \right] = 0. \tag{2.3}$$

The momentum conservation equation becomes then

$$\rho \frac{\partial \mathbf{v}}{\partial t} + \rho \left(\mathbf{v} \cdot \nabla\right) \mathbf{v} + \nabla P_{\text{th}} = 0. \tag{2.4}$$

With both mass and momentum conservation equations, the propagation of an outflow, on which different forces act, can be described. As part of this thesis, a specific model will be explored, for which a gravitational force and a P_{th} term act on the outflow, contributing to its propagation. Such an outflow is described as a thermally-driven model.

2.2 Thermally-driven outflow model

A thermally-driven outflow model refers to a scenario where the motion of a gas is induced by a thermal process due to a heat source playing a significant role. In this section, the mass conservation equation, Eq. (2.1), and the momentum conservation equation, Eq. (2.4) both in steady-state, are used to define such a model.

A source of matter is considered in the form of a mass loss rate, $\dot{M}$. Its expression can be obtained by considering the steady-state form of the mass equation, (see Eq. (2.1)). For a spherical symmetry, it is given by

$$\dot{M} = 4\pi\rho v r^2. \tag{2.5}$$

In the Galactic halo, a gas is also subject to the force of gravity, which is directed inward, and the gradient of P_{th}, an outward force. If an outflow is present, the fluid is also subject to a gradient of ram pressure. In the context of a hydrodynamic model, for a steady-state fluid, the equation of momentum conservation, Eq. (2.4), becomes

$$\underbrace{\mathbf{v}\nabla.\mathbf{v}}_{\text{Fluid acceleration}} + \frac{\overbrace{\nabla P_{\text{th}}}^{\text{Thermal acceleration}}}{\rho} = \underbrace{-\nabla\Phi}_{\text{Gravitational acceleration}} . \tag{2.6}$$

The term Φ represents the gravitational potential. Its expression depends on the considered system. For a star, it can be expressed with a simple spherical point source. However, it can be more complex for a galaxy since an important aspherical distribution of matter, as a disc, must be taken into account. The first term represents the acceleration of the gas that is produced by the gradient of P_{th} (second term) and the gravitational force (right-hand side term).

Along with mass and momentum, energy is a quantity that must be conserved. Since in this work the model considered is isothermal, the energy conservation equation can be omitted.

In 1958, Parker proposed a model for describing the dynamic of the hot solar corona (Parker 1958). His work started by considering that the solar corona was in static equilibrium. For such a model, the gas density goes to zero at an infinite distance from the Sun and a pressure of $\sim 7.15 \times 10^{-6}$ dynes cm^{-2} is found. However, at infinity, the pressure of the interstellar gas is estimated at $\sim 1.4 \times 10^{-13}$ dynes cm^{-2}. The gas pressure of the corona cannot therefore be balanced by the interstellar gas, leading to a constant pressure at infinity and therefore, a nonphysical solution. This result led Parker to consider an expanding solar corona. Assuming an isothermal distribution and using the mass and momentum conservation equations, he found that this expansion could correspond to a transonic solar wind.

For an isothermal model, P_{th} is expressed by

$$P_{\text{th}} = \frac{\rho c_s^2}{\gamma}, \tag{2.7}$$

where γ represents the adiabatic index. For an isothermal gas, $\gamma = 1$. c_s is the thermal velocity, also known as sound speed. Going back to the momentum conservation equation for the hydrodynamic model, Eq. (2.6), the gradient of P_{th} becomes

$$\frac{\nabla P_{\text{th}}}{\rho} = c_s^2 \frac{\nabla \rho}{\rho}. \tag{2.8}$$

By using the mass conservation equation, Eq. (2.1), the gradient of density can be expressed as

$$\frac{\nabla \rho}{\rho} = -\frac{\nabla v}{v} - \frac{2}{r}. \tag{2.9}$$

Substituting this expression into the momentum conservation equation for the hydrodynamic model, Eq. (2.6), leads to

$$\frac{\nabla v}{v} = \frac{1}{r}\left(\frac{2c_s^2 - r\nabla \Phi}{v^2 - c_s^2}\right). \tag{2.10}$$

Therefore, the equality $v^2 = c_s^2$ is a forbidden value, unless

$$r = \frac{2c_s^2}{\nabla \Phi}. \tag{2.11}$$

The radius where this equality occurs is called the critical radius, r_c. It is possible to predict the behaviour of the outflow by looking at the sign on the right-hand side of the Eq. (2.10) for different scenarios.

It is easier, to visualise the competition between P_{th} and $\nabla \Phi$ by expressing the Eq. (2.10) through P_{th}, P_{g} the rotational pressure induced by gravity, and P_{ram} the ram pressure as

$$\frac{\nabla v}{v} = \frac{1}{r}\left(\frac{2P_{\text{th}} - P_{\text{g}}}{P_{\text{ram}} - P_{\text{th}}}\right). \tag{2.12}$$

It can then be seen that the forbidden value $P_{\text{ram}} = P_{\text{th}}$ is possible only if, at r_c, $2P_{\text{th}} = P_g$. This relation is presented in figure 2.1. The distribution of $2P_{\text{th}}$ (solid red line) is compared with the distribution of P_{g} (dotted magenta line). For $r_c = 1$ kpc, $2P_{\text{th}}$=P_{g}. The ram pressure, P_{ram} (dashed green line), provided by a subsonic velocity profile, reaches a maximal value at r_c and decelerates beyond this point. P_{ram} is always smaller than P_{th} implying that the Galactic outflow is always thermally-driven.

There are three different possible solutions for a thermally-driven outflow: transonic (a wind), subsonic (a breeze) and supersonic. They are shown in figure 2.2. The transonic solution (solid orange line) is launched with a subsonic velocity and accelerates to reach c_s at $r_c = 1$ kpc and accelerates continuously beyond this point. The subsonic solution (dashed blue line) is launched with a velocity that is insufficient to be able to reach c_s at r_c. The outflow accelerates but reaches a maximum at $r_c = 1$ kpc and then decelerates continuously beyond this point. The supersonic solution (dotted green line) starts with a supersonic velocity and decelerates until it reaches $r_c = 1$ kpc and accelerates beyond this point in a similar way than the transonic solution. Φ used for determining those three solutions is the same as the

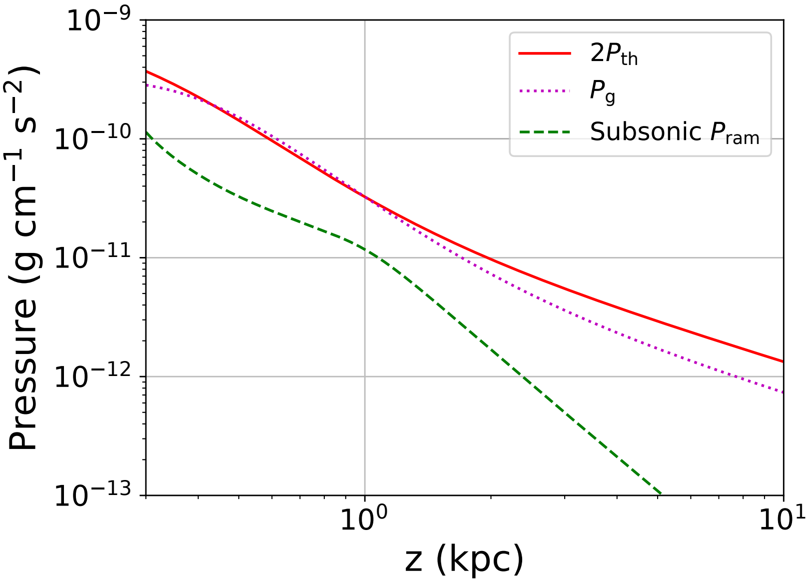

Figure 2.1: The thermal pressure, P_{th}, times a factor 2 is equal to the rotational pressure, P_{g}, induced by the presence of a gravitational field at $r_c = 1$ kpc. The ram pressure, P_{ram}, due to the subsonic nature of the outflow reaches a maximal value at r_c and decelerates continuously beyond this point.

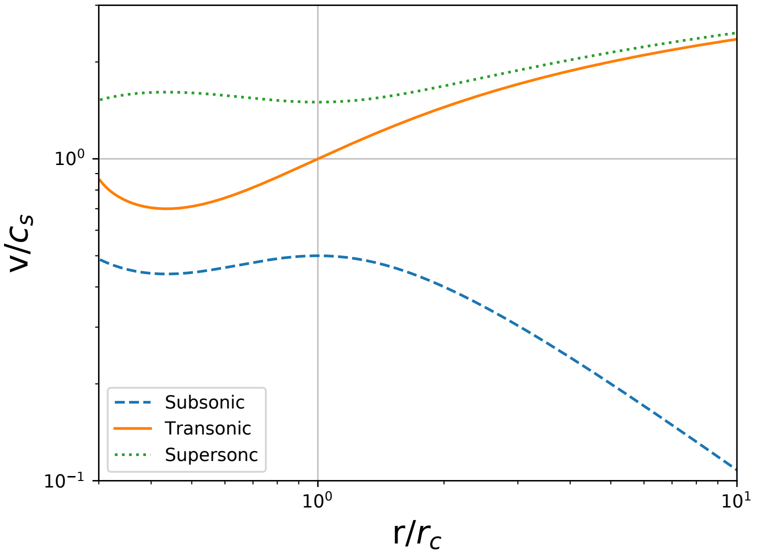

Figure 2.2: Three possible solutions for a thermally-driven outflow are illustrated here. A transonic solution (solid orange line) starts with a subsonic velocity that increases to reach a supersonic velocity at $r_c = 1$ kpc (solid vertical grey line) and accelerates continuously beyond this point. A subsonic solution (dashed blue line) starts with a subsonic velocity as well, but this velocity is less than for the transonic solution. As a consequence, the subsonic outflow cannot reach the supersonic velocity and stays subsonic, reaching a maximal velocity at r_c and decelerating continuously beyond this point. A third possible solution is the supersonic solution (dotted green line), which is a mirror image of the subsonic solution. This solution starts with a supersonic velocity and decelerates until it reaches r_c. Beyond this point, it accelerates in a way similar to the transonic solution. A Galactic Φ as been used for determining those three solutions (see section 2.3). The acceleration observed for the subsonic and transonic solutions as well as the acceleration of the supersonic profile at a distance of 0.3 to 0.45 kpc is due to the gravitational influence of the Galactic bulge.

one used for the numerical simulations (see section 2.3). The deceleration that can be observed, for the subsonic and transonic solutions, from 0.3 to 0.45 kpc is due to the gravitational influence of a Galactic bulge. The acceleration observed for the supersonic solution at the same distance is also due to the Galactic bulge influence.

Although the subsonic solution is a mathematical solution, it is not possible for a system like the Sun that is surrounded by a low pressure medium like the interstellar medium. This can be shown by pursuing the development of Eq. (2.10), which becomes

$$\frac{v^2}{c_s^2} - \ln\left(\frac{v^2}{c_s^2}\right) = \frac{v_c^2}{c_s^2} - \ln\left(\frac{v_c^2}{c_s^2}\right) + 4\ln\left(\frac{r}{r_c}\right) + \frac{2}{c_s^2}\left(\Phi_c - \Phi\right), \tag{2.13}$$

where v_c and Φ_c are the velocity of the outflow and Φ at r_c.

For the solar breeze solution, when $r \to \infty$, $\frac{v}{c_s} \ll 1$ and decreases continuously. For large r, the Eq. (2.13) reduces to

$$\ln\left(\frac{v}{c_s}\right) \approx -2\ln(r) \Rightarrow v \propto \frac{1}{r^2}. \tag{2.14}$$

From Eq. (2.1), it follows that the density of the Solar corona reaches a constant value and then leads to a constant pressure, when the pressure of the interstellar medium is close to zero.

For the solar wind solution, when $r \to \infty$, $\frac{v}{c_s} > 1$ and increases continuously. For large r, the Eq. (2.13) reduces to

$$\frac{v^2}{c_s^2} \approx 4\ln(r) \Rightarrow v \approx 2c_s\sqrt{\ln(r)}, \tag{2.15}$$

leading to $\rho \to 0$ and therefore $P_{\rm th} \to 0$. This solution is suitable for matching with the interstellar pressure.

A Solar subsonic outflow is then not possible because the Sun, as an isolated system, cannot maintain a pressure high enough at a distance large enough. However, the breeze solution is not invalid for a system like the Milky Way since the Galactic halo extends far and exhibits different temperature phases (Dutta et al. 2023). It is able to provide a support through $P_{\rm th}$ ($\sim 0.1 - 0.3$ eV cm^{-3} for a constant temperature of $T = 10^6$ K for the Galactic halo) but also possibly through both magnetic ($0.1 - 0.25$ eV cm^{-3} for a magnetic field of $\sim 1 - 2\ \mu$G in the Galactic halo) and CR pressure ($0.1 - 0.3$ eV cm^{-3}). The propagation of a thermally-driven Galactic outflow is considered and described by a subsonic solution in order to reproduce the velocity profile of the Fermi bubbles (Ashley et al. 2020). This Galactic breeze would therefore find its origin in the vicinity of the Galactic Center and be driven by the hot Galactic halo. To be able to simulate the propagation of such an outflow, it is first necessary to setup the different necessary parameters, i.e. a temperature distribution for the hot Galactic halo and a total Φ for the system.

In the following section, are introduced the expressions and parameters for the total Φ for the Milky Way that will be used for simulating the propagation of a Galactic breeze.

2.3 The Galactic gravitational potential

As r_c depends on a relation between c_s and Φ, it is necessary to define a Galactic Φ that will determine a propagation of the outflow.

However, this task is not that simple, as the Galactic Φ can only be deduced through observations of the rotational velocity of the different elements, mostly the stars, that compose the Milky Way. Moreover, the Galaxy is not a homogeneous system and is therefore considered to have different parts. The three main parts are the bulge, the disc and the dark matter halo. Other parts can be considered, such as the massive black hole at the center of the Galaxy (Reid 2009; Genzel, Eisenhauer and Gillessen 2010) or the central molecular zone (CMZ), a dense gas surrounding the black hole (Mills 2017; Tress et al. 2020), depending on the studied system.

Many observations have been made for determining the rotational curve of the Galaxy (Fich, Blitz and Stark 1989; Maciel and Lago 2005; Bovy, Hogg and Rix 2009; Sofue 2012; Bhattacharjee, Chaudhury and Kundu 2014) and continue to this day. The Gaia mission (Gaia Collaboration 2018) is so far the most ambitious project for the observation of the Milky Way and some of its data, as it will be seen later, has been used to provide a constraint on Φ. However, Gaia only measures the velocity of the stars and not their acceleration and therefore, not their Φ which can thus only be inferred. So far, several mass models for the Milky Way have been proposed (Schmidt 1956; Caldwell and Ostriker 1981; Dehnen and Binney 1998; Klypin, Zhao and Somerville 2002; McMillan 2011; McMillan 2017).

As part of the research carried out for this thesis, only the bulge, the disc and the halo are considered. The black hole and the CMZ have a too low Φ, compared with the other three components, for the distances involved. The total gravitational potential, Φ_{tot}, is then expressed as

$$\Phi_{\mathrm{tot}} = \Phi_{\mathrm{b}} + \Phi_{\mathrm{d}} + \Phi_{\mathrm{h}}, \tag{2.16}$$

where Φ_{b} represents the bulge, Φ_{d} represents the disc and Φ_{h} represents the dark matter halo.

The expression for each of those potentials must be determined. For this, a mathematical model has been used (Flynn, Sommer-Larsen and Christensen 1996), that aims to fit at best the observations of the rotation curve of the Milky Way. The following subsections introduce those different potentials: the bulge (2.3.1), the disc (2.3.2) and the dark matter halo (2.3.3).

2.3.1 The Galactic bulge

It has been more than seventy years since the Galactic bulge has been identified as a distinct component of the Galaxy by observations (Baade 1946) and yet its formation or its age are still under debate. A Colour-Magnitude Diagram (CMD) (Terndrup 1988) indicates, for the bulge stellar population, an age of ~ 10 Gyr (Ortolani et al. 1995; Clarkson et al. 2008; Gennaro et al. 2015).

Based on the velocities observed, a barred bulge shape has been proposed (de Vaucouleurs 1964). The presence of this bar has been confirmed by a numerical modelling of the gas motion in the bulge region (Binney et al. 1991; Englmaier and Gerhard 1999; Fux 1999) and by the near-infrared observations made by the COBE satellite (Blitz and Spergel 1991; Weiland et al. 1994; Binney, Gerhard and Spergel

Component	Parameter	Value
Φ_b	r_{C_1}	2.7 kpc
	M_{C_1}	6.0×10^9 $M_\odot$
	r_{C_2}	0.42 kpc
	M_{C_2}	3.2×10^{10} $M_\odot$
Φ_d	b	0.3 kpc
	a_1	5.81 kpc
	M_{D_1}	1.32×10^{11} $M_\odot$
	a_2	17.43 kpc
	M_{D_2}	-5.8×10^{10} $M_\odot$
	a_3	34.86 kpc
	M_{D_3}	6.6×10^9 $M_\odot$
Φ_h	r_s	21.5 kpc
	M_{200}	2×10^{12} $M_\odot$

Table 2.1: List of parameters for the Galactic Φ_tot model.

1997). More recent data have confirmed that the bulge has a box/peanut shape (McWilliam and Zoccali 2010; Nataf et al. 2010; Wegg and Gerhard 2013).

The bulge has therefore a complex shape and its mass distribution is subject to numerous estimations (Licquia and Newman 2015; Bland-Hawthorn and Gerhard 2016). For determining it, a combination of tracer densities and multiple field kinematics has been used (Portail et al. 2015; Portail et al. 2017). However, there are uncertainties due to the continuous transition between the box/peanut bulge and the central long bar, for which, an arbitrary distance must be chosen for determining which stars constitute the bulge. From those choices, a total mass of $\sim 1.85\times10^{10}$ $M_\odot$ has been determined (Portail et al. 2017).

For this thesis, a simpler model for the bulge has been chosen. The bulge potential is described by a Plummer potential (Plummer 1911; Flynn, Sommer-Larsen and Christensen 1996). Its expression is given by

$$\Phi_\mathrm{b} = \sum_{i=1}^{2} -\frac{GM_{\mathrm{C_i}}}{\sqrt{r^2 + r_{\mathrm{C_i}}^2}}, \tag{2.17}$$

where r represents the spherical radius, r_c the spherical scale radius and $M_{\mathrm{C_i}}$ represents the mass for the two components of the bulge. M_{C_1}, M_{C_2}, r_{C_1} and r_{C_2} are given in table 2.1. This potential has the advantage of having a simple analytical form and reproducing the central concentration observed in many galactic bulges.

2.3.2 The Galactic Disc

The Galactic disc is composed of a thin disc and a thick disc (Gilmore and Reid 1983), both being distinct by their chemistry, their age and their elevation (Bensby, Feltzing and Oey 2014; Masseron and Gilmore 2015; Hawkins et al. 2015). Photometric studies have found an exponential scale height distribution of $\sim$ 250 - 350 pc for the thin disc (Reid 1993; Gould, Flynn and Bahcall 1998; Ojha 2001; Jurić et al. 2008) and $\sim$ 700 - 1200 pc for the thick disc(Siebert et al. 2011).

Due to the low extinction at the poles of the disc, the scale height is well determined in the infrared and optical spectra. It is not the case for the scale length. More than one hundred papers exist about the determination of the disc parameters (Bland-Hawthorn and Gerhard 2016). So far, the estimation of the scale length for the thin disc is $\sim$ 2.6 kpc and $\sim$ 3.6 kpc for the thick disc (Jurić et al. 2008).

In addition, there is also an outer disc for which the detailed structure and physical extent are not well known. Its edge has been estimated to be between 10 and 15 kpc, based on infrared and optical surveys (Habing 1988; Robin, Creze and Mohan 1994; Ruphy et al. 1996; Minniti et al. 2011). Determining the edge is also made more difficult by the possible distribution of the stellar density. Some external galaxies have an inflection in their stellar density, expressed as a break in their exponential density profile (Pohlen and Trujillo 2006). This profile is common but models with no breaks and continuous exponential can also exist (Bland-Hawthorn et al. 2005; Irwin et al. 2005; Ellis and Bland-Hawthorn 2007). Moreover, the Galactic disc could be extended to $\sim$ 20 kpc due to the presence of the Monoceros Ring (Newberg et al. 2002; Ibata et al. 2003) and Molecular gas clouds having been observed beyond 20 kpc (Yasui et al. 2008; Kobayashi et al. 2008). The edge of the $\mathrm{H_I}$ gas has even been pushed until $\sim$ 60 kpc, within the range of the Magellanic clouds (Kalberla and Dedes 2008). The total mass of the Galactic disc is naturally not easy to determine as the lengths of the different components are unsure. This mass is usually considered to be between $\sim 3.75 \times 10^{10}\ M_{\odot}$ and $\sim 5.25 \times 10^{10}\ M_{\odot}$ (McMillan 2011; Binney 2012; Bovy and Rix 2013; Piffl et al. 2014; Sanders and Binney 2015; Binney and Piffl 2015). This mass range has been inferred from both the observation of the kinematics of stars present in the Galaxy and a numerical model offering a good comparison with the data.

Following the observations, the disc potential has three components that are based on a Miyamoto-Nagai potential (Miyamoto and Nagai 1975; Flynn, Sommer-Larsen and Christensen 1996) and is expressed by

$$\Phi_{\mathrm{d}} = \sum_{i=1}^{3} - \frac{G M_{D_{\mathrm{i}}}}{\sqrt{R^2 + \left(a_{\mathrm{i}} + \sqrt{z^2 + b^2}\right)^2}}, \tag{2.18}$$

where R and z are the cylindrical coordinates, b is the scale height, a_{i} is the cylindrical scale radius for the three different components and $M_{\mathrm{D_i}}$ their corresponding masses. These values are given in table 2.1.

2.3.3 The Galactic halo

Two different types of halo have been observed for the Milky-Way. A stellar halo and a hot gaseous halo. A third one, theorised to explain the constant rotational velocity observed for the Milky Way, is the dark matter halo.

Stellar halo

The stellar halo has been identified as composed of a population of old metal poor stars. This halo presents large random motions and no rotations or only a little and would have been formed by a smooth-envelope of old stars as the Galaxy collapsed during the first time of its formation (Eggen, Lynden-Bell and Sandage 1962). It has also been proposed that the stellar halo is due to independent infalling fragments since there exists a wide range of metal abundance independent of a Galactocentric distance (Searle and Zinn 1978).

The stellar density, as well as being used to determine the mass distribution, is used to study the past accretion history of the Milk Way. Several tracers are used as RR Lyrae, blue horizontal branch stars, red giants and near main sequence turnoff stars (Vivas and Zinn 2006; Ivezić et al. 2008; Belokurov et al. 2014; Xue et al. 2014). The total density profile is similar to an Einsato function (Xue et al. 2015).

Several estimations for the stellar halo mass have been done. A first estimation has given a radius between 1 and 40 kpc, the halo stellar mass being $\sim 3.7 \pm 1.2 \times 10^8\ M_\odot$. (Bell et al. 2008). A later estimation for a stellar halo mass within a radius of 10 to 45 kpc gave $\sim 3 \times 10^8\ M_\odot$ (Kimmig et al. 2015).

Hot halo

The existence of a hot halo surrounding the Galactic disc has been highlighted by the observations of $\mathrm{H_I}$ clouds that should be confined by an external medium (Spitzer 1956). Its extension and its proximity to the Galactic plane is still unclear. The presence of this hot halo gas is supported by numerical simulations (Nuza et al. 2014), for it has a uniform temperature profile ($\mathrm{T} \gtrapprox 10^5$ K) for each galaxy simulated and is in good agreement with the observed profiles (Miller and Bregman 2015). The observations of a hot halo are performed through the bright Active Galactic Nucleus (AGN). Through observations of sight lines, they are detected with $\mathrm{O_{VII}}$ and $\mathrm{O_{VIII}}$ in absorption, ram-pressure stripping of gas and high-resolution X-ray spectra with energies between 0.1 - 1 keV. This implies a temperature between 10^{6-7} K (Blitz and Robishaw 2000; Stanimirović et al. 2002; Paerels and Kahn 2003; Sembach et al. 2003; Bregman and Lloyd-Davies 2007; Gatto et al. 2013; Miller and Bregman 2015; Salem et al. 2015).

The early models for modelling the hot halo using X-ray observations assumed an isothermal distribution and a constant density (Bregman and Lloyd-Davies 2007; Gupta et al. 2012). However, observations found different density distributions for electrons. One at $n = 9 \times 10^{-4}$ cm^{-3} at $r = 19$ kpc and the other $n \geq 2 \times 10^{-4}$ cm^{-3} at $r \geq 139$ kpc (Wang and Yao 2012). Another model for which the hot halo is composed of an adiabatic gas in hydrostatic equilibrium with the Galactic potential has been proposed (Fang, Bullock and Boylan-Kolchin 2013). It must be noted that observations tend to show that the Galactic halo does not have a constant entropy profile (Miller and Bregman 2015; Crain et al. 2010). At the present day, the hot halo temperature, inferred from X-ray observations, seems to be fairly uniform, around a value of $\sim 2 \times 10^6$ K but this feature does not imply strictly an isothermal profile (Henley et al. 2010).

More recent observations of $\mathrm{O_{VII}}$ and $\mathrm{O_{VIII}}$ emission lines have been studied (Henley and Shelton 2012; Miller and Bregman 2013; Miller and Bregman 2015), in combination with X-ray measurements to determine a hot halo density of 10^{-4} cm^{-3} to 10^{-5} cm^{-3} for 10 kpc $\leq r \leq$ 100 kpc. The hot halo gas mass has been approximated to $10^{10}\ M_\odot$ within 250 kpc. To obtain this result, three assumptions have been made. First, the density profile for the hot halo is described by a spherically symmetric β-model taking the form $n(r) \propto r^{-\beta/2}$. Second, the hot halo is isothermal with a temperature of $T = 2 \times 10^6$ K. Third, it is in collisional ionisation equilibrium. Following those works, a physically plausible hot Galactic halo consistent with the observed halo dynamic and with the UV/X-ray measurements has been proposed (Tepper-Garcia, Bland-Hawthorn and Sutherland 2015). For this model, a dark matter halo is normalised to the density profile and the total mass is inferred from the observations of the kinematics of halo stars (Kafle et al. 2012). This model is valid if the Galactic dark matter halo is an isothermal sphere and in hydrostatic equilibrium with the gravitational potential (Bland-Hawthorn and Gerhard 2016). The study of the hot halo dispersion implies a gas temperature of $T \approx 10^6$ K. The total baryonic mass range for the hot halo gas, within the virial radius, has been deduced to be $\sim 8.8 \pm 1.2 \times 10^{10}\ M_\odot$ (Nuza et al. 2014; Miller and Bregman 2015).

Dark matter halo

The model of the Cold Dark Matter halo is often called a necessary element for explaining the quasi-constant rotation curve of the Galaxy. The mass of this dark matter must then be well known within the virial radius r_{vir}. As there is no direct observation of dark matter, different models can be adopted. In general, the virial mass, M_{vir}, is expressed as the mass within a central region for which the average density exceeds a multiple of the mean density of the Universe. The virial density is expressed as $\rho_{\text{vir}} = \Delta_{\text{vir}} \Omega_M \rho_{\text{crit}}$ (Klypin, Zhao and Somerville 2002; Kafle et al. 2014), where $\Delta_{\text{vir}} = 340$ is an overdensity constant, Ω_{M} is a density parameter and ρ_{crit} is the critical density of the Universe. The virial radius is expressed as

$$r_{\text{vir}} = 258 \left(\frac{\Delta_{\text{vir}} \Omega_{\text{M}}}{102} \right)^{-1/3} \left(\frac{M_{\text{vir}}}{10^{12}\ M_\odot} \right)^{1/3} \text{kpc.} \tag{2.19}$$

For a Navarro–Frenk–White (NFW) halo model, the scale height is $r_h \approx 25$ kpc assuming a concentration parameter of $c \approx 10$ (van der Marel et al. 2012). Another mass estimation used is M_{200} for which the average density within r_{200} is $\rho_{200} = 200\rho_{\text{crit}}$ (Bryan and Norman 1998; Klypin, Zhao and Somerville 2002). M_{vir} is not a total mass because the dark matter profiles extend and quickly drop beyond the virial radius. One constraint for the total mass of the Galaxy comes from what is called the timing mass (Kahn and Woltjer 1959). This implies that the mass of our Galaxy and Milky Way galaxy types, like the galaxy M31, must be sufficient to overcome the universal expansion to explain their observed kinematic movement. Observations of galaxy pair, after considering the orbit of M33 around M31, have led to estimate the total timing mass at $M_{\text{timing, vir}} = 3.2 \pm 0.6 \times 10^{12}\ M_\odot$. It has been estimated that the mass of M31 is comparable with the mass of the Milky Way, providing an upper limit for the virial mass of $M_{\text{vir}} = 1.6 \times 10^{12}\ M_\odot$ for our Galaxy (van der Marel et al. 2012).

Other methods that use the timing mass, for the estimation of the virial mass, are limited to the regions explored, for which the spatial distribution and kinematics are used for an estimation of the enclosed mass. The Galaxy mass has been estimated using the kinematics of halo stars, satellite galaxies and globular clusters. Those observations give a low total mass of $M_{200} \leq 10^{12}\ M_\odot$ (Xue et al. 2008; Deason et al. 2012; Kafle et al. 2012; Kafle et al. 2014). The estimations based on the kinematics of satellites and globular clusters result in a higher value of $M_{200} = 1 - 2 \times 10^{12}\ M_\odot$ if the Leo I dwarf satellite galaxy is assumed to be bound to the Milky Way. If Leo

I is assumed to be unbound, a value of $M_{200} \leq 10^{12}\ M_{\odot}$ is found (Wilkinson and Evans 1999; Li and White 2008; Watkins, Evans and An 2010).

For this thesis, the hot halo potential is based on a NFW profile (Navarro, Frenk and White 1996; Flynn, Sommer-Larsen and Christensen 1996) and is given by

$$\Phi_{\rm DM} = -\frac{GM_{200}}{r_s f(c_{200})} \frac{\ln(1 + r/r_s)}{r/r_s}, \tag{2.20}$$

where M_{200} is the mass inside the virial radius, $r_{200} = 258$ kpc (Taylor et al. 2016). c_{200} is the concentration parameter defined as $c_{200} = r_{200}/r_s$, where r_s is the scale radius. Both M_{200} and r_s are given in table 2.1. The function $f(c_{200})$ is expressed by $f(c_{200}) = \ln(1 + c_{200}) - c_{200}/(1 + c_{200})$.

This potential has been able to provide a good fit to the observed rotation curves of the Galaxy and the distribution of mass in galaxy clusters.

For the numerical simulations, only two halos have been considered. As the dark halo mass dominates over the two other halos, it has been chosen for defining the gravitational potential for the halo component. The hot halo gas is represented by its hot temperature and has been setup with a temperature of $\sim 4 \times 10^6$ K (see section 2.5).

2.3.4 Gravitational potential model

The normalisation of $\Phi_{\rm tot}$, i.e., the value of the masses for the different components, has been chosen based on observations. The Gaia mission (Gaia Collaboration 2016b; Gaia Collaboration 2016a; Gaia Collaboration 2018) has provided data about the proper motion of more than a billion stars. Those new data made it possible to provide a range of power-laws used for fitting the Milky Way gravitational potential (Watkins et al. 2019), allowing a constraint for a normalisation of $\Phi_{\rm tot}$ used for the numerical simulations.

The wind equation, see Eq. (2.10), shows that there is a relation between c_s from the hot halo gas and $\Phi_{\rm tot}$. For the simulations of a Galactic breeze, the value of c_s is of uttermost importance. The model must be able to reach the highest possible velocity for the breeze while maintaining r_c at 1 kpc. This is in order to get as close as possible to the observed velocity of ~ 300 km s^{-1} for the cold clouds at a distance of ~ 1 kpc from the Galactic Center (Bordoloi et al. 2017; Ashley et al. 2020). In figure 2.3, the fitting power-laws are given (dot-dashed black lines) and compared with $\Phi_{\rm tot}$ (solid red line), which is composed by the Galactic bulge potential (dot-dashed green line), $\Phi_{\rm b}$, the Galactic disc potential (dotted blue line), $\Phi_{\rm d}$ and the hot Galactic halo potential (dashed orange line), $\Phi_{\rm h}$. The two vertical dotted lines at $R = 2$ kpc and $R = 21$ kpc give the spatial range for which the constraints provided by the Gaia observations are applicable. The dot-dashed black lines show the extent of the best-fitting power laws, between the $2 - 21$ kpc region and their extension beyond this zone. The different potentials have been normalised so $\Phi_{\rm tot}$ reaches the vicinity of the upper limit of the fitting range (see table 2.1 and Eq. (2.16)), allowing to increase the constant temperature for the hot Galactic halo.

The next step is to consider the value that the temperature associated with the hot Galactic halo should have. For a thermally-driven outflow, the relation between $\Phi_{\rm tot}$ and c_s determines the position of r_c. For the Galactic breeze profile, based on

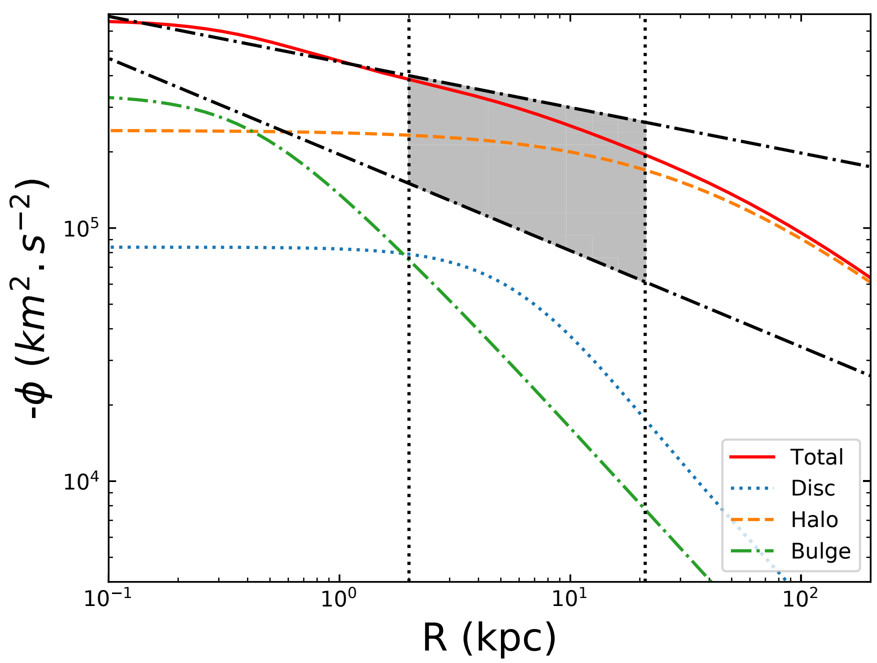

Figure 2.3: $\Phi_{\rm tot}$ (solid red line) and its different components used for the simulations are illustrated here. There is a Galactic bulge (dotted-dashed green line), that dominates until a Galactic radius of $\sim$ 500 pc. A Galactic disc (dotted blue line) and a hot Galactic halo gas (dashed orange line) dominate the Galactic radius above $\sim$ 500 pc. For the numerical simulations, in order to use the highest c_s possible, $\Phi_{\rm tot}$ has to be increased to the highest possible value. From (Watkins et al. 2019), a fitting range has been provided for $\Phi_{\rm tot}$ from 2 kpc to 21 kpc (grey zone). $\Phi_{\rm tot}$ has then been normalised to reach the upper limit of this fitting range, allowing to get the highest c_s possible for the galactic breeze model.

the observations, $r_c \approx 1$ kpc. From this constraint, it is possible to determine a value for c_s. This is discussed in the following section.

2.4 Analytic Galactic breeze profile

The subsonic solution, Eq. (2.13), can be solved numerically to get a steady-state solution that can be compared with observations of the UV absorption lines provided by the high-velocity cold clouds present inside the Fermi bubbles (Fox et al. 2015; Bordoloi et al. 2017; Savage et al. 2017; Karim et al. 2018; Ashley et al. 2020; Cashman et al. 2021; Sofue 2022). This comparison can be seen in figure 2.4. The solid blue line represents the steady-state subsonic solution. The blue and orange dots come from recent observations of the Fermi bubbles velocity profile (Bordoloi et al. 2017; Ashley et al. 2020). The green dot comes from an observation provided by a cylindrical $\rm H_I$ high-velocity cold cloud at a Galactic radius of $\sim$ 1 kpc (Sofue 2022). For the resolution of the Eq. (2.13) it has been considered that the subsonic outflow reaches $\sim$ 85% of $c_{\rm s} \approx 250$ km s^{-1} at the critical radius $r_{\rm c} \approx 1$ kpc. This configuration has been chosen since, for the numerical simulations, a Mach number at r_c too close to 1 could create instabilities leading to a supersonic outflow. Hence, a Mach number, $M = 0.85$, has been chosen as it implies a velocity at r_c close to c_s that stays stable and provides a steady-state simulation. The subsonic solution then shows a continuous deceleration profile similar to the one deduced from observations.

However, it must be noted that the subsonic velocity profile does not reach the observed velocity of 300 km s^{-1} (Bordoloi et al. 2017; Ashley et al. 2020). Such a velocity, for the Galactic breeze model considered here, could be reached for a larger Φ_{tot}. However, this would go beyond the upper fitting-range provided by the observations (see section 2.3.4). Moreover, it can be seen in figure 2.4 that the subsonic velocity profile first decelerates and reaches a minima at $\sim$ 400 pc, accelerates until it reaches r_c. This effect is due to the gravitational influence of the Galactic bulge and imposes a minimal radius for the numerical simulations of $\sim$ 300 pc since for a lesser value, the outflow would be supersonic.

As a distribution for Φ_{tot} has been defined (see section 2.3) and a value for c_s has been fixed, the last step is to define a density distribution for the hot Galactic halo. So far, the observations of these distributions did not show strong variations that could indicate the presence of a shock (Martynenko 2022). This is another possible reason to consider a Galactic breeze model, as it has no influence on a density distribution. This is discussed in the following section.

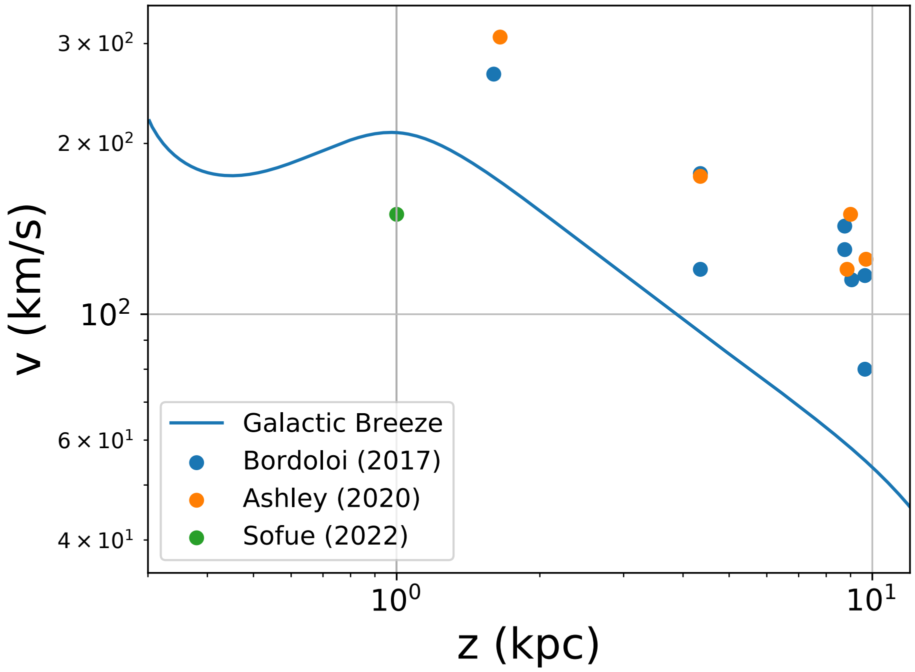

Figure 2.4: The deceleration exhibited in a steady-state subsonic velocity profile (solid blue line) matches well with the observed velocity profile of the Fermi bubbles along the Galactic height (blue, orange and green dots). Those observations have been provided by the UV absorption lines from the high-velocity cold clouds present in the bubbles. Although the deceleration matches well, the magnitude of the velocity does not match with the observations, for which the maximal velocity is $\sim$ 300 km s^{-1}. For the Galactic breeze model, for which the maximal possible thermal velocity is $c_s \approx 250$ km s^{-1}, assuming a Mach number, M = 0.85, at $r_c = 1$ kpc, the maximal velocity is $\sim$ 200 km s^{-1}.

2.5 Density distribution for the hot Galactic halo

In the previous section, the Galactic breeze profile was introduced (see section 2.4). This profile has been defined to be as close as possible to the observations. That is, to reach a maximum velocity at ~ 1 kpc and decelerate continuously beyond this point. As the breeze solution is independent of the density distribution, only $\Phi_{\rm tot}$ and c_s are necessary. Those parameters can be used to define a hydrostatic density distribution.

2.5.1 Hydrostatic density profile

In addition to $\Phi_{\rm tot}$ and c_s, the density of the hot Galactic halo gas, in which the subsonic outflow will propagate, must be defined for the numerical simulations. For this, a hydrostatic density distribution has been chosen. A model proposed during the 1960s explored this model based on stability considerations between gas, magnetic field and CR (Parker 1966). Numerical simulations are in good agreement with all-sky survey data from radio to gamma-ray energy range (Buote and Canizares 1996; Kalberla and Kerp 1998; Pietz et al. 1998; Anderson and Bregman 2010; Gupta et al. 2012) but also observations of absorption lines (Miller and Bregman 2013; Meiring et al. 2013). The hydrostatic density profile is dictated by $\Phi_{\rm tot}$ and c_s. The initial gas number density for the hydrodynamic simulations is expressed by

$$n_{\rm halo} = n_{\rm 10\ kpc} \exp\left(-\frac{\Phi_{\rm tot}}{c_{\rm s}^2}\right), \tag{2.21}$$

where $n_{\rm 10\ kpc}$ is a normalisation constant. Its value has been fixed at $n_{\rm 10\ kpc} = 6.35 \times 10^{-4}\ {\rm cm^{-3}}$ in order to be compatible with the observational values from 10 to 100 kpc (Gupta, Mathur and Krongold 2017; Martynenko 2022). Figure 2.5 shows the density distribution obtained for the normalisation of $\Phi_{\rm tot}$ and the resulting c_s. The red area represents the fitting-range provided by both X-ray spectroscopic observations and satellite galaxies ram pressure stripping studies (Martynenko 2022). The combination of the normalised $\Phi_{\rm tot}$ (see section 2.3) and $c_{\rm s} = 250\ {\rm km\ s^{-1}}$ corresponding to $kT = 400$ eV ($\approx 4 \times 10^6$ K) (see section 2.4) provides a hydrostatic density distribution matching well with the provided fitting range.

2.5.2 Influence of a breeze and a wind solution on the density distribution

Transonic and subsonic outflows have a different effect on the density distribution of the medium in which they propagate. As a subsonic outflow produces no shock, the surrounding gas is not disrupted. It is not the same for a transonic outflow that produces a shock as it goes from a subsonic to a supersonic phase. This shock propagates with the outflow and sweeps up the surrounding gas, significantly changing its density distribution. Figure 2.6 shows the influence of a subsonic solution (solid blue line) and a transonic solution (solid red line) on an initial hydrostatic density distribution similar to the one that will be used for the numerical simulations. For $r < r_c$, both solutions exhibit a subsonic velocity profile and the density distribution is not perturbed. At r_c, the transonic solution becomes supersonic, sweeping up the surrounding density. The initial hydrostatic density distribution, which can be approximated by $n \propto 1/r$ (dashed light blue line), goes to $n \propto 1/r^2$ (dashed orange line) due to the influence of the sweeping effect of shock propagation. However, recent observations of $\rm O_{VII}$ and ram-pressure stripping have provided a fitting

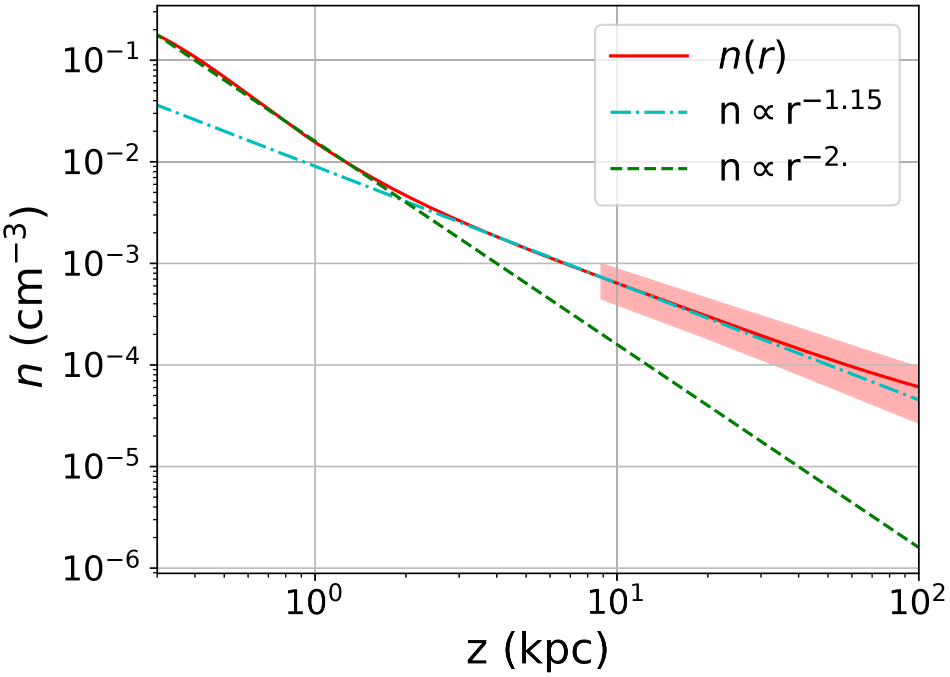

Figure 2.5: The number density distribution used for the hydrodynamic simulations (solid red line) is compared with observational data provided by (Martynenko 2022). The fitting range is represented by the red zone, for which the hydrostatic number density distribution matches well. It depends on both Φ_{tot} and c_s. Here $c_s = 250$ km s^{-1} corresponds to a temperature of $kT = 400$ eV. Φ_{tot} has been normalised to correspond to the largest possible value following a fitting range provided by observations as described in section 2.3.

range for a distance going from ~ 8 kpc to 100 kpc that matches with a hydrostatic density distribution (Martynenko 2022). At a distance of ~ 10 kpc, the edges of the eROSITA bubbles (Predehl et al. 2020) should have an impact on the density distribution if they have been produced by a transonic outflow, but such an effect does not seem to be observed. Now that a steady-state subsonic solution has been obtained, the next step is to use a hydrodynamic code set up with the expressions and values of Φ_{tot}, c_s and the hydrostatic density distribution. This code is introduced, its setup and results are introduced in the following section.

2.6 Hydrodynamic simulation

Both mass and momentum conservation equations in steady-state (see Eq. (2.1) and Eq. (2.4)) have been used to get a Galactic breeze solution. However, to be able to study the influence of a Galactic breeze model on Fermi bubbles features, a hydrodynamic code is required.

2.6.1 PLUTO code

The PLUTO code (Mignone et al. 2007), standing for Parallel Linear Unstructured Transient Operator, is an open-source magnetohydrodynamic (MHD) simulation code. It can solve the equations governing hydrodynamic fluid dynamic, which are the mass conservation equation, the momentum conservation equation and the en-

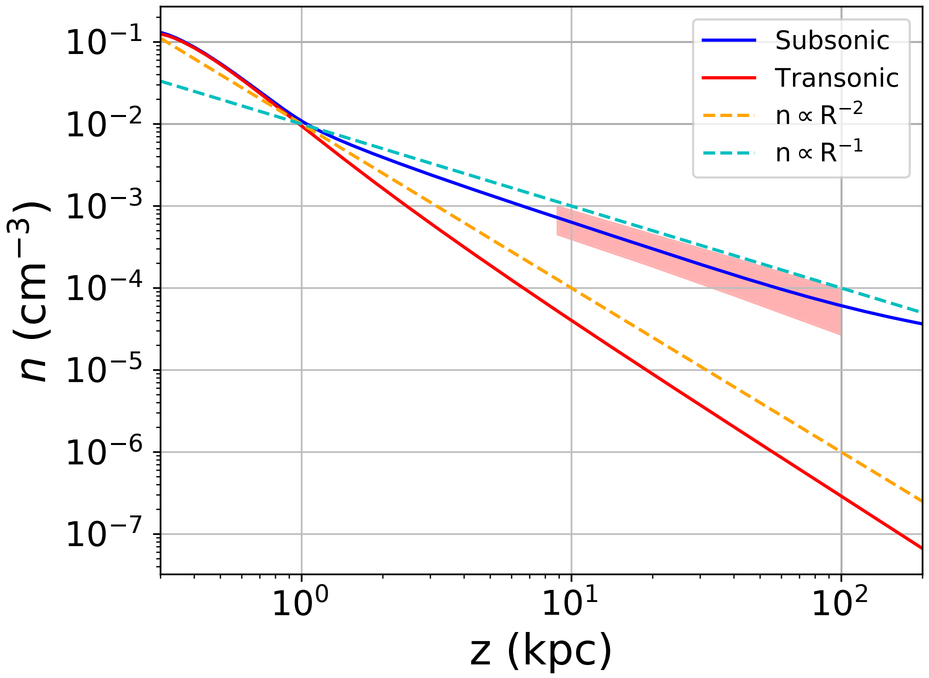

Figure 2.6: The effects of a subsonic and a transonic solution on an initial hydrostatic density distribution are presented here. The subsonic solution does not produce a shock and does not influence the initial hydrostatic density distribution of the surrounding hot Galactic halo (solid blue line), which can be approximated by $n \propto 1/r$ (dashed light blue line). The transonic solution, starting with a subsonic velocity, reaches a supersonic velocity at $r_c = 1$ kpc. This has the effect of sweep up the gas (solid red line). The initial density distribution decreases along the radius and can be approximated by $n \propto 1/r^2$ (dashed orange line). The observations have provided a fitting range (red zone) for a distance of ~ 8 kpc to 100 kpc that matches with an hydrostatic density distribution (Martynenko 2022).

ergy conservation equation. When MHD equations are considered, it also solves the evolution of a magnetic field. The code takes advantage of parallel computing architectures. PLUTO manages various numerical methods to solve the hydrodynamic equations and uses a finite volume method that discretizes the solution domain into a set of control volumes. For each of those volumes, an integral form of the conservation equations is applied. Several Riemann solvers are available to calculate fluxes across cell interfaces. The PLUTO code has been applied to a large variety of astrophysical problems, like the study of the accretion disc around a black hole (Hogg and Reynolds 2018), the dynamical behaviour of Supernovae (Matsuoka and Sawada 2024), the behaviour of stellar or Galactic winds and jets and the study of the emission of the Fermi bubbles (Sarkar, Nath and Sharma 2017).

2.6.2 Numerical Setup

For solving the hydrodynamic equations, a linear reconstruction method has been selected (Mignone 2014). It assumes a linear variation of the conserved variables within each cell. It is a second order accurate in space, with a stencil three points wide. For time stepping, a second order Runge-Kutta method has been used. Also, a Van Leer limiter has been chosen. It is a slope limiter used to prevent unphysical oscillations. A HLL (Harten-Lax-van Leer) Riemann solver has been selected

(Mignone 2007). This solver is known for its simplicity and computational efficiency, making it a popular choice for many simulations.

Computational grid

The computational grid has been setup as a spherical logarithmic 2D grid (r, θ). 256 bins are used in the r-direction and 92 bins in the θ-direction. The inner radius has been fixed at 300 pc and the outer radius at 300 kpc. This last value has been chosen in order to prevent some unphysical perturbations in the computation grid. It appears that the very low velocity of the outflow at large radii has the effect, when the outflow reaches the outer boundary, of causing a large disturbance that propagates through the grid. The outer radius has then been set up at a far enough distance that this effect does not occur. The simulation domain covering a quarter of a single hemisphere, θ ranges from 0 to $\pi/2$.

Boundary conditions

As a linear reconstruction has been chosen for the simulations, the ghost zone, i.e., the region that surrounds the computational grid, is two cells deep.

The outflow is injected at the inner radius. The initial velocity is calculated by solving numerically the Eq. (2.13) for a breeze solution defined with a Mach number of $M = 0.85$ at r_c.

For the outer radius, the boundary has been set up as an outflow one. The purpose of such a boundary is to simulate the natural behaviour of the system when a fluid is allowed to freely leave the computational domain without significant reflections or artificial effects. For the θ direction, both inner and outer boundaries have been set up to be reflective.

Initial setup

The computational grid at $t = 0$ represents the hot Galactic halo in which the outflow will propagate once $t > 0$. The hot Galactic halo is represented by a hydrostatic density distribution ρ, as it has been defined in section 2.5.1. The two components needed for describing this density distribution , Φ_{tot} and c_s are defined as described in section 2.3 for Φ_{tot} and in section 2.5 for c_{s}. As an isothermal gas is considered for describing the hot Galactic halo, the initial thermal pressure is described as (see Eq. (2.7))

$$P_{\text{th}} = \rho c_{\text{s}}^2. \tag{2.22}$$

2.6.3 Subsonic velocity distribution

A first step is to check that the numerical simulations are able to provide the correct velocity profile. In figure 2.7, a comparison is made between a steady-state subsonic profile (dashed black line) and the velocity profile obtained with PLUTO (solid blue line), along the z-axis, after the simulation reaches a steady-state. The simulated breeze appears to match well with the expected velocity at $r_c = 1$ kpc but presents a deceleration less steep than the steady-state. This difference is not due to the resolution of the numerical grid as larger resolutions produce the same distribution. The steady-state solution corresponds to the analytic subsonic solution of the outflow. It does not include the dynamic of the system as do the 2D model provided by the numerical simulation with PLUTO. For this model, the asymmetry of the Galactic potential drives the asymmetry of the velocity profile. The outflow propagates mainly and is accelerated along the z-direction. The largest difference between the two profiles is only of ~ 15 km s^{-1}. The setup of the code seems then to be able to simulate well a subsonic profile propagating into the hydrostatic density distribution of a hot Galactic halo and an asymmetric $\Phi_{\rm tot}$.

Figure 2.8 shows the 2D map of the velocity distribution for the subsonic profile in both R and z-directions. The outflow propagates mainly along the z-direction and a pinch is formed. This is due to the asphericity of the disc component for $\Phi_{\rm tot}$. Close to the Galactic Center, the outflow takes a conic shape and extends progressively to a lobular shape as the outflow decelerates.

2.7 Conclusion for this chapter

Observations of the Fermi bubbles have shown that the line-of-sight velocity exhibits a velocity of ~ 300 km s^{-1} at a Galactic height of ~ 1 kpc from the Galactic Center and decelerates continuously beyond this distance (Bordoloi et al. 2017; Ashley et al. 2020). This velocity profile is reminiscent of a subsonic solution for the hydrodynamic equations proposed first by Bondi for a mechanism of accretion around stars (Bondi and Hoyle 1944) and explored then by Parker for describing a solar outflow (Parker 1965). If the subsonic solution cannot be applied to an isolated system like the Sun it is still possible to apply this solution to a complex system like the Milky Way.

The subsonic solution has been first explored analytically. It is defined by two parameters. A gravitational potential, able to describe the rotation velocity observed for the Milky Way (Rubin, Ford and Thonnard 1980) and a thermal velocity for the hot Galactic halo (Miller and Bregman 2015). The Galactic gravitational potential used is composed of a bulge, a disc and a dark matter halo that has been normalised through a fitting range based on the observations provided by the Gaia mission (Martynenko 2022). With this normalised Galactic gravitational potential and considering a maximum velocity for the outflow, reached at a Galactic height of 1 kpc, the corresponding thermal velocity for the hot Galactic halo is equal to 250 km s^{-1}. This is equivalent to a temperature of 400 eV or $\sim 4\times10^6$ K in accordance with observations (Das et al. 2019b; Das et al. 2019a).

Following this work, a numerical simulation has been performed with the PLUTO code (Mignone et al. 2007). It appears that the subsonic solution is able to produce a steady-state solution. Under the influence of the disc, through its gravitational potential, a pinch appears in the subsonic velocity distribution at the base of the outflow. A Galactic breeze is able to produce a bubble shape and its profile along the cylindrical axis z matches with the analytic solution. However, it appears that the hydrodynamic model alone is not enough to be able to reach a velocity of ~ 300 km s^{-1} at a Galactic height of 1 kpc and that an additional mechanism must be considered.

Now that a subsonic steady-state solution has been obtained by solving numerically the hydrodynamic equations, the output of the velocity profile can be used

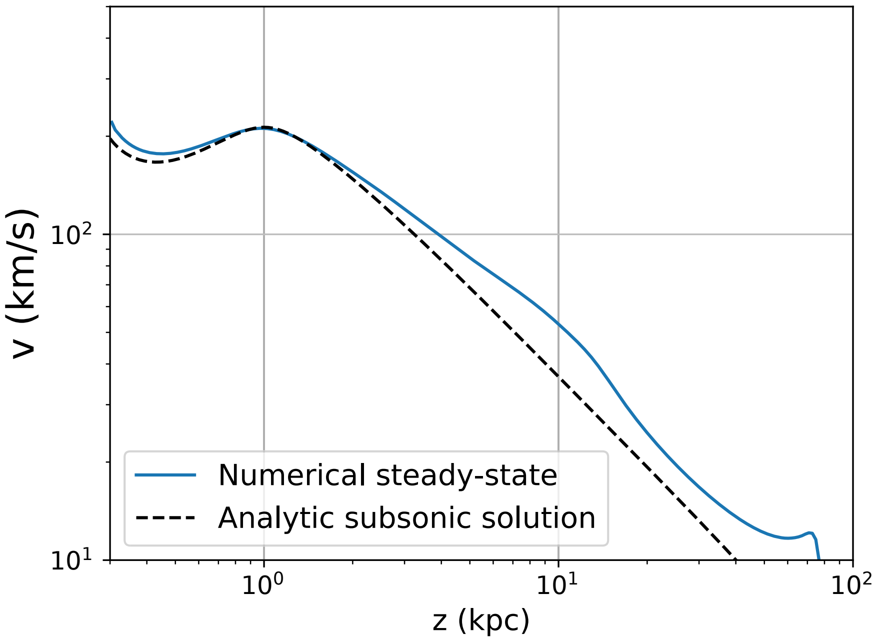

Figure 2.7: The simulated subsonic outflow for the hydrodynamic model after the simulation reaches a steady-state (solid blue line) is compared with the analytic steady-state solution (dashed black line).

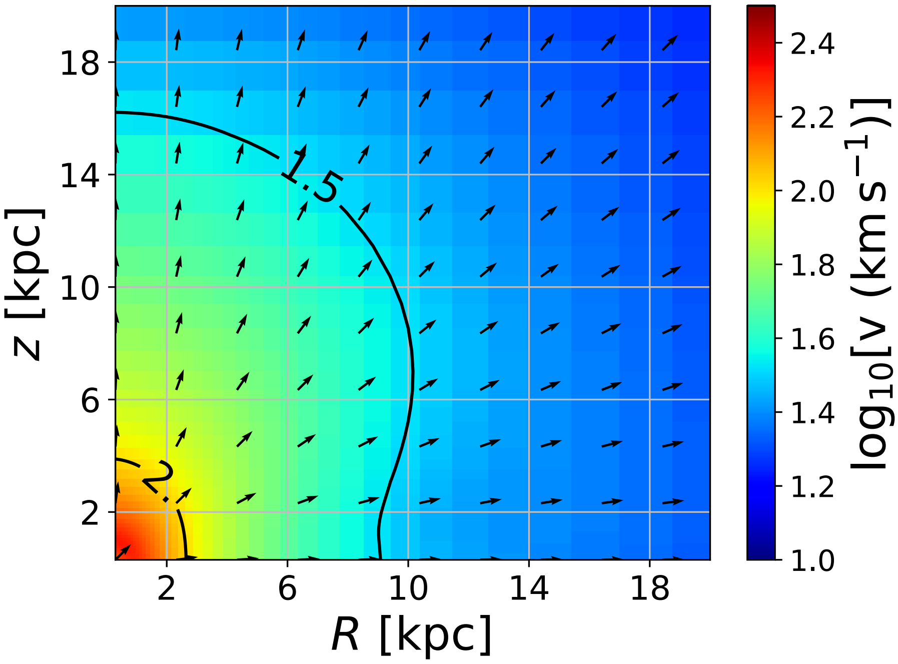

Figure 2.8: The figure shows a 2D spatial distribution of the Galactic breeze profile. The arrows represent the direction of propagation of the outflow. The continuous colourbar indicates the logarithm, of base 10, of the magnitude of the velocity. From the colourbar, the continuous deceleration of the outflow along both z and $R-$directions can be seen. The black contour lines represent the velocity distribution for two specific values of 100 km s^{-1} and 30 km s^{-1}. The outflow propagates mainly along the z-direction due to the asphericity of the disc component for the total gravitational potential.

for solving a CR transport equation. This will allow to determine a γ-ray energy flux distribution for the hydrodynamic case and compare it with the Fermi bubbles γ-ray emission. This work is presented and described in the following chapter.

Chapter 3

Propagation of cosmic rays and γ-ray emission for the hydrodynamic model

Cosmic rays (CR) are an essential component for observations of the various types of radiation that exist in the universe. To be able to describe their transport and their interaction with an ambient medium, it is necessary to propose a realistic astrophysical model that can be compared with observations (Ackermann et al. 2014; Yang and Razzaque 2019). CR interact with other particles and participate in different leptonic and hadronic interactions and contribute to different emission processes. CR are a significant part of every galaxy and their energy contribution can be increased through acceleration. In section 3.1, the CR transport equation is introduced. In section 3.2, the setup for solving numerically the CR transport equation is presented. Following these simulations, the section 3.3 introduces the CR density map obtained for the subsonic velocity profile, leading to a γ-ray energy flux distribution that is compared with observations.

3.1 CR transport equation

Various approximations of what is called a CR transport equation can be done for various studies. This equation requires that the CR distribution function be determined according to three spatial dimensions, time and momentum. It first takes the form of a continuity equation of the form

$$\frac{\partial f}{\partial t} + \nabla_x \cdot \mathbf{j}_x + \nabla_p \cdot \mathbf{j}_p = Q. \tag{3.1}$$

Here, f represents the CR phase space density and is expressed as $f = \frac{dN}{d^3x d^3p}$, where N is the number of particles and p is the CR momenutum. Q is a source term. $\nabla_x \equiv \frac{\partial}{\partial x}$ represents the spatial derivative and $\nabla_p \equiv \frac{1}{p^2}\frac{\partial}{\partial p}$ is the momentum derivative. $\mathbf{j}_x$ and $\mathbf{j}_p$ are the spatial current density and momentum current density, respectively and are expressed by

$$\mathbf{j}_x = \overbrace{\dot{\mathbf{x}} f}^{\text{Advective current}} - \underbrace{D\nabla f}_{\text{Diffusive current}}, \tag{3.2}$$

and

$$\mathbf{j}_p = -\overbrace{\frac{p^3}{3}\left(\nabla\cdot\dot{\mathbf{x}}\right)}^{\text{Advective momentum current}} f, \tag{3.3}$$

where $\dot{\mathbf{x}}$ is the vector velocity for the considered outflow and D is a homogeneous and isotropic diffusion coefficient (Compton and Getting 1935; Gleeson and Axford 1968; Caballero-Lopez and Moraal 2004). After inserting a energy loss time scale term into this continuity equation, the transport equation can be written in the following form

$$\frac{\partial f}{\partial t} = \overbrace{\nabla\cdot\left(D\nabla f\right)}^{\text{Diffusion}} - \underbrace{\dot{\mathbf{x}}\cdot\nabla f}_{\text{Advection}} + \overbrace{\frac{1}{3}\left(\nabla\cdot\dot{\mathbf{x}}\right)\frac{\partial f}{\partial \ln p}}^{\text{Momentum advection}} - \underbrace{\frac{f}{\tau_{\text{loss}}}}_{\text{CR loss rate}} + \overbrace{Q}^{\text{Source}}. \tag{3.4}$$

On the right-hand side of the equality,

1. The first term represents the spatial diffusion coefficient, which describes the random walk of CR in the magnetic field of the Galactic halo. It then quantifies the rate at which CR spread out over space due to random scattering.

2. The second term represents the advection, which accounts for the bulk motion of the CR that is due to the motion of the outflow through the Galactic halo.

3. The third term represents the momentum advection, which contributes to moving the CR to lower energy as they are transported by the expanding outflow.

4. The fourth term is the CR energy loss scale, τ_{loss}, i.e. the rate at which the CR lose their energy through inelastic *pp* collisions. The energy loss time scale depends on the medium density and proton cross section (Gabici, Aharonian and Blasi 2007).

5. The fifth term is a source term, Q, that is the rate at which CR are injected into the system and accounts for the production of CR from astrophysical sources.

This CR transport equation can be solved numerically in order to obtain a density distribution for the CR, which will be used to get the corresponding γ-ray energy flux distribution. The numerical solution of this CR transport equation and the results produced are introduced and discussed in the following section.

3.2 CR transport simulation

To be able to produce a γ-ray emission map, a CR transport code must be used to simulate the propagation of CR. The result of these simulations is a CR density distribution map that is used for determining the γ-ray energy flux distribution and is compared with the observations of the Fermi bubbles γ-ray emission.

3.2.1 CR transport code

The CR transport code (Rodgers-Lee et al. 2017; Rodgers-Lee et al. 2020) solves the CR transport equation (see Eq. (3.4)) by calculating the value of f, through a spatial and momentum computational grid for each time step. The advection and the momentum advection are defined by using the subsonic velocity profile simulated with the PLUTO code (see section 2.6.3). The CR transport equation is advanced in time using a forward in time method. The diffusive term is resolved with a centered in space differencing scheme. A Lax-Wendroff scheme (Lax and Wendroff 1960) is used for solving the advective term spatially. The overall scheme is first order in time and second order in space.

Computational grid

The computational grid has been setup as a cylindrical logarithmic 2D grid (R, z). 350 bins are used for both the R and z-directions. Their inner coordinates, $R_{\rm in}$ and $z_{\rm in}$, are setup at 100 pc and their outer coordinates, $R_{\rm out}$ and $z_{\rm out}$, at 100 kpc. In addition to the spatial grid, another one is needed for the momentum, p. This grid has been setup with 5 bins and extends from 10 GeV/c to 30 GeV/c. As the PLUTO simulations has been performed with a spherical grid, and the CR transport code has been written with a cylindrical grid, the velocity distribution has been linearly interpolated from the 2D spherical grid to a 2D cylindrical gird.

Diffusion coefficient

For the hydrodynamic model, D is defined as being isotropic and homogeneous. The diffusion length, D/c, is defined as (Jokipii 1966; Schlickeiser 1989)

$$\frac{D}{c} = 0.1 \left(\frac{p}{10 \text{ GeV/c}} \right)^{2-\gamma} \text{ pc}, \tag{3.5}$$

where γ is the Kolmogorov turbulence power-spectrum slope for which γ=5/3 and c is the speed of light. As D describes the random walk of CR induced by a magnetic field, fixing the diffusion length implies a specific constant value for the magnetic field. For a particle with a momentum of 10 GeV/c, a diffusion length of 0.1 pc corresponds to a magnetic field of $\sim$ 0.1 nG through all the grid. This value of 0.1 pc has been chosen to match with the value of D, deduced from observations of the amount of radioactive ^{10}Be nuclei in CR for the Galactic halo and estimated to be $\sim 10^{28}$ cm^2 s^{-1}, i.e. $\sim$ 0.1 pc (Ginzburg, Khazan and Ptuskin 1980).

The numerical scheme used for solving D in space is described in appendix A.1.1.

Advective and momentum advective term

Both advection and momentum advection are defined by the movement of a gas, which is described by its velocity profile. This profile takes the form of a subsonic solution in a steady-state that has been solved numerically with the hydrodynamic PLUTO code defined with a spherical grid (see section 2.6). As the CR transport code uses a cylindrical grid (R, z), an interpolation has then been made for the data points of the velocity profile from the spherical grid used by the hydrodynamic code to the cylindrical grid used by the CR transport code.

The numerical scheme used for solving the advection and the momentum advection is described in appendix A.1.2 and A.1.3.

Energy loss time scale

The loss time scale term depends on the energy of CR and on the density of the gas that has been travelled through. For the simulations of the transport of CR, a simplification has been made as a constant density has been assumed for the hot Galactic halo gas of $n_{\rm gas} = 3 \times 10^{-3}$ cm^{-3}. Its expression is given by (Gabici, Aharonian and Blasi 2007)

$$\tau_{loss} = \frac{1}{n_{gas} c \kappa \sigma_{pp}} = 20 \left(\frac{3 \times 10^{-3} \text{ cm}^{-3}}{n_{gas}} \right) \text{ Gyr}, \tag{3.6}$$

where $\kappa = 0.45$ and σ_{pp} is the cross section for a proton-proton interaction, its value is 40 mbarn (4×10^{-26} cm^2).

CR source

The source term expresses the injection of particles into the computational grid following a specific law of distribution dependent on the particle energy. For the simulations, the source term is described by a power-law distribution with an exponential cutoff. Its expression is given by

$$Q \propto N_0 \left(\frac{p}{p_0} \right)^{1-\alpha} \exp \left(-\frac{p}{p_{\rm max}} \right), \tag{3.7}$$

where $p_0 = 1.876$ GeV/c, $p_{\rm max} = 10^7$ GeV/c, $\alpha = 2$ is representative of diffusive shock acceleration (Bell 1978) and N_0 is a constant of normalisation.
The injection is performed through multiple cells, for which 100 pc $< r_{\rm cell} <$ 400 pc and $r_{\rm cell} = \sqrt{R_{\rm cell}^2 + z_{\rm cell}^2}$. $R_{\rm cell}$ and $z_{\rm cell}$ being the position of each cell in the cylindrical computation grid. As this grid is logarithmic, the area of each cell considered for the injection must be taken into account, this area varying with the distance. The surface element of a cell is expressed by

$$dS_{\rm cell} = R_{\rm cell} z_{\rm cell} d \left(\ln \left(R_{\rm cell} \right) \right) d \left(\ln \left(z_{\rm cell} \right) \right). \tag{3.8}$$

With this expression, Eq. (3.7) is rewritten as

$$Q_{\rm cell} \propto \frac{dS_{\rm cell}}{S_{\rm cell}} N_0 \left(\frac{p}{p_0} \right)^{1-\alpha} \exp \left(-\frac{p}{p_{\rm max}} \right), \tag{3.9}$$

where $S_{\rm cell}$ represents the total area of injection that is expressed by

$$S_{\rm cell} = \int_{100 \text{ pc}}^{400 \text{ pc}} dS_{\rm cell}. \tag{3.10}$$

Boundary conditions

The boundary conditions for the inner spatial coordinates, R_{in} and z_{in}, are reflective, meaning that the CR cannot enter or leave the grid through the boundary. As the computational grid is a quadrant, the injection site will be near the inner boundaries and it is therefore of the utmost importance to ensure that the boundaries are sealed.

There are two ways to implement a reflective boundary in the code:

1. The first one is to treat spatial diffusion and advection together. For this method, at the boundary interface, the diffusive and advective fluxes must be

$$D_{i+1/2}\left(\nabla f\right)_{i+1/2} - v_{i+1/2} f_{i+1/2} = 0, \tag{3.11}$$

   where i represents the spatial dimension that can be R or z. As the cells are self-centred, the subscript $1/2$ represents the value of the corresponding variable at the interface between two cells.

2. The second way is to treat separately the spatial advection and diffusion. For this method, at the boundary cell, the spatial advective term is set to be opposite to the velocity at the cell beside the boundary, ensuring that the advective flux through the boundary is zero. Thus, $v_0 = -v_1$ implying $v_{0+1/2} f_{0+1/2} = 0$ at the interface. The condition for the diffusive flux to be zero at the boundary implies that the phase space density at the boundary cell is equal to that at the adjacent cell. Thus, $D_{i+1/2}\left(\nabla f\right)_{i+1/2} = 0$ implying that at the inner boundary, $f_0 = f_1$.

To test these methods, several simulations have been done. The grid goes from 0.3 kpc to 800 kpc, with 60 bins, to ensure that no particles interact with the outer boundaries, which have been setup with an outflow condition. This condition implies that matter from the computational grid can leave it but no matter from outside the grid can enter it. The momentum advection term is suppressed from the CR transport equation by considering a simple free-divergent velocity profile expressed as

$$\mathbf{v}(R,z) = \begin{cases} v_R = & v_{\max}\left(\frac{300\ \mathrm{pc}}{R}\right) \\ v_z = & v_{\max}, \end{cases} \tag{3.12}$$

where $v_{\max} = 300$ km s^{-1} and a single injection is performed in order to control more easily the variation of particles for the simulation time.

There are two different schemes possible for the advection of the injected CR, a Lax-Wendroff scheme or an Upwind scheme. Both have been used and compared to determine which scheme conserves particles, at the interface between the computational grid and the boundary cells, the best. Two different times for the simulations have been considered, one lasting 1 Myr and a second one lasting 300 Myr.

The first method for defining the reflective boundary condition in combination with the Lax-Wendroff scheme is the best combination for conserving particles during a simulation time of 300 Myr. The variation in the number of particles was only 0.5% from the initial injection.

With this setup, the CR transport code has been solved numerically. The results are introduced and discussed in the following section.

3.3 Galactic breeze γ-ray signature

Solving numerically the CR transport code equation allows to obtain a CR density distribution map. This distribution is dependent on the velocity profile of the outflow in which travel CR. Advection and diffusion are then in competition for the transport of CR. From the CR density distribution, the γ-ray emission can be obtained and will be compared with the observations for determining the viability of the Galactic breeze model for describing the Fermi bubbles.

3.3.1 CR density distribution

Diffusion time versus advection time

Once the velocity profile has been obtained for the hydrodynamic model, it can be used to define the advection that competes with the diffusion for the transport of CR. The diffusion mechanism is not significant if the outflow velocity is high enough and low energy particles (<10 GeV) are considered. However, in the case of a Galactic breeze, the velocity is sufficiently small for both terms to play an important role in dictating the CR spatial distribution. For a spherical symmetry, the diffusion time is determined by the expression

$$t_{\mathrm{Diff}} = \frac{r^2}{D}. \tag{3.13}$$

Here D is given by the Eq. (3.5). For CR with a momentum of $p = 10$ GeV/c, $D = 10^{28}$ cm^2 s^{-1}.

The advection time is expressed by

$$t_{\mathrm{Adv}} = \frac{r}{v_r}, \tag{3.14}$$

where v_r is the velocity profile for the Galactic breeze solution previously simulated (see section 2.6.3).

Figure 3.1 shows the relation between t_{Diff} (solid orange line) and t_{adv} (solid blue line) along both the R-axis (left figure) and the z-axis (right figure). It must be noted that if t_{adv} is faster than t_{Diff}, for the considered example, the relation depends on CR momentum (see Eq. (3.5)). As the momentum increases, the influence of diffusion becomes more important.

CR density distribution map

The CR number density, n_{CR}, is expressed through the space phase density distribution, f, whose values are computed by the CR transport code

$$n_{\mathrm{CR}} = \int 4\pi f(t, r, p) p^3 d \ln(p). \tag{3.15}$$

A 2D distribution map for n_{CR} obtained from the simulation, including the advection due to a Galactic breeze, can be seen in figure 3.2. As a quarter-grid simulation is performed, the CR distribution has been mirrored. A symmetry is then assumed between the north and south bubble. Based on the time scale for

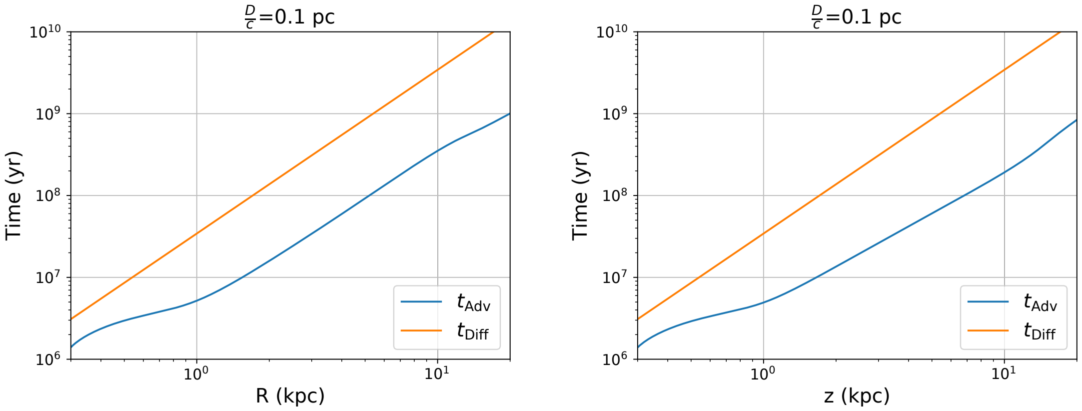

Figure 3.1: Following both Eq. (3.13) and Eq. (3.14), the diffusion time (solid orange line) for $D/c\,(p = 10\ \mathrm{GeV}/c) = 0.1$ pc and the advection time for the subsonic outflow (solid blue line) are compared for both the R-direction (left) and the z-direction (right). For both figures, the advection time is inferior to the diffusion time. The difference, however, is not large and diffusion still plays a role in the propagation of particles.

$D/c\,(p = 10\ \mathrm{GeV}/c) = 0.1$ pc and for the subsonic velocity profile numerically simulated, the advection dominates over the diffusion (see figure 3.1). Although the effect of the diffusion cannot be neglected, n_{CR} is mainly influenced by the velocity profile (see figure 2.8). As a result, n_{CR} shows an asymmetry in its distribution. As the subsonic velocity profile for the advection propagates mainly along the z-direction, n_{CR} follows a similar distribution and takes an oblong shape.

With the n_{CR} distribution, it is possible to obtain the corresponding γ-ray emission that can be compared with the observations of the Fermi bubbles provided by the Fermi-LAT instruments (Ackermann et al. 2014).

3.3.2 γ-ray emission

Inelastic CR collisions with the ambient gas in the Galactic halo result in the creation of charged and neutral pions (see section 1.5.2). The dominant decay mode for the neutral pions is into two photons (Particle Data Group et al. 2020). A photon produced by such a collision obtains ~10 % of the initial energy of an incident CR proton. Therefore, for the CR energy range considered, which is included between 10 and 30 GeV, photons with an energy included between 1 and 3 GeV are produced.

To be correctly interpreted, the photon emission resulting from n_{CR} must be considered from the point of view of an observer. The resulting γ-rays brightness, $E_\gamma F_\gamma$, seen by an observer along a particular solid angle of angular size $\Delta\Omega$ is obtained from summing the contribution of the energy flux, $\dfrac{L_\gamma}{4\pi r^2}$, over the full line-of-sight. $E_\gamma F_\gamma$ is expressed by

$$E_\gamma F_\gamma = \frac{1}{3\Delta\Omega}\int \frac{dL_\gamma}{4\pi r_{\mathrm{obs}}^2} = \frac{1}{12\pi\tau_{\mathrm{loss}}}\int e_{\mathrm{CR}}\,dr_{\mathrm{obs}}, \tag{3.16}$$

where r_{obs} is the distance between the source of emission and the observer. L_γ is the total γ-ray luminosity. The factor of $\frac{1}{3}$ accounts for the fraction of neutral pions produced for inelastic CR interactions with the target gas. Those neutral pions, π^0, quickly decay into γ-ray photons. The two other charged pions, π^+ and π^-, do not

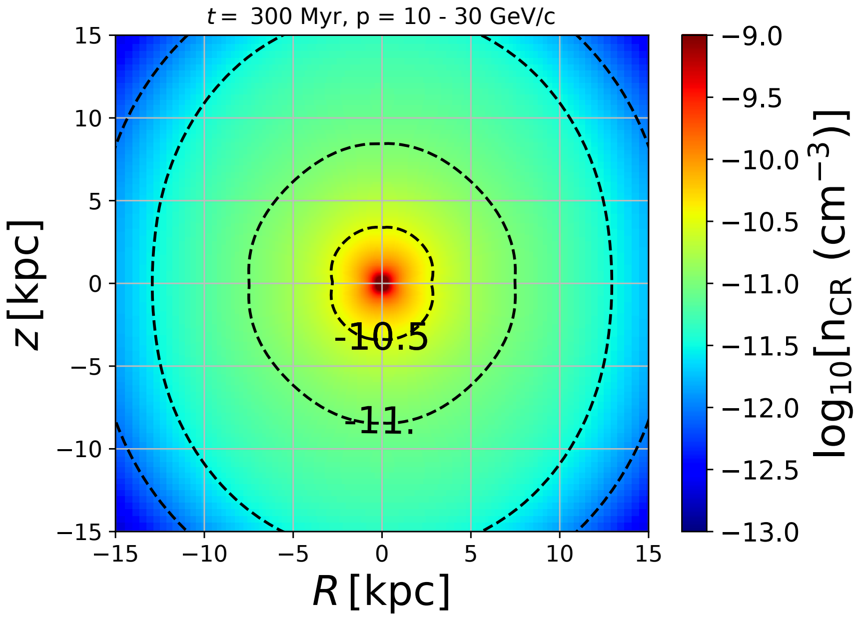

Figure 3.2: A 2D CR distribution map for n_{CR}, based on $f(t, R, z, p)$, is obtained for a Galactic breeze profile and for an energy range of $E_{CR} = 10 - 30$ GeV. As a quarter-grid simulation is performed, the CR distribution is mirrored. A symmetry is then assumed between the north and south bubble. The dashed black lines are contours representing the distribution of n_{CR} along the R and z directions. The continuous colourbar indicates the logarithm (base 10) of the CR density. As the Galactic breeze profile defined for the advection dominates over the diffusion, the distribution of n_{CR} follows a similar profile, that is distributed mainly in the z-direction.

decay directly into γ-ray photons (see section 1.5.2). The position of the observer from the Galactic Center has been fixed at 8 kpc (Gillessen et al. 2017).

The CR energy density, e_{CR}, is expressed by

$$e_{\mathrm{CR}} = \int_{p_{\mathrm{min}}}^{p_{\mathrm{max}}} 4\pi f p^3 dp. \tag{3.17}$$

The γ-ray energy flux from all the computational cells contained along the line-of-sight within each solid angle direction is summed up. The skymap of the γ-ray energy flux density is shown in figure 3.3. The Galactic breeze profile, in combination with a CR luminosity $L_{\mathrm{CR}} \approx 1.4 \times 10^{40}$ erg s^{-1}, produces bilobal γ-ray emission. From observations, the latitude of the Fermi bubbles is $\sim 50°$, corresponding to ~ 10 kpc for an observer at 8 kpc from the Galactic Center.

The brightness of the γ-ray energy flux appears broadly consistent with the Fermi-LAT observations (see figure 3.4). However, the width of the observed Fermi bubbles, estimated to be around 20° from the central axis (Ackermann et al. 2014) are narrower than the results shown in figure 3.3, which extend to a width of $\sim 30°$. This difference originates from the assumptions in the adopted setup. Specifically, both the value of the diffusion length and the isothermal gas temperature, collectively dictate the subsequent lobe width.

In figure 3.4, a direct comparison is made between the simulation data provided by the Fermi-LAT collaboration (Ackermann et al. 2014) for latitudes of $b = 30° - 40°$ and $b = 40° - 50°$. The solid blue line represents the γ-ray energy flux provided by the simulations for the subsonic velocity profile. The red error bars come from the

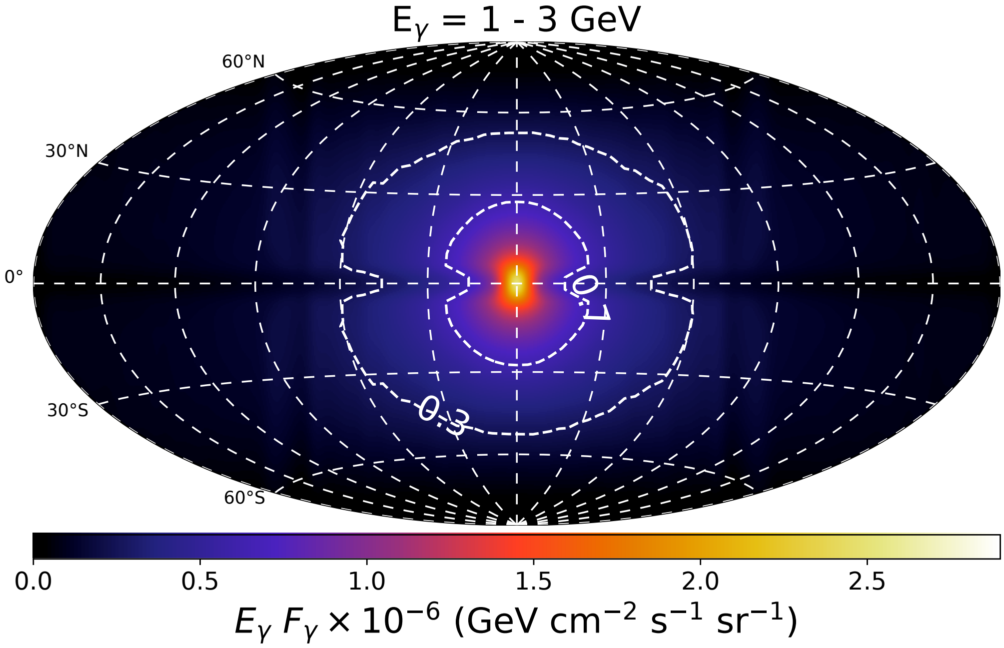

Figure 3.3: A γ-ray emission map is produced, based on the spatial distribution of $n_{\rm CR}$ obtained for a Galactic breeze profile. This map takes into account the position of the observer fixed at $R = 8$ kpc and $z = 0$ kpc from the Galactic Center. The emission is produced by photons with energy ranging from 1 to 3 GeV. The bubble shape of the emission is clearly visible. However, the width appears to be too large when compared with the Fermi bubbles that extend to a Galactic longitude of $\sim 20°$ for $40° < b < 50°$.

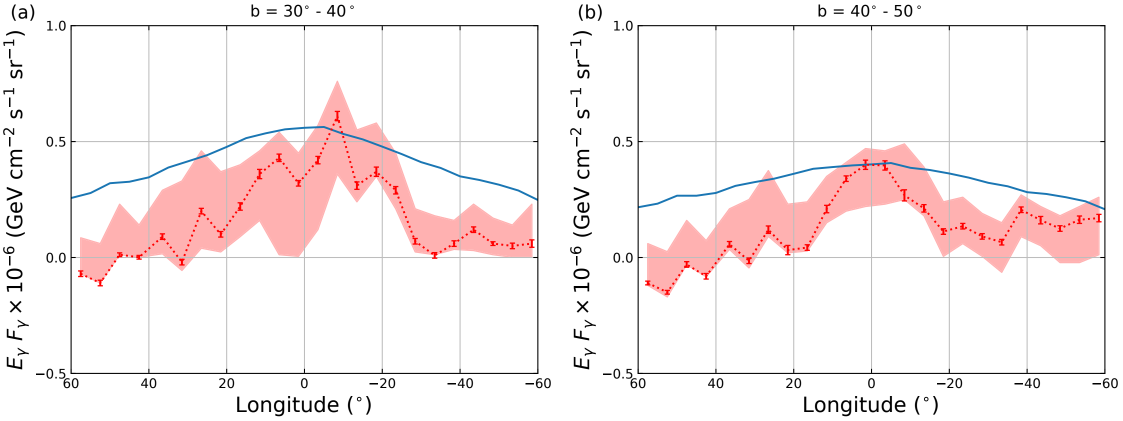

Figure 3.4: $E_\gamma F_\gamma$ produced by the γ-ray emission is plotted as a function of the Galactic longitude for different latitude ranges. The solid blue line represents the γ-ray energy flux provided by the spatial distribution of $n_{\rm CR}$ for a Galactic breeze presented in section 2.6.3. The error bar ranges and the shaded red region are provided by the Fermi-LAT observational results. The red error bars represent the γ-ray energy flux determined from observations of the Fermi bubbles. The shaded red region has been computed from the uncertainties of different models and different possible templates. Figure (a) corresponds to the data provided by the Fermi-LAT for a latitude of $b = 30° - 40°$. Figure (b) corresponds to the data provided by the Fermi-LAT for a latitude of $b = 40° - 50°$. For both figures, the γ-ray energy flux produced by the numerical simulations matches roughly with the observations for $L_{\rm CR} \approx 1.4 \times 10^{40}$ erg s^{-1} but is broader beyond a Galactic longitude of $l \approx 15°$.

data defined with the GALPROP CR propagation and interactions code (Vladimirov et al. 2011) as templates. The red shaded regions were computed from the uncertainties of different models and different definitions of the templates. Both the red error bar ranges and the red shaded regions have been provided by the Fermi-LAT collaboration (Ackermann et al. 2014). At latitudes between $30^\circ < b < 40^\circ$ and $40^\circ < b < 50^\circ$, for a longitude between $-15^\circ < l < 15^\circ$, the γ-ray energy flux is broadly compatible with the observations, although as already noted previously, beyond a longitude of 15° the γ-ray energy flux no longer falls within the red shaded region due to the broader width of the simulated lobes.

With the $E_\gamma F_\gamma$ distribution, it is possible to determine the velocity distribution observed from the Earth, called the line-of-sight-velocity and compare the Galactic breeze profile with the velocity profile observed from the shifted spectrum of high-velocity cold clouds present in the Fermi bubbles (see section 1.3.3).

3.3.3 Line-of-sight velocity profile for the hydrodynamic model

The hydrodynamic simulation has provided the velocity distribution for the Galactic breeze (see section 2.6.3) but does not take into account the position of the observer. For this, the line-of-sight velocity must be considered. It is computed, as a function of the Galactic longitude and latitude, to be compared with observations. The emission weighted line-of-sight velocity, $v_{\rm los}$, with respect to the observer is expressed by

$$v_{\rm los}(l,b) = \frac{\int_{b-\Delta b}^{b+\Delta b}\int_{l-\Delta l}^{l+\Delta l} v_r E_\gamma F_\gamma dl' db'}{\int_{b-\Delta b}^{b+\Delta b}\int_{l-\Delta l}^{l+\Delta l} E_\gamma F_\gamma dl' db'}, \tag{3.18}$$

where v_r is the velocity profile of the Galactic breeze. b expresses the Galactic latitude and l the Galactic longitude. $E_\gamma F_\gamma$ is given by Eq. (3.16).

In figure 3.5, the steady-state solution for the Galactic breeze profile obtained numerically is plotted along the latitude (solid blue line). A position for an observer at 8 kpc from the Galactic Center and at a Galactic longitude of 0° has been considered. This line-of-sight velocity is then compared with several data points provided by different observations (Ryans et al. 1997; Fox et al. 2015; Bordoloi et al. 2017; Ashley et al. 2020; Sofue 2022) (see section 1.3.3). From this comparison, it appears that the Galactic breeze profile follows well the continuous deceleration that has been observed. However, the fitted model is not able to provide the necessary conditions for a breeze solution to reach a velocity of ~ 300 km s^{-1} at r_c. Therefore, the velocity profile of the Galactic breeze is less than the observations (see section 2.4).

3.4 Conclusion for this chapter

A numerical solution to the hydrodynamic equations has provided a steady-state Galactic breeze profile. In order to make a comparison with the Fermi bubbles observations, this profile is not enough. The γ-ray emission produced by pp interactions must be taken into account. For this, a CR transport equation has been resolved numerically. The advection is expressed through the Galactic breeze profile simulated previously. A homogeneous and isotropic diffusion coefficient has been

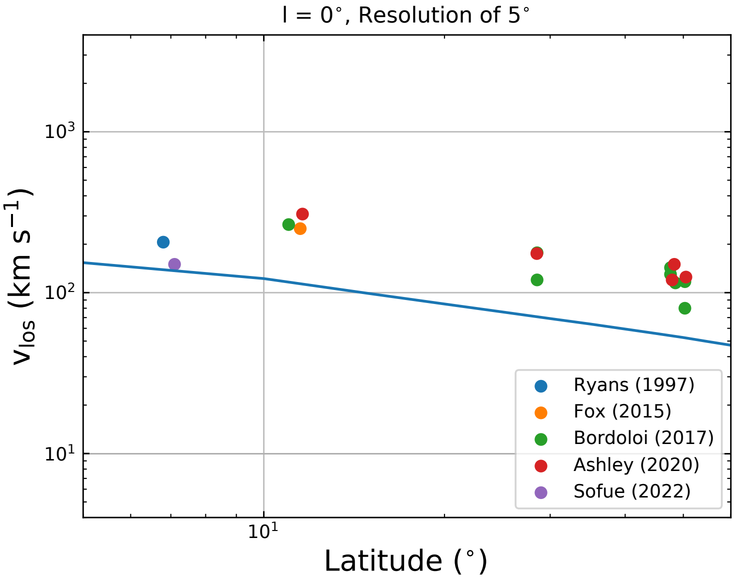

Figure 3.5: The line-of-sight velocity (solid blue line) is compared with different observations of high-velocity clouds (coloured dots). A distance of 8 kpc between the observer and the Galactic Center has been considered and the Galactic longitude fixed a 0°. The continuous deceleration profile matches well with the data points beyond a galactic height of 1 kpc but the velocity is less than what has been observed (see section 2.4).

considered and a diffusion length of 0.1 pc has been fixed. The CR have been injected through an area ranging from 100 pc to 400 pc. For their transport, both advection and diffusion play an important role. As the Galactic breeze profile forms a shape expanding mainly in the z-direction, the CR density distribution follows a similar distribution and takes an oblong shape.

From these results, a γ-ray energy flux distribution has been obtained. This distribution shows a clear bubble shape. For an injected CR luminosity of 1.4×10^{40} erg s^{-1}, the emission related to the Galactic breeze profile is able to match approximately with observations for a latitude ranging from 40° to 50°. The γ-ray energy flux distribution has then been used for getting the line-of-sight velocity profile, for an observer placed at 8 kpc from the Galactic Center. The Galactic breeze profile matches well with the continuous deceleration observed for the Fermi bubbles.

However, the bubbles produced through this emission are too large when compared with the Fermi bubbles since, at a Galactic longitude of $\sim 15°$, the emission shows no sharpness. This feature can be clearly seen in the Fermi bubbles. A hydrodynamic model is not enough for describing the Fermi bubbles with a Galactic breeze profile and another mechanism is needed. A MHD model, introducing a magnetic field distribution, could be able to provide a better description. Such a model is introduced and described in the following chapter.

Chapter 4

Thermally-driven subsonic outflow for a MHD model

The Milky Way has intense magnetic activity for each of its components. If the magnetic field configuration is well known for the Galactic disc, it is not the case for both the Galactic bulge and the Galactic halo (Han 2017). By its presence, the magnetic field can have an important effect on the propagation of an outflow through magnetic tension and magnetic pressure. It is therefore a feature that must be explored to be able to offer a correct explanation for the emission associated with the Fermi bubbles. Section 4.1 presents the expression corresponding to the MHD momentum equation. In section 4.2, an analytic study of the effect of a magnetic distribution on the subsonic solution is discussed. In section 4.3, the setup for MHD numerical simulations is presented as well as the obtained results.

4.1 MHD momentum equation

As for the hydrodynamic model (see chapter 2), the MHD momentum equation can be expressed in a conservative form given by

$$\frac{\partial \rho \mathbf{v}}{\partial t} + \nabla . \mathbf{T} = 0, \tag{4.1}$$

where $\mathbf{T}$ represents the stress-energy tensor composed of two parts, both related to hydrodynamic and MHD components.

Compared to the hydrodynamic momentum equation (see Eq. (2.4)), the MHD momentum equation includes additional terms

$$\frac{\partial \rho \mathbf{v}}{\partial t} + \nabla . \left[\underbrace{\rho \mathbf{v}\mathbf{v}^T}_{\text{Ram pressure}} + \underbrace{P_{\text{th}}\mathbf{I}}_{\text{Thermal pressure}} - \underbrace{\frac{\mathbf{B}\mathbf{B}^T}{4\pi}}_{\text{Magnetic tension}} + \underbrace{\frac{B^2\mathbf{I}}{8\pi}}_{\text{Magnetic pressure}} \right] \tag{4.2}$$

In the bracket, the first two terms are related to the hydrodynamic version of the momentum equation (see section 2.1.2). The two other terms are related to the inclusion of a magnetic field. The last term, the magnetic pressure, is an equivalent of the thermal pressure. The third term, the magnetic tension, acts to straighten out the field lines when those ones are bended by another force.

From Eq. (4.2), it is possible to study the effect of a magnetic field on the subsonic solution. This is covered in the following section.

4.2 Effects of a magnetic field distribution

4.2.1 Influence of the magnetic field distribution on the critical radius

Following the results produced for a hydrodynamic model (see chapter 2), the inclusion of a magnetic field is a natural step. Historically, after having worked on an expanding Solar corona model (Parker 1958), Parker included a Solar magnetic field (Parker 1965), since its influence cannot be ignored for the propagation of an outflow and for the diffusion of CR, whether on a stellar or a galactic scale. As for the hydrodynamic model, the MHD momentum equation (see Eq. (4.2)) can be used to determine the effect of the magnetic field on the position of r_c and the different possible initial values for the magnetic field. It is extended by considering $\Phi_{\rm tot}$, previously used for the hydrodynamic model (see section 2.3).

$$\frac{\partial \mathbf{v}}{\partial t} + (\mathbf{v}.\nabla)\,\mathbf{v} + \frac{\nabla P_{\rm th}}{\rho} - \frac{1}{4\pi\rho}\left[(\mathbf{B}.\nabla)\,\mathbf{B} - \nabla\left(\frac{B^2}{2}\right)\right] = -\nabla\Phi_{\rm tot}. \tag{4.3}$$

By considering the radial component of the MHD momentum equation in spherical coordinates and for a steady-state, i.e., for $\frac{\partial \mathbf{v}}{\partial t} = 0$, the Eq. (4.3) becomes

$$v_r\frac{\partial v_r}{\partial r} - \frac{v_\phi^2}{r} + \frac{1}{\rho}\frac{\partial P_{\rm th}}{\partial r} - \frac{1}{4\pi\rho}\left[B_r\frac{\partial B_r}{\partial r} - \frac{B_\phi^2}{r} - \frac{\partial}{\partial r}\left(\frac{B^2}{2}\right)\right] = -\frac{\partial \Phi_{\rm tot}}{\partial r}, \tag{4.4}$$

where $v_r(r)$ and $B_r(r)$ are respectively the radial component of the velocity and the magnetic field. $v_\phi(r)$ and $B_\phi(r)$ are respectively the azimuthal component of the velocity and the magnetic field. By considering $B_\theta(r) = 0$ μG, the total magnetic field $B(r)$ is written as $B(r) = \sqrt{B_r^2(r) + B_\phi^2(r)}$. The magnetic field as then an helicoid structure. By including this expression in Eq. (4.4), the radial gradient of the radial component $B_r(r)$ for both the magnetic tension and magnetic pressure cancel each other. The Eq. (4.4) becomes then

$$v_r\frac{\partial v_r}{\partial r} - \frac{v_\phi^2}{r} - \frac{c_{\rm s}^2}{v_r}\frac{\partial v_r}{\partial r} - \frac{2c_{\rm s}^2}{r} - \frac{B_\phi}{4\pi\rho}\left(\frac{B_\phi}{r} + \frac{\partial B_\phi}{\partial r}\right) = -\frac{\partial \Phi_{\rm tot}}{\partial r}. \tag{4.5}$$

It can be seen that $B_\phi(r)$ influences the propagation of an outflow. The variations of $B_\phi(r)$ can help to accelerate or decelerate it.

In order to analyse more easily the influence of a magnetic field distribution on the position of r_c, $B_\phi(r)$ is expressed as a simple inverse power-law and is expressed as

$$B_\phi(r) = B_{\phi_0}\left(\frac{r_0}{r}\right)^\alpha, \tag{4.6}$$

where B_{ϕ_0} represents the value of $B_\phi(r)$ at r_0. For the model presented here, r_0 = 0.3 kpc and α is the power index.

As for the hydrodynamic model, the Eq. (4.5) can be rewritten in a more convenient form to get an intuition of the outflow evolution and the relation with the magnetic field

$$\frac{1}{v_r}\nabla v_r = \frac{1}{r}\left(\frac{2c_{\mathrm{s}}^2 + v_\phi^2 - r\nabla\Phi_{\mathrm{tot}} + \frac{B_\phi^2}{4\pi\rho}\left(1-\alpha\right)}{v_r^2 - c_{\mathrm{s}}^2}\right). \tag{4.7}$$

The equation is similar to the hydrodynamic model (see Eq. (2.10)) but there is now a term that depends on $B_\phi(r)$. It appears then, from Eq. (4.5) and Eq. (4.7), that the presence of a gradient of $B_\phi(r)$ can switch the position of r_c, which is defined for the MHD case as the position where

$$2c_s^2 + v_\phi^2 - r\nabla\Phi_{\mathrm{tot}} + \frac{B_\phi^2}{4\pi\rho}\left(1-\alpha\right) = 0. \tag{4.8}$$

The effect will be different depending on how fast $B_\phi(r)$ decreases. There are three different possible effects on the position of r_c, depending on the value of the index α.

$$\begin{cases} \alpha & = 1 \Rightarrow B_\phi^2\left(1-\alpha\right) = 0 \\ \alpha & > 1 \Rightarrow B_\phi^2\left(1-\alpha\right) < 0 \\ \alpha & < 1 \Rightarrow B_\phi^2\left(1-\alpha\right) > 0. \end{cases} \tag{4.9}$$

The index α implies that if $\alpha = 1$, the presence of $B_\phi(r)$ has no effect on the position of r_c. If $\alpha > 1$, $B_\phi(r)$ will shift r_c closer from the Galactic Center. If $\alpha < 1$, r_c will be shifted farther away from the Galactic Center. For this last case, based on Eq. (4.7), it is possible, by increasing the temperature of the hot Galactic halo and therefore the value of c_s, to shift back r_c closer from the Galactic Center. This allows to increase the peak velocity of the subsonic solution at r_c.

An example is shown in figure 4.1. This figure compares the Galactic breeze profile for the hydrodynamic model (solid blue line) and the MHD model (dashed orange line). The dotted red line corresponds to $c_s = 250$ km s^{-1}. The $B_\phi(r)$ profile is described by the Eq. (4.6), with the parameters defined as $B_{\phi 0} = 30$ μG at $r_0 = 0.3$ kpc and $\alpha = 0.6$. For this configuration, r_c is shifted farther from the Galactic Center passing from $r_c = 1$ kpc to $r_c = 2.5$ kpc. By correctly choosing a value for $B_{\phi 0}$ and the index α, it is possible for this simple model to increase c_s for keeping $r_c \approx 1$ kpc. However, this raises the problem of the distribution of the hydrostatic density of the hot Galactic halo as it depends on c_s (see section 4.2.2).

As for the hydrodynamic model (see Eq. (2.12)), it can be convenient to express the Eq. (4.7) in terms of the different pressures involved, giving

$$\frac{1}{v_r}\nabla v_r = \frac{1}{r}\left(\frac{2P_{\mathrm{th}} + P_\phi - P_{\mathrm{g}} + 2P_{\mathrm{B}_\phi}\left(1-\alpha\right)}{P_{\mathrm{ram}} - P_{\mathrm{th}}}\right). \tag{4.10}$$

P_{th} is the thermal pressure. P_{ram} is the ram pressure induced by $v_r(r)$. P_ϕ is the pressure induced by $v_\phi(r)$. P_{g} represents the pressure of the rotational velocity induced by Φ_{tot} (see section 2.3) and P_{B_ϕ} is the pressure induced by $B_\phi(r)$.

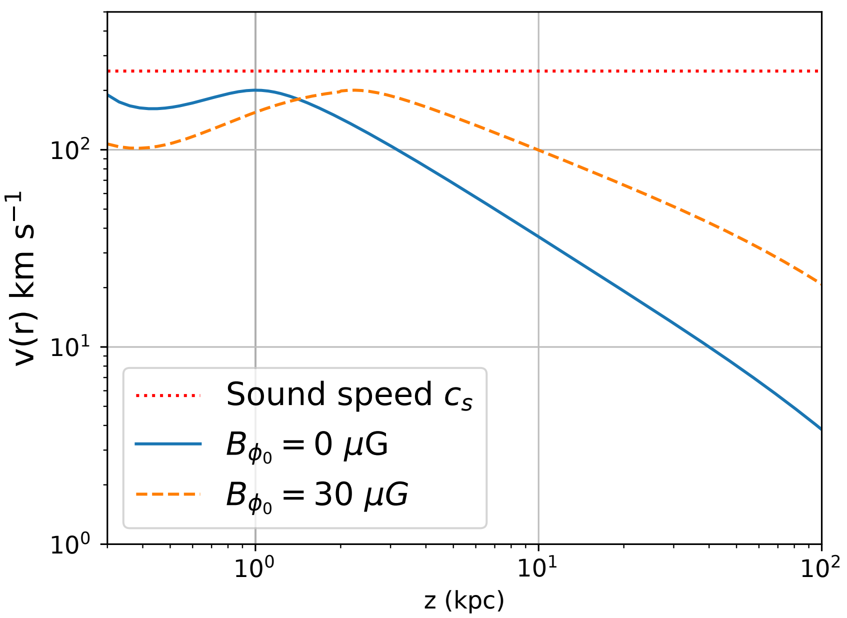

Figure 4.1: The subsonic solution in steady-state for both the hydrodynamic and the MHD model is compared to show the influence of $B_\phi(r)$ on the value of r_c. c_s (dotted red line) has been fixed at 250 km s^{-1}. The hydrodynamic model (solid blue line) is based on the model presented in chapter 2 for which there is no magnetic field. The MHD model (dashed orange line) is based on the parameter given in section 4.2.1. With such a model, r_c, which is at 1 kpc from the Galactic Center for the hydrodynamic model, is shifted farther away to a Galactic height of $\sim$ 2.5 kpc.

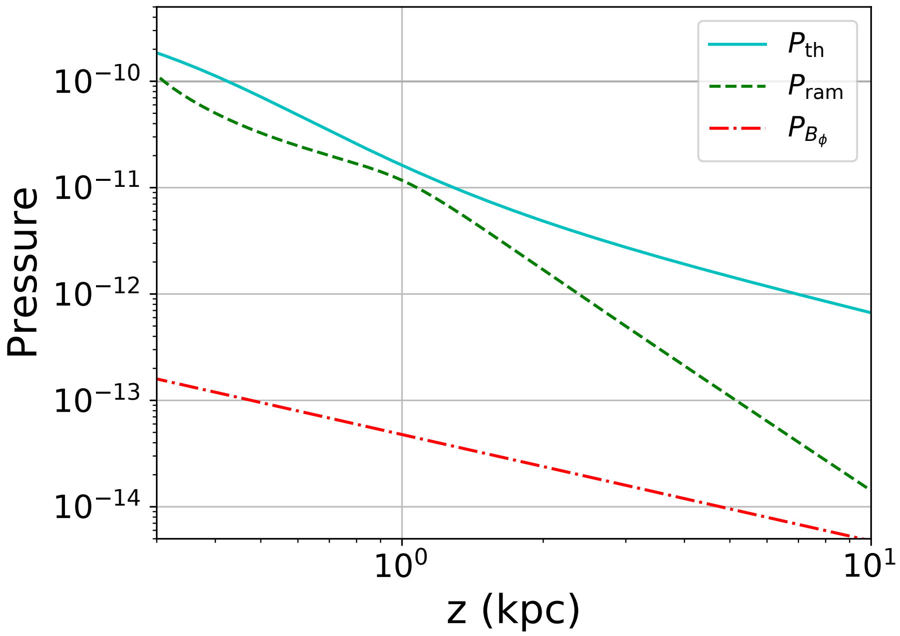

Figure 4.2: The figure compares three different pressures, the thermal pressure $P_{\rm th}$ (solid blue line), the ram pressure $P_{\rm ram}$ (dashed green line) and the magnetic pressure for the azimuthal component $P_{\rm B_\phi}$ (dash-dotted red line). $P_{\rm th}$ and $P_{\rm ram}$ are the same as for the hydrodynamic model. Here $B_\phi(r = 0.3 \text{ kpc}) = 2$ μG, this value corresponds to the observations of the magnitude of the magnetic field in the Galactic halo. The power index has been set up to $\alpha = 0.5$.

Depending on the value of α, the magnetic pressure can contribute to the acceleration or the deceleration of the outflow. However, to have such an effect, P_{B_ϕ} must have a value comparable to $P_{\rm th}$. In figure 4.2, $P_{\rm th}$ (solid blue line) , $P_{\rm ram}$ (dashed green line) and P_{B_ϕ} (dash-dotted red line) are compared. $B_{\phi_0} = 2$ μG, a value comparable with the observations of the magnetic field distribution in the Galactic halo (see section 4.2.3 on this subject), and $\alpha = 0.5$. $P_{\rm th}$ and $P_{\rm ram}$ have been defined in the same way as for the hydrodynamic model (see section 2.2). Compared to $P_{\rm th}$, P_{B_ϕ} appears to be negligible. However, as $P_{\rm ram}$ decreases faster than P_{B_ϕ}, the two pressures can become comparable.

4.2.2 Constraints imposed by observations for the Galactic density profile

The expression of a hydrostatic density distribution, Eq. (2.21), exhibits a relation between $\Phi_{\rm tot}$, and c_s. Increasing c_s has the effect of changing the density distribution. This aspect must be taken into account for deciding which maximum value c_s can be chosen. Considering the same normalisation for $\Phi_{\rm tot}$ that has been done for the hydrodynamic model, different density distributions resulting for different values of c_s values are shown in figure 4.3. In addition to the initial value, $c_s = 250$ km s^{-1} used in chapter 2 (solid red line), the effect of four higher values is shown: 275 km s^{-1}, 300 km s^{-1}, 350 km s^{-1} and 400 km s^{-1}. As for figure 2.5, the red zone corresponds to the fitting-range provided by both X-ray spectroscopic observations and satellite galaxies ram pressure stripping studies (Martynenko 2022). Following its lower limit at 10 kpc, the hydrostatic density at this distance has been fixed at 3.8×10^{-4} cm^{-3}. Both $c_s = 275$ km s^{-1} and $c_s = 300$ km s^{-1} match with the fitting range but higher velocities of c_s do not.

4.2.3 Determining a suitable distribution for $B_\phi(r)$

Exploration through the MHD momentum equation

As the $B_\phi(r)$ has an effect on the determination of the position of r_c, a distribution allowing to reach $r_c = 1$ kpc for $c_s = 300$ km s^{-1} can be explored. A value for B_{ϕ_0} and α (see Eq. 4.6) must be determined. For this, the numerator at the right-hand side of the Eq. (4.7) can be solved for different values of B_{ϕ_0} and α. The root of the equation will determine the position of r_c. In figure 4.4, several different configurations are shown for $c_s = 300$ km s^{-1}. r_c is defined as the point where the numerator goes from a negative value to a positive value. Only some values of B_{ϕ_0} and α allow a r_c to exist. For instance, with a configuration of B_{ϕ_0}=12 μG and α=0.35 (solid blue line), $r_c \approx 1$ kpc. With an identical value for α but a lesser value for B_{ϕ_0}, here B_{ϕ_0}=2 μG (dashed yellow line), the numerator has no root and then r_c cannot exist.

By fixing a value to B_{ϕ_0}, it is therefore possible to see the influence of the index α. Considering $B_{\phi_0} = 20$ μG and $\alpha = 0.5$ (dotted-dashed green line), results in $r_c \simeq 2.25$ kpc, by increasing the index alpha, as $\alpha = 0.7$ (dotted red line), no root exists. A too high value for B_ϕ gives no root if the field does not decrease fast enough. This effect is shown by a configuration with $B_{\phi_0} = 20$ μG and $\alpha = 0.4$ (solid purple line). Therefore, B_{ϕ_0} can be strictly tied to α. For some values of B_{ϕ_0}

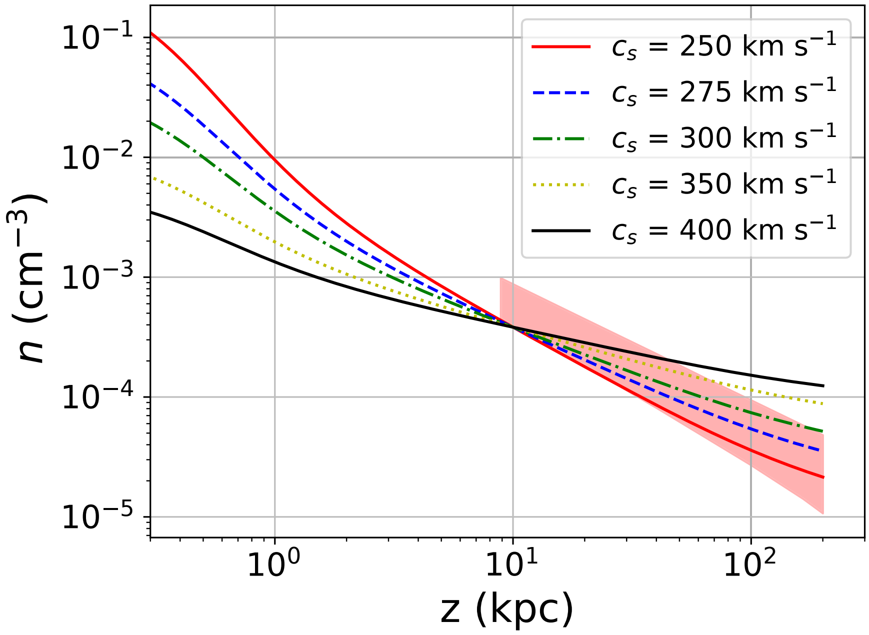

Figure 4.3: The hydrostatic density distribution for the hydrodynamic model (solid red line) with $c_s = 250$ km s^{-1} is compared with three other values of c_s, 275 km s^{-1} (dashed blue line), 300 km s^{-1} (dotted dashed green line), 350 km s^{-1} (dotted yellow line) and 400 km s^{-1} (solid black line). $\Phi_{\rm tot}$ is the same for all the different values and the number density distribution has been fixed at 3.8×10^{-4} cm^{-3} at a distance of 10 kpc from the Galactic Center coinciding with the lower fitting range provided by observations (Martynenko 2022).

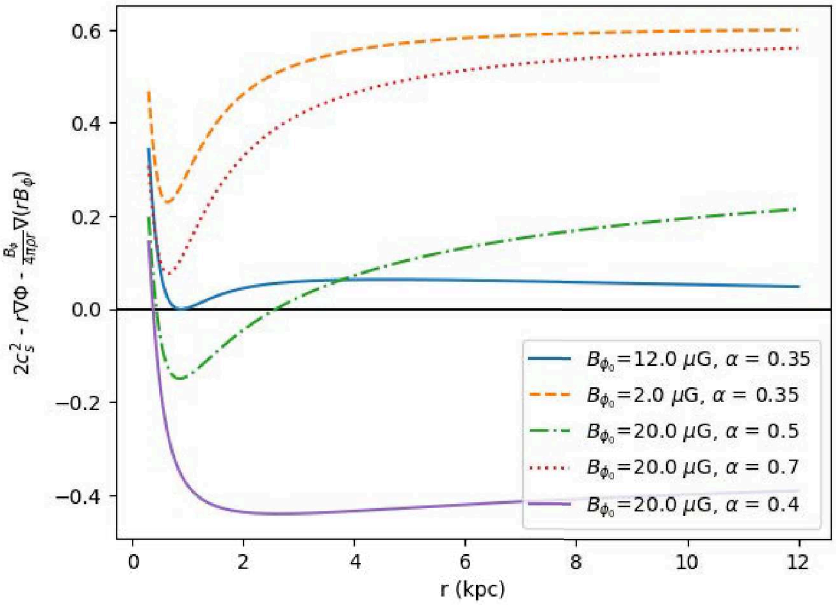

Figure 4.4: The figure shows the different values along r for the numerator at the RHS of the Eq. (4.7) for different configurations of B_{ϕ_0} and α. Considering $c_s = 300$ km s^{-1} and the same normalisation for $\Phi_{\rm tot}$ used for the hydrodynamic numerical simulations, B_{ϕ_0}= 12 μG and α=0.35 lead to $r_c = 1$ kpc (solid blue line). A too small value for B_{ϕ_0} does not give any value for r_c for instance, with $B_{\phi_0} = 2$ μG (dashed orange line). A larger value for B_{ϕ_0} is possible if α is not too large.$B_{\phi_0} = 20$ μG and α=0.5, leading to $r_c = 2.25$ kpc (dashed-dotted green line). But for α=0.7, $B_\phi(r)$ decreases too fast and no value for r_c exists (dotted red line). Moreover, if B_{ϕ_0} is large enough for a value of α too small, there is also no value for r_c (solid purple line).

no root can exist if a strong magnetic field does not decrease fast enough or if a weak field decreases too fast.

Determining B_{ϕ_0} from observations

To be able to increase c_s to its maximal possibility and keep $r_c = 1$ kpc, a possible configuration, according to the numerator at the RHS of the Eq. (4.7), is $B_{\phi_0} = 12\ \mu$G with an $\alpha = 0.35$. This configuration allows $c_s = 300$ km s^{-1}. However, the distribution of $B_\phi(r)$ does not match with the observations and simulations that have been done so far for the Galactic halo. In this region, little is known about the magnetic field but several works have proposed a distribution model based on observations of Faraday rotation measures and synchrotron radiation emission (Jansson and Farrar 2012; Shaw, van Vliet and Taylor 2022; Unger and Farrar 2023). Those works provided an estimation for the magnetic field, at a height between $\sim 1-6$ kpc, of $\sim 1-2.5\ \mu$G.

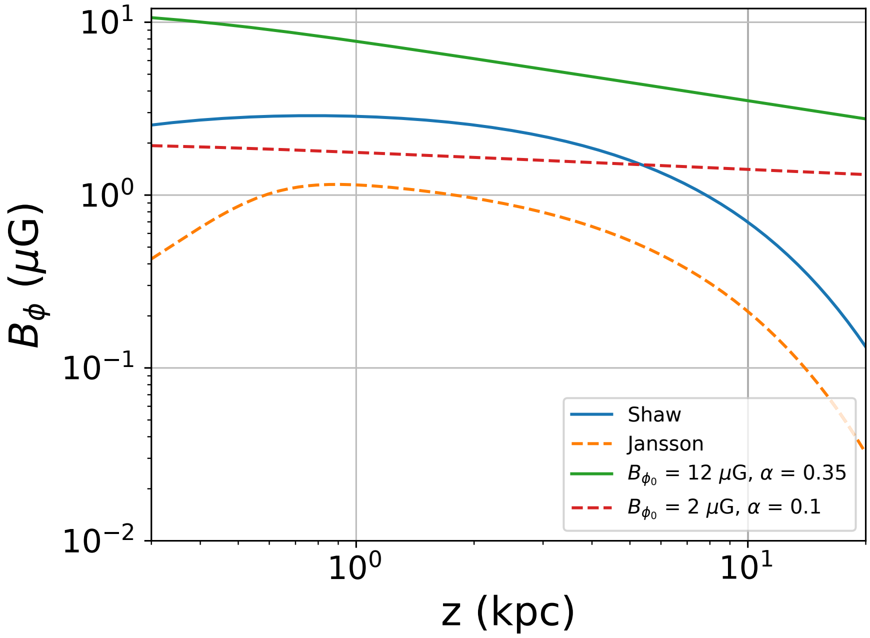

Figure 4.5: Two power-law distributions for $B_\phi(r)$ are compared with the toroidal magnetic field in the Galactic halo deduced from the observations. The $B_\phi(r)$ distribution for which $B_{\phi_0} = 12\ \mu$G and $\alpha = 0.35$ (solid green line) that allows $r_c = 1$ kpc for $c_s = 300$ km s^{-1} do not match with the observations. Based on two models, (Jansson and Farrar 2012) (dashed orange line) and (Shaw, van Vliet and Taylor 2022) (solid blue line), the magnetic field from ~ 1 to 6 kpc ranges from 2 to 3 μG. A power-law distribution for $B_\phi(r)$ with $B_{\phi_0} = 2\ \mu$G and $\alpha = 0.1$ (dashed red line) matches roughly with the observations until a Galactic height of ~ 8 kpc.

In figure 4.5, the toroidal distribution is presented for two previous works by Jansson et al. (Jansson and Farrar 2012) and Shaw et al. (Shaw, van Vliet and Taylor 2022) as well as two configurations, $B_{\phi_0} = 12\ \mu$G for $\alpha = 0.35$ and $B_{\phi_0} = 2\ \mu$G for $\alpha = 0.1$. It can be seen that the first configuration is too high when compared with observations. The second configuration shows a better match but a simple power-law profile is not enough to provide a well-fitted comparison. It shows however, that a value of $\sim 2-3\ \mu$G in the first kiloparsec can roughly match observations.

The frozen-in field approximation

For determining a realistic distribution of $B_\phi(r)$ that will be compared with results provided by a MHD simulation, it is useful to consider the frozen-in field approximation. This approximation states that for a highly conducting fluid, like plasma, embedded with a magnetic field, this last one has to move together with the fluid. This can be shown by considering the expression for a current density, $\mathbf{j}$ for an electromagnetic fluid

$$\mathbf{j} = \sigma \left(\mathbf{E} + \frac{\mathbf{v} \times \mathbf{B}}{c} \right), \tag{4.11}$$

where σ is the coefficient of conductivity. As it is considered infinite for a plasma, this implies that for $\mathbf{j}$ to remain finite, a necessary condition is that

$$\mathbf{E} = -\frac{\mathbf{v} \times \mathbf{B}}{c}, \tag{4.12}$$

given the frozen-in approximation. This one can be included in Faraday's law, expressed by

$$\nabla \times \mathbf{E} = -\frac{1}{c}\frac{\partial \mathbf{B}}{\partial t}. \tag{4.13}$$

Assuming a steady-state condition gives

$$\nabla \times (\mathbf{v} \times \mathbf{B}) = 0. \tag{4.14}$$

This last equation can be used to obtain the expression of $B_\phi(r)$ depending on $v_r(r)$, $v_\phi(r)$ and $B_r(r)$.

$$\frac{1}{r}\frac{d}{dr}\left(r\left(v_r B_\phi - v_\phi B_r\right)\right) = 0, \tag{4.15}$$

leading to

$$r\left(v_r B_\phi - v_\phi B_r\right) = r_0\left(v_{r_0} B_{\phi_0} - v_{\phi_0} B_{r_0}\right). \tag{4.16}$$

It can be easier to understand the relationship between the different components by approximating their distribution. Considering the following power-law distributions

$$v_r = v_{r_0}\left(\frac{r_0}{r}\right)^{\alpha}, \tag{4.17}$$

$$v_\phi = v_{\phi_0}\left(\frac{r_0}{r}\right), \tag{4.18}$$

$$B_r = B_{r_0}\left(\frac{r_0}{r}\right)^{2}, \tag{4.19}$$

gives

$$B_\phi = \left[B_{\phi_0} + B_{r_0}\frac{v_{\phi_0}}{v_{r_0}}\left(\frac{r_0^2}{r^2} - 1\right)\right]\left(\frac{r_0}{r}\right)^{1-\alpha} . \tag{4.20}$$

It can be seen then that it is not necessary to have $B_{\phi_0} \neq 0$ for a $B_\phi(r)$ distribution to exist. For this, if $B_{\phi_0} = 0$ μG, v_{ϕ_0} and B_{r_0} must be different from zero. Even if the combination $B_{r_0}v_{\phi_0}$ is enough to produce a $B_\phi(r)$ distribution, this one will decrease proportionally to $r^{-2-1+\alpha}$. A large value for B_{r_0} or v_{ϕ_0} will be necessary to have a $B_\phi(r)$ value of a few μG for a Galactic height of ~ 1 to 10 kpc. However, a too large value for v_{ϕ_0} would disrupt deeply the propagation of the outflow as it would compete with v_{r_0}.

Also, the distribution of $B_\phi(r)$ depends mostly of α representing the distribution of $v_r(r)$. Considering the Galactic breeze profile (see chapter 2), for which the deceleration corresponds to $\alpha \approx 1$, the distribution of $B_\phi(r)$ should not be steep and looks like a quasi-constant along r. Finally, $B_\phi(r)$ can switch of sign for $B_{\phi_0} > 0$ and $B_{\phi_0} < B_{r_0}\frac{v_{\phi_0}}{v_{r_0}}$.

The analytic study of the influence of a magnetic field distribution on an outflow has provided insight that can be compared with numerical simulations. For this, a MHD code must be used. The setup for such simulations and the subsequent results are introduced and discussed in the following section.

4.3 MHD simulations

As described in section 3.4, the inclusion of a magnetic field is a natural step in trying to explain the features of the Fermi bubbles. This requires the use of a MHD numerical code for solving the MHD equations.

4.3.1 Numerical setup

For solving the MHD equations, the numerical setup is mostly the same as for the hydrodynamic model presented previously (see section 2.6.2). The only difference is the use of a 2.5D logarithmic grid instead of a 2D one. As numerical methods do not naturally preserve the condition of free divergence for a magnetic field, it must be ensured by a specific module. For the simulations, the module *DIV_CLEANING* has been used. With this module, the magnetic field retains a cell average representation and a divergence cleaning technique is used (Dedner et al. 2002; Mignone, Tzeferacos and Bodo 2010).

Computational grid

The computational grid has been setup as a spherical logarithmic 2.5D grid (r, θ). A 2.5D simulation is a computational model that represents a physical system studied in two dimensions while taking into account the effects of components depending on a third dimension, here the azimuthal angle ϕ. B_ϕ is defined as depending on the radial and polar directions and assumes then an axisymmetry. The advantage of a 2.5D simulation over a 3D one is, above all, due to computational efficiency. A 2.5D simulation is less demanding than a 3D simulation for both resources and time. As the main interest is to gain insights into the mutual influence between the radial propagation of the outflow and the radial distribution of $B_r(r,\theta)$ and $B_\phi(r,\theta)$ it is not necessary to fully compute the ϕ-direction.

As for the hydrodynamic model, 256 bins are used in the r-direction and 92 bins in the θ-direction. The inner radius has been fixed at 300 pc and the outer radius at 300 kpc. For the polar direction, the inner θ is 0 and the outer θ is $\pi/2$.

Boundary conditions

At the inner radius, the outflow is injected into the computational grid in the same manner as the hydrodynamic model (see section 2.6.2). The outer radius has been set up with an outflowing boundary. There is a difference with the hydrodynamic model that lies in the setup of the inner θ boundary. For the MHD model, this boundary condition has been setup with an axisymmetric boundary condition. It is identical to a reflective one, except for $v_\phi(r,\theta=0)$ and $B_\phi(r,\theta=0)$ which also change sign. As for the hydrodynamic model (see section 2.6), v_{r_0} is setup at the inner radial boundary. v_{ϕ_0}, B_{r_0} and B_{ϕ_0} are also injected at this boundary. Different values have been considered that depend on the different configurations considered (see section 4.3.2).

Initial setup

The main goal of the MHD simulations is to study the distribution of a magnetic field confined in the bubble produced by a Galactic breeze profile. Therefore, the computation grid at $t=0$ has been setup with no initial distribution for the total magnetic field. Thus, the magnetic field distribution that will be obtained will depend only on its interaction with the Galactic breeze profile. As for the hydrodynamic model, at $t=0$ the computation grid contains an initial density distribution representing the hot Galactic halo gas that is expressed with a hydrostatic distribution. It is defined through Φ_{tot} and c_s (see section 2.5.1). As for the hydrodynamic model, the isothermal temperature for the hot Galactic halo is defined with $kT = 400$ eV, corresponding to $c_s = 250$ km s^{-1}. The expression for P_{th} is then identical to the hydrodynamic model (see section 2.6.2).

4.3.2 Magnetic field distribution in interaction with a Galactic breeze profile

In section 4.2, the effect of the magnetic field has been studied in an analytic way. For $B_\phi(r,\theta)$, described with a simple power-law distribution, it is possible to increase c_s to 300 km s^{-1} and keep $r_c = 1$ kpc. However, for this, $B_{\phi_0} = 12$ μG and $\alpha = 0.35$. Unfortunately, this distribution does not match with the observations of the magnetic field distribution for the Galactic halo (Jansson and Farrar 2012; Shaw, van Vliet and Taylor 2022; Unger and Farrar 2023). Moreover, such a solution, based on a power-law distribution for a steady-state model is extremely difficult to reproduce numerically as the influence of $B_\phi(r,\theta)$ over the velocity profile is not taken into account.

In order to do a first exploration of the influence of the magnetic field on the velocity distribution, several configurations, including small values for B_{r_0}, B_{ϕ_0} and v_{ϕ_0} have been considered. With this, $c_s = 250$ km s^{-1} and $r_c = 1$ kpc as for the hydrodynamic model guaranteeing that the Galactic breeze profile will not be disrupted. Therefore, this allows an easier study of the influence of the magnetic field but also an easier comparison with the hydrodynamic model. The initial values for the different configurations are given in table 4.1.

Configuration	B_{r_0}	B_{ϕ_0}	v_{ϕ_0}
A	20 μG	0 μG	0 km s^{-1}
B 1	2 μG	0 μG	2 km s^{-1}
B 2	-	-	20 km s^{-1}
B 3	-	-	50 km s^{-1}
C 1	20 μG	1 μG	20 km s^{-1}
C 2	-	2 μG	-
C 2.2	40 μG	4 μG	-
C 2.3	20 μG	-	40 km s^{-1}

Table 4.1: List of the different values for the initial setup of the different configurations that are presented.

Configuration A

With this configuration, a test model is first made to explore the influence of $B_r(r, \theta)$ on the velocity distribution. This is done to ensure that the velocity profile stays subsonic throughout the entire computation grid. As described by the Eq. (4.5), $v_r(r, \theta)$ is influenced by $B_\phi(r, \theta)$. $B_r(r)$ playing no roles. It is then not expected to see a difference from the hydrodynamic model. The configuration (A) considers here $B_{r_0} = 20\ \mu$G. In figure 4.6 (a), the 2D map distribution of the Galactic breeze profile is presented. In figure 4.6 (b), the distribution of the Galactic breeze profile along the r-axis can be seen. Both figures show results similar to the hydrodynamic model (see figure 2.8). Figure (b) compares the velocity distribution for the hydrodynamic model (dashed orange line) and for the MHD model (solid blue line) both obtained through numerical computation. Under the influence of $B_r(r)$ the velocity distribution is very similar to the hydrodynamic model.

In figure 4.7 (a), the corresponding magnetic field distribution map can be seen. As the magnetic field is injected with the plasma, its distribution follows the propagation of the outflow and takes a slightly conic shape. In figure 4.7 (b), the distribution of $B_r(r)$ along the z-axis is shown. Following Maxwell laws, the divergence of $B_r(r)$ is null, implying that $B_r(r) \propto r^{-2}$. This power-law is well reproduced through the computational grid. As indicated by the Eq. (4.20), the mere presence of B_{r_0} is not sufficient to imply a distribution for $B_\phi(r, \theta)$. Its value is then null throughout the simulation.

Configuration B

A next step for the simulations is to include a ϕ-component for the propagation of the outflow. The combination of $B_r(r)$ and both $v_r(r, \theta)$ and $v_\phi(r, \theta)$ has an effect on the $B_\phi(r, \theta)$ distribution. As seen with the Eq. (4.20), $B_{\phi_0} = 0$ does not imply that a distribution for $B_\phi(r, \theta)$ is not present for t >0.

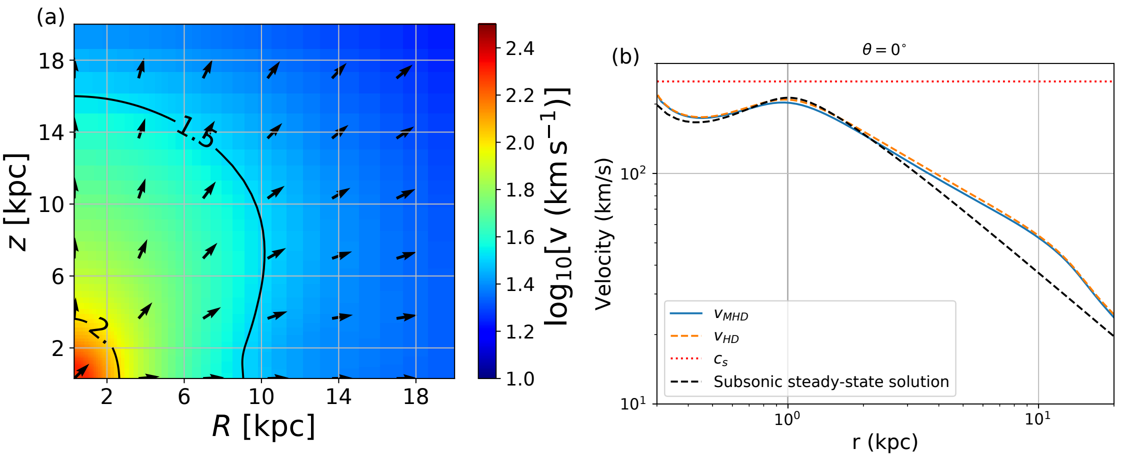

Figure 4.6: **Configuration (A):** For B_{r_0}= 20 μG, B_{ϕ_0} = 0 μG and v_{ϕ_0} = 0 km s^{-1}. In figure (a), a 2D spatial distribution for the Galactic breeze profile with the presence of a $B_r(r)$ field is presented. The arrows represent the direction of propagation of the outflow. The continuous colourbar indicates the logarithm, in base 10, of the magnitude of the velocity. The black contour lines represent the velocity distribution for two specific values of 100 km s^{-1} and 30 km s^{-1}.
In figure (b), the distribution of the Galactic breeze profile along z is plotted (solid blue line) and compared with the hydrodynamic model (orange dashed line) and the analytic steady-state solution (dashed black line).

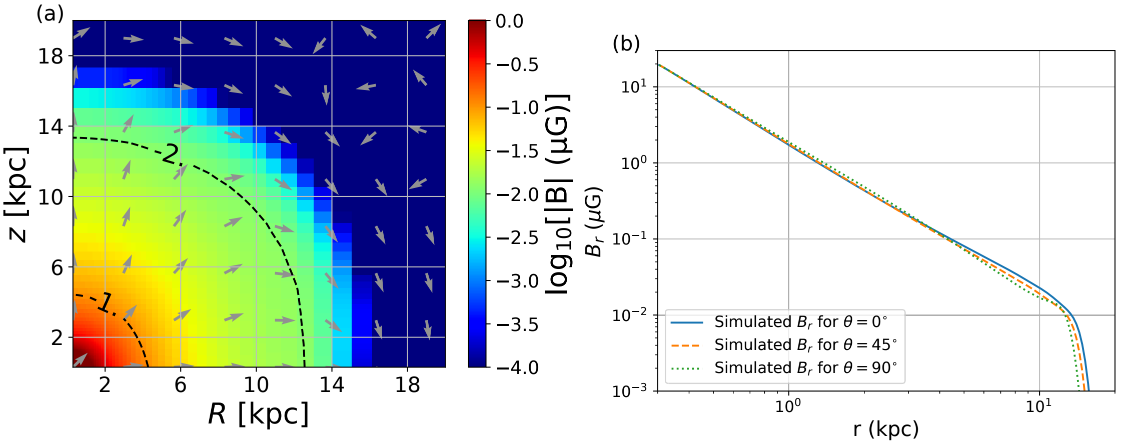

Figure 4.7: **Configuration (A):** For B_{r_0}= 20 μG, B_{ϕ_0} = 0 μG and v_{ϕ_0} = 0 km s^{-1}. In figure (a), the 2D map distribution of the magnetic field is presented. The arrows represent the direction of propagation of $B_R(R, z)$ and $B_z(R, z)$. The colourbar indicates the logarithm, in base 10, of the magnitude of $|B|$. The dashed black contour lines represent the magnetic field distribution for two specific values of 0.1 μG and 0.01 μG.
In figure (b), the loglog plot shows the distribution of B_r for three different fixed polar angles, 0° (solid blue line), 45° (dashed orange line) and 90° (dotted green line).

For the configuration (B), three models have been considered, for which $B_{\phi_0} = 0$ and $B_{r_0} = 2$ μG. This last value is one order of magnitude less than the configuration (A). It has been chosen to allow the $B_\phi(r, \theta)$ field to be larger than the $B_r(r)$ field at a distance depending on each configuration. This gives the opportunity to study the effect that $B_\phi(r, \theta)$ can create on the outflow. The setup for the three different configurations is

1. Configuration (B 1): $B_{r_0} = 2$ μG, $B_{\phi_0} = 0$ μG, $v_{\phi_0} = 2$ km s^{-1}
2. Configuration (B 2): $B_{r_0} = 2$ μG, $B_{\phi_0} = 0$ μG, $v_{\phi_0} = 20$ km s^{-1}

3. Configuration (B 3): $B_{r_0} = 2\ \mu\text{G}$, $B_{\phi_0} = 0\ \mu\text{G}$, $v_{\phi_0} = 50$ km s^{-1}

By using the steady-state solution for the distribution of $v_r(r, \theta)$ (see chapter 2), as presented in figure 2.4 and assuming a value for v_{ϕ_0}, the distribution of $B_\phi(r, \theta)$ can be estimated and compared with the numerical simulations. It must be noted that this comparison can work only in the case where the distribution of $v_r(r, \theta)$ is not strongly modified by the $B_\phi(r, \theta)$ distribution. As it will be seen for the configurations (B) and (C), even if for some models strong perturbations of the outflow can be observed, those perturbations are confined to some regions and the estimation of the distribution of $B_\phi(r, \theta)$ and its comparison with other models stay valid.

The first model, the configuration (B 1), has been tested by considering the following initial values, $B_{r_0} = 2\ \mu$G and $v_{\phi_0} = 2$ km s^{-1}. For those weak values, the resulting velocity distribution is similar to the configuration (A) (see figure 4.6 (a)). In figure 4.8 (a), a comparison is made between the expected distribution for $B_\phi(r, \theta)$ in steady-state (dashed green line) and the distribution provided by the numerical simulation (solid orange line), for $\theta = 45°$. It can be seen that the two profiles fit very well. Also, as expected, $B_r(r) \propto r^{-2}$. The $B_\phi(r, \theta)$ distribution decreases slowly, following a power-law index of ~ 0.3 for 0.4 kpc $< r < 15$ kpc and exceeding $B_r(r)$ at ~ 8 kpc. This distribution of both $B_r(r)$ and $B_\phi(r, \theta)$ is reflected in the distribution of the total magnetic field, as shown in figure 4.8 (b). In the first 8 kpc, the total magnetic field distribution is dominated by B_r, decreasing then $\propto r^{-2}$. Beyond 8 kpc, $B_\phi(r, \theta)$ dominates. As its distribution decreases slowly, it looks homogeneous.

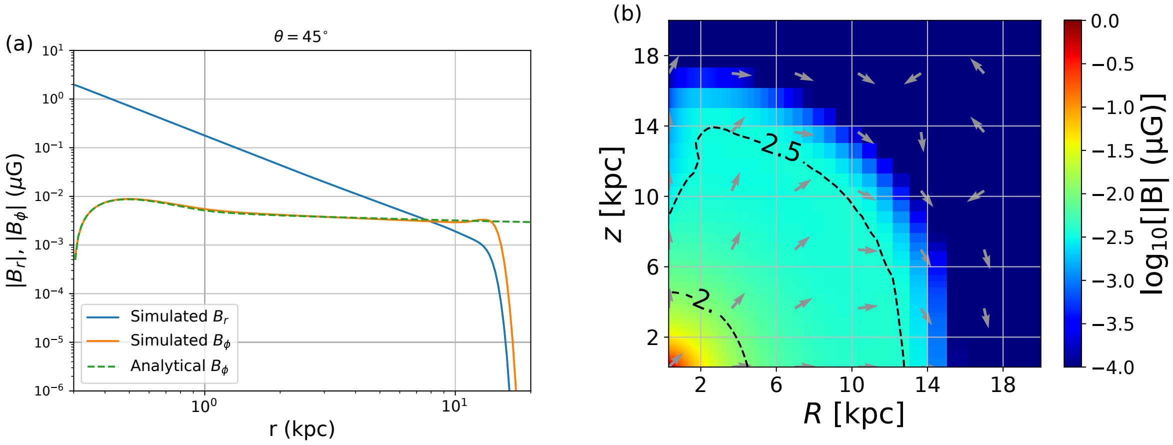

Figure 4.8: **Configuration (B 1):** B_{r_0}= 2 μG, $B_{\phi_0} = 0\ \mu$G and $v_{\phi_0} = 2$ km s^{-1}. In figure (a), a comparison is made between the distribution of $B_\phi(r, \theta)$ obtained numerically (solid orange line) and analytically (dashed green line) for $\theta = 45°$. The distribution of $B_r(r)$ is also presented (solid blue line).
Figure (b), the 2D map distribution of the magnetic field is presented. The arrows represent the direction of propagation of $B_R(R, z)$ and $B_z(R, z)$. The colourbar indicates the logarithm, in base 10, of the magnitude of $|B|$. The dashed black contour lines represent the magnetic field distribution for two specific values of 0.01 μG and 0.003 μG.

For the second model, the configuration (B 2), v_{ϕ_0} has been increased by one order of magnitude, giving $v_{\phi_0} = 20$ km s^{-1}. By considering Eq. (4.20), for such an increase, it is expected that the distribution for $B_\phi(r, \theta)$ will also increase by one order of magnitude. Figure 4.9 (a) shows the distribution of $B_r(r)$ and $B_\phi(r, \theta)$ along

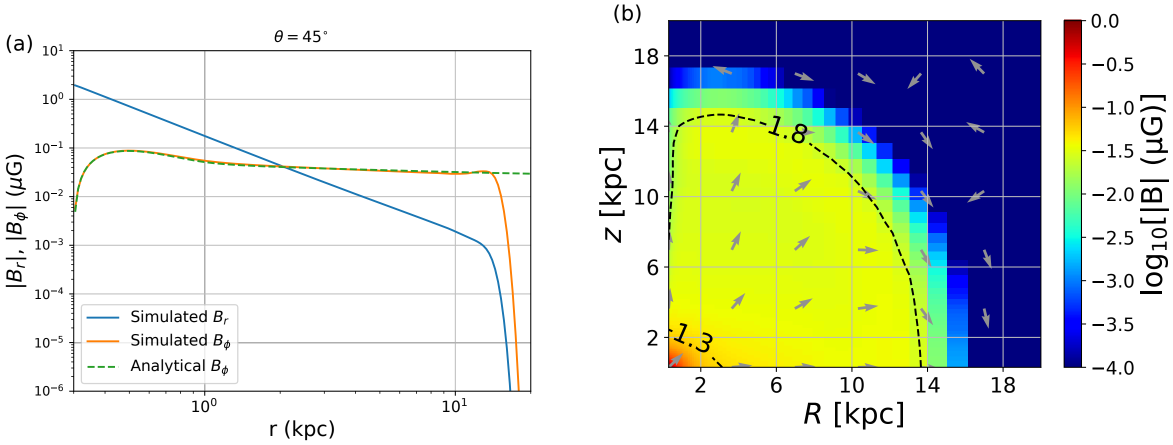

Figure 4.9: **Configuration (B 2):** B_{r_0}= 2 μG, B_{ϕ_0} = 0 μG and v_{ϕ_0} = 20 km s^{-1}. In figure (a), a comparison is made between the distribution of $B_\phi(r,\theta)$ obtained numerically (solid orange line) and analytically (dashed green line) for $\theta = 45°$. The distribution of $B_r(r)$ is also presented (solid blue line).
Figure (b), the 2D map distribution of the magnetic field is presented. The arrows represent the direction of propagation of $B_R(R,z)$ and $B_z(R,z)$. The colourbar indicates the logarithm, in base 10, of the magnitude of $|B|$. The dashed black contour lines represent the magnetic field distribution for two specific values of 0.05 μG and 0.015 μG.

r for $\theta = 45°$. As expected, the $B_\phi(r,\theta)$ distribution is one order of magnitude higher than the configuration (B 1) (see figure 4.8 (a)). Therefore, $B_\phi(r,\theta)$ dominates from a shorter distance than previously, here at $\sim$ 2 kpc. In figure 4.9 (b), the 2D map distribution for the total magnetic field is presented. Until a distance of $r \approx 2$ kpc, $B_r(r)$ dominates. For $r > 2$ kpc, $B_\phi(r,\theta)$ dominates. This domination of $B_\phi(r,\theta)$ at a smaller radius than for the configuration (B 1) (see figure 4.8 (a)) has the effect of creating a shell at the border of the distribution. This happens because the magnetic field lines are anchored in the outflow and move away due to their propagation. As the outflow decelerates, the magnetic field lines pile up. However, the weak intensity of the $B_\phi(r,\theta)$ field does not create a shell with a significant intensity.

As the outflow, due to the asymmetry of $\Phi_{\rm tot}$ induced by the disc component, propagates mainly along the z-direction (see section 2.6.3), the compression of the magnetic field is larger at the top of the bubble. This compression, although weak, is still enough to twist the magnetic field lines, causing a deceleration through the effect of magnetic tension. This effect can be seen in figure 4.10 for which the 2D map of the distribution of the total velocity has been plotted. At the top of the bubble, for a height of $\sim$14 kpc, the deceleration of the outflow due to magnetic tension can be observed on the contour line standing for $\log_{10}(v) = 1.5$.

The third model, configuration (B 3), explores further the effect of the magnetic tension on the velocity distribution. This effect can be better observed by increasing $v_\phi(r,\theta)$ and thus reducing even more the radial distance over which $B_\phi(r,\theta)$ dominates over $B_r(r)$. Both velocity and magnetic field distributions can be seen in figure 4.11. In figure (a), the 2D map of the total magnetic field distribution shows a strong compression on the top of the bubble at a height of $\sim$ 8 kpc. As shown by the arrows in this zone, the magnetic field is twisted around this compression, causing a deceleration of the outflow. In figure (b), the 2D map of the velocity distribution is presented. As the compression of the magnetic field lines happens at a smaller height, the effect on the outflow leads to a larger deformation. An important zone of

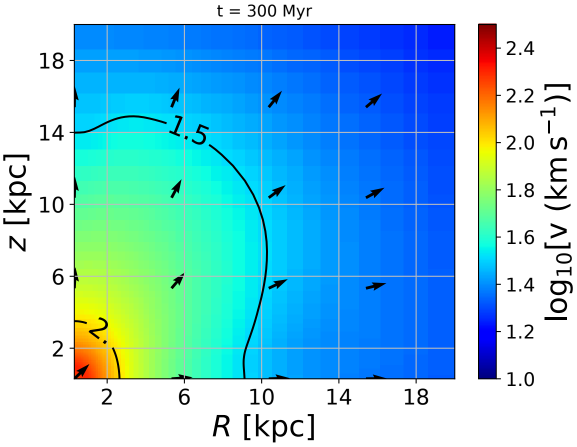

Figure 4.10: **Configuration (B 2):** B_{r_0}= 2 μG, B_{ϕ_0} = 0 μG and v_{ϕ_0} = 20 km s^{-1}. A 2D spatial distribution for the Galactic breeze profile under the influence of a magnetic field is presented. The arrows represent the direction of propagation of the outflow. The continuous colourbar indicates the logarithm, in base 10, of the magnitude of the velocity. The black contour lines represent the velocity distribution for two specific values of 100 km s^{-1} and 30 km s^{-1}. At z = 14 kpc, for $0 < R < 2$ kpc, the contour line shows a deceleration happening because of a magnetic tension effect.

deceleration can be seen coinciding with the zone of magnetic compression. Moreover, the velocity distribution formed by the Galactic breeze is larger than for the hydrodynamic model (see figure 2.8). Since the magnetic tension acts to decelerate the outflow, the compression zone is then bypassed and the outflow propagates in broader directions. Following the conservation of momentum equation, the outflow is accelerated along those directions.

Configuration C

The last step is to consider $B_{\phi_0} \neq 0$. This will lead to larger values for the distribution of $B_\phi(r, \theta)$. As a result, the value of B_{r_0} that was of 2 μG for the configuration (B) has been switched back to 20 μG. For the configuration (C), two models have been considered.

1. Configuration (C 1): $B_{r_0} = 20\ \mu$G, $B_{\phi_0} = 1\ \mu$G, $v_{\phi_0} = 20$ km s^{-1}
2. Configuration (C 2) : $B_{r_0} = 20\ \mu$G, $B_{\phi_0} = 2\ \mu$G, $v_{\phi_0} = 20$ km s^{-1}

Keeping a constant value for B_{r_0} and v_{ϕ_0} ensures that the differences that will appear between the two models will be only due to the variation of the B_{ϕ_0} value.

For the configuration (C 1), the corresponding 2D velocity distribution map can be seen in figure 4.12. From the results that have been studied for the configurations (B 2) and (B 3), the magnetic tension leads to a deceleration of the outflow at a Galactic height of $\sim$ 13 kpc but this deceleration is not as pronounced as for the configuration (B 3). Here, the compressed magnetic field is bypassed by the outflow, creating an extension in the velocity distribution when compared to the hydrodynamic model (see figure 2.8). In figure 4.13 (a), the distribution of $B_r(r)$ and $B_\phi(r, \theta)$ along the spherical radius for $\theta = 45°$ is presented. $B_r(r) \propto r^{-2}$ and the distribution for $B_\phi(r, \theta)$ is quite similar to the configurations (B 1) and (B 2)

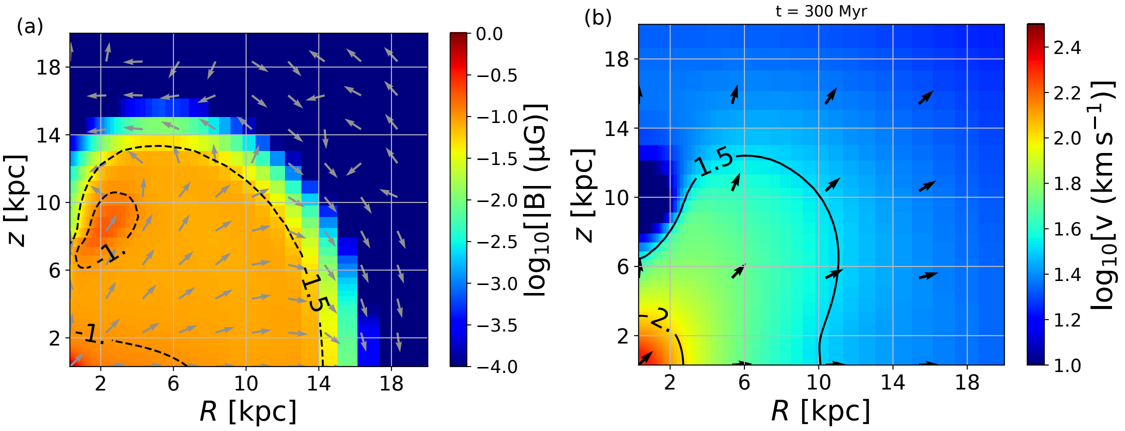

Figure 4.11: **Configuration (B 3):** B_{r_0}= 2 μG, B_{ϕ_0} = 0 μG and v_{ϕ_0} = 50 km s^{-1}. For figure (a), the 2D map distribution of the magnetic field is presented. The arrows represent the direction of propagation of $B_R(R,z)$ and $B_z(R,z)$. The colourbar indicates the logarithm, in base 10, of the magnitude of $|B|$. The dashed black contour lines represent the magnetic field distribution for two specific values of 0.1 μG and 0.03 μG. At $z \approx 8$ kpc and $R \approx 2$ kpc, the contour lines show the compression of the magnetic field lines, leading to an increase in the intensity.
In figure (b), a 2D spatial distribution for the Galactic breeze profile under the influence of a magnetic field is presented. The arrows represent the direction of propagation of the outflow. The continuous colourbar indicates the logarithm, in base 10, of the magnitude of the velocity. The black contour lines represent the velocity distribution for two specific values of 100 km s^{-1} and 30 km s^{-1}. The contour line for $\log_{10}(v) = 1.5$, shows a large zone of deceleration that is due to the compression of the magnetic field (see figure (a)).

(see figures 4.8 (a) and 4.9 (a)). However, the first difference lies in the intensity of $B_\phi(r,\theta)$ that is four times larger than for the configuration (B 2). The second one is in the change of direction that can be seen at $r \approx 0.4$ kpc. This transition can be understood by looking at Eq. (4.20). For the configuration (C 1), the initial parameters are $B_{r_0} = 20$ μG, $v_{\phi_0} = 20$ km s^{-1} and $v_{r_0} = 211$ km s^{-1}. This leads to $B_{r0}\frac{v_{\phi 0}}{v_{r0}} \approx 2$ μG. At the inner boundary, $B_{\phi_0} = 1$ μG but as the radius increases and $r > r_0$ the second term of Eq. (4.20) leads to a negative direction.

In figure 4.13 (b), the 2D distribution map for the total magnetic field is presented. As implied by figure (a), the field strength is found to be quasi-uniform from a distance of 1 kpc to 12 kpc. The intensity of the shell at the border of the distribution or at the zone of compression is not large enough to be clearly visible. The distribution shows an extension reaching a height of ~ 18 kpc. As the magnetic field lines are anchored to the outflow, the extension visible in the velocity distribution (see figure 4.12) leads to the extension in the magnetic field distribution.

For the configuration (C 2), the value $B_{\phi_0} = 2$ μG has been considered. It exhibits a specific magnetic field distribution, as shown in figure 4.14 (a) and (b). Figure (a) presents the distribution of $B_r(r)$ and $B_\phi(r,\theta)$ along the spherical radius for $\theta = 45°$. The distribution of $B_\phi(r,\theta)$ (solid orange line) matches well with the steady-state solution (dashed green line), except for the extremity of the distribution, at $r \approx 13$ kpc, where $B_\phi(r,\theta)$ presents a surge in the intensity. Moreover, the direction of the $B_\phi(r,\theta)$ distribution in this surge is negative when it is positive from 0.3 kpc to ~ 13 kpc. As presented in figure 4.14 (b), this $B_\phi(r,\theta)$ distribution with a negative direction forms a shell as it is pushed along with the outflow propagation. This is shown in figure 4.15 for four different time steps. For $t = 3$ Myr (figure (a)), B_{ϕ_0} is injected with a positive value. However, the direction of $B_\phi(r,\theta)$ switches

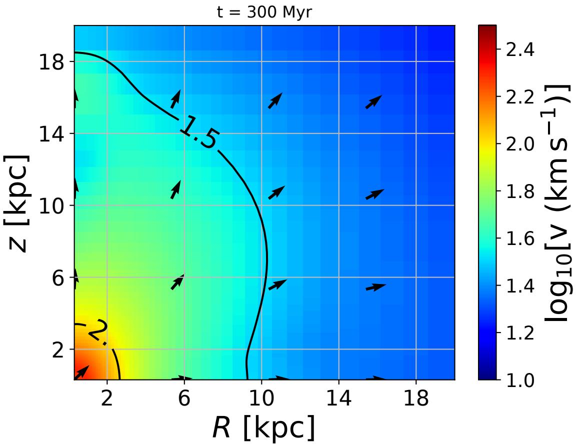

Figure 4.12: **Configuration (C 1):** B_{r_0}= 20 μG, B_{ϕ_0} = 1 μG and v_{ϕ_0} = 20 km s^{-1}. The figure shows the 2D spatial distribution for the Galactic breeze profile. The arrows represent the direction of propagation of the outflow. The continuous colourbar indicates the logarithm, in base 10, of the magnitude of the velocity. The black contour lines represent the velocity distribution for two specific values of 100 km s^{-1} and 30 km s^{-1}. The contour line for $\log_{10}(v)$ = 1.5, shows a zone where the velocity is larger than for the hydrodynamic model (see figure 2.8) for $z > 14$ kpc.

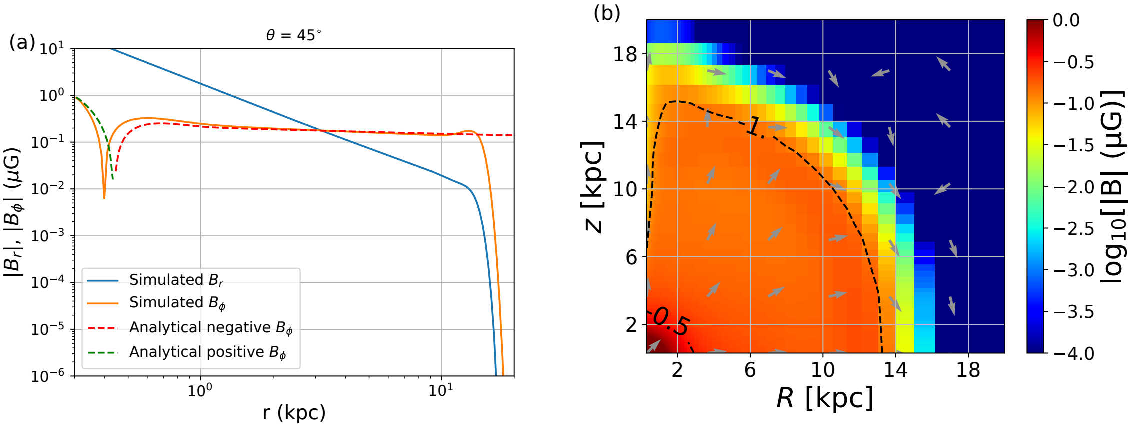

Figure 4.13: **Configuration (C 1):** B_{r_0}= 20 μG, B_{ϕ_0} = 1 μG and v_{ϕ_0} = 20 km s^{-1}. In figure (a), a comparison is made between the distribution of $B_\phi(r,\theta)$ obtained numerically (solid orange line) and analytically for $\theta = 45°$. The transition of $B_\phi(r,\theta)$ between a positive (dashed green line) and negative value (dashed red line) is shown. The distribution of $B_r(r)$ is also presented (solid blue line).

For figure (b), the 2D map distribution of the magnetic field is presented. The arrows represent the direction of propagation of $B_R(R,z)$ and $B_z(R,z)$. The colourbar indicates the logarithm, in base 10, of the magnitude of $|B|$. The dashed black contour lines represent the magnetic field distribution for two specific values of 0.3 μG and 0.1 μG.

almost immediately. In figure (b), $B_\phi(r,\theta)$ propagates along r with the outflow for t = 30 Myr. The direction of $B_\phi(r,\theta)$ is negative for $0.4 < r < 3$ kpc. It can be seen that the direction of $B_\phi(r,\theta)$, which was switching almost immediately after the injection, switches now at a farther distance. In figure (c), for t = 150 Myr, the direction of $B_\phi(r,\theta)$, from the inner radius to a distance of $\sim$ 4.5 kpc, is positive. The $B_\phi(r,\theta)$ distribution presenting a negative direction has been moved away due to the propagation of the outflow and is compressed and starts to form a shell. In figure (d), for t = 300 Myr, the shell has been formed. It is composed by the $B_\phi(r,\theta)$ distribution exhibiting a negative direction. The rest of the $B_\phi(r,\theta)$ distribution, from a distance of 0.3 kpc to ∼ 12 kpc, shows a positive direction.

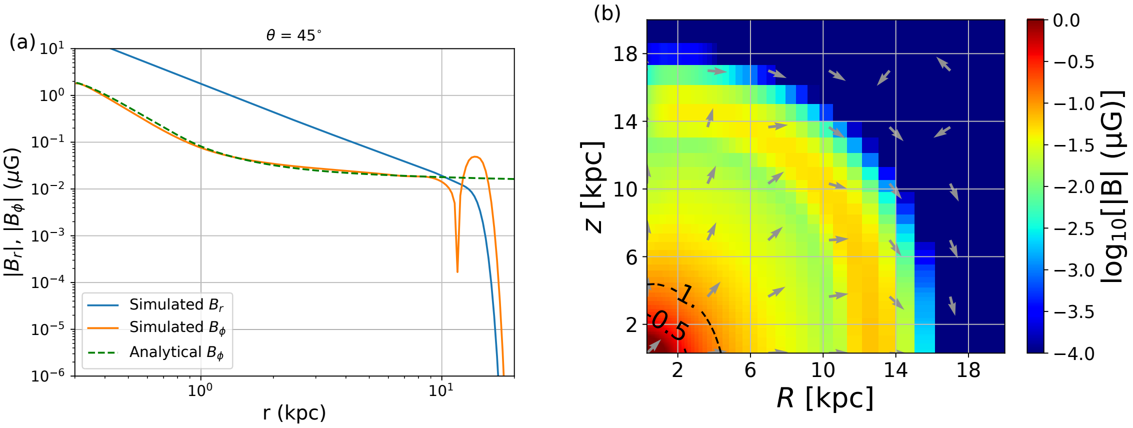

Figure 4.14: **Configuration (C 2):** B_{r_0}= 20 μG, B_{ϕ_0} = 2 μG and v_{ϕ_0} = 20 km s^{-1}. In figure (a), a comparison is made between the distribution of $B_\phi(r,\theta)$ obtained numerically (solid orange line) and analytically (dashed gree line) for $\theta = 45°$. The distribution of $B_r(r)$ is also presented (solid blue line).
Figure (b), presents the 2D map distribution of the magnetic field. The arrows represent the direction of propagation of $B_R(R,z)$ and $B_z(R,z)$. The colourbar indicates the logarithm, in base 10, of the magnitude of $|B|$. The dashed black contour lines represent the magnetic field distribution for two specific values of 0.3 μG and 0.1 μG.

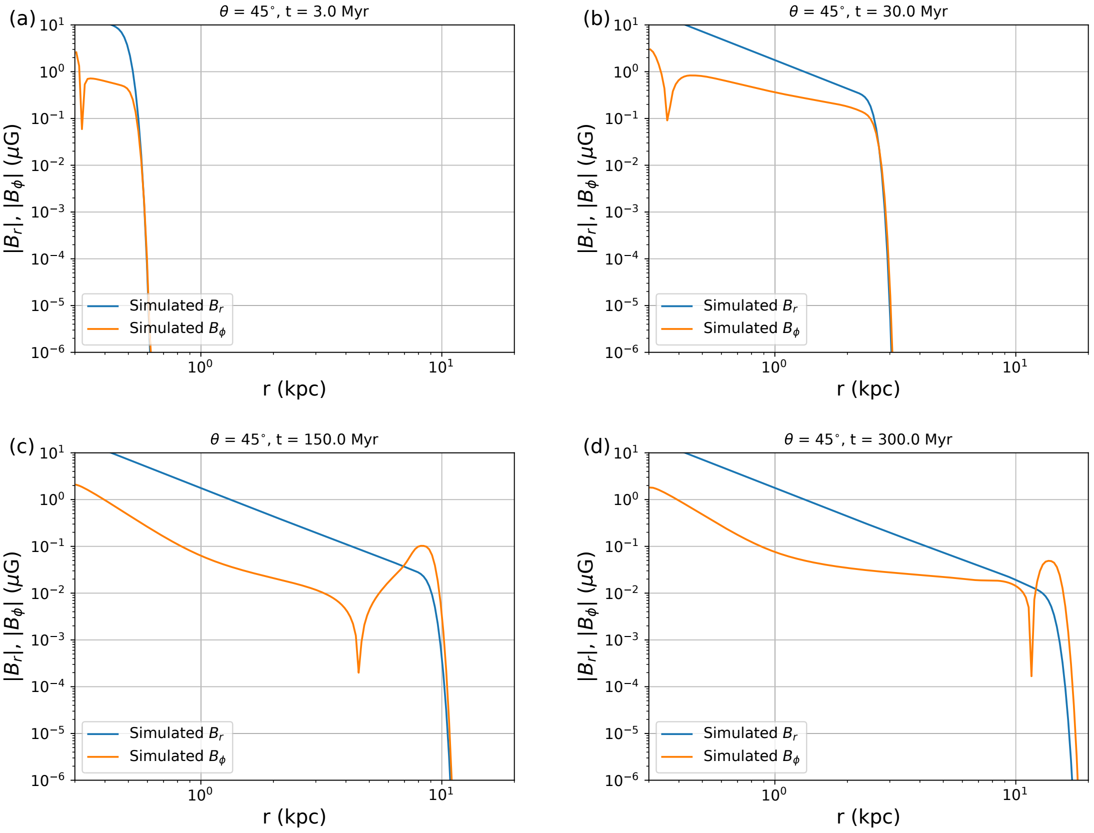

Figure 4.15: **Configuration (C 2):** B_{r_0}= 20 μG, B_{ϕ_0} = 2 μG and v_{ϕ_0} = 20 km s^{-1}. The different figures show the temporal evolution of both $B_\phi(r,\theta)$ (solid orange line) and $B_r(r)$ (solid blue line). In figure (a), t = 3 Myr. In figure (b), t = 30 Myr. In figure (c), t = 150 Myr. In figure (d), t = 300 Myr.

This distribution is particularly interesting since, from the first observations of the Fermi bubbles, a magnetic field strength of $6 - 12$ μG for the lobes and $13 - 15$ μG for the edges has been inferred (Carretti et al. 2013). As the different models aiming to reproduce the features of the Fermi bubbles consider a supersonic velocity, the stronger strength of the magnetic field at the edges is associated with a shock structure. However, for a subsonic model such a shock does not exist (see section 2.5.2). Therefore, the configuration (C 2) offers a possibility for the Galactic breeze model to produce a shell that increases locally the strength of the magnetic field. This specific distribution could be due to the fact that for, the configuration (C 2) (see table 4.1), Eq. (4.20) is equal to zero when $r = r_0$. To test this possibility, two additional configurations have been considered.

1. Configuration (C 2.2) : $B_{r_0} = 40$ μG, $B_{\phi_0} = 4$ μG, $v_{\phi_0} = 20$ km s^{-1}
2. Configuration (C 2.3) : $B_{r_0} = 20$ μG, $B_{\phi_0} = 4$ μG, $v_{\phi_0} = 40$ km s^{-1}

For both configurations, $B_{r0}\frac{v_{\phi0}}{v_{r0}} \approx 4$ μG leading to an Eq. (4.20) close to zero as $B_{\phi0} = 4$ μG.

For the configuration (C 2.2), figure 4.16 (a) presents the distribution of $B_r(r)$ and $B_\phi(r,\theta)$ for $\theta = 45°$. The comparison between the analytic steady-state of $B_\phi(r)$ (dashed green line) and the simulated $B_\phi(r,\theta)$ (orange solid line) shows a discrepancy.

For the configuration (C 2.3), figure 4.16 (b) presents the distribution of $B_r(r)$ and $B_\phi(r,\theta)$ for $\theta = 45°$. The comparison between the analytic steady-state of $B_\phi(r)$ (dashed green line) and the simulated $B_\phi(r,\theta)$ (orange solid line) is identical, except for a distance of ~ 13 kpc where a surge can be seen. This configuration presents then a distribution qualitatively identical to the configuration (C 2). Those two configurations show that the values of B_{r_0} and v_{ϕ_0} are important for creating a shell. It also shows that for the configuration (C 2.2), the larger value for B_{r_0} causes the discrepancy.

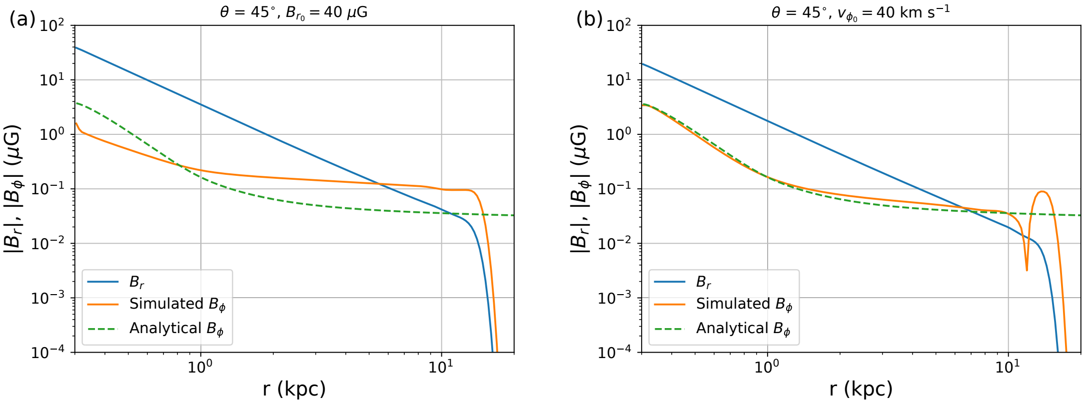

Figure 4.16: The figures present and compare the distribution of $B_\phi(r,\theta)$ obtained numerically (solid orange line) and analytically (dashed green line) for $\theta = 45°$. The distribution of $B_r(r)$ is also shown (solid blue line).
Figure (a) presents the different distributions for the configuration (C 2.2): B_{r_0}= 40 μG, $B_{\phi_0} = 4$ μG and $v_{\phi_0} = 20$ km s^{-1}.
Figure (b) presents the different distributions for configuration (C 2.3): B_{r_0}= 20 μG, $B_{\phi_0} = 4$ μG and $v_{\phi_0} = 40$ km s^{-1}.

4.4 Conclusion for the chapter

The hydrodynamic model proved that a Galactic breeze profile is able to provide a velocity distribution with a deceleration similar to the observations. This velocity profile has been used to produce a γ-ray emission based on *pp* interactions. This emission exhibits a bubble shape but is too wide when compared with observations. That is, the model does not seem to be able to reproduce the sharpness of the Fermi bubbles edges. An additional mechanism is therefore needed and a magnetic field distribution has been considered.

The first step was to study the influence of a magnetic field distribution on the Galactic breeze profile through the MHD momentum equation for a steady-state. From this, it has been deduced that only the $B_\phi(r,\theta)$ field has an influence on the velocity profile. Moreover, $B_\phi(r,\theta)$ can have an effect on the position of the critical radius, r_c. Considering that $B_\phi(r,\theta)$ can be approximated by an inverse power-law for a power index $\alpha < 1$, $B_\phi(r,\theta)$ can shift r_c farther away from the Galactic Center. This effect allows to increase the temperature, which will have the effect of shifting back r_c closer from the Galactic Center. It is possible, at least in an analytic way, to propose a model for which the subsonic profile can reach a velocity of 300 km s^{-1} at $r_c = 1$ kpc. However, as a hydrostatic density distribution seems to be able to describe the hot Galactic halo for a distance $r > 8$ kpc, the influence of the temperature on the density distribution must be taken into account. The analysis has shown that, based on observations, the maximal thermal velocity possible is $c_s \approx 300$ km s^{-1}. With such a result, the Galactic breeze profile remains an option. Moreover, it is possible to use the frozen-in field approximation to predict the distribution of $B_\phi(r,\theta)$. This prediction has been compared with the results provided by a MHD numerical simulation for different configurations. It must be noted that such a prediction of $B_\phi(r,\theta)$ can be done because the hydrodynamic Galactic breeze profile has been assumed. The comparison can therefore only hold if the magnetic field distribution does not largely disrupt the velocity profile.

To be able to produce a numerical simulation for a Galactic breeze profile reaching 300 km s^{-1} by including a magnetic field is an extremely difficult task. As part of this thesis, only weak values for both $B_r(r)$ and $B_\phi(r,\theta)$ have been considered. With those values, $c_s = 250$ km s^{-1}, i.e., the thermal velocity is identical to the hydrodynamic model. This allowed an easier comparison between the hydrodynamic model and the MHD model and to study more easily the influence of the $B_r(r)$ and $B_\phi(r,\theta)$ distributions on the velocity profile. Several numerical simulations have been done based on different configurations.

The first configuration (A), has been setup for testing the consistency of the simulations with the MHD simulations. Based on the MHD momentum equation, $B_r(r)$ does not influence the velocity profile. It has been defined with $B_{r_0} = 20$ μG, $B_{\phi_0} = v_{\phi_0} = 0$. The result is in accordance with the prediction. The velocity profile is identical to the hydrodynamic model and $B_r(r) \propto r^{-2}$ as expected from the free divergence of a magnetic field.

The configurations (B) have been focused on the influence of $v_\phi(r,\theta)$ on the $B_\phi(r,\theta)$ distribution. From the prediction, it is indeed possible to see that an initial value for $B_\phi(r,\theta)$ is not necessary if $B_{r_0} \neq 0$ and $v_{\phi_0} \neq 0$. Three different models have been considered that each have a different value for $v_\phi(r.\theta)$. The models have shown the impact of a compression of the magnetic field on the velocity distribution. This compression leads to a bending of the magnetic field lines, which has the effect of decelerating the outflow in the compression zone due to a magnetic tension effect.

Finally, the configuration (C) has introduced the parameter B_{ϕ_0}, i.e., an initial value for the injection of $B_\phi(r, \theta)$. The configuration (C 2) is the most interesting because it shows a shell for which the magnetic strength is largely increased compared to the previous configuration. This feature is reminiscent of the shell observed on the Fermi bubbles, for which the magnetic field is stronger than the one from the lobes.

The MHD simulations have then shown promising results about the consistence of a Galactic breeze model combined with a magnetic field. The next step, as for the hydrodynamic model, is to use the simulated velocity and magnetic field distribution to numerically solve the CR transport equation. The presence of the magnetic field allows for a more complex definition of the diffusion coefficient.

Chapter 5

Propagation of cosmic rays and γ-ray emission for a MHD model

For the MHD model, a magnetic field has been injected alongside a velocity field. This has given a spatial distribution for the magnetic field that depends on each configuration considered. As this magnetic field is not homogeneous, the $n_{\rm CR}$ distribution and the related γ-ray energy flux distribution cannot be obtained by considering a homogeneous density coefficient anymore. The CR transport code for a MHD model must then include an inhomogeneous diffusion coefficient that can be isotropic or anisotropic. In section 5.1, the expression for an isotropic and inhomogeneous diffusion length is introduced. The configurations introduced in chapter 4 are used to determine the $n_{\rm CR}$ distribution and the resulting γ-ray energy flux and are compared with the hydrodynamic model presented in chapter 3. In section 5.2, the expression of the anisotropic diffusion coefficient is given. Its implementation into the CR transport code is discussed and the results are presented.

5.1 Isotropic diffusion coefficient

5.1.1 Diffusion length

As a spatial distribution of a magnetic field is considered, an isotropic and inhomogeneous diffusion coefficient is first used for solving the CR transport equation. From quasi-linear theory, the diffusion length is given by (Jokipii 1966; Schlickeiser 1989)

$$\frac{D}{c} = \left(\frac{B_0^2}{\delta B(r_L)^2}\right) r_L, \tag{5.1}$$

where $r_L = p/\left(eB_0\right)$ is the Larmor radius. B_0^2 represents the mean magnetic field and $\delta B^2(r_L)$ represents the turbulent component and can be expressed as

$$\delta B^2(\lambda) = \lambda \frac{d\delta B^2}{d\lambda}, \tag{5.2}$$

where λ is a wavelength. δB^2 can be expressed by the summed power of the turbulent modes

$$\delta B^2 = \int \frac{d\delta B^2}{d\lambda} d\lambda, \tag{5.3}$$

for which

$$\frac{d\delta B^2}{d\lambda} = \frac{d\delta B^2}{dk}\frac{dk}{d\lambda} = a\lambda^{\gamma-2}, \tag{5.4}$$

where k $\propto \lambda^{-1}$ is a wave number and $d\delta B^2/dk$ represents the power spectrum $\propto k^{\gamma}$. $\gamma = 5/3$ is the Kolmogorov index spectrum. The Eq. (5.3) can therefore be expressed by

$$\delta B^2 = \int_{\lambda_{\mathrm{min}}}^{\lambda_{\mathrm{max}}} a\lambda^{\gamma-2} d\lambda \approx a\lambda_{\mathrm{max}}^{\gamma-1}, \tag{5.5}$$

where λ_{max} corresponds to the longest wavelength and λ_{min} the shortest. λ_{max} represents the characteristic distance over which the magnetic field maintains its coherence. Considering $a = \delta B^2 \lambda_{\mathrm{max}}^{1-\gamma}$ and Eq. (5.2) leads to

$$\delta B^2(\lambda) = \delta B^2 \left(\frac{\lambda}{\lambda_{\mathrm{max}}}\right)^{\gamma-1} \tag{5.6}$$

Using this expression with Eq. (5.1) gives

$$\frac{D}{c} = \frac{B_0^2}{\delta B^2}\left(\frac{r_L}{\lambda_{\mathrm{max}}}\right)^{1-\gamma} r_L. \tag{5.7}$$

Throughout this work, $B_0^2 = \delta B^2$ is assumed. The value for λ_{max} depends on the size of the astrophysical system considered. Here, the maximal radius of a shock wave produced by a supernova is considered. For an ambient medius gas with a density of 2×10^{-24} g cm^{-3} and an energy of $E = 10^{51}$ erg, this shock radius is ~ 2 pc (Shu 1992).

From observations, the diffusion lenth of the Galactic halo has been deduced to be $D/c \approx 10^{28}$ cm^2 s^{-1} or ~ 0.1 pc (Ginzburg, Khazan and Ptuskin 1980). This value has been used to define an isotropic and homogeneous D/c for the hydrodynamic model (see chapter 3). However, as r_L depends on the magnetic field distribution, D/c cannot be considered homogeneous anymore. A first step, for a comparison with the hydrodynamic model, is to select a suitable value for λ_{max} for each configuration explored in the previous chapter (see chapter 4). In such a way, D/c will be close enough to 0.1 pc. The different values considered for λ_{max} are listed for each configuration in table 5.1.

Configuration	λ_{max}
A	1 pc
B 1	0.5 pc
B 2	1.5 pc
B 3	2 pc
C 1	3 pc
C 2	1.5 pc

Table 5.1: List of the different values of λ_{max} for each considered configuration.

Configuration A

For configuration (A), the total magnetic field only depends on its radial component (see table 4.1) that follows a power-law distribution $\propto r^{-2}$. A variation of D/c for the spatial grid is then expected (see Eq (5.7)). $\lambda_{\max} = 1$ pc has been chosen and the corresponding 2D spatial distribution map for D/c can be seen in figure 5.1. In the inner part of the distribution, D/c ranges from ~ 0.03 pc to 0.1 pc (dark blue to light blue). At the border of the distribution, the diffusion length ranges from ~ 0.15 pc to 0.3 pc (green to yellow).

As $\lambda_{\max} = 1$ pc has been assumed, r_L is not allowed to go beyond this value. $r_L = 1$ pc corresponds to $B_r(r) = 10^{-5}$ μG for a 10 GeV particle. Thus, anywhere on the computational grid where $B_r(r) < 10^{-5}$ μG, $B_r(r)$ has been fixed with the minimal value $B_{r_{\min}} = 10^{-5}$ μG. Then, beyond the bubble, at a distance of $r \approx 14$ kpc (see figure 4.7), D/c is assumed to be constant and equals to 1 pc (orange).

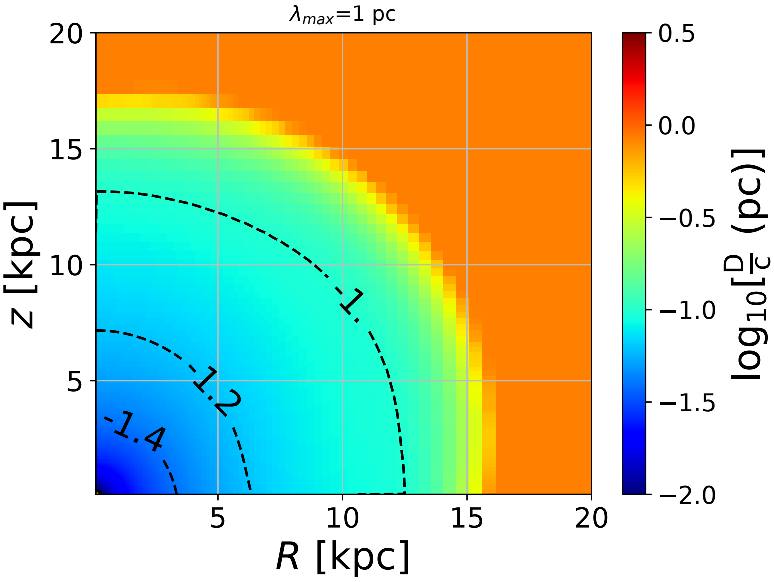

Figure 5.1: **Configuration (A):** B_{r_0}= 20 μG, $B_{\phi_0} = 0$ μG and $v_{\phi_0} = 0$ km s^{-1}. The figure represents the 2D spatial distribution map for D/c. In the inner part, D/c ranges from $\sim$0.03 pc to 0.1 pc (dark blue to light blue). At the border, D/c ranges from $\sim$0.15 pc to 0.3 pc (green to yellow). As $\lambda_{\max} = 1$ pc, the minimal value for $B_r(r)$ has been fixed to be 10^{-5} μG corresponding to $r_L = 1$ pc (orange) for a 10 GeV particle.

Configuration B

For the three different models discussed for the configuration B, where $B_{\phi_0} = 0$, the combination of B_{r_0} and v_{ϕ_0} is able to produce a non-zero $B_\phi(r, \theta)$ distribution (see Eq. (4.20)).

For configuration (B 1), the $B_\phi(r, \theta)$ distribution is quasi-constant for a distance ranging from $\sim$ 1 kpc to 15 kpc (see figure 4.8). However, $B_\phi(r, \theta)$ only becomes larger than $B_r(r)$ at a distance of $\sim$ 8 kpc. As a result, D/c increases along the radius and stabilises at a distance of $\sim$ 8 kpc. In figure 5.2, the 2D map for the spatial distribution of D/c is presented. $\lambda_{\max} = 0.5$ pc has been chosen. From ~ 8 kpc $< r < 15$ kpc, $D/c = 0.1$ pc (light blue zone). At the border, $D/c \approx 0.3$ pc (green zone). For $r > 16$ kpc, $r_L = \lambda_{\max}$ for 10 GeV particles, giving $D/c = 0.5$ pc (yellow zone).

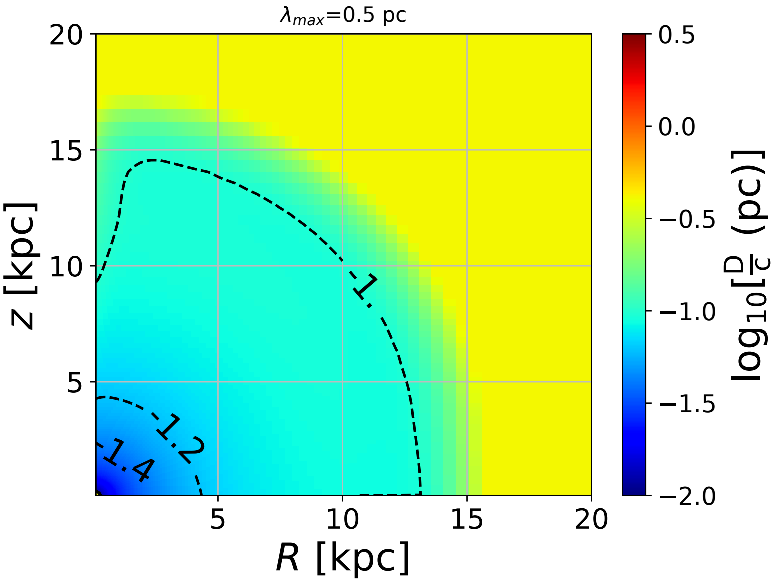

Figure 5.2: **Configuration (B 1):** B_{r_0}= 2 μG, B_{ϕ_0} = 0 μG and v_{ϕ_0} = 2 km s^{-1}. The figure represents the 2D map for the spatial distribution of D/c. For this configuration, $\lambda_{\max} = 0.5$ pc. With this value, at ~ 8 kpc $< r <$ 15 kpc, $D/c = 0.1$ pc (light blue zone). At the border, $D/c \approx 0.3$ pc (green zone) and for $r >$16 kpc, $D/c = \lambda_{\max}$ (yellow zone).

For configuration (B 2), as v_{ϕ_0} is increased by one order of magnitude (see table 4.1), $B_\phi(r, \theta)$ is increased by the same amount and becomes larger than $B_r(r)$ at $r \approx 2.5$ kpc (see figure 4.9). For this configuration, $\lambda_{\max} = 1.5$ pc has been chosen to have $D/c = 0.1$ pc in a large part of the bubble. In figure 5.3, the 2D map for the spatial distribution map of D/c is shown. For this configuration, $B_\phi(r, \theta)$ is larger than $B_r(r)$ at $r = 2.5$ kpc and exhibits a spatial magnetic field distribution that can be considered quasi-constant, giving $D/c = 0.1$ pc inside most of the bubble.

For configuration (B 3), the diffusion is slightly different from configuration (B 2). The larger value of v_{ϕ_0} (see table 4.1) leads to a zone of compression where the strength of $B_\phi(r, \theta)$ is increased (see figure 4.11). However, this zone is small in comparison to the size of the magnetic spatial distribution. As seen in figure 5.4, the $B_\phi(r, \theta)$ distribution becomes larger than $B_r(r)$ at a distance of $r \approx 1.5$ kpc. Thus, $D/c = 0.1$ pc for most of the spatial magnetic field distribution.

Configuration C

For the two models considered here, configurations (C 1) and (C 2), a value for B_{ϕ_0} is included (see table 4.1).

For configuration (C 1), $B_\phi(r, \theta)$ becomes larger than $B_r(r)$ at a distance of ~ 3 kpc (see figure 4.12). Figure 5.5, shows the 2D map for the spatial distribution of D/c for $\lambda_{\max} = 3$ pc. For this value , a quasi-constant value of $D/c = 0.1$ pc can be obtained for a distance of ~ 3 kpc $< r <$ 15 kpc (light blue zone).

For configuration (C 2), the spatial magnetic field distribution is more complex than for configuration (C 1). The values chosen for B_{r_0}, B_{ϕ_0} and v_{ϕ_0} lead to the formation of a shell at the border of the distribution. Moreover, $B_\phi(r, \theta)$ is not

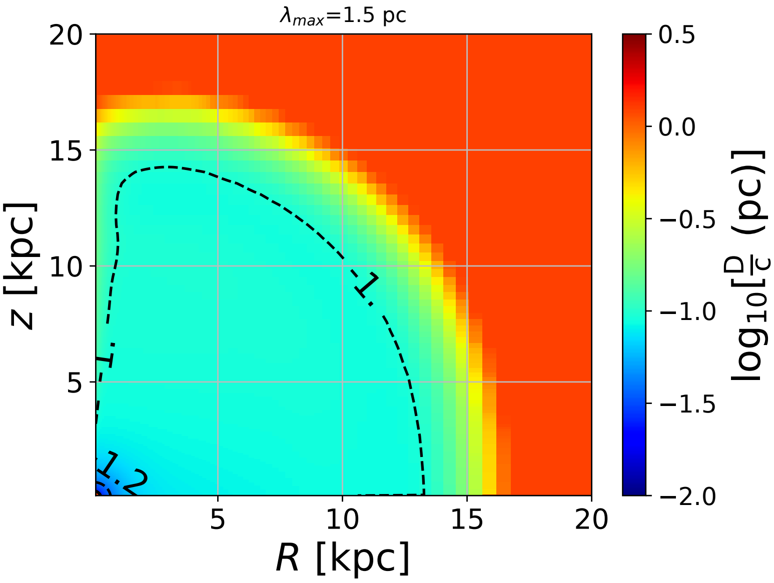

Figure 5.3: **Configuration (B 2):** B_{r_0}= 2 μG, B_{ϕ_0} = 0 μG and v_{ϕ_0} = 20 km s^{-1}. The figure represents the 2D map for the spatial distribution of D/c with $\lambda_{\max} = 1.5$ kpc. $B_\phi(r, \theta)$ becomes larger than $B_r(r)$ at a distance of $r \approx 2.5$ kpc and $D/c = 0.1$ pc (light blue zone) for most of the spatial magnetic field distribution.

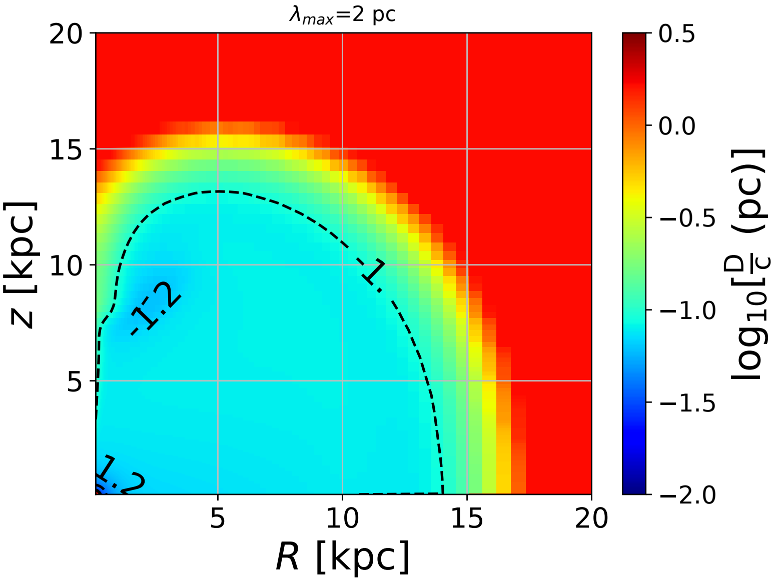

Figure 5.4: **Configuration (B 3):** B_{r_0}= 2 μG, B_{ϕ_0} = 0 μG and v_{ϕ_0} = 50 km s^{-1}. The figure represents the 2D spatial distribution map for D/c with $\lambda_{\max} = 2$ pc. The configuration is quite similar to the configuration (B 2). $B_\phi(r, \theta)$ becomes larger than $B_r(r, \theta)$ at a distance of $r \approx 1.5$ kpc and stays quasi-constant. This allows to have $D/c = 0.1$ pc for most of the magnetic distribution (light blue zone). At a height of ~ 6 kpc a zone of compression leads to an increase of the $B_\phi(r, \theta)$ strength and consequently of D/c. However, the area of this zone is small when compared with the rest of the D/c distribution.

larger than $B_r(r)$ except for the shell part (see figure 4.14). Thus, getting a fixed value for D/c in the bubble is not possible. In figure 5.6, the 2D map for the spatial distribution of D/c is presented. A value of $\lambda_{\max} = 1.5$ pc has here been chosen. This allows to have $D/c = 0.1$ pc for the shell part and for ~ 6 kpc $< r < 10$ kpc.

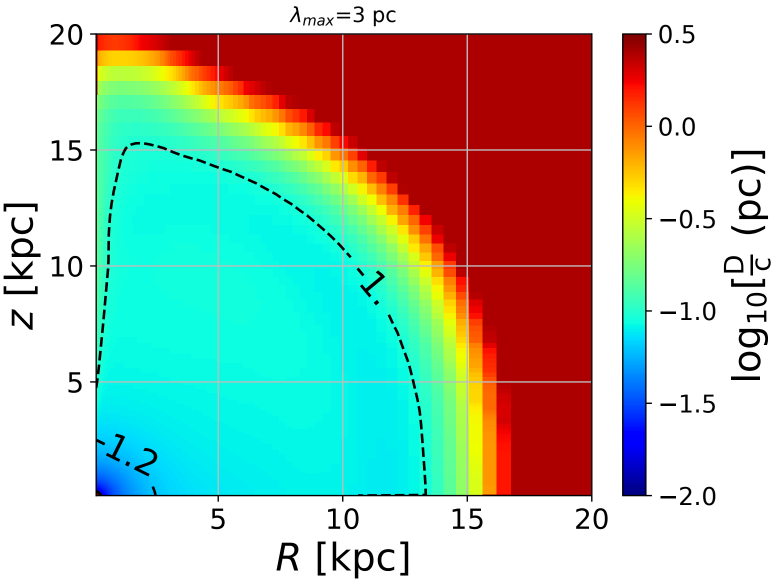

Figure 5.5: **Configuration (C 1):** For B_{r_0}= 20 μG, B_{ϕ_0} = 1 μG and v_{ϕ_0} = 20 km s^{-1}. The figure presents the 2D map for the spatial distribution of D/c with $\lambda_{\rm max}$ = 3 pc. As $B_\phi(r,\theta)$ becomes larger than $B_r(r)$ at $r \approx 3$ kpc, a quasi-constant value of D/c = 0.1 pc can be obtained for the largest part of the spatial magnetic field distribution (light blue zone).

In the inner region, for $r < 6$ kpc, D/c presents a lesser value due to the larger strength of the magnetic field.

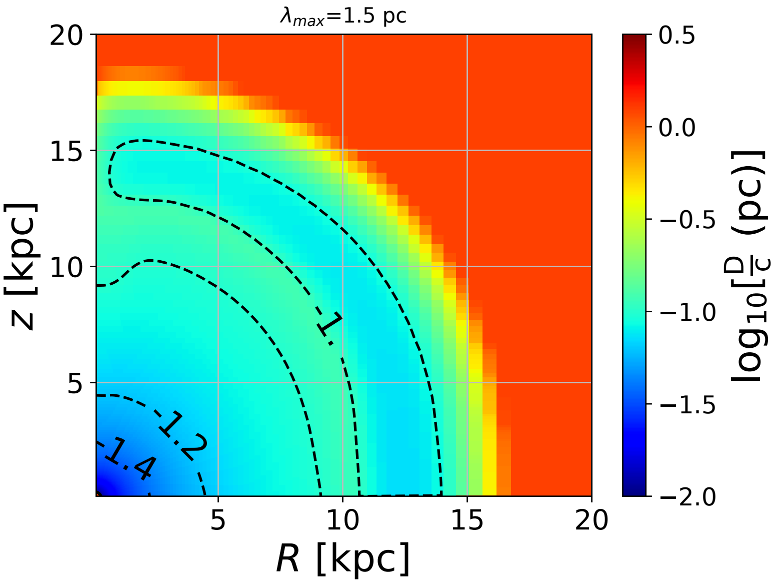

Figure 5.6: **Configuration (C 2):** For B_{r_0}= 20 μG, B_{ϕ_0} = 2 μG and v_{ϕ_0} = 20 km s^{-1}. The figure presents the 2D map for the spatial distribution of D/c with $\lambda_{\rm max}$ = 1.5 pc. $B_\phi(r,\theta)$ is not larger than $B_r(r)$ except at the position of the shell. This does not allow a quasi-constant value for D/c. However, $\lambda_{\rm max}$ = 1.5 pc allows this value to be present for a distance of 6 kpc $< r <$ 10 kpc and in the shell zone (light blue zone).

With a defined expression for the isotropic and inhomogeneous diffusion coefficient (see Eq. 5.7) and $\lambda_{\rm max}$ fixed for each configuration, the next step is to proceed with the numerical solving of the CR transport equation. The numerical setup and the results are presented in the following section.

5.1.2 Cosmic rays transport simulations

Computational grid

For the isotropic and inhomogeneous diffusion coefficient, motivated by the MHD numerical results, the setup of the simulation is, for the most part, equivalent to the hydrodynamic simulation. Therefore, no important changes are needed for the algorithm (see section 3.2). However, the maximal value considered for D/c is a least one order of magnitude larger than the hydrodynamic model for which the diffusion is homogeneous and $D/c = 0.1$ pc. This larger value for D/c implies a smaller diffusion time and therefore a larger time step to satisfy the CFL conditions. To be able to consider a high enough spatial resolution allowing to study the different results in a minimum of computation time, the computation grid has been reduced. The grid ranges from 0.1 to 100 kpc for the hydrodynamic model has been reduced to 20 kpc. Therefore, it must first be ensured that the grid boundaries do not affect the resultant spatial $n_{\rm CR}$ distribution in a significant way. In figure 5.7, a comparison of $n_{\rm CR}$ for the hydrodynamic model, identical to the one presented in chapter 3, is shown for two different grids. The red curve corresponds to the grid used in chapter 3, i.e., ranging from 0.1 to 100 kpc with 60 bins. The black curve corresponds to a grid ranging from 0.1 to 20 kpc with 45 bins. Qualitatively, $n_{\rm CR}$ for the two grids are identical. The difference in values between the two comes naturally from the difference in the total volume, which implies a change in the grid. From those results, the outer boundary can be placed at 20 kpc from the centre of the grid without altering the results.

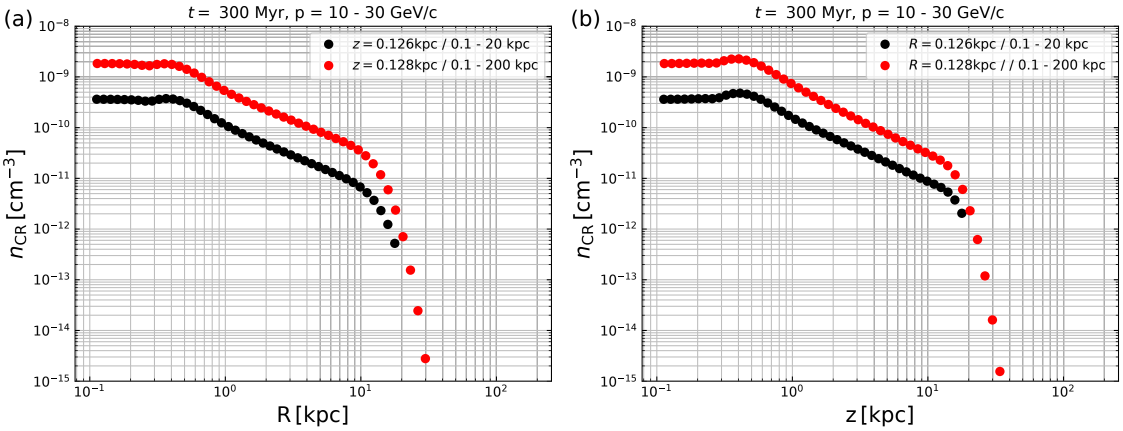

Figure 5.7: The figure presents the spatial distribution of $n_{\rm CR}$ along the axis R (figure (a)) and z (figure (b)). The red curve corresponds to a grid ranging from 0.1 to 100 kpc for 60 bins. The black curves correspond to a grid ranging from 0.1 to 20 kpc for 45 bins. The distributions for both grids are qualitatively identical. The difference in values lies in the different total volume of the grid.

Configuration A

In a similar way than for the hydrodynamic model (see section 3.3), the velocity profile from the MHD simulation is used in the CR transport equation. In addition, the spatial magnetic field distribution is also used for the diffusion coefficient (see section 4.3.2). The CR transport code allows then to get the $n_{\rm CR}$ spatial distribution for which $E_\gamma F_\gamma$ is derived (see Eq. (3.16)).

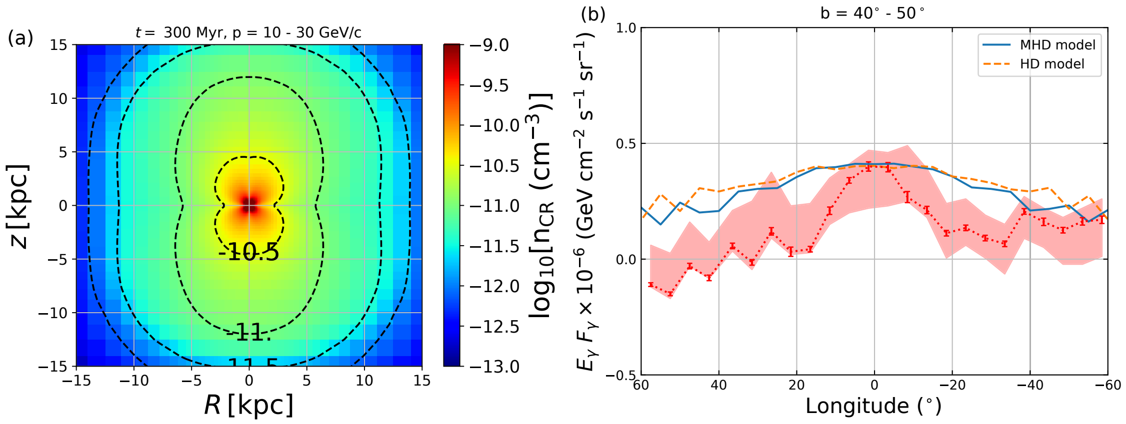

Figure 5.8: **Configuration (A):** B_{r_0}= 20 μG, B_{ϕ_0} = 0 μG and v_{ϕ_0} = 0 km s^{-1}. In figure (a), the 2D map of the spatial distribution for $n_{\rm CR}$ is presented. As D/c is smaller than the value adopted for the hydrodynamic model in the inner 10 kpc of the grid, the advection plays a more important role and exhibits a more elongated profile. In figure (b), the $E_\gamma F_\gamma$ distribution is presented for 40° $< b <$ 50° (solid blue line) and compared with the hydrodynamic model (orange dashed line). As the spatial distribution of $n_{\rm CR}$ appears more elongated, sharper edges than the hydrodynamic model can be observed for $l >$ 15° but stays consistent with the hydrodynamic model for $l <$ 15°.

In figure 5.8 (a), the 2D map for the spatial distribution of $n_{\rm CR}$ is presented. As D/c (see figure 5.1) is smaller than 0.1 pc until a distance of $\sim$ 10 kpc, the advection plays a more important role. This leads to a more elongated shape for the resultant $n_{\rm CR}$ distribution when compared with the hydrodynamic model (see figure 3.2). In figure 5.8 (b), the γ-ray energy flux distribution derived from the $n_{\rm CR}$ distribution is presented (solid blue line) and compared with the hydrodynamic model (orange dashed line) for 40° $< b <$ 50°. As $n_{\rm CR}$ is more elongated and less wider, the $E_\gamma F_\gamma$ distribution shows slightly sharper edges beyond a longitude of $\sim$ 15° but stays consistent with the hydrodynamic model for l $<$ 15°. For this configuration, the injected CR luminosity needed for reaching the observed energy flux for 40° $< b <$ 50° is $L_{\rm CR} \approx 1.4 \times 10^{40}$ erg s^{-1}.

Configuration B

For the configuration (B 1), $D/c = 0.1$ pc for a distance ranging from 8 kpc $\lesssim r \lesssim$ 15 kpc (see figure 5.2). The distribution for $n_{\rm CR}$ is then expected to be less extended in height than the configuration (A) as diffusion plays a more important role in this region. However, as $D/c <$ 0.1 pc for $r \lesssim$ 8 kpc the $n_{\rm CR}$ distribution will be less wide than for the hydrodynamic model (see figure 3.2). Figure 5.9 (a) presents the 2D map for the spatial distribution of $n_{\rm CR}$. As expected, this distribution is less elongated than the configuration (A). This can be seen through the contour lines that extend less far in the z-direction. The resulting spatial $E_\gamma F_\gamma$ distribution is presented (solid blue line) in figure 5.9 (b). It is similar to the hydrodynamic model (orange dashed line). For this configuration, the injected luminosity needed for reaching the observed γ-ray energy flux for 40° − 50° in latitude is $L_{\rm CR} \approx 1.3 \times 10^{40}$ erg s^{-1}.

For the configuration (B 2), $D/c = 0.1$ pc covers most of the grid, except in the

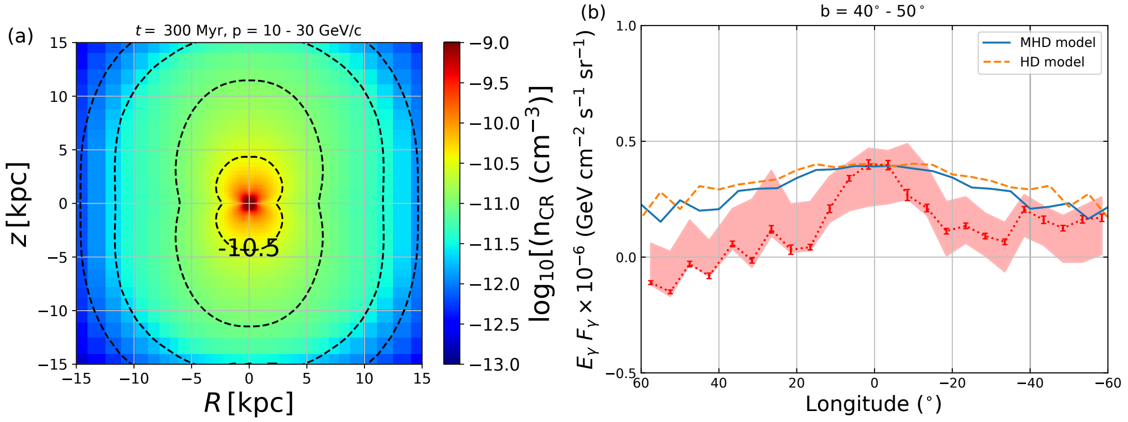

Figure 5.9: **Configuration (B 1):** B_{r_0}= 2 μG, B_{ϕ_0} = 0 μG and v_{ϕ_0} = 2 km s^{-1}. Figure (a) shows the 2D map spatial distribution for $n_{\rm CR}$. D/c is smaller than the hydrodynamic model for $r <$ 8 kpc (see figure 5.2) and the advection plays a more important role and gives a oblong shape to the $n_{\rm CR}$ distribution (red to yellow zone). For 8 kpc $< r <$ 15 kpc (green to dark blue zone), $D/c = 0.1$ pc, the $n_{\rm CR}$ distribution presents an elongated profile that becomes rounder as r increases.
In figure (b), the resulting $E_\gamma F_\gamma$ distribution is presented (solid blue line). For a latitude of 40° $< b <$ 50° the γ-ray emission is comparable to that of the hydrodynamic model (dashed orange line). The MHD model shows slightly sharper edges for $l > 15°$.

inner region for $r \lesssim 2.5$ kpc (see figure 5.3). Subsequently, diffusion plays a more important role than for both configurations (A) and (B 1). The $n_{\rm CR}$ distribution is therefore expected to be less elongated and present a rounder shape. This effect can indeed be seen in figure 5.10 (a) where in the inner 5 kpc, the $n_{\rm CR}$ distribution is less elongated and extended than for both configurations (A) and (B 1) and presents a round shape. However, one feature is present. As shown in figure 4.10, the compressed $B_\phi(r, \theta)$ lines, through a magnetic tension effect, decelerate abruptly the outflow at a height of $z \approx 12$ kpc. This feature can be observed through the contour lines since it exhibits a flatter distribution of $n_{\rm CR}$. This is due to the diffusion becoming the main transport mechanism for the CR as the advection becomes less important in this zone. Figure 5.10 (b) presents the resulting γ-ray energy flux distribution. As for configurations (A) and (B 1), the spatial distribution of n_{CR} for configuration (B 2) (solid blue line) does not show a large difference with the hydrodynamic model (dashed orange line). The injected CR luminosity needed for reaching the observed γ-ray energy flux at $40° - 50°$ in latitude is $L_{\rm CR} \approx 1.35 \times 10^{40}$ erg s^{-1}.

For configuration (B 3), the larger value for v_{ϕ_0} (see table 4.1) creates a larger zone of compression of the B_ϕ lines as a consequence of a magnetic tension effect. It disturbs strongly the distribution of the velocity profile along the z-axis for $z \approx 6$ kpc (see figure 4.11). This feature is subsequently reflected in the $n_{\rm CR}$ distribution. $B_\phi(r, \theta)$ becomes larger than $B_r(r)$ at a distance of $r \approx 1.5$ kpc and exhibits a quasi-constant value of $D/c = 0.1$ pc for most of the rest of the grid (see figure 5.4). Figure 5.11 (a) presents a 2D map for the spatial distribution of $n_{\rm CR}$. The main difference with the other configurations is the presence of a concave distribution. This concavity can be seen through the contour line at a height of ~ 9 kpc. In figure 5.11 (b), the corresponding $E_\gamma F_\gamma$ distribution is shown. The MHD model results (solid blue line) appear to be very similar to those obtained for the hydrodynamic

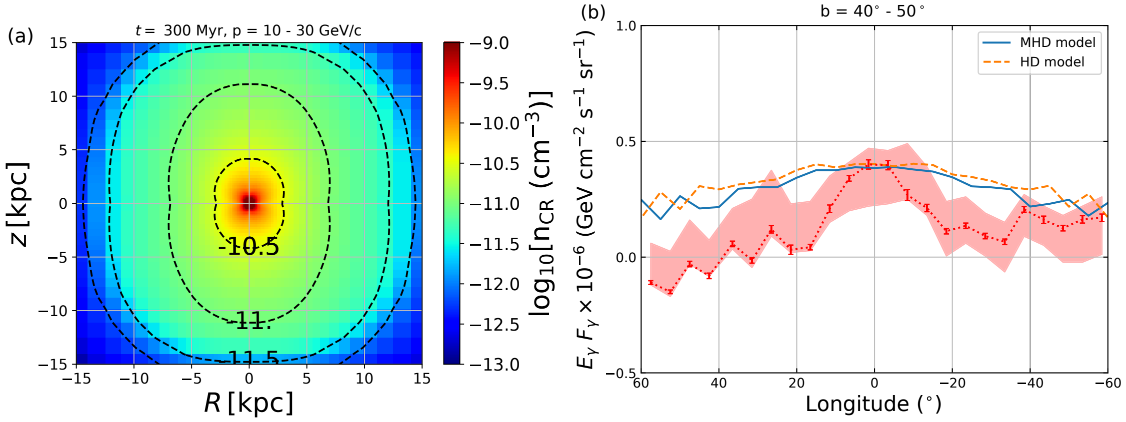

Figure 5.10: **Configuration (B 2):** B_{r_0}= 2 μG, B_{ϕ_0} = 0 μG and v_{ϕ_0} = 20 km s^{-1}. Figure (a) shows the 2D map for the spatial distribution of n_{CR}. As $D/c = 0.1$ pc for $r > 2.5$ kpc (see figure 5.3) the distribution of n_{CR} is rounder than for configuration (B 1) (red to green zone). At a height of ∼ 14 kpc the contour lines show a flat profile as the velocity is strongly decelerated (see figure 4.9 (a)).
Figure (b) shows the resulting $E_\gamma F_\gamma$ distribution (solid blue line). For $40° < b < 50°$ it is comparable to the γ-ray emission from the hydrodynamic model (dashed orange line). The MHD model shows slightly sharper edges for $l > 15°$

model (dashed orange line). For this configuration, the injected CR luminosity needed for reaching the observed energy flux at $40° - 50°$ in latitude is $L_{\mathrm{CR}} \approx 1.4 \times 10^{40}$ erg s^{-1}.

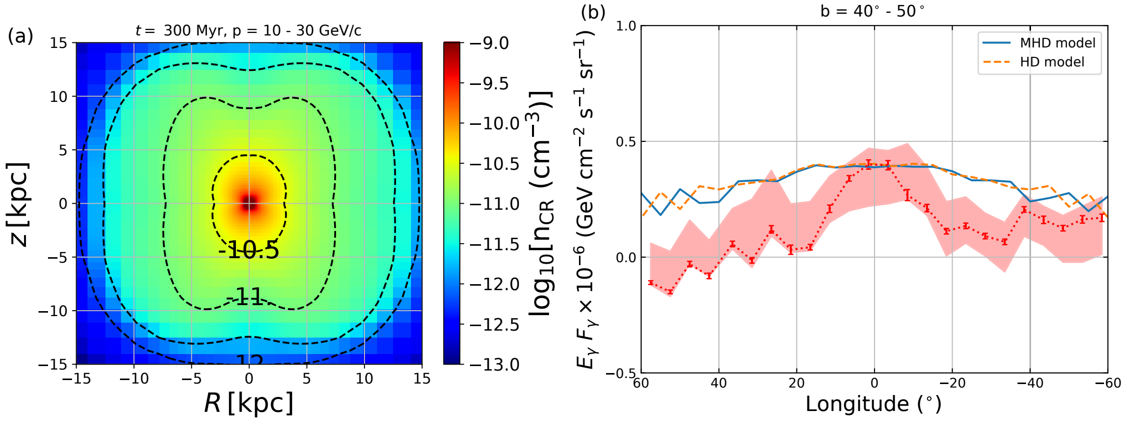

Figure 5.11: **Configuration (B 3):** B_{r_0} = 2 μG, B_{ϕ_0} = 0 μG and v_{ϕ_0} = 50 km s^{-1}. Figure (a) shows the 2D map of the spatial distribution of n_{CR}. This distribution takes an oblong shape under the influence of the advection in the inner region (red to yellow zone). The velocity profile (see figure 4.11 (b)) causes a concavity in the n_{CR} distribution at $z \approx 10$ kpc as shown by the contour lines.
Figure (b) shows the $E_\gamma F_\gamma$ distribution at a latitude of $40° - 50°$ (solid blue line). The MHD profile is very similar to the $E_\gamma F_\gamma$ emission for the hydrodynamic profile (dashed orange line).

Configuration C

The configuration (C 1), like the configurations (B 2) and (B 3), exhibits a distribution for $B_\phi(r,\theta)$ that is quasi-constant for $r \gtrsim 3$ kpc. Therefore, $D/c = 0.1$ pc can be obtained for most of the spatial magnetic field distribution (see 5.5). As shown in figure 5.12 (a), $n_{\rm CR}$ in the inner 5 kpc is similar to both configurations (B 2) and (B 3). Configuration (C 1) and (B 2) share a similar deceleration at a Galactic height of $\sim$ 12 kpc (see figures 4.10 and 4.12), resulting in both a less extended $n_{\rm CR}$ distribution. In figure 5.12 (b), the resulting $E_\gamma F_\gamma$ distribution can be seen (solid blue line). As for the previous configurations, the profile looks very similar to the hydrodynamic model (dashed orange line). The injected CR luminosity needed for reaching the observed $E_\gamma F_\gamma$ at $40^\circ - 50^\circ$ in latitude is $L_{\rm CR} \approx 1.4 \times 10^{40}$ erg s^{-1}.

For configuration (C 2), as the spatial magnetic field distribution presents a complex structure, it is not possible to have a constant value for D/c (see figure 5.6). It is then difficult to predict the resulting $n_{\rm CR}$ distribution. As in the inner $\sim$ 6 kpc $D/c < 0.1$ pc, the advection plays a more important role than for the hydrodynamic model. Thus, a more extended distribution in the z-direction can be expected. For 8 kpc $\lesssim r \lesssim$ 13 kpc, $D/c > 0.1$ pc and in the shell zone, $D/c = 0.1$ pc. However, the variations of D/c are not large and the velocity profile is not disrupted as for the configuration (B 3) (see figure 4.11 (b)). Moreover, the shell zone is at a distance of $\sim$ 15 kpc from the Galactic Center, i.e., at the outer limit of the $n_{\rm CR}$ distribution and therefore, will not play an important role. The $n_{\rm CR}$ profile should look similar to the one that can be observed for the configuration (A) (see figure 5.8 (a)). In figure 5.13 (a), the 2D map for the spatial distribution of $n_{\rm CR}$ is presented. As expected from the diffusion profile (see figure 5.6), the distribution does not show a large difference with the configuration (A) (see figure 5.8 (a)). As the diffusion coefficient is isotropic, the shell does not play an important role. In figure 5.13 (b), the $E_\gamma F_\gamma$ distribution is presented for $40^\circ < b < 50^\circ$. As for the other configurations, the sharpness is slightly larger for $l > 15^\circ$ but the profile stays coherent with the hydrodynamic model.

The CR luminosity needed for reaching the observed $E_\gamma F_\gamma$ at $40^\circ - 50^\circ$ in latitude is $L_{\rm CR} \approx 1.4 \times 10^{40}$ erg s^{-1}.

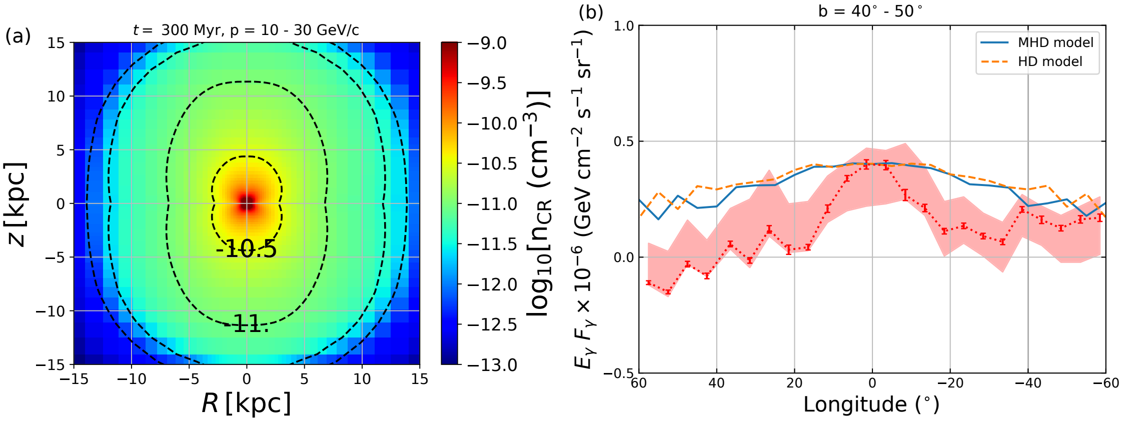

Figure 5.12: **Configuration (C 1):** B_{r_0}= 20 μG, B_{ϕ_0} = 1 μG and v_{ϕ_0} = 20 km s^{-1}. Figure (a) presents the 2D map for the spatial distribution of $n_{\rm CR}$. In the first 10 kpc (red to yellow green zone), the distribution is similar to configuration (B 2) (see figure 5.10). At a Galactic height of $\sim$ 12 kpc, the contour line (dashed black line) is flattened due to the deceleration of the outflow in this region.
Figure (b) presents the resulting $E_\gamma F_\gamma$ distribution (solid blue line) for a latitude of $40^\circ < b < 50^\circ$. For $l < 15^\circ$, the γ-ray emission is similar to the hydrodynamic model (dashed orange line). For $l > 15^\circ$, the MHD model shows slightly sharper edges.

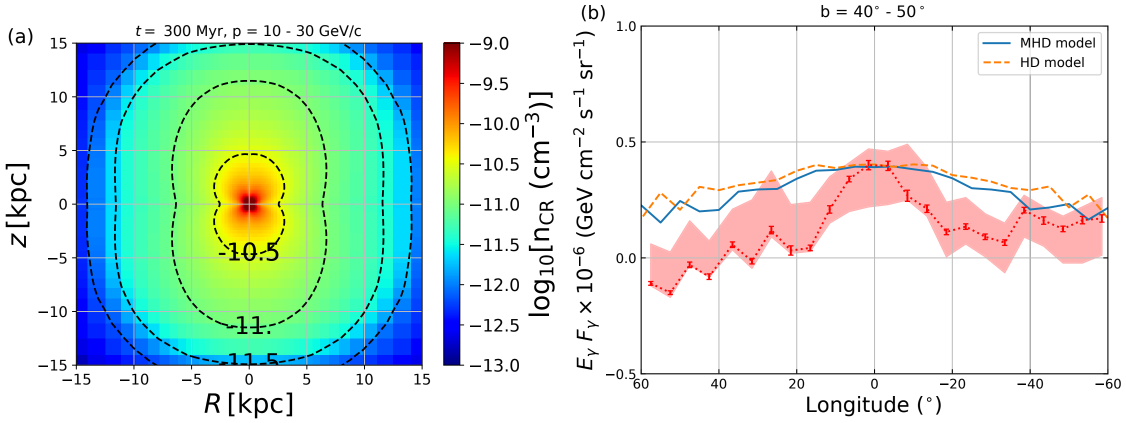

Figure 5.13: **Configuration (C 2):** B_{r_0}= 20 μG, B_{ϕ_0} = 2 μG and v_{ϕ_0} = 20 km s^{-1}. Figure (a) presents the 2D map for the spatial distribution of $n_{\rm CR}$. This distribution shows an elongated profile twice as high as wide (yellow to yellow green zone). The second contour line from the centre (dashed black line) reaches a Galactic height of $\sim$ 12 kpc and a width of $\sim$ 6 kpc. This ratio diminished as the CR propagate farther (green to light blue zone)
Figure (b) shows the distribution of $E_\gamma F_\gamma$ for 40° $< b <$ 50° (solid blue line) that is compared with the hydrodynamic model (dashed orange line). The profile is similar for $l <$ 15° and shows slightly sharper edges for $l >$ 15°.

5.1.3 Line-of-sight velocity profiles for the MHD model

As for the hydrodynamic model (see section 3.3.3), the $E_\gamma F_\gamma$ distribution for the different configurations can be used to get the line-of-sight velocity profile to be compared with observations. As the $B_\phi(r,\theta)$ distribution can affect the velocity profile, it is interesting to study the different line-of-sight velocity profiles for each configuration.

In figure 5.14, the line-of-sight velocity profile is shown for the six configurations considered in the previous section (see section 5.1.2). Except for the configuration (B 3), all the different configurations present a similar profile. The Fermi bubbles extend up to $\sim$ 10 kpc in Galactic height, corresponding to $\sim$ 50° for an observer at a distance of $\sim$ 8 kpc from the Galactic Center. However, the specific features observed in the velocity profile of most configurations are beyond this height of 10 kpc. This explains why the different figures show a similar line-of-sight velocity profile. For the configuration (B 3), the velocity profile is disrupted by the compression of the $B_\phi(r,\theta)$ lines at $\sim$ 6 kpc (see figure 4.11 (b)) and appears then in the plot.

5.1.4 Intermediate conclusion

The inclusion of the different spatial magnetic field distributions obtained from the MHD simulations has allowed to consider an inhomogeneous diffusion for the transport of CR. As a first step, an isotropic and inhomogeneous diffusion coefficient has been considered and several configurations have been tested. In order to compare the coherence of the results with the hydrodynamic model, a specific $\lambda_{\rm max}$ has been fixed for each configuration. This $\lambda_{\rm max}$ has been chosen in such a way that $D/c \approx$ 0.1 pc for most of the considered spatial magnetic field distributions. The $E_\gamma F_\gamma$ distributions obtained are similar, for $l <$ 15°, to the hydrodynamic model and for an equivalent $L_{\rm CR}$. Some configurations, due to the influence of a magnetic tension effect, exhibit a local disruption of the velocity profile. With the exception

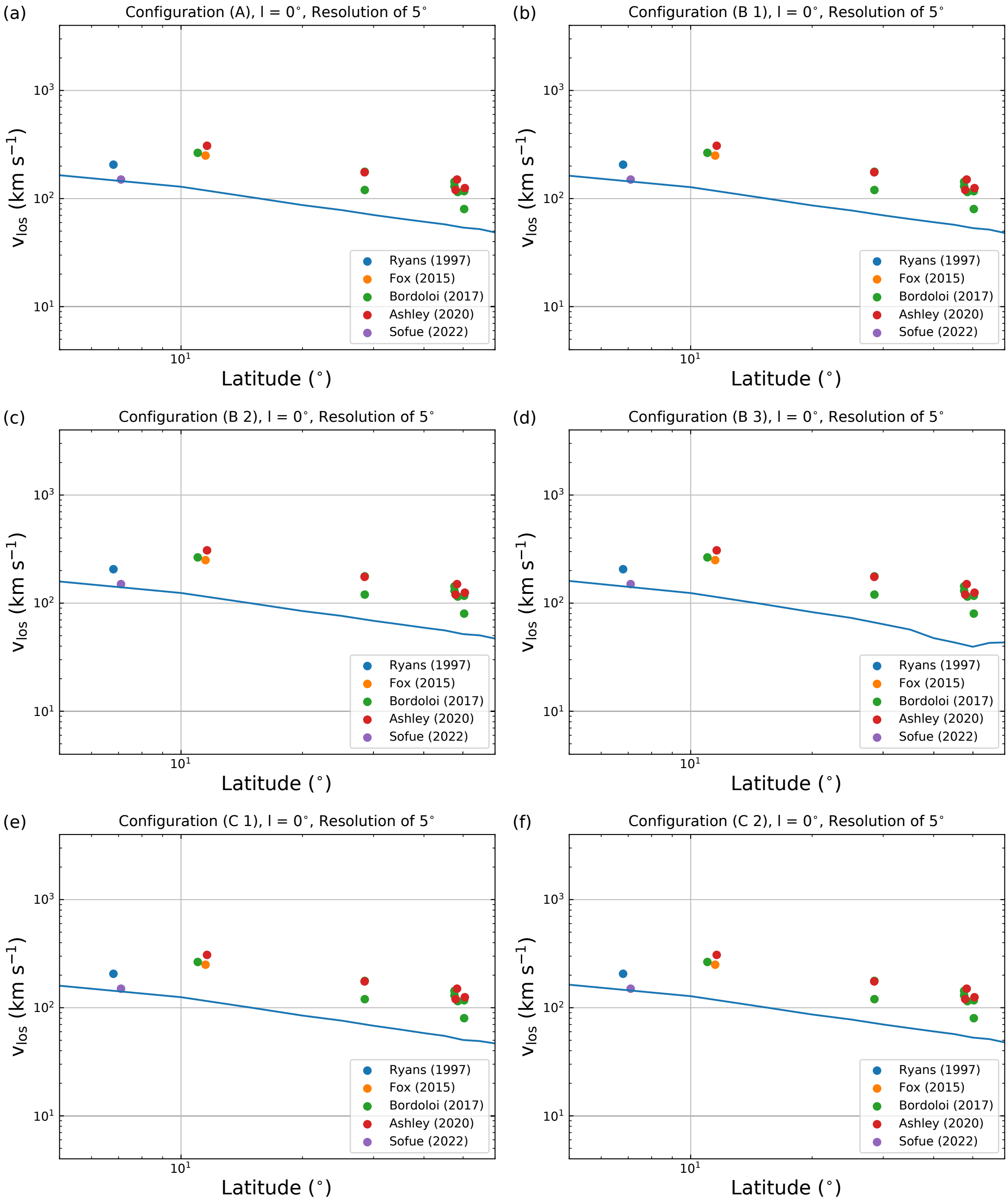

Figure 5.14: The line-sight-velocity profile (solid blue line) for the six different configurations considered for a model including an isotropic and inhomogeneous diffusion coefficient. The different velocities of high-velocity cold clouds are represented by colour dots provided by five different observations. The observer is considered to be at 8 kpc from the Galactic Center and at a Galactic longitude of $l = 0°$.

of configuration (B 3), these disruptions happen for $z > 10$ kpc, i.e., above the estimated height of the Fermi bubbles. Most of the different line-of-sight velocity profiles are then similar for $b < 50°$. The magnetic field distributions presented here only shows weak values. Their main interest is then to provide a setup for an anisotropic diffusion for the propagation of CRs.

The next step is to include an anisotropic diffusion coefficient for the numerical solution of the CR transport equation.

5.2 Anisotropic diffusion coefficient

5.2.1 Definition

An anisotropic diffusion coefficient is defined through a parallel and a perpendicular term, $D_\parallel$ and $D_\perp$. Its expression is given by (Günter et al. 2005; Potgieter et al. 2013)

$$D_{ij} = D_\perp \delta_{ij} + \left(D_\parallel - D_\perp\right) \frac{B_i}{|\mathbf{B}|} \frac{B_j}{|\mathbf{B}|}, \tag{5.8}$$

where the indexes i and j represent the directions R and z. The development of this expression is detailed in appendix B. There are 4 components for the diffusion tensor that must be considered, D_{RR}, D_{zz}, D_{Rz} and D_{zR}. From this expression, it can be deduced that when $D_\parallel = D_\perp$ the expression for the isotropic model is obtained, where $D_{RR} = D_{zz}$ and $D_{Rz} = D_{zR} = 0$. The next step is to include this expression in the CR transport code.

5.2.2 Numerical setup

The computational setup is similar to the one used for the hydrodynamic model (see section 3.2). To include an anisotropic coefficient of diffusion, the components D_{Rz} and D_{zR} must be implemented. The diffusion part of the CR transport equation (see Eq. (3.4)) must be modified, as well as the expression for the boundary conditions (see (Eq. 3.11)). The development of these expressions is left to the appendix A. In order to test the correct implementation of the anisotropic diffusion coefficient, a numerical test has been performed.

Test problem: Ellipse

A simple test problem has been considered for testing the implementation of the anisotropic diffusion coefficient. This test consists of considering the propagation of CR without an advection term for the transport equation. The diffusion model is based on a constant spatial distribution of the magnetic field in the computational grid. From Eq. (5.8), the terms D_{Rz} and D_{zR} can be eliminated and $D_{RR} = D_{zz}$ if $D_\parallel = D_\perp$ leading to an isotropic and homogeneous model.

A first test has been performed to check that a disc shape is obtained when this isotropic and homogeneous model is used. Figure 5.15 (a) shows the distribution for this model. As expected, the distribution takes a disc shape.

A second test considered a magnetic field defined along the R-axis only, i.e., for which $B_z = 0$. For this model, $D_\parallel = 0.1$ pc and $D_\perp = 0.1 D_\parallel$. The result of this configuration is shown in figure 5.15 (b). As expected, the CR distribution takes an elliptic shape elongated along the R-axis.

A third test considered a magnetic field defined along the z-axis only, i.e., for which $B_R = 0$. $D_\parallel$ and $D_\perp$ are defined in the same way as the previous test model. The result is shown n figure 5.15 (c). The CR distribution also takes an elliptic shape but is elongated this time along the z-axis.

Finally, the last test was to consider a spherical distribution for a constant magnetic field and the same ratio between the values of $D_\parallel$ and $D_\perp$, i.e., $D_\perp = 0.1 D_\parallel$.

The result is shown in figure 5.15 (d). The resulting CR distribution forms an ellipse propagating mainly along an axis, forming an angle of 45° with both the R and z-axis.

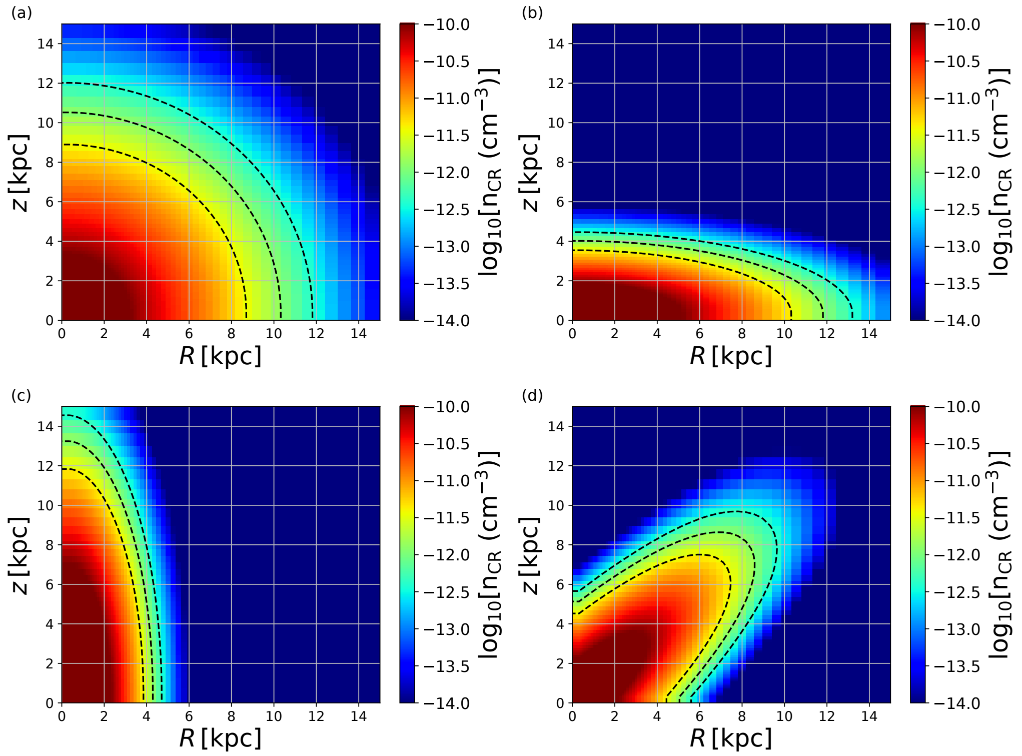

Figure 5.15: The figure shows different spatial distributions of $n_{\rm CR}$ corresponding to different configurations of the magnetic field in order to test the implementation of an anisotropic diffusion for the computational grid and boundaries. In figure (a), $B_R = B_z$ and $D_\parallel = D_\perp$ give an isotropic and homogeneous configuration and therefore a disc shape. For the next three configurations, a ratio $D_\perp/D_\parallel = 0.1$ has been considered. In figure (b), the configuration has been setup with $B_z = 0$ and B_R has a non zero value. As $D_\perp = 0.1D_\parallel$, $n_{\rm CR}$ takes an elliptic shape oriented along the R-axis. In figure (c), the configuration is $B_R = 0$ and B_z has a non zero value. As for the previous setup, $n_{\rm CR}$ takes an elliptic shape but this time the diffusion happens along the z-axis. In figure (d), the two components for the magnetic field have been set up as $B_R = B_z$. The CR are diffused with an angle of 45° from both the R and z-axis.

It must be noted that a difference exists between the CR distribution along the R-axis (see figure 5.15 (b)) and the z-axis (see figure 5.15 (c)). It can be seen that the distribution along the z-axis extent farther than along the R-axis. This difference can be explained by Green's function for the diffusion of particles for a cylindrical symmetry

$$G_{\rm cyl} = \frac{\exp\left(-\frac{R^2}{4Dt}\right)}{4\pi Dt}\frac{\exp\left(-\frac{z^2}{4Dt}\right)}{\sqrt{4\pi Dt}}. \tag{5.9}$$

The diffusion of particles along R decreases faster. This happens because R is composed of the two Cartesian coordinates x and y as it can be expressed by $R = \sqrt{x^2 + y^2}$. It represents then two dimensions, where z only represents one. All the results for these test models are in line with expectations. The next step is to check what is the maximal ratio between $D_\parallel$ and $D_\perp$ that can be handled by the numerical scheme adopted. Figure 5.15 (d) shows that a ratio of $D_\perp/D_\parallel = 0.1$

is possible. In figure 5.16, two different ratios are presented. Figures (a) and (b) represent the n_{CR} distribution for a ratio $D_{\perp}/D_{\parallel} = 0.025$. Figure (a) is for a simulation with 120 bins. Figure (b) is for a simulation with 240 bins. For 120 bins, two peaks in n_{CR}, either side of the ellipse, appear. This is due to a number of bins being insufficient for computing the CR transport code with such an anisotropic diffusion coefficient ratio, since this feature does not appear when the number of bins is increased to 240 bins. The same effect can be seen for figures (c) and (d) that represent the density distribution for a ratio of $D_{\perp}/D_{\parallel} = 0.015$. In figure (c), a grid with 240 bins has been considered. The same feature, for an anisotropic distribution coefficient ratio of 0.025, for 120 bins, can be seen but disappears when the number of bins is increased, here to 480 bins, as shown in figure (d). The ratio that can be handled by the numerical scheme depends on the number of spatial bins. More bins mean a better resolution and a better precision but they increase largely the necessary computation time needed to resolve the transport of CR. It must be noted, however, that even if the number of bins is low, the n_{CR} distribution is not dramatically affected.

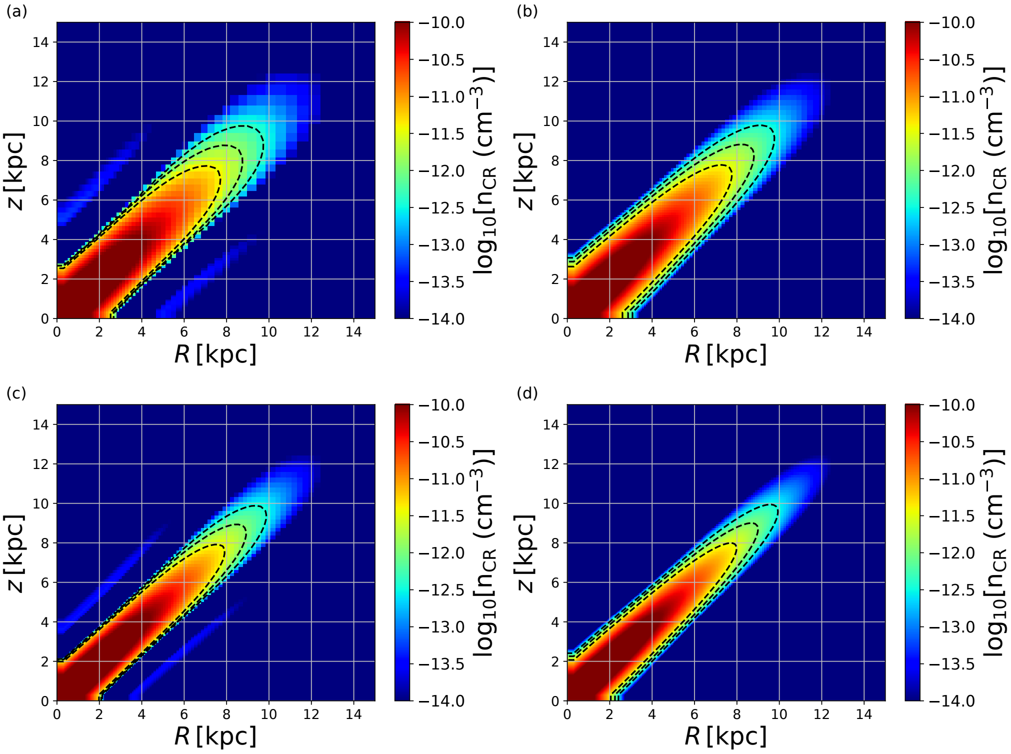

Figure 5.16: Two ratios for $D_{\perp}/D_{\parallel}$ are presented. Figure (a) represents n_{CR} for a ratio of 0.025 for a grid with 120 bins. Two peaks surrounding the ellipse appear. But this feature is not present in figure (b) for which 240 bins have been used. Indicating that those features are due to an insufficient number of bins. The same effect can be seen in both figures (c) and (d) which correspond to a ratio of 0.015. On the left, 240 bins have been used and the feature appears but disappears on the right figure, for which 480 bins have been used. A larger ratio therefore requires a larger number of bins to be correctly computed.

The advection problem

The consideration of anisotropic diffusion for CR transport can have an adverse effect on the resultant CR distribution. Figure 5.17 shows an example by considering a constant spherical velocity distribution, $v_r = 300$ km s^{-1}, projected along the cylindrical axis, R and z, to get v_R and v_z. In order to eliminate the effects due to the expansion of the outflow, the module solving the momentum advection has been turned off. A first step is to consider the case where D is isotropic and homogeneous and the grid ranges from 0.1 to 20 kpc with 180 bins. In figure (a), for $D/c = 0.1$ pc, the $n_{\rm CR}$ distribution is spherical as expected from the numerical setup. In figure (b), for $D/c = 0.01$ pc, a discrepancy can be seen. The $n_{\rm CR}$ distribution should be spherical but along the R-axis the distribution is less than expected. In figure (c), for $D/c = 0.001$ pc, the effect is amplified. As the diffusion becomes negligible for the propagation of the CR, a conic shape for the velocity profile can clearly be seen. This is due to the inner radius of the grid, which is at $R_{\rm in} = z_{\rm in} = 100$ pc. This implies that the area of injection represents only a fraction of the total spherical area that has its origin point at zero.

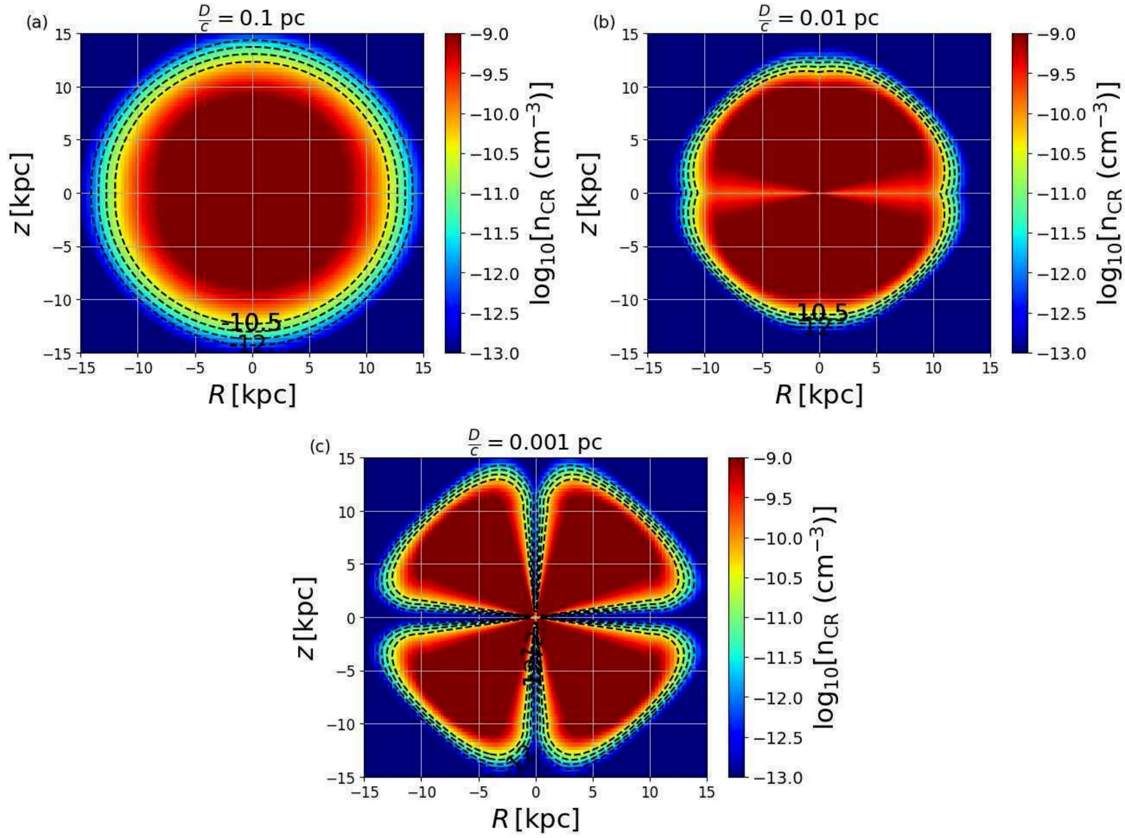

Figure 5.17: The figure represents the behaviour of the $n_{\rm CR}$ distribution for a constant spherical velocity, no momentum advection and an isotropic and homogeneous diffusion. The grid ranges from 0.1 to 20 kpc and is defined with 180 bins. For figure (a), $D/c = 0.1$ pc. The spatial distribution of $n_{\rm CR}$ takes a spherical shape. For figure (b), $D/c = 0.01$ pc. The spatial distribution of $n_{\rm CR}$ shows a discrepancy with the expectations, as it is not spherical anymore. For figure (c), $D/c = 0.001$ pc and the $n_{\rm CR}$ distribution takes a conical shape.

However, the data provided by the hydrodynamic model and the MHD model cannot be extended to a radius smaller than 300 pc. Given that the analytic model used for defining the Galactic breeze profile has a velocity that increases as the radius decreases for $r < 400$ pc. For $r < 300$ pc, the velocity would become supersonic (see chapter 2). A solution has then been explored, for which the inner radius of the grid has been extended to 10 pc. In the region between 10 pc and 300 pc, no magnetic field is present for the MHD simulations. The region is filled out with a magnetic field distribution for which $r_L = \lambda_{\rm max}$ (see section 5.1.1). In figure 5.18, the $n_{\rm CR}$ distribution is shown for the same setup and $D/c = 0.01$ pc but with an inner grid starting at 10 pc. It can be seen that, contrary to figure 5.17 (b), the $n_{\rm CR}$ distributions appear to be continuous. However, the 180 bins for the grid that have been increased by one decade are not large enough to provide a full spherical shape.

Increasing the inner range of the grid therefore helps to improve the distribution of $n_{\rm CR}$. The data provided by the MHD numerical code can now be used to obtain the γ-ray emission for the anisotropic diffusion model.

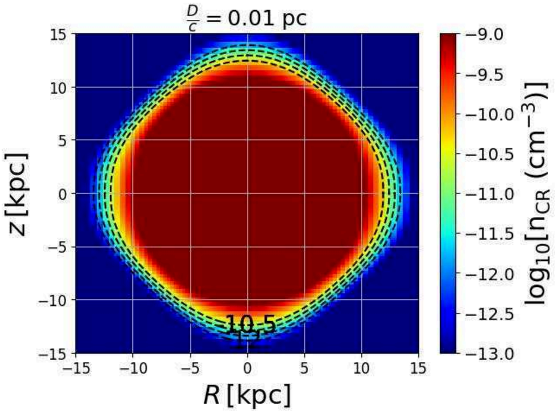

Figure 5.18: the figure shows the distribution of $n_{\rm CR}$ for a setup identical to figure 5.17 (b). The inner radius of the computation grid has been extended from 100 pc to 10 pc. As the diffusion dominates from 10 to 300 pc, it allows the distribution to emulate a spherical shape.

5.2.3 γ-ray emission for the MHD model

For getting the γ-ray emission and comparing it with the Fermi bubble observations, only three configurations have been considered. The configurations (A), (C 1) and (C 2). The configuration (B) has been put aside as its purpose was only to study the effect of $v_\phi(r, \theta)$ on both $v_r(r, \theta)$ and $B_\phi(r.\theta)$. Moreover, the spatial distribution of $B_\phi(r, \theta)$ for each of the three setups of the configuration (B) is close to the configuration (C 1).

Configuration A

As described in section 5.2.2, the computational grid ranges from 10 pc to 20 kpc. The grid is logarithmic, with 60 bins. This is a small amount of bins when the grid has $\sim$ 3 decades in space. However, as $r_{L_{\rm max}} = 1$ pc, the computational time is greatly increased and the number of bins must be kept low to be able to finish the simulations during the 48 hours allocated by the cluster used. Figure 5.19 presents the $n_{\rm CR}$ distribution and the resulting γ-ray emission for $30° < b < 40°$ and $40° < b < 50°$ for $D_\perp = 0.1 D_\parallel$. In figure (a), the $n_{\rm CR}$ distribution is shown. At the base of the distribution, an extension can be seen. This extension is due to diffusion being the only transport mechanism for the propagation of the CR as the grid had to be extended. In this region, $D/c = 1$ pc, a value too large for the Galactic Center and the disc (Han 2017). However, this extension does not disrupt the distribution at a range of 6 to 10 kpc, which is the region of interest. The distribution is clearly less wide than for the hydrodynamic model (see figure 3.2) or the MHD isotropic model (see figure 5.8 (a)). Figures (b) and (c) present the γ-ray emission obtained for the n_{CR} distribution and the pp interactions (see section 3.3.2). It can be clearly seen that the $E_\gamma F_\gamma$ emission shows a pronounced sharpness that matches with the fitting range provided by the Fermi collaboration (Ackermann et al. 2014). An anisotropic diffusion in combination with a Galactic breeze model is therefore able to provide an explanation for the observed sharp edges. For matching with the observations, the injected CR luminosity is $L_{\mathrm{CR}} \approx 8 \times 10^{39}$ erg s^{-1}. But since the resolution is low, this value must be considered only as an approximation. A larger resolution will be needed for a better estimation.

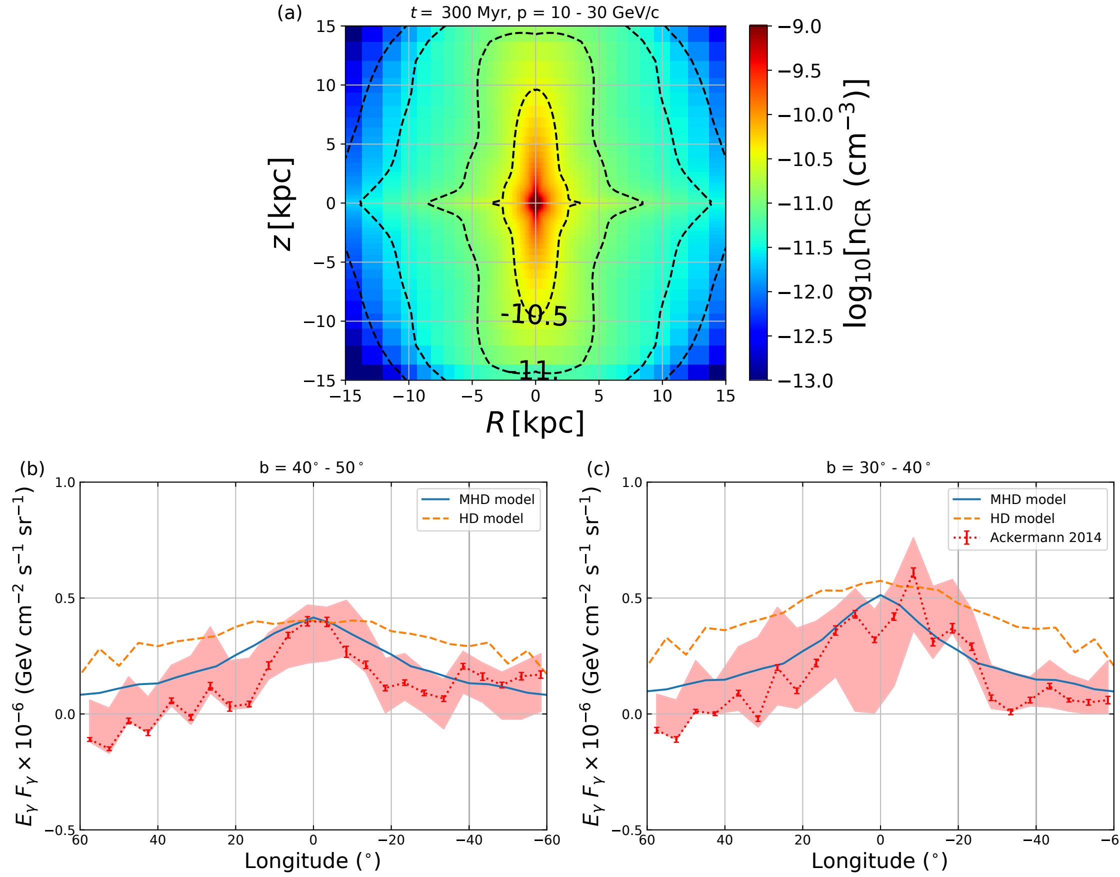

Figure 5.19: The figure presents the results for the configuration (A) for $D_\perp = 0.1 D_\parallel$. Figure (a) shows the spatial distribution for n_{CR}. For $R < 5$ kpc, the contour lines show a much larger extension in the z-direction (red to green zone) than the hydrodynamic model (see figure 3.2) or for the isotropic diffusion for the MHD model (see figure 5.8 (a)). Figures (b) and (c) show the resulting $E_\gamma F_\gamma$ emission for $40° < b < 50°$ and $30° < b < 40°$. The emission (solid blue line) exhibits a clear sharpness that follows the fitting-range provided by the Fermi collaboration (dotted red line). The γ-ray emission for the hydrodynamic model (dashed orange line) is shown for comparison.

Following these results, another setup has been considered for which $D_\perp = 0.01 D_\parallel$. Figure 5.20 presents the distribution for n_{CR} (figure (a)) and the $E_\gamma F_\gamma$ distribution for $40° < b < 50°$ (figure (b)) and for $30° < b < 40°$ (figure (c)). The n_{CR} distribution is thinner than for the case $D_\perp = 0.1 D_\parallel$ (see figure 5.19 (a)). The emission shows a slightly better fit with the sharpness observed for the Fermi bubbles. It must be noted that the low resolution of the grid introduces imprecision.

However, the results suggest that for an anisotropic diffusion, the sharpness of the edges can be provided for $0.01D_\parallel \leq D_\perp \leq 0.1D_\parallel$.

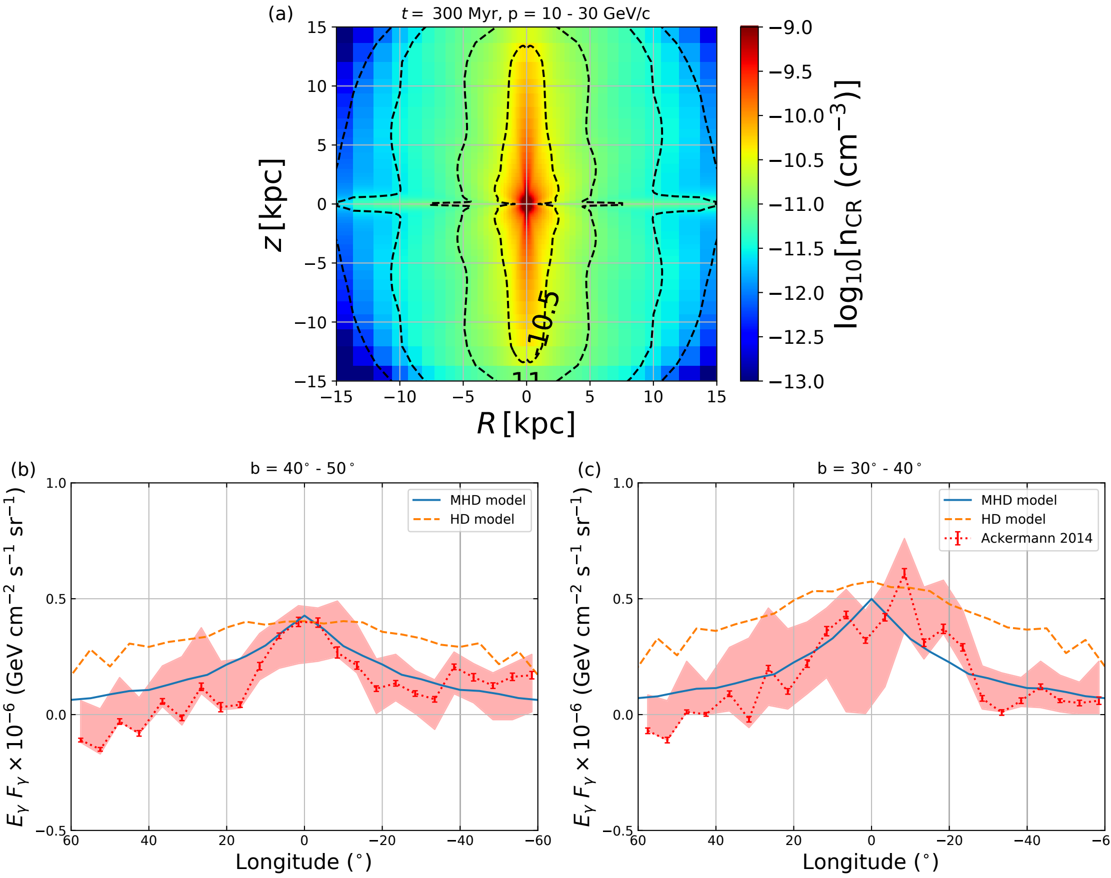

Figure 5.20: The figure presents results for the configuration (A) and for $D_\perp = 0.01D_\parallel$. Figure (a) shows the spatial distribution for $n_{\rm CR}$. This distribution exhibits a pronounced vertical structure (red to green zone) that extends farther than for $D_\perp = 0.1D_\parallel$ (see figure 5.19 (a)). Figures (b) and (c) show the resulting $E_\gamma F_\gamma$ emission for $40° < b < 50°$ and $30° < b < 40°$ (solid blue line). The emission exhibits a sharpness that matches very well with the fitting range provided by observations (dotted red line). The γ-ray emission for the hydrodynamic model (dashed orange line) is shown for comparison.

Figures 5.19 and 5.20 show an extension at the base of the $n_{\rm CR}$ distribution. This extension is due to the necessity to increase the inner radius of the grid to 10 pc but also the low resolution that must be used for reaching a computation time of 300 Myr. As shown in figure 5.21, for a simulation time of 49 Myr, for the configuration (A), the $n_{\rm CR}$ distribution for a grid of 60 bins (figure (a)) shows an extension at the base of the distribution reaching a distance of $R \approx 7$ kpc. As the number of bins is doubled (figure (b)) an extension appears only for the last contour line and does not extend far when compared with the 60 bins resolution.

Configuration C

The configuration (C 2) has been set up with $\lambda_{\rm max} = 1.5$ pc (see section 5.1.1). This value and a grid of 60 bins do not allow to reach a computation time of 300 Myr. A time of 276 Myr has been reached and the configuration can be studied as close to steady-state. For this configuration, $D_\perp = 0.1D_\parallel$.

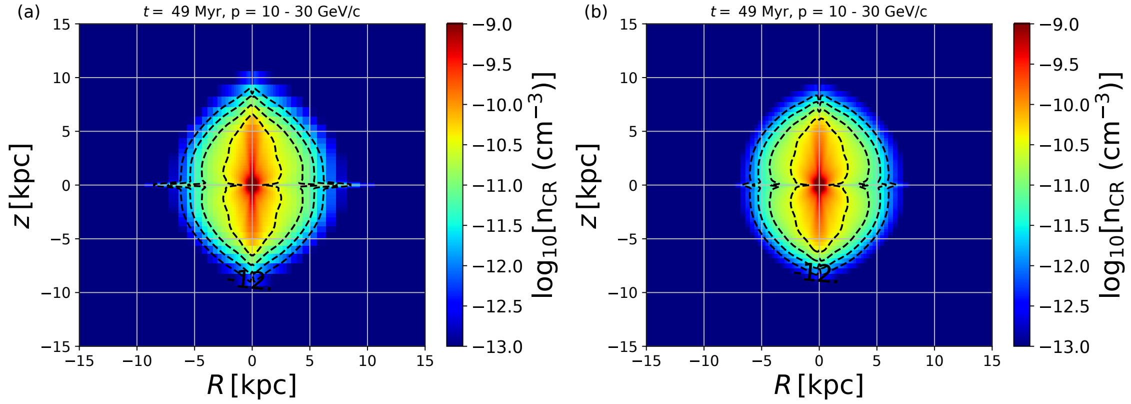

Figure 5.21: The figure presents a comparison of the n_{CR} distribution for the configuration (A) for $D_\perp = 0.01 D_\parallel$ for $t = 49$ Myr. For figure (a), a resolution of 60 bins has been used. At the base of the distribution, the contour lines show an extension reaching a distance of $R \approx 7$ kpc. For figure (b) a resolution of 120 bins has been used. The spatial distribution of n_{CR} shows only a small extension for the last contour line.

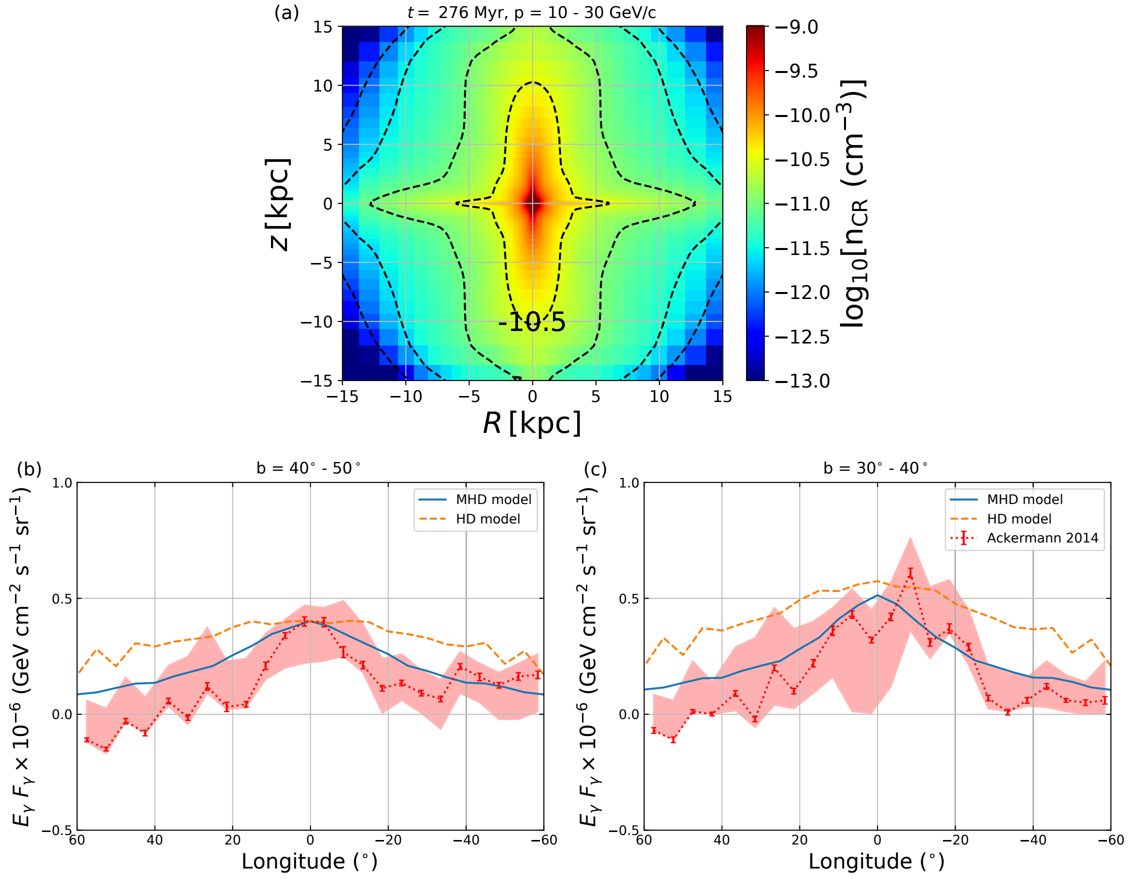

Figure 5.22: The figure presents the results for the configuration (C 2) for $D_\perp = 0.1 D_\parallel$ and for a simulation time of 276 Myr. Figure (a) shows the spatial distribution of n_{CR}. The distribution presents a profile extended along the z-direction (red to green zone) similar to the configuration (A) (see figure 5.19 (a)). Figures (b) and (c) show the resulting $E_\gamma F_\gamma$ distribution for $40° < b < 50°$ and $30° < b < 40°$ (solid blue line). It exhibits a profile with a sharpness comparable to the Fermi bubbles (dotted red line). The γ-ray emission for the hydrodynamic model (dashed orange line) is shown for comparison.

Figure 5.22 (a) presents the spatial distribution of n_{CR}. Figures (b) and (c) present the $E_\gamma F_\gamma$ distribution for $40° < b < 50°$ and for $30° < b < 40°$. The spatial magnetic field distribution of the configuration (C 2), as for the configuration (A), is dominated by $B_r(r)$, except at the formed shell (see figure 4.14). But this shell is at a Galactic height of ~ 15 kpc and therefore, its effect on the spatial distribution of n_{CR} is not visible. Figure (a) shows a distribution fairly close to the configuration (A). The same applies for the $E_\gamma F_\gamma$ distribution (figures (b) and (c)).

The configuration (C 1) has been set up with $\lambda_{\max} = 3$ pc (see section 5.1.1). With this value, only a computation time of 152 Myr has been reached. As the numerical simulation is not in a steady-state the results themselves cannot be analysed. However, it is possible to compare the n_{CR} distribution with the two other configurations for the same computation time. Figure 5.23 (a), shows the configuration (C 1). Figure 5.23 (b) shows the configuration (A) and figure 5.23 (c) the configuration (C 2). For configuration (C 1), $B_\phi(r, \theta)$ dominates $B_r(r)$. The diffusion of the CR is done mainly in the direction of this field. As shown by the three last contour lines, for $t = 152$ Myr, the spatial distribution of n_{CR} extends less far than for the configurations (A) and (C 2).

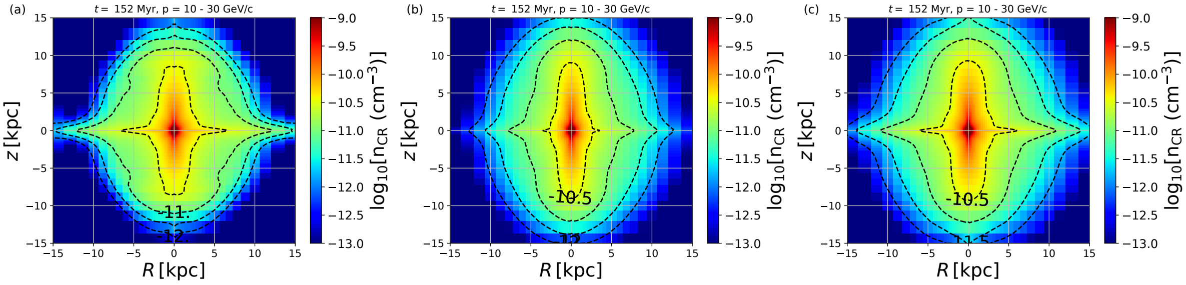

Figure 5.23: The figure presents the n_{CR} distribution for the configuration (C 1) (figure (a)) for a computation time of 152 Myr. This configuration is compared with the configurations (A) (figure (b)) and (C 2) (figure (c)) at the same time. Since for the configuration (C 1), $B_\phi(r, \theta)$ dominates, the CR are confined and n_{CR} decreases faster than for the configurations (A) and (C 2). This effect can be seen on the last three contour lines that are closer for the configuration (C 1) than for the two other configurations.

5.3 Conclusion for the chapter

The different configurations considering an isotropic and inhomogeneous diffusion coefficient have been able to reproduce both the CR and γ-ray maps obtained using the simple hydrodynamic model. The next step has been to consider an anisotropic diffusion coefficient.

The larger value for the diffusion length leads to a larger time needed for the computation of the code. Thus, only one configuration of the three considered has been able to reach the simulated time of 300 Myr. The results still allow to study the effect of an anisotropic diffusion on the distribution of n_{CR}. This anisotropy brings a constraint on the CR propagation and the configurations show a sharpness in their $E_\gamma F_\gamma$ profile that matches well with the fitting-range provided for the Fermi bubbles. Therefore, a Galactic breeze model in combination with an anisotropic diffusion is able to approximate both the velocity and the $E_\gamma F_\gamma$ profile of the Fermi bubbles.

Chapter 6

Conclusion

The discovery of the Fermi bubbles (Dobler et al. 2010; Carretti et al. 2013; Ackermann et al. 2014) has revealed the presence of a large scale bubble around the Galaxy emitting in the γ-ray energy range. This emission seems to be correlated with the Microwave Haze (Dobler et al. 2010; Dobler 2012) and the recently observed eROSITA bubbles (Predehl et al. 2020). These bubbles find their origin in the Galactic Center. The observations of high velocity cold clouds, present inside the bubbles have provided a velocity profile that reaches a maximal velocity of $\sim$ 300 km s^{-1} at a Galactic height of 1 kpc and subsequently decelerates beyond this point (Fox et al. 2015; Bordoloi et al. 2017; Karim et al. 2018; Lockman, Di Teodoro and McClure-Griffiths 2020; Ashley et al. 2020; Cashman et al. 2021).

For chapter 2, the aim was to explore a specific solution in order to provide an explanation for the velocity profile of the Fermi bubbles. A subsonic solution could provide an explanation for the deceleration observed. As a first step, a hydrodynamic model was considered.

This solution involves a subsonic velocity outflow, called a breeze solution, for which the initial velocity is not high enough to be able to become supersonic. The velocity profile reaches its maximum at a point called the critical radius, r_c, and decelerates continuously beyond this point. Such a solution had previously been explored analytically for a divergent free velocity field, providing promising results (Taylor and Giacinti 2017). For this thesis, this work has been extended by using a hydrodynamic code for relaxing the divergence free assumption of the subsonic velocity field.

For proceeding with the simulations, the first step was to define the total Galactic gravitational potential. For this, three different components were considered. A bulge, expressed with a Plummer potential (Plummer 1911). A disc, described by a three components Miyamoto-Nagai potential (Miyamoto and Nagai 1975) and a dark matter halo described by a Navarro-Frenk-White potential (Navarro, Frenk and White 1996). The normalisation of this total Galactic gravitational potential has been done by using a fitting range provided through recent observations by the Gaia mission (Watkins, Evans and An 2010). The total Galactic potential has then been normalised to reach the upper limit of the fitted range. This allows to consider the highest possible thermal velocity for the hot Galactic halo, here $c_s = 250$ km s^{-1} ($kT \approx 400$ eV), while maintaining $r_c = 1$ kpc.

A second step has been to set up a density distribution for the hot Galactic halo. For this, a hydrostatic density distribution has been considered that is defined through the total Galactic gravitational potential and the thermal velocity of the gas. This distribution has been compared with a recent fitting range, given for 10 - 100 kpc from the Galactic Center, based on the observations of hot Galactic gas halo from O VII and H I spectra and ram-pressure stripping (Martynenko 2022). The density distribution defined for the considered model matches well with the fitting range.

As both the Galactic gravitational potential and the thermal velocity considered have provided satisfactory results. These two parameters have been implemented for a spherically 2D hydrodynamic simulation. For this, the PLUTO code has been used (Mignone et al. 2007). First, the initial grid has been setup with a hot halo gas in a hydrostatic density distribution and an isothermal temperature profile. The initial velocity of the breeze, at a distance of 300 pc from the Galactic Center, has been calculated by solving numerically the outflow equation obtained from the momentum equation in steady-state. The peak outflow velocity has been chosen to be ~ 210 km s^{-1}, reaching a Mach number of 0.85 at r_c. The numerical simulation has been performed until it reaches a steady-state. The outflow spreads mainly along the z-direction due to the asphericity of the disc component for the Galactic gravitational potential, forming an elongated bubble shape.

For chapter 3, the aim was to provide a γ-ray emission distribution that would be compared with the observations. For this, the CR transport equation has been solved numerically to determine the CR density distribution based on the outputs of the Galactic breeze profile numerically simulated in chapter 2. For the transport of CR, an isotropic and homogeneous diffusion coefficient has been adopted (Jokipii 1966; Schlickeiser 1989). The diffusion length has been set to 0.1 pc for an energy of 10 GeV. The advection, is represented by the velocity distribution obtained with the PLUTO code (see chapter 2). As the velocity profile is not divergence free, adiabatic losses have been taken into account. The CR are all considered to be protons. To simulate their transport, a constant number density for the hot Galactic halo gas of $n_{\text{gas}} = 3 \times 10^{-3}$ cm^{-3} has been assumed. For this density, and proton-proton interactions, the loss time scale is around 20 Gyr (Gabici, Aharonian and Blasi 2007). The injected energy-spectrum of CR into the computation grid has been expressed with a power-law distribution. The energy range for the injection goes from 10 GeV to 30 GeV. For the chosen diffusion length and the simulated velocity profile, the diffusion time is larger than the advection time. The advection is therefore the main mechanism for the propagation of CR. The CR density distribution follows the outflow and shows an elongated structure along the z-axis. The energy flux distribution for such a CR density distribution has been compared with the observations provided by the Fermi-LAT instruments (Ackermann et al. 2014). A CR luminosity of 1.4×10^{40} erg s^{-1} approximately matches with the γ-ray brightness of the observations. However, the model does not reproduce the sharp edges that can be observed at a Galactic longitude of $l \approx 15^\circ$. This hydrodynamic model based on a Galactic breeze profile is therefore able to produce a bubble shape. But this model alone is not sufficient to provide a full explanation of the origin and formation of the Fermi bubbles.

Chapter 4 aimed to extend the hydrodynamic model with a magnetic field distribution. From observations, the presence of a magnetic field for the Galactic halo has been revealed, through the WMAP Haze (Dobler and Finkbeiner 2008; Dobler 2012) and S-PASS bubble (Carretti et al. 2013). Their bases coincide with the base of the Fermi bubbles (Dobler et al. 2010; Ackermann et al. 2014) and extend up to $\sim$ 6 kpc in height. The soft X-ray emission from the eROSITA bubbles (Predehl et al. 2020) is thought to originate from energetic thermal electrons. This would be consistent with a heating mechanism, potentially due to a magnetic field. Moreover, magnetic fields certainly play a role in the diffusion of CR and may underlie some aspects of the morphology of the Fermi bubbles. A lead explored in this thesis is the relation between the edges of the Fermi bubbles and the magnetic field geometry in this region.

The hydrodynamic momentum equation used in chapter 2 has been extended to include a magnetic field distribution in the form of a magnetic tension and a magnetic pressure. A magnetic tension acts to straighten out the magnetic field lines when they are bent by another force. The magnetic pressure is an equivalent to the thermal pressure.

The influence of a magnetic distribution on the position of the critical radius, r_c, has been studied. This position depends on the azimuthal component of a magnetic field, $B_\phi(r)$. In order to carry out an analytic study, a simple magnetic field configuration has been considered, with $B_\phi(r)$ taking a spatially dependent power-law distribution with a power index α. Depending on the value of α the effect of $B_\phi(r)$ on the position of r_c will be different. For $\alpha = 1$, $B_\phi(r)$ has no effect on the position of r_c. For $\alpha > 1$, $B_\phi(r)$ has the effect of shifting r_c closer to the Galactic Center. For $\alpha < 1$, r_c is shifted farther away from the Galactic Center. In this case, it is possible to consider a higher temperature for the Galactic halo. This has the consequence of increasing the thermal velocity, shifting back r_c to 1 kpc and increasing the velocity of the galactic breeze profile.

However, in the Galactic halo region, little is known about the magnetic field distribution. Several works proposed a distribution based on observations of Faraday rotation measures and synchrotron radiation emission (Jansson and Farrar 2012; Shaw, van Vliet and Taylor 2022; Unger and Farrar 2023). Those works have provided an estimation for the magnitude of the toroidal magnetic field of $\sim$ 1-2.5 μG for a galactic height of 1-6 kpc. As part of this thesis, the focus has been on weak magnetic field strengths. These values do not perturb in a significant way the propagation and the profile of the galactic breeze and allow a first analysis of the model. Several configurations have been tested in which a magnetic field is injected into the computational grid along with the initial velocity, leading to the formation of an outflow.

Based on the MHD momentum equation, a radial magnetic field $B_r(r)$ does not influence the velocity profile of the outflow. A first configuration explored $B_{r_0} = 20$ μG and $B_{\phi_0} = v_{\phi_0} = 0$. Following Maxwell equations, $\nabla \cdot \mathbf{B} = 0$ and as $B_r(r)$ is the only component for the magnetic field, the 2D distribution in the grid follows a power-law proportional to r^{-2}. As expected, the velocity distribution is not disturbed by the presence of $B_r(r)$ and therefore the 2D map for the velocity distribution is identical to the hydrodynamic model.

A second set of configurations has been simulated to compare the effect of different values for v_{ϕ_0} and keeping fixed $B_{r_0} = 2$ μG and $B_{\phi_0} = 0$ μG. Based on the frozen field approximation, it is possible to estimate the distribution of B_ϕ for a velocity distribution close to the hydrodynamic model. From this approximation, it appears that an initial value for $B_\phi(r)$ is not needed as long as both B_{r_0} and v_{ϕ_0} are not equal to zero. A first configuration considered $v_{\phi_0} = 2$ km s^{-1}. For such a small value, the velocity distribution does not show any difference with the hydrodynamic model. A weak strength for the $B_\phi(r,\theta)$ distribution is present with a maximal value of 10^{-2} μG at a Galactic height of ~500 pc. $B_\phi(r,\theta)$ dominates in value $B_r(r)$ at a Galactic height of ~9 kpc. A second configuration increased v_{ϕ_0} by one order of magnitude, giving $v_{\phi_0} = 20$ km s^{-1}. Following the frozen-field approximation, the $B_\phi(r)$ distribution is also increased by one order of magnitude and becomes superior to $B_r(r)$ at a Galactic height of ~2 kpc. The velocity distribution shows a slight deceleration along the z-axis. The third configuration considered has been simulated for v_{ϕ_0}=50 km s^{-1}. This value has a strong impact on the velocity distribution along the z-axis. As the $B_\phi(r,\theta)$ value is larger than $B_r(r)$, the magnetic field lines are piled up, creating a zone of larger magnetic field but where the magnetic field lines are also twisted. This has the effect of decelerating the outflow at this zone due to a magnetic tension effect. The outflow bypasses this zone and the bubbles shape of the outflow shows a larger size.

A third set of configurations includes a value for B_{ϕ_0}. The first configuration considered had B_{ϕ_0}=1 μG for $B_{r_0} = 20$ μG and $v_{\phi_0} = 20$ km s^{-1}. The 2D map for the velocity distribution shows an extension at the top of the bubble shape. This corresponds to an acceleration of the outflow when compared with the hydrodynamic model. As for the previous configuration, a magnetic tension decelerates the outflow at the zone where the magnetic field lines are twisted. However, the effect is less for this configuration. The outflow bypasses the zone more easily and causes the visible extension. For the second configuration, a value of B_{ϕ_0}=2 μG has been considered. This configuration shows a specific distribution of the magnetic field. A shell is formed as B_{ϕ_0} creates a positive direction for $B_\phi(r,\theta)$ at the beginning of the numerical simulation. As it progresses, a negative direction for $B_\phi(r,\theta)$ dominates, pushes and compresses the positive $B_\phi(r,\theta)$ field at the outer boundary of the bubbles.

Similar to the hydrodynamic model, those different configurations and their velocity and magnetic distribution have been used to map their associated CR density distribution and γ-ray energy flux.

For chapter 5, the aim was to provide a γ-ray emission distribution in a similar way to chapter 3 by including the magnetic field distribution obtained in chapter 4. Both the velocity and the magnetic field distribution outputs are used to numerically solve the CR transport equation. The magnetic field distribution is not homogeneous. For the numerical simulation of CR transport, two models have been considered. The first one has an isotropic diffusion coefficient. The second one has an anisotropic diffusion coefficient.

The isotropic and inhomogeneous model allows to compare the CR density distribution and the resulting γ-ray emission with the results obtained for the hydrodynamic model. The diffusion length is expressed through the ratio of the Larmor radius and the maximum Alfven wavelength, λ_{max} which represents the characteristic distance over which the magnetic field maintains its coherence. For each configuration, a value of λ_{max} has been fixed in order to have a diffusion length as close as possible to the constant value of 0.1 pc used for the hydrodynamic model. As the magnetic field distribution is inhomogeneous, a constant value for the diffusion length is not possible. However, some configurations, for which $B_\phi(r,\theta)$ is the dominant component and is quasi-constant, allowed for a good approximation. Each configuration has shown an energy flux emission similar to the hydrodynamic model. In chapter 4, some features have been observed for some configurations due to the influence of a magnetic tension, leading to a deceleration or an acceleration effect in the velocity distribution and a compression of the magnetic field lines. As those features are beyond the height of the Fermi bubbles, i.e. ~ 10 kpc, their possible effects are not visible in the γ-ray emission.

Following these results, an anisotropic diffusion coefficient has been adopted. For this, the CR transport code has to be modified to include transverse components for the diffusion tensor. A test problem has been performed in order to check that the anisotropic diffusion was solved correctly. Once this test was carried out with coherent results, the next step was to proceed with some configurations. However, the need for a $\lambda_{\max}$ ranging from 1 to 3 pc had the effect of largely increasing the computation time. Moreover, the anisotropic model has an effect on the advection. In order to be able to reach a computation time of 300 Myr, a low resolution grid of 60 bins has been used. The grid ranges from 10 pc to 20 kpc. However, with those parameters, only the configuration (A) was able to reach 300 Myr. The configuration (C 2) reached a computation time of 276 Myr and the configuration (C 1) reached 152 Myr. However, these simulations provided results that showed a strong similarity with the observed γ-ray emission for the Fermi bubbles. The anisotropic diffusion is then able to reproduce the sharpness of the Fermi bubbles.

As a general conclusion, the work provided in this thesis offers a serious alternative for describing the Fermi bubbles features. The Galactic breeze model developed here is able to reproduce the observed deceleration ranging from ~ 1 kpc to ~ 10 kpc (Keeney et al. 2006; Bowen et al. 2008; Zech et al. 2008; Fang and Jiang 2014; Fox et al. 2015; Bordoloi et al. 2017; Savage et al. 2017; Karim et al. 2018; Ashley et al. 2020; Cashman et al. 2021; Ashley et al. 2022). In combination with anisotropic and inhomogeneous diffusion, the Galactic breeze model is able to reproduce the sharpness in the Fermi bubbles emission (Ackermann et al. 2014).

Three future points to focus on to further improve this model are the following, the gravitational potential of the bulge, the temperature distribution in the hot Galactic halo and the magnetic field distribution. First and foremost, the velocity profile at a distance of ~ 300 pc from the Galactic Center must be modified. A large deceleration can be observed at this distance (see figure 2.4). This effect is due to the gravitational potential of the Galactic bulge. A bubble formed by a subsonic outflow, for a thermally-driven model, should start with a low-velocity at its base that increases continuously until it reaches r_c. A better description than proposed in this work is then necessary for the gravitational influence of the Galactic bulge and the subsequent velocity profile. This will also have the effect of improving the setup for the CR transport code, offering better results for the γ-ray emission.

Secondly, a better constraint of the temperature in the hot Galactic halo must be explored. The isothermal model used in this work is not able to provide a maximum velocity of ~ 300 km s^{-1} at r_c. For the hot Galactic halo, observations have highlighted a hotter phase that seems to permeate the entire halo (Das et al. 2019b; Das et al. 2019a; Das et al. 2021b; Gupta et al. 2021; Ramesh, Nelson and Pillepich 2023). Those observations motivate the consideration of a more complex temperature profile expressed through a multi-thermal phase model.

Lastly, a more complete study must be carried out to find a suitable magnetic field distribution. This work has shown that an azimuthal magnetic field distribution can lead to an increase in thermal velocity and consequently, the velocity distribution. However, the Galactic breeze profile explored for the MHD simulations was identical to the hydrodynamic simulations. A fully satisfying model must then be able to emulate a maximum velocity of ~ 300 km s^{-1} at a Galactic height of $\sim 1 - 1.5$ kpc (Ashley et al. 2020) as well as the deceleration observed along the Galactic latitude (Fox et al. 2015; Bordoloi et al. 2017; Savage et al. 2017; Karim et al. 2018; Ashley et al. 2020; Cashman et al. 2021; Ashley et al. 2022).

Appendix A

The numerical CR transport code

In this appendix, details about the discretisation of the CR transport equation are given as well as the implementation of the boundary conditions.

A.1 Numerical scheme

The code assumes a cylindrical symmetry with two spatial dimensions, R and$z$. A logarithmic spaced spatial grid and a logarithmic spaced momentum grid are used. A change of variables is introduced as $u \equiv \ln R$ and $s \equiv \ln z$. D_{ij} is the diffusion coefficient, where i and j represent the two directions R and z.

A.1.1 Diffusive term

For the diffusive term, a first order forward in time and second order centered in space scheme is used. The anistropic diffusion equation is expressed as

$$\begin{aligned}\nabla.\left(D\nabla f\right) = \frac{1}{R^2}\frac{\partial}{\partial \ln R}\left(D_{RR}\frac{\partial f}{\partial \ln R}\right) + \frac{1}{R^2}\frac{\partial}{\partial \ln R}\left(RD_{Rz}\frac{1}{z}\frac{\partial f}{\partial \ln z}\right) \\ + \frac{1}{z}\frac{\partial}{\partial \ln z}\left(D_{zR}\frac{1}{R}\frac{\partial f}{\partial \ln R}\right) + \frac{1}{z}\frac{\partial}{\partial \ln z}\left(D_{zz}\frac{1}{z}\frac{\partial f}{\partial \ln z}\right). \quad \text{(A.1)}\end{aligned}$$

Its discretisation giving

$$\begin{aligned}\nabla.\left(D\nabla f\right) = \overbracket{\frac{e^{-2u_i}}{\Delta u}\left[D_{RR_{i+\frac{1}{2},j}}\nabla_u f|_{i+\frac{1}{2},j} - D_{RR_{i-\frac{1}{2},j}}\nabla_u f|_{i-\frac{1}{2},j}\right]}^{\text{RR}} \\ \underbracket{+\frac{e^{-2u_i}e^{-s_j}}{\Delta u}\left[e^{\frac{u_{i+1}+u_i}{2}}D_{Rz_{i+\frac{1}{2},j}}\nabla_s f|_{i+\frac{1}{2},j} - e^{\frac{u_i+u_{i-1}}{2}}D_{Rz_{i-\frac{1}{2},j}}\nabla_s f|_{i-\frac{1}{2},j}\right]}_{\text{Rz}} \\ + \underbracket{\frac{e^{-u_i}e^{-s_j}}{\Delta s}\left[D_{zR_{i,j+\frac{1}{2}}}\nabla_u f|_{i,j+\frac{1}{2}} - D_{zR_{i},j-\frac{1}{2}}\nabla_u f|_{i,j-\frac{1}{2}}\right]}_{\text{zR}} \\ + \underbracket{\frac{e^{-s_j}}{\Delta s}\left[e^{-\frac{s_{j+1}+s_j}{2}}D_{zz_{i,j+\frac{1}{2}}}\nabla_s f|_{i,j+\frac{1}{2}} - e^{-\frac{s_j+s_{j-1}}{2}}D_{zz_{i,j-\frac{1}{2}}}\nabla_s f|_{i,j-\frac{1}{2}}\right]}_{\text{zz}}, \quad \text{(A.2)}\end{aligned}$$

where

$$\frac{\partial f}{\partial u}\Big|_{i+\frac{1}{2},j} = \frac{f_{i+1,j} - f_{i,j}}{\Delta u} \tag{A.3}$$

$$\frac{\partial f}{\partial s}\Big|_{i,j+\frac{1}{2}} = \frac{f_{i,j+1} - f_{i,j}}{\Delta s} \tag{A.4}$$

$$\frac{\partial f}{\partial s}\Big|_{i+\frac{1}{2},j} = \frac{f_{i+1,j+1} + f_{i,j+1} - f_{i,j-1} - f_{i+1,j-1}}{4\Delta s} \tag{A.5}$$

$$\frac{\partial f}{\partial u}\Big|_{i,j+\frac{1}{2}} = \frac{f_{i+1,j+1} + f_{i+1,j} - f_{i-1,j+1} - f_{i-1,j}}{4\Delta u}. \tag{A.6}$$

A.1.2 Advective term

For the spatial advective term, a Lax-Wendroff scheme has been used. It is a second-order accurate method for both time and space. It is a explicit method, meaning it updates the solution at each time step based of the value from the previous time step. For the advection the conservation form is expressed as

$$\frac{\partial f}{\partial t} = -\frac{v_R}{R}\frac{\partial f}{\partial \ln R} - \frac{v_z}{z}\frac{\partial f}{\partial \ln z}. \tag{A.7}$$

Its discretisation giving

$$\begin{aligned} f^{n+1}_{i,j} = f^{n}_{i,j} &\overbrace{- \Delta t v^{n}_{R_{i,j}} e^{-u_i} \frac{f^{n}_{i+1,j} - f^{n}_{i-1,j}}{2\left(u_{i+1} - u_{i-1}\right)} + \frac{\Delta t^2}{2} v^{n}_{R_{i,j}} e^{-u_i} \left[\frac{F^{n}_{i+\frac{1}{2},j} - F^{n}_{i-\frac{1}{2},j}}{u_{i+1} - u_{i-1}}\right]}^{\text{R direction}} \\ &\underbrace{- \Delta t v^{n}_{z_{i,j}} e^{-s_j} \frac{f^{n}_{i,j+1} - f^{n}_{i,j-1}}{2\left(s_{j+1} - s_{j-1}\right)} + \frac{\Delta t^2}{2} v^{n}_{z_{i,j}} e^{-s_j} \left[\frac{F^{n}_{i,j+\frac{1}{2}} - F^{n}_{i,j-\frac{1}{2}}}{s_{j+1} - s_{j-1}}\right]}_{\text{z direction}}, \end{aligned} \tag{A.8}$$

where

$$F^{n}_{i+\frac{1}{2},j} = \frac{e^{-\frac{u_{i+1}+u_i}{2}} \left(v_{R_{i+1,j}} + v_{R_{i,j}}\right) \left(f^{n}_{i+1,j} - f^{n}_{i,j}\right)}{u_{i+1} - u_i} \tag{A.9}$$

$$F^{n}_{i-\frac{1}{2},j} = \frac{e^{-\frac{u_{i}+u_{i-1}}{2}} \left(v_{R_{i,j}} + v_{R_{i-1,j}}\right) \left(f^{n}_{i,j} - f^{n}_{i-1,j}\right)}{u_{i} - u_{i-1}} \tag{A.10}$$

$$F^{n}_{i,j+\frac{1}{2}} = \frac{e^{-\frac{v_{j+1}+v_j}{2}} \left(v_{z_{i,j+1}} + v_{z_{i,j}}\right) \left(f^{n}_{i,j+1} - f^{n}_{i,j}\right)}{s_{j+1} - s_j} \tag{A.11}$$

$$F^{n}_{i,j-\frac{1}{2}} = \frac{e^{-\frac{v_{j}+v_{j-1}}{2}} \left(v_{z_{i,j}} + v_{z_{i,j-1}}\right) \left(f^{n}_{i,j} - f^{n}_{i,j-1}\right)}{s_{j} - s_{j-1}}. \tag{A.12}$$

A.1.3 Momentum advection term

The momentum advection term is discretised with an upwind scheme. As for the spatial term, the momentum is expressed with a logarithmic spacing, here $w = \ln p$. It is expressed as

$$\frac{\partial f}{\partial t} = \frac{\nabla.\mathbf{v}}{3}\frac{\partial f}{\partial w} \tag{A.13}$$

Its discretisation gives

$$f_{i,j}^{n+1} = f_{i,j}^{n} = \Delta t e^{-2u_i} v_R^* \frac{(f_{R_1} - f_{R_2})}{3\Delta w} + \Delta t e^{-v_j} v_z^* \frac{(f_{z_1} - f_{z_2})}{3\Delta w}, \tag{A.14}$$

where

$$v_R^* = \frac{e^{\frac{u_{i+1}+u_i}{2}}\left(v_{R_{i+1,j}} + v_{R_{i,j}}\right) - e^{\frac{u_i+u_{i-1}}{2}}\left(v_{R_{i,j}} + v_{R_{i-1,j}}\right)}{2\Delta u} \tag{A.15}$$

$$v_z^* = \frac{\left(v_{z_{i,j+1}} + v_{z_{i,j}}\right) - \left(v_{z_{i,j}} + v_{z_{i,j-1}}\right)}{2\Delta s}, \tag{A.16}$$

and

$$f_{R_1} = \begin{cases} f_{i,j,k}^n & \text{if } v_R^* > 0 \\ f_{i,j,k+1}^n & \text{if } v_R^* < 0 \end{cases} \tag{A.17}$$

$$f_{R_2} = \begin{cases} f_{i,j,k-1}^n & \text{if } v_R^* > 0 \\ f_{i,j,k}^n & \text{if } v_R^* < 0 \end{cases} \tag{A.18}$$

$$f_{z_1} = \begin{cases} f_{i,j,k}^n & \text{if } v_z^* > 0 \\ f_{i,j,k+1}^n & \text{if } v_z^* < 0 \end{cases} \tag{A.19}$$

$$f_{z_2} = \begin{cases} f_{i,j,k-1}^n & \text{if } v_z^* > 0 \\ f_{i,j,k}^n & \text{if } v_z^* < 0 \end{cases} \tag{A.20}$$

A.1.4 Boundary conditions

The inner boundary condition for both the R and z directions are reflective. To implement this boundary condition the spatial diffusion and advection are treated together. The flux across the boundary must zero implying the following equation

$$D\nabla f - \mathbf{v}f = 0. \tag{A.21}$$

Considering an anisotropic expression for the diffusion, its discretisation for the boundary in the R-direction is

$$D_{RR_{i+\frac{1}{2},j}} \nabla_R f|_{i+\frac{1}{2},j} + D_{Rz_{i+\frac{1}{2},j}} \nabla_z f|_{i+\frac{1}{2},j} - v_{R_{i+\frac{1}{2},j}} f_{i+\frac{1}{2},j} = 0. \tag{A.22}$$

For the z direction the discretisation gives

$$D_{zz_{i,j+\frac{1}{2}}} \nabla_z f|_{i,j+\frac{1}{2}} + D_{zR_{i,j+\frac{1}{2}}} \nabla_R f|_{i,j+\frac{1}{2}} - v_{z_{i,j+\frac{1}{2}}} f_{i,j+\frac{1}{2}} = 0. \tag{A.23}$$

The expression of the space density, $f_{i,j}$, in the boundary zone for the R-direction is then given by

$$f_{i,j} = \frac{\left(\frac{D_{RR_{i+\frac{1}{2},j}}}{R\Delta R} - \frac{v_{R_{i+\frac{1}{2},j}}}{2}\right) f_{i+1,j} + D_{Rz_{i+\frac{1}{2},j}} \nabla_z f|_{i+\frac{1}{2},j}}{\left(\frac{D_{RR_{i+\frac{1}{2},j}}}{R\Delta R} + \frac{v_{R_{i+\frac{1}{2},j}}}{2}\right)}. \tag{A.24}$$

For the boundary zone in the z-direction, the space phase density is given by

$$f_{i,j} = \frac{\left(\frac{D_{zz_{i,j+\frac{1}{2}}}}{z\Delta z} - \frac{v_{R_{i,j,+\frac{1}{2}}}}{2}\right) f_{i,j+1} + D_{zR_{i,j+\frac{1}{2}}} \nabla_R f|_{i,j+\frac{1}{2}}}{\left(\frac{D_{zz_{i,j+\frac{1}{2}}}}{z\Delta z} + \frac{v_{R_{i,j+\frac{1}{2}}}}{2}\right)} \tag{A.25}$$

Appendix B

The expression of the diffusion coefficient

A 2D cylindrical symmetry (R, z) is considered here. Assuming that the parallel diffusion is done along the z-axis, $D_{\parallel} = D_{zz}$ and then the perpendicular is done along the R-axis, $D_{\perp} = D_{RR}$. The cross-diffusion terms are considered to be zero, $D_{Rz} = D_{zR} = 0$.
The transformation of a tensor is expressed by

$$T = R^{-1} T' R, \tag{B.1}$$

where T represent a tensor and R is the transformation matrix, here

$$R = \begin{pmatrix} \cos\theta & \sin\theta \\ -\sin\theta & \cos\theta \end{pmatrix}. \tag{B.2}$$

The transformation of the diffusion tensor lead then to the following expression

$$\begin{pmatrix} D_{RR} & D_{Rz} \\ D_{zR} & D_{zz} \end{pmatrix} = \begin{pmatrix} \cos\theta & -\sin\theta \\ \sin\theta & \cos\theta \end{pmatrix} \begin{pmatrix} D_{\perp} & 0 \\ 0 & D_{\parallel} \end{pmatrix} \begin{pmatrix} \cos\theta & \sin\theta \\ -\sin\theta & \cos\theta \end{pmatrix}, \tag{B.3}$$

giving

$$D_{RR} = D_{\perp} \cos^2\theta + D_{\parallel} \sin^2\theta = D_{\perp} \left(1 - \sin^2\theta\right) + D_{\parallel} \sin^2\theta \tag{B.4}$$

$$D_{Rz} = D_{zR} = \left(D_{\parallel} - D_{\perp}\right) \cos\theta \sin\theta \tag{B.5}$$

$$D_{zz} = D_{\perp} sin^2\theta + D_{\parallel} \cos^2\theta = D_{\perp} \left(1 - \cos^2\theta\right) + D_{\parallel} cos^2\theta. \tag{B.6}$$

The function $\cos\theta$ and $\sin\theta$ can be related to the components of the total magnetic field as

$$B_R = |\mathbf{B}| \sin\theta \tag{B.7}$$

$$B_z = |\mathbf{B}| \cos\theta, \tag{B.8}$$

leading to the expression for the general expression for the diffusion coefficient

$$D_{i,j} = D_{\perp} \delta_{i,j} + \left(D_{\parallel} - D_{\perp}\right) \frac{B_i}{|\mathbf{B}|} \frac{B_j}{|\mathbf{B}|} \tag{B.9}$$

Bibliography

Abeysekara, A. U. et al. (Dec. 2013). “Sensitivity of the high altitude water Cherenkov detector to sources of multi-TeV gamma rays”. In: *Astroparticle Physics* 50, pp. 26–32. DOI: `10.1016/j.astropartphys.2013.08.002`. arXiv: `1306.5800 [astro-ph.HE]`.

Abeysekara, A. U. et al. (May 2021). “HAWC observations of the acceleration of very-high-energy cosmic rays in the Cygnus Cocoon”. In: *Nature Astronomy* 5, pp. 465–471. DOI: `10.1038/s41550-021-01318-y`. arXiv: `2103.06820 [astro-ph.HE]`.

Ackermann, M. et al. (Nov. 2011). “A Cocoon of Freshly Accelerated Cosmic Rays Detected by Fermi in the Cygnus Superbubble”. In: *Science* 334.6059, p. 1103. DOI: `10.1126/science.1210311`.

Ackermann, M. et al. (Sept. 2014). “The Spectrum and Morphology of the Fermi Bubbles”. In: *APJ* 793.1, 64, p. 64. DOI: `10.1088/0004-637X/793/1/64`. arXiv: `1407.7905 [astro-ph.HE]`.

Agostinelli, S. et al. (July 2003). “G EANT4—a simulation toolkit”. In: *Nuclear Instruments and Methods in Physics Research A* 506.3, pp. 250–303. DOI: `10.1016/S0168-9002(03)01368-8`.

Akita, Masahiro et al. (July 2018). “Diffuse X-Ray Emission from the Northern Arc of Loop I Observed with Suzaku”. In: *APJ* 862.1, 88, p. 88. DOI: `10.3847/1538-4357/aacd08`. arXiv: `1806.08058 [astro-ph.GA]`.

Almeida, S. P. et al. (Oct. 1968). “pp Interactions at 10 GeV/c”. In: *Physical Review* 174.5, pp. 1638–1661. DOI: `10.1103/PhysRev.174.1638`.

Amenomori, M. et al. (May 2019). “Test of the hadronic interaction models SIBYLL2.3, EPOS-LHC and QGSJETII- 04 with Tibet EAS core data”. In: *European Physical Journal Web of Conferences*. Vol. 208. European Physical Journal Web of Conferences, 08013, p. 08013. DOI: `10.1051/epjconf/201920808013`.

Anderson, H. L. et al. (Mar. 1952). “Total Cross Sections of Positive Pions in Hydrogen”. In: *Physical Review* 85.5, pp. 936–936. DOI: `10.1103/PhysRev.85.936`.

Anderson, Michael E. and Bregman, Joel N. (May 2010). “Do Hot Halos Around Galaxies Contain the Missing Baryons?” In: *APJ* 714.1, pp. 320–331. DOI: `10.1088/0004-637X/714/1/320`. arXiv: `1003.3273 [astro-ph.CO]`.

Anderson, Michael E., Bregman, Joel N. and Dai, Xinyu (Jan. 2013). “Extended Hot Halos around Isolated Galaxies Observed in the ROSAT All-Sky Survey”. In: *APJ* 762.2, 106, p. 106. DOI: `10.1088/0004-637X/762/2/106`. arXiv: `1211.5140 [astro-ph.CO]`.

Ashkin, J. et al. (Feb. 1956). “Pion-Proton Scattering at 150 and 170 Mev”. In: *Physical Review* 101.3, pp. 1149–1158. DOI: `10.1103/PhysRev.101.1149`.

Ashley, Trisha et al. (Aug. 2020). “Mapping Outflowing Gas in the Fermi Bubbles: A UV Absorption Survey of the Galactic Nuclear Wind”. In: *APJ* 898.2, 128, p. 128. DOI: `10.3847/1538-4357/ab9ff8`. arXiv: `2006.13254 [astro-ph.GA]`.

Ashley, Trisha et al. (July 2022). “Diverse metallicities of Fermi bubble clouds indicate dual origins in the disk and halo”. In: *Nature Astronomy* 6, pp. 968–975. DOI: `10.1038/s41550-022-01720-0`. arXiv: `2207.08838 [astro-ph.GA]`.

Atwood, W. B. et al. (June 2009). “The Large Area Telescope on the Fermi Gamma-Ray Space Telescope Mission”. In: *APJ* 697.2, pp. 1071–1102. DOI: `10.1088/0004-637X/697/2/1071`. arXiv: `0902.1089 [astro-ph.IM]`.

Baade, W. (Aug. 1946). “A Search For the Nucleus of Our Galaxy”. In: *PASP* 58.343, pp. 249–252. DOI: `10.1086/125835`.

Bähr, Manuel et al. (Dec. 2008). “Herwig++ physics and manual”. In: *European Physical Journal C* 58.4, pp. 639–707. DOI: `10.1140/epjc/s10052-008-0798-9`. arXiv: `0803.0883 [hep-ph]`.

Bartoli, B. et al. (Aug. 2014). “Identification of the TeV Gamma-Ray Source ARGO J2031+4157 with the Cygnus Cocoon”. In: *APJ* 790.2, 152, p. 152. DOI: `10.1088/0004-637X/790/2/152`. arXiv: `1406.6436 [astro-ph.HE]`.

Beck, R. and Krause, M. (July 2005). “Revised equipartition and minimum energy formula for magnetic field strength estimates from radio synchrotron observations”. In: *Astronomische Nachrichten* 326.6, pp. 414–427. DOI: `10.1002/asna.200510366`. arXiv: `astro-ph/0507367 [astro-ph]`.

Beck, Rainer and Wielebinski, Richard (2013). “Magnetic Fields in Galaxies”. In: *Planets, Stars and Stellar Systems. Volume 5: Galactic Structure and Stellar Populations*. Ed. by Oswalt, Terry D. and Gilmore, Gerard. Vol. 5, p. 641. DOI: `10.1007/978-94-007-5612-0_13`.

Bell, A. R. (Jan. 1978). “The acceleration of cosmic rays in shock fronts - I.” In: *MNRAS* 182, pp. 147–156. DOI: `10.1093/mnras/182.2.147`.

Bell, A. R. et al. (May 2013). “Cosmic-ray acceleration and escape from supernova remnants”. In: *MNRAS* 431.1, pp. 415–429. DOI: `10.1093/mnras/stt179`. arXiv: `1301.7264 [astro-ph.HE]`.

Bell, Eric F. et al. (June 2008). “The Accretion Origin of the Milky Way’s Stellar Halo”. In: *APJ* 680.1, pp. 295–311. DOI: `10.1086/588032`. arXiv: `0706.0004 [astro-ph]`.

Belokurov, V. et al. (Jan. 2014). “Precession of the Sagittarius stream”. In: *MNRAS* 437.1, pp. 116–131. DOI: `10.1093/mnras/stt1862`. arXiv: `1301.7069 [astro-ph.GA]`.

Bennett, C. L. et al. (Sept. 2003). “First-Year Wilkinson Microwave Anisotropy Probe (WMAP) Observations: Preliminary Maps and Basic Results”. In: *APJS* 148.1, pp. 1–27. DOI: `10.1086/377253`. arXiv: `astro-ph/0302207 [astro-ph]`.

Bennett, C. L. et al. (Oct. 2013). “Nine-year Wilkinson Microwave Anisotropy Probe (WMAP) Observations: Final Maps and Results”. In: *APJS* 208.2, 20, p. 20. DOI: `10.1088/0067-0049/208/2/20`. arXiv: `1212.5225 [astro-ph.CO]`.

Bensby, T., Feltzing, S. and Oey, M. S. (Feb. 2014). “Exploring the Milky Way stellar disk. A detailed elemental abundance study of 714 F and G dwarf stars in the solar neighbourhood”. In: *AAP* 562, A71, A71. DOI: `10.1051/0004-6361/201322631`. arXiv: `1309.2631 [astro-ph.GA]`.

Berezinskii, V. S. et al. (1984). *Astrophysics of cosmic rays*.

Bhattacharjee, Pijushpani, Chaudhury, Soumini and Kundu, Susmita (Apr. 2014). “Rotation Curve of the Milky Way out to ∼200 kpc”. In: *APJ* 785.1, 63, p. 63. DOI: `10.1088/0004-637X/785/1/63`. arXiv: `1310.2659 [astro-ph.GA]`.

Bierlich, Christian et al. (Mar. 2022). “A comprehensive guide to the physics and usage of PYTHIA 8.3”. In: *arXiv e-prints*, arXiv:2203.11601, arXiv:2203.11601. DOI: `10.48550/arXiv.2203.11601`. arXiv: `2203.11601 [hep-ph]`.

Binney, J. and Piffl, T. (Dec. 2015). “The distribution function of the Galaxy’s dark halo”. In: *MNRAS* 454.4, pp. 3653–3663. DOI: `10.1093/mnras/stv2225`. arXiv: `1509.06877 [astro-ph.GA]`.

Binney, James (Oct. 2012). “More dynamical models of our Galaxy”. In: *MNRAS* 426.2, pp. 1328–1337. DOI: `10.1111/j.1365-2966.2012.21692.x`. arXiv: `1207.4917 [astro-ph.GA]`.

Binney, James, Gerhard, Ortwin and Spergel, David (June 1997). “The photometric structure of the inner Galaxy”. In: *MNRAS* 288.2, pp. 365–374. DOI: `10.1093/mnras/288.2.365`. arXiv: `astro-ph/9609066 [astro-ph]`.

Binney, James et al. (Sept. 1991). “Understanding the kinematics of Galactic Centre gas.” In: *MNRAS* 252, p. 210. DOI: `10.1093/mnras/252.2.210`.

Bland-Hawthorn, J. et al. (Aug. 2005). “NGC 300: An Extremely Faint, Outer Stellar Disk Observed to 10 Scale Lengths”. In: *APJ* 629.1, pp. 239–249. DOI: `10.1086/430512`. arXiv: `astro-ph/0503488 [astro-ph]`.

Bland-Hawthorn, Joss and Gerhard, Ortwin (Sept. 2016). “The Galaxy in Context: Structural, Kinematic, and Integrated Properties”. In: *ARAA* 54, pp. 529–596. DOI: `10.1146/annurev-astro-081915-023441`. arXiv: `1602.07702 [astro-ph.GA]`.

Blitz, Leo and Robishaw, Timothy (Oct. 2000). “Gas-Rich Dwarf Spheroidals”. In: *APJ* 541.2, pp. 675–687. DOI: `10.1086/309457`. arXiv: `astro-ph/0001142 [astro-ph]`.

Blitz, Leo and Spergel, David N. (Oct. 1991). “Direct Evidence for a Bar at the Galactic Center”. In: *APJ* 379, p. 631. DOI: `10.1086/170535`.

Blumenthal, George R. and Gould, Robert J. (Jan. 1970). “Bremsstrahlung, Synchrotron Radiation, and Compton Scattering of High-Energy Electrons Traversing Dilute Gases”. In: *Reviews of Modern Physics* 42.2, pp. 237–271. DOI: `10.1103/RevModPhys.42.237`.

Bondi, H. and Hoyle, F. (Jan. 1944). “On the mechanism of accretion by stars”. In: *MNRAS* 104, p. 273. DOI: `10.1093/mnras/104.5.273`.

Bopp, F. W. et al. (Jan. 2008). “Antiparticle to particle production ratios in hadron-hadron and d-Au collisions in the DPMJET-III Monte Carlo model”. In: *PhyS Rev C* 77.1, 014904, p. 014904. DOI: `10.1103/PhysRevC.77.014904`. arXiv: `hep-ph/0505035 [hep-ph]`.

Bordoloi, Rongmon et al. (Jan. 2017). “Mapping the Nuclear Outflow of the Milky Way: Studying the Kinematics and Spatial Extent of the Northern Fermi Bubble”. In: *APJ* 834.2, 191, p. 191. DOI: `10.3847/1538-4357/834/2/191`. arXiv: `1612.01578 [astro-ph.GA]`.

Bovy, Jo, Hogg, David W. and Rix, Hans-Walter (Oct. 2009). “Galactic Masers and the Milky Way Circular Velocity”. In: *APJ* 704.2, pp. 1704–1709. DOI: `10.1088/0004-637X/704/2/1704`. arXiv: `0907.5423 [astro-ph.GA]`.

Bovy, Jo and Rix, Hans-Walter (Dec. 2013). “A Direct Dynamical Measurement of the Milky Way’s Disk Surface Density Profile, Disk Scale Length, and Dark

Matter Profile at 4 kpc $\lesssim$R $\lesssim$9 kpc”. In: *APJ* 779.2, 115, p. 115. DOI: 10.1088/0004-637X/779/2/115. arXiv: 1309.0809 [astro-ph.GA].

Bowen, David V. et al. (May 2008). “The Far Ultraviolet Spectroscopic Explorer Survey of O VI Absorption in the Disk of the Milky Way”. In: *APJS* 176.1, pp. 59–163. DOI: 10.1086/524773. arXiv: 0711.0005 [astro-ph].

Bregman, Joel N. and Lloyd-Davies, Edward J. (Nov. 2007). “X-Ray Absorption from the Milky Way Halo and the Local Group”. In: *APJ* 669.2, pp. 990–1002. DOI: 10.1086/521321. arXiv: 0707.1699 [astro-ph].

Brüns, C. et al. (May 2000). “The head-tail structure of high-velocity clouds. A survey of the northern sky”. In: *AAP* 357, pp. 120–128. DOI: 10.48550/arXiv.astro-ph/0003110. arXiv: astro-ph/0003110 [astro-ph].

Bryan, Greg L. and Norman, Michael L. (Mar. 1998). “Statistical Properties of X-Ray Clusters: Analytic and Numerical Comparisons”. In: *APJ* 495.1, pp. 80–99. DOI: 10.1086/305262. arXiv: astro-ph/9710107 [astro-ph].

Buote, David A. and Canizares, Claude R. (Feb. 1996). “X-Ray Constraints on the Intrinsic Shapes and Baryon Fractions of Five Abell Clusters”. In: *APJ* 457, p. 565. DOI: 10.1086/176753. arXiv: astro-ph/9504049 [astro-ph].

Bykov, A. M. and Fleishman, G. D. (Mar. 1992). “On non-thermal particle generation in superbubbles.” In: *MNRAS* 255, pp. 269–275. DOI: 10.1093/mnras/255.2.269.

Bykov, A. M. et al. (Feb. 2018). “Cosmic Ray Production in Supernovae”. In: *SSR* 214.1, 41, p. 41. DOI: 10.1007/s11214-018-0479-4. arXiv: 1801.08890 [astro-ph.HE].

Bykov, Andrei M. (Nov. 2014). “Nonthermal particles and photons in starburst regions and superbubbles”. In: *AAPR* 22, 77, p. 77. DOI: 10.1007/s00159-014-0077-8. arXiv: 1511.04608 [astro-ph.HE].

Bykov, Andrei M. et al. (Apr. 2020). “High-Energy Particles and Radiation in Star-Forming Regions”. In: *SSR* 216.3, 42, p. 42. DOI: 10.1007/s11214-020-00663-0. arXiv: 2003.11534 [astro-ph.HE].

Caballero-Lopez, R. A. and Moraal, H. (Jan. 2004). “Limitations of the force field equation to describe cosmic ray modulation”. In: *Journal of Geophysical Research (Space Physics)* 109.A1, A01101, A01101. DOI: 10.1029/2003JA010098.

Caldwell, J. A. R. and Ostriker, J. P. (Dec. 1981). “The mass distribution within our Galaxy - A three component model”. In: *APJ* 251, pp. 61–87. DOI: 10.1086/159441.

Cao, Zhen et al. (June 2021). “Ultrahigh-energy photons up to 1.4 petaelectronvolts from 12 γ-ray Galactic sources”. In: *Nature* 594.7861, pp. 33–36. DOI: 10.1038/s41586-021-03498-z.

Carretti, Ettore et al. (Jan. 2013). “Giant magnetized outflows from the centre of the Milky Way”. In: *Nature* 493.7430, pp. 66–69. DOI: 10.1038/nature11734. arXiv: 1301.0512 [astro-ph.GA].

Cashman, Frances H. et al. (Dec. 2021). “Molecular Gas within the Milky Way’s Nuclear Wind”. In: *APJL* 923.1, L11, p. L11. DOI: 10.3847/2041-8213/ac3cbc. arXiv: 2112.03335 [astro-ph.GA].

Cesarsky, C. J. and Montmerle, T. (Oct. 1983). “Gamma-Rays from Active Regions in the Galaxy - the Possible Contribution of Stellar Winds”. In: *SSR* 36.2, pp. 173–193. DOI: 10.1007/BF00167503.

Cherenkov Telescope Array Consortium et al. (2019). *Science with the Cherenkov Telescope Array*. DOI: 10.1142/10986.

Clarkson, Will et al. (Sept. 2008). “Stellar Proper Motions in the Galactic Bulge from Deep Hubble Space Telescope ACS WFC Photometry”. In: *APJ* 684.2, pp. 1110–1142. DOI: 10.1086/590378. arXiv: 0809.1682 [astro-ph].

Compton, Arthur H. and Getting, Ivan A. (June 1935). “An Apparent Effect of Galactic Rotation on the Intensity of Cosmic Rays”. In: *Physical Review* 47.11, pp. 817–821. DOI: 10.1103/PhysRev.47.817.

Cox, Erin G. et al. (Dec. 2015). “High-resolution 8 mm and 1 cm Polarization of IRAS 4A from the VLA Nascent Disk and Multiplicity (VANDAM) Survey”. In: *APJL* 814.2, L28, p. L28. DOI: 10.1088/2041-8205/814/2/L28. arXiv: 1511.00685 [astro-ph.SR].

Crain, Robert A. et al. (Sept. 2010). “X-ray coronae in simulations of disc galaxy formation”. In: *MNRAS* 407.3, pp. 1403–1422. DOI: 10.1111/j.1365-2966.2010.16985.x. arXiv: 1005.1642 [astro-ph.CO].

Cristofari, Pierre (Aug. 2021). “The Hunt for Pevatrons: The Case of Supernova Remnants”. In: *Universe* 7.9, p. 324. DOI: 10.3390/universe7090324. arXiv: 2110.07956 [astro-ph.HE].

Crocker, Roland M. and Aharonian, Felix (Mar. 2011). “Fermi Bubbles: Giant, Multibillion-Year-Old Reservoirs of Galactic Center Cosmic Rays”. In: *Phys Rev Lett* 106.10, 101102, p. 101102. DOI: 10.1103/PhysRevLett.106.101102. arXiv: 1008.2658 [astro-ph.GA].

Crocker, Roland M. et al. (Aug. 2015). “A Unified Model of the Fermi Bubbles, Microwave Haze, and Polarized Radio Lobes: Reverse Shocks in the Galactic Center’s Giant Outflows”. In: *APJ* 808.2, 107, p. 107. DOI: 10.1088/0004-637X/808/2/107. arXiv: 1412.7510 [astro-ph.HE].

Crutcher, R., Heiles, C. and Troland, T. (2003). “Observations of Interstellar Magnetic Fields”. In: *Turbulence and Magnetic Fields in Astrophysics*. Ed. by Falgarone, E. and Passot, T. Vol. 614, pp. 155–181.

Das, Kaustav K. et al. (Nov. 2020). “Constraining the distance to the North Polar Spur with Gaia DR2”. In: *MNRAS* 498.4, pp. 5863–5872. DOI: 10.1093/mnras/staa2702. arXiv: 2009.01320 [astro-ph.GA].

Das, Sanskriti et al. (Sept. 2019a). “Discovery of a Very Hot Phase of the Milky Way Circumgalactic Medium with Non-solar Abundance Ratios”. In: *APJL* 882.2, L23, p. L23. DOI: 10.3847/2041-8213/ab3b09. arXiv: 1907.07176 [astro-ph.GA].

Das, Sanskriti et al. (Dec. 2019b). “Multiple Temperature Components of the Hot Circumgalactic Medium of the Milky Way”. In: *APJ* 887.2, 257, p. 257. DOI: 10.3847/1538-4357/ab5846. arXiv: 1909.06688 [astro-ph.GA].

— (Jan. 2021a). “Empirical estimates of the Galactic halo contribution to the dispersion measures of extragalactic fast radio bursts using X-ray absorption”. In: *MNRAS* 500.1, pp. 655–662. DOI: 10.1093/mnras/staa3299. arXiv: 2007.11542 [astro-ph.GA].

Das, Sanskriti et al. (Sept. 2021b). “The Hot Circumgalactic Medium of the Milky Way: Evidence for Supervirial, Virial, and Subvirial Temperatures; Nonsolar Chemical Composition; and Nonthermal Line Broadening”. In: *APJ* 918.2, 83, p. 83. DOI: 10.3847/1538-4357/ac0e8e. arXiv: 2106.13243 [astro-ph.GA].

de Vaucouleurs, G. (Oct. 1964). “Luminosity Classification of Galaxies and Some Applications.” In: *AJ* 69, p. 561. DOI: `10.1086/109329`.

Deason, A. J. et al. (July 2012). “Broken degeneracies: the rotation curve and velocity anisotropy of the Milky Way halo”. In: *MNRAS* 424.1, pp. L44–L48. DOI: `10.1111/j.1745-3933.2012.01283.x`. arXiv: `1204.5189 [astro-ph.GA]`.

Dedner, A. et al. (Jan. 2002). “Hyperbolic Divergence Cleaning for the MHD Equations”. In: *Journal of Computational Physics* 175.2, pp. 645–673. DOI: `10.1006/jcph.2001.6961`.

Dehnen, Walter and Binney, James (Mar. 1998). “Mass models of the Milky Way”. In: *MNRAS* 294.3, pp. 429–438. DOI: `10.1046/j.1365-8711.1998.01282.x10.1111/j.1365-8711.1998.01282.x`. arXiv: `astro-ph/9612059 [astro-ph]`.

di Sciascio, G. and Lhaaso Collaboration (Oct. 2016). “The LHAASO experiment: From Gamma-Ray Astronomy to Cosmic Rays”. In: *Nuclear and Particle Physics Proceedings* 279-281, pp. 166–173. DOI: `10.1016/j.nuclphysbps.2016.10.024`. arXiv: `1602.07600 [astro-ph.HE]`.

Di Teodoro, Enrico M. et al. (Mar. 2018). “Blowing in the Milky Way Wind: Neutral Hydrogen Clouds Tracing the Galactic Nuclear Outflow”. In: *APJ* 855.1, 33, p. 33. DOI: `10.3847/1538-4357/aaad6a`. arXiv: `1802.02152 [astro-ph.GA]`.

Dobler, Gregory (May 2012). “A Last Look at the Microwave Haze/Bubbles with WMAP”. In: *APJ* 750.1, 17, p. 17. DOI: `10.1088/0004-637X/750/1/17`. arXiv: `1109.4418 [astro-ph.GA]`.

Dobler, Gregory and Finkbeiner, Douglas P. (June 2008). “Extended Anomalous Foreground Emission in the WMAP Three-Year Data”. In: *APJ* 680.2, pp. 1222–1234. DOI: `10.1086/587862`. arXiv: `0712.1038 [astro-ph]`.

Dobler, Gregory et al. (July 2010). “The Fermi Haze: A Gamma-ray Counterpart to the Microwave Haze”. In: *APJ* 717.2, pp. 825–842. DOI: `10.1088/0004-637X/717/2/825`. arXiv: `0910.4583 [astro-ph.HE]`.

Dutta, Alankar et al. (Sept. 2023). “Beyond profiles: Using log-normal distributions to model the multiphase circumgalactic medium”. In: *arXiv e-prints*, arXiv:2310.03717, arXiv:2310.03717. DOI: `10.48550/arXiv.2310.03717`. arXiv: `2310.03717 [astro-ph.GA]`.

Eggen, O. J., Lynden-Bell, D. and Sandage, A. R. (Nov. 1962). “Evidence from the motions of old stars that the Galaxy collapsed.” In: *APJ* 136, p. 748. DOI: `10.1086/147433`.

Ellis, S. C. and Bland-Hawthorn, J. (May 2007). “GALAXYCOUNT: a JAVA calculator of galaxy counts and variances in multiband wide-field surveys to 28 AB mag”. In: *MNRAS* 377.2, pp. 815–828. DOI: `10.1111/j.1365-2966.2007.11651.x`. arXiv: `astro-ph/0602573 [astro-ph]`.

Engel, J. et al. (Dec. 1992). “Nucleus-nucleus collisions and interpretation of cosmic-ray cascades”. In: *Phys Rev D* 46.11, pp. 5013–5025. DOI: `10.1103/PhysRevD.46.5013`.

Engel, R., Ranft, J. and Roesler, S. (Aug. 1995). “Hard diffraction in hadron-hadron interactions and in photoproduction”. In: *PhyS Rev D* 52.3, pp. 1459–1468. DOI: `10.1103/PhysRevD.52.1459`. arXiv: `hep-ph/9502319 [hep-ph]`.

Englmaier, Peter and Gerhard, Ortwin (Apr. 1999). “Gas dynamics and large-scale morphology of the Milky Way galaxy”. In: *MNRAS* 304.3, pp. 512–534. DOI: `10.1046/j.1365-8711.1999.02280.x`. arXiv: `astro-ph/9810208 [astro-ph]`.

Fang, Taotao, Bullock, James and Boylan-Kolchin, Michael (Jan. 2013). “On the Hot Gas Content of the Milky Way Halo”. In: *APJ* 762.1, 20, p. 20. DOI: 10.1088/0004-637X/762/1/20. arXiv: 1211.0758 [astro-ph.CO].

Fang, Taotao and Jiang, Xiaochuan (Apr. 2014). “High Resolution X-Ray Spectroscopy of the Local Hot Gas along the 3C 273 Sightline”. In: *APJL* 785.2, L24, p. L24. DOI: 10.1088/2041-8205/785/2/L24. arXiv: 1403.2028 [astro-ph.HE].

Fermi, Enrico (Apr. 1949). “On the Origin of the Cosmic Radiation”. In: *Physical Review* 75.8, pp. 1169–1174. DOI: 10.1103/PhysRev.75.1169.

Fich, Michel, Blitz, Leo and Stark, Antony A. (July 1989). “The Rotation Curve of the Milky Way to 2R 0”. In: *APJ* 342, p. 272. DOI: 10.1086/167591.

Finkbeiner, Douglas P. (Oct. 2004). “Microwave Interstellar Medium Emission Observed by the Wilkinson Microwave Anisotropy Probe”. In: *APJ* 614.1, pp. 186–193. DOI: 10.1086/423482. arXiv: astro-ph/0311547 [astro-ph].

Fletcher, R. S. et al. (Nov. 1994). “sibyll: An event generator for simulation of high energy cosmic ray cascades”. In: *phys Rev D* 50.9, pp. 5710–5731. DOI: 10.1103/PhysRevD.50.5710.

Flynn, Chris, Sommer-Larsen, J. and Christensen, P. R. (Aug. 1996). “Kinematics of the outer stellar halo”. In: *MNRAS* 281.3, pp. 1027–1032. DOI: 10.1093/mnras/281.3.1027. arXiv: astro-ph/9603106 [astro-ph].

Ford, Amanda Brady et al. (June 2013). “Hydrogen and metal line absorption around low-redshift galaxies in cosmological hydrodynamic simulations”. In: *MNRAS* 432.1, pp. 89–112. DOI: 10.1093/mnras/stt393. arXiv: 1206.1859 [astro-ph.CO].

Fox, Andrew J., Savage, Blair D. and Wakker, Bart P. (July 2006). “A Survey of O VI, C III, and H I in Highly Ionized High-Velocity Clouds”. In: *APJS* 165.1, pp. 229–255. DOI: 10.1086/504800. arXiv: astro-ph/0604091 [astro-ph].

Fox, Andrew J. et al. (Jan. 2015). “Probing the Fermi Bubbles in Ultraviolet Absorption: A Spectroscopic Signature of the Milky Way’s Biconical Nuclear Outflow”. In: *APJL* 799.1, L7, p. L7. DOI: 10.1088/2041-8205/799/1/L7. arXiv: 1412.1480 [astro-ph.GA].

Fux, R. (May 1999). “3D self-consistent N-body barred models of the Milky Way. II. Gas dynamics”. In: *AAP* 345, pp. 787–812. DOI: 10.48550/arXiv.astro-ph/9903154. arXiv: astro-ph/9903154 [astro-ph].

Gabici, Stefano, Aharonian, Felix A. and Blasi, Pasquale (June 2007). “Gamma rays from molecular clouds”. In: *APSS* 309.1-4, pp. 365–371. DOI: 10.1007/s10509-007-9427-6. arXiv: astro-ph/0610032 [astro-ph].

Gaia Collaboration (Nov. 2016a). “Gaia Data Release 1. Summary of the astrometric, photometric, and survey properties”. In: *AAP* 595, A2, A2. DOI: 10.1051/0004-6361/201629512. arXiv: 1609.04172 [astro-ph.IM].

— (Nov. 2016b). “The Gaia mission”. In: *AAP* 595, A1, A1. DOI: 10.1051/0004-6361/201629272. arXiv: 1609.04153 [astro-ph.IM].

— (Aug. 2018). “Gaia Data Release 2. Summary of the contents and survey properties”. In: *AAP* 616, A1, A1. DOI: 10.1051/0004-6361/201833051. arXiv: 1804.09365 [astro-ph.GA].

Gatto, A. et al. (Aug. 2013). “Unveiling the corona of the Milky Way via ram-pressure stripping of dwarf satellites”. In: *MNRAS* 433.4, pp. 2749–2763. DOI: 10.1093/mnras/stt896. arXiv: 1305.4176 [astro-ph.GA].

Gennaro, M. et al. (May 2015). “The Initial Mass Function and Star Formation History of the Galactic Bulge from HST*”. In: *Fifty Years of Wide Field Studies in the Southern Hemisphere: Resolved Stellar Populations of the Galactic Bulge and Magellanic Clouds*. Ed. by Points, S. and Kunder, A. Vol. 491. Astronomical Society of the Pacific Conference Series, p. 182.

Genzel, Reinhard, Eisenhauer, Frank and Gillessen, Stefan (Oct. 2010). “The Galactic Center massive black hole and nuclear star cluster”. In: *Reviews of Modern Physics* 82.4, pp. 3121–3195. DOI: `10.1103/RevModPhys.82.3121`. arXiv: `1006.0064 [astro-ph.GA]`.

Gillessen, S. et al. (Mar. 2017). “An Update on Monitoring Stellar Orbits in the Galactic Center”. In: *APJ* 837.1, 30, p. 30. DOI: `10.3847/1538-4357/aa5c41`. arXiv: `1611.09144 [astro-ph.GA]`.

Gilmore, G. and Reid, N. (Mar. 1983). “New light on faint stars - III. Galactic structure towards the South Pole and the Galactic thick disc.” In: *MNRAS* 202, pp. 1025–1047. DOI: `10.1093/mnras/202.4.1025`.

Ginzburg, V. L., Khazan, Ia. M. and Ptuskin, V. S. (Apr. 1980). “Origin of Cosmic-Rays - Galactic Models with Halo - Part One - Proton Nucleon Component”. In: *APSS* 68.2, pp. 295–314. DOI: `10.1007/BF00639701`.

Girart, Josep M. et al. (June 2009). “Magnetic Fields in the Formation of Massive Stars”. In: *Science* 324.5933, p. 1408. DOI: `10.1126/science.1171807`.

Gleeson, L. J. and Axford, W. I. (Dec. 1968). “The Compton-Getting Effect”. In: *APSS* 2.4, pp. 431–437. DOI: `10.1007/BF02175919`.

Gleisberg, T. et al. (Feb. 2009). “Event generation with SHERPA 1.1”. In: *Journal of High Energy Physics* 2009.2, 007, p. 007. DOI: `10.1088/1126-6708/2009/02/007`. arXiv: `0811.4622 [hep-ph]`.

Gould, Andrew, Flynn, Chris and Bahcall, John N. (Aug. 1998). “Spheroid Luminosity and Mass Functions from Hubble Space Telescope Star Counts”. In: *APJ* 503.2, pp. 798–808. DOI: `10.1086/306023`. arXiv: `astro-ph/9711263 [astro-ph]`.

Govoni, Federica (Jan. 2003). “Magnetic Fields in Galaxy Clusters”. In: *IAU Joint Discussion*. Vol. 25. IAU Joint Discussion, E47. DOI: `10.48550/arXiv.astro-ph/0311385`. arXiv: `astro-ph/0311385 [astro-ph]`.

Günter, S. et al. (Oct. 2005). “Modelling of heat transport in magnetised plasmas using non-aligned coordinates”. In: *Journal of Computational Physics* 209.1, pp. 354–370. DOI: `10.1016/j.jcp.2005.03.021`.

Guo, Fulai (2016). “The AGN Jet Model of the Fermi Bubbles”. In: *Proceedings of the International Astronomical Union* 11.S322, pp. 189–192. DOI: `10.1017/S1743921316012023`.

Guo, Fulai and Mathews, William G. (Sept. 2012). “The Fermi Bubbles. I. Possible Evidence for Recent AGN Jet Activity in the Galaxy”. In: *APJ* 756.2, 181, p. 181. DOI: `10.1088/0004-637X/756/2/181`. arXiv: `1103.0055 [astro-ph.HE]`.

Gupta, A., Mathur, S. and Krongold, Y. (Feb. 2017). “Probing the Anisotropy of the Milky Way Gaseous Halo-II: Sightline toward Mrk 509”. In: *APJ* 836.2, 243, p. 243. DOI: `10.3847/1538-4357/836/2/243`. arXiv: `1611.05389 [astro-ph.GA]`.

Gupta, A. et al. (Sept. 2012). “A Huge Reservoir of Ionized Gas around the Milky Way: Accounting for the Missing Mass?” In: *APJL* 756.1, L8, p. L8. DOI: `10.1088/2041-8205/756/1/L8`. arXiv: `1205.5037 [astro-ph.HE]`.

Gupta, Anjali et al. (Mar. 2021). “Supervirial Temperature or Neon Overabundance? Suzaku Observations of the Milky Way Circumgalactic Medium”. In: *APJ* 909.2, 164, p. 164. DOI: `10.3847/1538-4357/abdbb6`. arXiv: `2010.03038 [astro-ph.HE]`.

Gupta, Anjali et al. (July 2023). “Thermal and chemical properties of the eROSITA bubbles from Suzaku observations”. In: *Nature Astronomy* 7, pp. 799–804. DOI: `10.1038/s41550-023-01963-5`. arXiv: `2201.09915 [astro-ph.GA]`.

Gupta, Siddhartha et al. (Jan. 2018). “Lack of thermal energy in superbubbles: hint of cosmic rays?” In: *MNRAS* 473.2, pp. 1537–1553. DOI: `10.1093/mnras/stx2427`. arXiv: `1705.10448 [astro-ph.GA]`.

Habing, H. J. (July 1988). “Mixing and Nucleosynthesis in - and Intermediate - AGB Stars”. In: *AAP* 200, p. 40.

Hahn, T. M. et al. (Mar. 1952). “Neutrons and Gamma-Rays from the Proton Bombardment of Beryllium”. In: *Physical Review* 85.5, pp. 934–934. DOI: `10.1103/PhysRev.85.934`.

Hale, George E. (Nov. 1908). “On the Probable Existence of a Magnetic Field in Sun-Spots”. In: *APJ* 28, p. 315. DOI: `10.1086/141602`.

Hall, John S. (Feb. 1949). “Observations of the Polarized Light from Stars”. In: *Science* 109.2825, pp. 166–167. DOI: `10.1126/science.109.2825.166`.

Han, J. L. (Aug. 2017). “Observing Interstellar and Intergalactic Magnetic Fields”. In: *ARAA* 55.1, pp. 111–157. DOI: `10.1146/annurev-astro-091916-055221`.

Han, J. L., Manchester, R. N. and Qiao, G. J. (June 1999). “Pulsar rotation measures and the magnetic structure of our Galaxy”. In: *MNRAS* 306.2, pp. 371–380. DOI: `10.1046/j.1365-8711.1999.02544.x`. arXiv: `astro-ph/9903101 [astro-ph]`.

Han, J. L. and Qiao, G. J. (Aug. 1994). “The magnetic field in the disk of our Galaxy”. In: *AAP* 288, pp. 759–772.

Han, J. L. et al. (June 1997). “Antisymmetric rotation measures in our Galaxy: evidence for an A0 dynamo.” In: *AAP* 322, pp. 98–102.

Haslam, C. G. T. et al. (Jan. 1982). “A 408-MHZ All-Sky Continuum Survey. II. The Atlas of Contour Maps”. In: *AAPS* 47, p. 1.

Hawkins, K. et al. (Oct. 2015). “Using chemical tagging to redefine the interface of the Galactic disc and halo”. In: *MNRAS* 453.1, pp. 758–774. DOI: `10.1093/mnras/stv1586`. arXiv: `1507.03604 [astro-ph.GA]`.

Heiles, C. and Crutcher, R. (2005). “Magnetic Fields in Diffuse HI and Molecular Clouds”. In: *Cosmic Magnetic Fields*. Ed. by Wielebinski, Richard and Beck, Rainer. Vol. 664, p. 137. DOI: `10.1007/3540313966_7`.

Henley, David B. and Shelton, Robin L. (Oct. 2012). “An XMM-Newton Survey of the Soft X-Ray Background. II. An All-Sky Catalog of Diffuse O VII and O VIII Emission Intensities”. In: *APJS* 202.2, 14, p. 14. DOI: `10.1088/0067-0049/202/2/14`. arXiv: `1208.4360 [astro-ph.GA]`.

Henley, David B. et al. (Nov. 2010). “The Origin of the Hot Gas in the Galactic Halo: Confronting Models with XMM-Newton Observations”. In: *APJ* 723.1, pp. 935–953. DOI: `10.1088/0004-637X/723/1/935`. arXiv: `1005.1085 [astro-ph.GA]`.

Higdon, J. C. and Lingenfelter, R. E. (Aug. 2005). “OB Associations, Supernova-generated Superbubbles, and the Source of Cosmic Rays”. In: *APJ* 628.2, pp. 738–749. DOI: `10.1086/430814`.

Hillas, A. M. (Jan. 1984). “The Origin of Ultra-High-Energy Cosmic Rays”. In: *ARAA* 22, pp. 425–444. DOI: `10.1146/annurev.aa.22.090184.002233`.

Hiltner, W. A. (Feb. 1949). “Polarization of Light from Distant Stars by Interstellar Medium”. In: *Science* 109.2825, p. 165. DOI: `10.1126/science.109.2825.165`.

Hodges-Kluck, Edmund J., Miller, Matthew J. and Bregman, Joel N. (May 2016). “The Rotation of the Hot Gas around the Milky Way”. In: *APJ* 822.1, 21, p. 21. DOI: `10.3847/0004-637X/822/1/21`. arXiv: `1603.07734 [astro-ph.GA]`.

Hogg, J. Drew and Reynolds, Christopher S. (Feb. 2018). “The Dynamics of Truncated Black Hole Accretion Disks. II. Magnetohydrodynamic Case”. In: *APJ* 854.1, 6, p. 6. DOI: `10.3847/1538-4357/aaa6c6`. arXiv: `1801.05836 [astro-ph.HE]`.

Hu, Yue et al. (Feb. 2024). “Synchrotron intensity gradient revealing magnetic fields in galaxy clusters”. In: *Nature Communications* 15, 1006, p. 1006. DOI: `10.1038/s41467-024-45164-8`. arXiv: `2306.10011 [astro-ph.CO]`.

Ibata, R. A. et al. (Apr. 2003). “One ring to encompass them all: a giant stellar structure that surrounds the Galaxy”. In: *MNRAS* 340.3, pp. L21–L27. DOI: `10.1046/j.1365-8711.2003.06545.x`. arXiv: `astro-ph/0301067 [astro-ph]`.

Irwin, Mike J. et al. (Aug. 2005). “A Minor-Axis Surface Brightness Profile for M31”. In: *APJL* 628.2, pp. L105–L108. DOI: `10.1086/432718`. arXiv: `astro-ph/0505077 [astro-ph]`.

Ivezić, Željko et al. (Sept. 2008). “The Milky Way Tomography with SDSS. II. Stellar Metallicity”. In: *APJ* 684.1, pp. 287–325. DOI: `10.1086/589678`. arXiv: `0804.3850 [astro-ph]`.

Jansson, Ronnie and Farrar, Glennys R. (Sept. 2012). “A New Model of the Galactic Magnetic Field”. In: *APJ* 757.1, 14, p. 14. DOI: `10.1088/0004-637X/757/1/14`. arXiv: `1204.3662 [astro-ph.GA]`.

Jokipii, J. R. (Nov. 1966). “Cosmic-Ray Propagation. I. Charged Particles in a Random Magnetic Field”. In: *APJ* 146, p. 480. DOI: `10.1086/148912`.

Jurić, Mario et al. (Feb. 2008). “The Milky Way Tomography with SDSS. I. Stellar Number Density Distribution”. In: *APJ* 673.2, pp. 864–914. DOI: `10.1086/523619`. arXiv: `astro-ph/0510520 [astro-ph]`.

Kafle, Prajwal R. et al. (Dec. 2012). “Kinematics of the Stellar Halo and the Mass Distribution of the Milky Way Using Blue Horizontal Branch Stars”. In: *APJ* 761.2, 98, p. 98. DOI: `10.1088/0004-637X/761/2/98`. arXiv: `1210.7527 [astro-ph.GA]`.

Kafle, Prajwal Raj et al. (Oct. 2014). “On the Shoulders of Giants: Properties of the Stellar Halo and the Milky Way Mass Distribution”. In: *APJ* 794.1, 59, p. 59. DOI: `10.1088/0004-637X/794/1/59`. arXiv: `1408.1787 [astro-ph.GA]`.

Kahn, F. D. and Woltjer, L. (Nov. 1959). “Intergalactic Matter and the Galaxy.” In: *APJ* 130, p. 705. DOI: `10.1086/146762`.

Kalberla, P. M. W. and Dedes, L. (Sept. 2008). “Global properties of the H I distribution in the outer Milky Way. Planar and extra-planar gas”. In: *AAP* 487.3, pp. 951–963. DOI: `10.1051/0004-6361:20079240`. arXiv: `0804.4831 [astro-ph]`.

Kalberla, P. M. W. and Kerp, J. (Nov. 1998). “Hydrostatic equilibrium conditions in the galactic halo”. In: *AAP* 339, pp. 745–758.

Karim, Tanveer et al. (June 2018). “Probing the Southern Fermi Bubble in Ultraviolet Absorption Using Distant AGNs”. In: *APJ* 860.2, 98, p. 98. DOI: `10.3847/1538-4357/aac167`. arXiv: `1804.10617 [astro-ph.GA]`.

Kataoka, J. et al. (Dec. 2013). “Suzaku Observations of the Diffuse X-Ray Emission across the Fermi Bubbles’ Edges”. In: *APJ* 779.1, 57, p. 57. DOI: 10.1088/0004-637X/779/1/57. arXiv: 1310.3553 [astro-ph.HE].

Kataoka, J. et al. (July 2015). “Global Structure of Isothermal Diffuse X-Ray Emission along the Fermi Bubbles”. In: *APJ* 807.1, 77, p. 77. DOI: 10.1088/0004-637X/807/1/77. arXiv: 1505.05936 [astro-ph.HE].

Kataoka, Jun et al. (Feb. 2018). “X-Ray and Gamma-Ray Observations of the Fermi Bubbles and NPS/Loop I Structures”. In: *Galaxies* 6.1, p. 27. DOI: 10.3390/galaxies6010027. arXiv: 1802.07463 [astro-ph.HE].

Kataoka, Jun et al. (Feb. 2021). “Origin of Galactic Spurs: New Insight from Radio/X-Ray All-sky Maps”. In: *APJ* 908.1, 14, p. 14. DOI: 10.3847/1538-4357/abdb31. arXiv: 2101.03302 [astro-ph.HE].

Keeney, Brian A. et al. (Aug. 2006). “Does the Milky Way Produce a Nuclear Galactic Wind?” In: *APJ* 646.2, pp. 951–964. DOI: 10.1086/505128. arXiv: astro-ph/0604323 [astro-ph].

Kimmig, Brian et al. (Feb. 2015). “Measuring Consistent Masses for 25 Milky Way Globular Clusters”. In: *AJ* 149.2, 53, p. 53. DOI: 10.1088/0004-6256/149/2/53. arXiv: 1411.1763 [astro-ph.GA].

Klypin, Anatoly, Zhao, HongSheng and Somerville, Rachel S. (July 2002). “ΛCDM-based Models for the Milky Way and M31. I. Dynamical Models”. In: *APJ* 573.2, pp. 597–613. DOI: 10.1086/340656. arXiv: astro-ph/0110390 [astro-ph].

Kobayashi, Naoto et al. (Aug. 2008). “Star Formation in the Most Distant Molecular Cloud in the Extreme Outer Galaxy: A Laboratory of Star Formation in an Early Epoch of the Galaxy’s Formation”. In: *APJ* 683.1, pp. 178–188. DOI: 10.1086/588421. arXiv: 0803.3369 [astro-ph].

Lacy, Mark and Sajina, Anna (Apr. 2020). “Active galactic nuclei as seen by the Spitzer Space Telescope”. In: *Nature Astronomy* 4, pp. 352–363. DOI: 10.1038/s41550-020-1071-x. arXiv: 2008.05424 [astro-ph.GA].

Lang, Cornelia C., Morris, Mark and Echevarria, Luis (Dec. 1999). “A Radio Polarimetric Study of the Galactic Center Threads”. In: *APJ* 526.2, pp. 727–743. DOI: 10.1086/308012. arXiv: astro-ph/9906336 [astro-ph].

LaRosa, T. N. et al. (May 2004). “New Nonthermal Filaments at the Galactic Center: Are They Tracing a Globally Ordered Magnetic Field?” In: *APJ* 607.1, pp. 302–308. DOI: 10.1086/383233. arXiv: astro-ph/0402061 [astro-ph].

LaRosa, T. N. et al. (June 2005). “Evidence of a Weak Galactic Center Magnetic Field from Diffuse Low-Frequency Nonthermal Radio Emission”. In: *APJL* 626.1, pp. L23–L27. DOI: 10.1086/431647. arXiv: astro-ph/0505244 [astro-ph].

Law, C. J., Brentjens, M. A. and Novak, G. (Apr. 2011). “A Constraint on the Organization of the Galactic Center Magnetic Field Using Faraday Rotation”. In: *APJ* 731.1, 36, p. 36. DOI: 10.1088/0004-637X/731/1/36. arXiv: 1102.2204 [astro-ph.GA].

Lax, P. and Wendroff, B. (1960). In: *Communications on Pure and Applied Mathematics* 13, p. 217.

Lehner, N. et al. (Apr. 2009). “The Connection Between a Lyman Limit System, a Very Strong O VI Absorber, and Galaxies at z $\sim$0.203”. In: *APJ* 694.2, pp. 734–750. DOI: 10.1088/0004-637X/694/2/734. arXiv: 0812.4231 [astro-ph].

Letessier-Selvon, Antoine and Stanev, Todor (July 2011). "Ultrahigh energy cosmic rays". In: *Reviews of Modern Physics* 83.3, pp. 907–942. DOI: `10.1103/RevModPhys.83.907`. arXiv: `1103.0031 [astro-ph.HE]`.

Li, Weidong et al. (Apr. 2011). "Nearby supernova rates from the Lick Observatory Supernova Search - II. The observed luminosity functions and fractions of supernovae in a complete sample". In: *MNRAS* 412.3, pp. 1441–1472. DOI: `10.1111/j.1365-2966.2011.18160.x`. arXiv: `1006.4612 [astro-ph.SR]`.

Li, Yang-Shyang and White, Simon D. M. (Mar. 2008). "Masses for the Local Group and the Milky Way". In: *MNRAS* 384.4, pp. 1459–1468. DOI: `10.1111/j.1365-2966.2007.12748.x`. arXiv: `0710.3740 [astro-ph]`.

Licquia, Timothy C. and Newman, Jeffrey A. (June 2015). "Improved Estimates of the Milky Way's Stellar Mass and Star Formation Rate from Hierarchical Bayesian Meta-Analysis". In: *APJ* 806.1, 96, p. 96. DOI: `10.1088/0004-637X/806/1/96`. arXiv: `1407.1078 [astro-ph.GA]`.

Lingenfelter, Richard E. (Feb. 2013). "Superbubble origin of cosmic rays". In: *Centenary Symposium 2012: Discovery of Cosmic Rays*. Ed. by Ormes, Jonathan F. Vol. 1516. American Institute of Physics Conference Series, pp. 162–166. DOI: `10.1063/1.4792561`. arXiv: `1209.5728 [astro-ph.HE]`.

— (Nov. 2018). "Cosmic rays from supernova remnants and superbubbles". In: *Advances in Space Research* 62.10, pp. 2750–2763. DOI: `10.1016/j.asr.2017.04.006`. arXiv: `1807.09726 [astro-ph.HE]`.

Liu, Siming et al. (Dec. 2022). "The origin of galactic cosmic rays". In: *Reviews of Modern Plasma Physics* 6.1, 19, p. 19. DOI: `10.1007/s41614-022-00080-6`.

Lockman, Felix J., Di Teodoro, Enrico M. and McClure-Griffiths, N. M. (Jan. 2020). "Observation of Acceleration of H I Clouds within the Fermi Bubbles". In: *APJ* 888.1, 51, p. 51. DOI: `10.3847/1538-4357/ab55d8`. arXiv: `1911.06864 [astro-ph.GA]`.

Mac Low, Mordecai-Mark and McCray, Richard (Jan. 1988). "Superbubbles in Disk Galaxies". In: *APJ* 324, p. 776. DOI: `10.1086/165936`.

Maciel, W. J. and Lago, L. G. (Oct. 2005). "A New Determination of the Rotation Curve from Galactic Disk Planetary Nebulae". In: *RMXAA* 41, pp. 383–388.

Mao, S. A. et al. (May 2010). "A Survey of Extragalactic Faraday Rotation at High Galactic Latitude: The Vertical Magnetic Field of the Milky Way Toward the Galactic Poles". In: *APJ* 714.2, pp. 1170–1186. DOI: `10.1088/0004-637X/714/2/1170`. arXiv: `1003.4519 [astro-ph.GA]`.

Marcowith, Alexandre et al. (Oct. 2018). "Core-collapse supernovae as cosmic ray sources". In: *MNRAS* 479.4, pp. 4470–4485. DOI: `10.1093/mnras/sty1743`. arXiv: `1806.09700 [astro-ph.HE]`.

Martynenko, Nickolay (Mar. 2022). "Constraining density and metallicity of the Milky Way's hot gas halo from O VII spectra and ram-pressure stripping". In: *MNRAS* 511.1, pp. 843–858. DOI: `10.1093/mnras/stac164`. arXiv: `2105.02557 [astro-ph.GA]`.

Masseron, T. and Gilmore, G. (Oct. 2015). "Carbon, nitrogen and α-element abundances determine the formation sequence of the Galactic thick and thin discs". In: *MNRAS* 453.2, pp. 1855–1866. DOI: `10.1093/mnras/stv1731`. arXiv: `1503.00537 [astro-ph.SR]`.

Matsuoka, Tomoki and Sawada, Ryo (Mar. 2024). "Binary Interaction Can Yield a Diversity of Circumstellar Media around Type II Supernova Progenitors". In:

APJ 963.2, 105, p. 105. DOI: 10.3847/1538-4357/ad1829. arXiv: 2307.00727 [astro-ph.SR].

McClure-Griffiths, N. M. et al. (June 2013). "Atomic Hydrogen in a Galactic Center Outflow". In: *APJL* 770.1, L4, p. L4. DOI: 10.1088/2041-8205/770/1/L4. arXiv: 1304.7538 [astro-ph.GA].

McMillan, Paul J. (July 2011). "Mass models of the Milky Way". In: *MNRAS* 414.3, pp. 2446–2457. DOI: 10.1111/j.1365-2966.2011.18564.x. arXiv: 1102.4340 [astro-ph.GA].

— (Feb. 2017). "The mass distribution and gravitational potential of the Milky Way". In: *MNRAS* 465.1, pp. 76–94. DOI: 10.1093/mnras/stw2759. arXiv: 1608.00971 [astro-ph.GA].

McWilliam, Andrew and Zoccali, Manuela (Dec. 2010). "Two Red Clumps and the X-shaped Milky Way Bulge". In: *APJ* 724.2, pp. 1491–1502. DOI: 10.1088/0004-637X/724/2/1491. arXiv: 1008.0519 [astro-ph.GA].

Meiring, J. D. et al. (Apr. 2013). "QSO Absorption Systems Detected in Ne VIII: High-metallicity Clouds with a Large Effective Cross Section". In: *APJ* 767.1, 49, p. 49. DOI: 10.1088/0004-637X/767/1/49. arXiv: 1201.0939 [astro-ph.CO].

Mignone, A. (Aug. 2007). "A simple and accurate Riemann solver for isothermal MHD". In: *Journal of Computational Physics* 225.2, pp. 1427–1441. DOI: 10.1016/j.jcp.2007.01.033. arXiv: astro-ph/0701798 [astro-ph].

— (Aug. 2014). "High-order conservative reconstruction schemes for finite volume methods in cylindrical and spherical coordinates". In: *Journal of Computational Physics* 270, pp. 784–814. DOI: 10.1016/j.jcp.2014.04.001. arXiv: 1404.0537 [physics.comp-ph].

Mignone, A. et al. (May 2007). "PLUTO: A Numerical Code for Computational Astrophysics". In: *APJ* 170.1, pp. 228–242. ISSN: 1538-4365. DOI: 10.1086/513316.

Mignone, Andrea, Tzeferacos, Petros and Bodo, Gianluigi (Aug. 2010). "High-order conservative finite difference GLM-MHD schemes for cell-centered MHD". In: *Journal of Computational Physics* 229.17, pp. 5896–5920. DOI: 10.1016/j.jcp.2010.04.013. arXiv: 1001.2832 [astro-ph.HE].

Miller, Matthew J. and Bregman, Joel N. (June 2013). "The Structure of the Milky Way's Hot Gas Halo". In: *APJ* 770.2, 118, p. 118. DOI: 10.1088/0004-637X/770/2/118. arXiv: 1305.2430 [astro-ph.GA].

— (Feb. 2015). "Constraining the Milky Way's Hot Gas Halo with O VII and O VIII Emission Lines". In: *APJ* 800.1, 14, p. 14. DOI: 10.1088/0004-637X/800/1/14. arXiv: 1412.3116 [astro-ph.GA].

Mills, E. A. C. (May 2017). "The Milky Way's Central Molecular Zone". In: *arXiv e-prints*, arXiv:1705.05332, arXiv:1705.05332. DOI: 10.48550/arXiv.1705.05332. arXiv: 1705.05332 [astro-ph.GA].

Minniti, D. et al. (June 2011). "The Edge of the Milky Way Stellar Disk Revealed Using Clump Giant Stars as Distance Indicators". In: *APJL* 733.2, L43, p. L43. DOI: 10.1088/2041-8205/733/2/L43. arXiv: 1105.3151 [astro-ph.GA].

Miyamoto, M. and Nagai, R. (Jan. 1975). "Three-dimensional models for the distribution of mass in galaxies." In: *PASJ* 27, pp. 533–543.

Mondal, Santanu et al. (Aug. 2022). "Fermi bubbles: the collimated outburst needed to explain forward-shock edges". In: *MNRAS* 514.2, pp. 2581–2598. DOI: 10.1093/mnras/stac1084. arXiv: 2109.03834 [astro-ph.HE].

Morlino, G. et al. (July 2021). “Particle acceleration in winds of star clusters”. In: *MNRAS* 504.4, pp. 6096–6105. DOI: `10.1093/mnras/stab690`. arXiv: `2102.09217 [astro-ph.HE]`.

Morris, Mark and Serabyn, Eugene (Jan. 1996). “The Galactic Center Environment”. In: *ARAA* 34, pp. 645–702. DOI: `10.1146/annurev.astro.34.1.645`.

Moskalenko, I. V. and Strong, A. W. (Jan. 1998). “Production and Propagation of Cosmic-Ray Positrons and Electrons”. In: *APJ* 493.2, pp. 694–707. DOI: `10.1086/305152`. arXiv: `astro-ph/9710124 [astro-ph]`.

Moskalenko, Igor V., Strong, Andrew W. and Reimer, Olaf (Jan. 2004). “Diffuse Gamma Rays”. In: *Cosmic Gamma-Ray Sources*. Ed. by Cheng, K. S. and Romero, Gustavo E. Vol. 304. Astrophysics and Space Science Library, p. 279. DOI: `10.1007/978-1-4020-2256-2_12`. arXiv: `astro-ph/0402243 [astro-ph]`.

Mou, Guobin et al. (Aug. 2014). “Fermi Bubbles Inflated by Winds Launched from the Hot Accretion Flow in Sgr A*”. In: *APJ* 790.2, 109, p. 109. DOI: `10.1088/0004-637X/790/2/109`. arXiv: `1403.2129 [astro-ph.HE]`.

Mou, Guobin et al. (Sept. 2015). “The Accretion Wind Model of Fermi Bubbles. II. Radiation”. In: *APJ* 811.1, 37, p. 37. DOI: `10.1088/0004-637X/811/1/37`. arXiv: `1505.00892 [astro-ph.HE]`.

Mou, Guobin et al. (Feb. 2023). “Asymmetric eROSITA bubbles as the evidence of a circumgalactic medium wind”. In: *Nature Communications* 14, 781, p. 781. DOI: `10.1038/s41467-023-36478-0`. arXiv: `2212.02270 [astro-ph.GA]`.

Murase, Kohta, Thompson, Todd A. and Ofek, Eran O. (May 2014). “Probing cosmic ray ion acceleration with radio-submm and gamma-ray emission from interaction-powered supernovae”. In: *MNRAS* 440.3, pp. 2528–2543. DOI: `10.1093/mnras/stu384`. arXiv: `1311.6778 [astro-ph.HE]`.

Nataf, D. M. et al. (Sept. 2010). “The Split Red Clump of the Galactic Bulge from OGLE-III”. In: *APJL* 721.1, pp. L28–L32. DOI: `10.1088/2041-8205/721/1/L28`. arXiv: `1007.5065 [astro-ph.GA]`.

Navarro, Julio F., Frenk, Carlos S. and White, Simon D. M. (May 1996). “The Structure of Cold Dark Matter Halos”. In: *APJ* 462, p. 563. DOI: `10.1086/177173`. arXiv: `astro-ph/9508025 [astro-ph]`.

Newberg, Heidi Jo et al. (Apr. 2002). “The Ghost of Sagittarius and Lumps in the Halo of the Milky Way”. In: *APJ* 569.1, pp. 245–274. DOI: `10.1086/338983`. arXiv: `astro-ph/0111095 [astro-ph]`.

Nishiyama, Shogo et al. (Oct. 2010). “Magnetic Field Configuration at the Galactic Center Investigated by Wide-field Near-infrared Polarimetry: Transition from a Toroidal to a Poloidal Magnetic Field”. In: *APJL* 722.1, pp. L23–L27. DOI: `10.1088/2041-8205/722/1/L23`. arXiv: `1009.0584 [astro-ph.GA]`.

Novak, G. et al. (Feb. 2003). “First Results from the Submillimeter Polarimeter for Antarctic Remote Observations: Evidence of Large-Scale Toroidal Magnetic Fields in the Galactic Center”. In: *APJL* 583.2, pp. L83–L86. DOI: `10.1086/368156`. arXiv: `astro-ph/0109074 [astro-ph]`.

Nuza, Sebastián E. et al. (July 2014). “The distribution of gas in the Local Group from constrained cosmological simulations: the case for Andromeda and the Milky Way galaxies”. In: *MNRAS* 441.3, pp. 2593–2612. DOI: `10.1093/mnras/stu643`. arXiv: `1403.7528 [astro-ph.GA]`.

Ojha, D. K. (Apr. 2001). "Radial scalelengths of the galactic thin and thick disc with 2MASS data". In: *MNRAS* 322.2, pp. 426–432. DOI: `10.1046/j.1365-8711.2001.04155.x`.

Oppermann, N. et al. (Mar. 2015). "Estimating extragalactic Faraday rotation". In: *AAP* 575, A118, A118. DOI: `10.1051/0004-6361/201423995`. arXiv: `1404.3701 [astro-ph.IM]`.

Oren, Abraham L. and Wolfe, Arthur M. (June 1995). "A Faraday Rotation Search for Magnetic Fields in Quasar-damped LY alpha Absorption Systems". In: *APJ* 445, p. 624. DOI: `10.1086/175726`.

Ortolani, Sergio et al. (Oct. 1995). "Near-coeval formation of the Galactic bulge and halo inferred from globular cluster ages". In: *Nature* 377.6551, pp. 701–704. DOI: `10.1038/377701a0`.

Ostapchenko, S. (Jan. 2006). "QGSJET-II: towards reliable description of very high energy hadronic interactions". In: *Nuclear Physics B Proceedings Supplements* 151, pp. 143–146. DOI: `10.1016/j.nuclphysbps.2005.07.026`. arXiv: `hep-ph/0412332 [hep-ph]`.

Owen, Ellis R. et al. (Nov. 2018). "Interactions between ultra-high-energy particles and protogalactic environments". In: *MNRAS* 481.1, pp. 666–687. DOI: `10.1093/mnras/sty2279`. arXiv: `1808.07837 [astro-ph.HE]`.

Owen, Ellis R. et al. (July 2023). "Cosmic Ray Processes in Galactic Ecosystems". In: *Galaxies* 11.4, p. 86. DOI: `10.3390/galaxies11040086`. arXiv: `2306.09924 [astro-ph.GA]`.

Paerels, Frederik B. S. and Kahn, Steven M. (Jan. 2003). "High-Resolution X-Ray Spectroscopy with CHANDRA and XMM-NEWTON". In: *ARAA* 41, pp. 291–342. DOI: `10.1146/annurev.astro.41.071601.165952`.

Page, L. et al. (June 2007). "Three-Year Wilkinson Microwave Anisotropy Probe (WMAP) Observations: Polarization Analysis". In: *APJS* 170.2, pp. 335–376. DOI: `10.1086/513699`. arXiv: `astro-ph/0603450 [astro-ph]`.

Panopoulou, G. V. et al. (Dec. 2021). "Revisiting the Distance to Radio Loops I and IV Using Gaia and Radio/Optical Polarization Data". In: *APJ* 922.2, 210, p. 210. DOI: `10.3847/1538-4357/ac273f`. arXiv: `2106.14267 [astro-ph.GA]`.

Parizot, E. et al. (Sept. 2004). "Superbubbles and energetic particles in the Galaxy. I. Collective effects of particle acceleration". In: *AAP* 424, pp. 747–760. DOI: `10.1051/0004-6361:20041269`. arXiv: `astro-ph/0405531 [astro-ph]`.

Parker, E. N. (Nov. 1958). "Dynamics of the Interplanetary Gas and Magnetic Fields." In: *APJ* 128, p. 664. DOI: `10.1086/146579`.

— (May 1965). "Dynamical Properties of Stellar Coronas and Stellar Winds, IV. The Separate Existence of Subsonic and Supersonic Solutions." In: *APJ* 141, p. 1463. DOI: `10.1086/148235`.

— (Sept. 1966). "The Dynamical State of the Interstellar Gas and Field". In: *APJ* 145, p. 811. DOI: `10.1086/148828`.

Particle Data Group et al. (Aug. 2020). "Review of Particle Physics". In: *Progress of Theoretical and Experimental Physics* 2020.8, 083C01, p. 083C01. DOI: `10.1093/ptep/ptaa104`.

Patrignani, C. et al. (Oct. 2016). "Review of Particle Physics". In: *Chinese Physics C* 40.10, 100001, p. 100001. DOI: `10.1088/1674-1137/40/10/100001`.

Petropoulou, M. et al. (Sept. 2017). “Point-source and diffuse high-energy neutrino emission from Type IIn supernovae”. In: *MNRAS* 470.2, pp. 1881–1893. DOI: `10.1093/mnras/stx1251`. arXiv: `1705.06752 [astro-ph.HE]`.

Pietrobon, Davide et al. (Aug. 2012). “Analysis of WMAP 7 Year Temperature Data: Astrophysics of the Galactic Haze”. In: *APJ* 755.1, 69, p. 69. DOI: `10.1088/0004-637X/755/1/69`. arXiv: `1110.5418 [astro-ph.GA]`.

Pietz, J. et al. (Apr. 1998). “The Galactic X-ray halo”. In: *AAP* 332, pp. 55–70.

Piffl, T. et al. (Dec. 2014). “Constraining the Galaxy’s dark halo with RAVE stars”. In: *MNRAS* 445.3, pp. 3133–3151. DOI: `10.1093/mnras/stu1948`. arXiv: `1406.4130 [astro-ph.GA]`.

Planck Collaboration (June 2013). “Planck intermediate results. IX. Detection of the Galactic haze with Planck”. In: *AAP* 554, A139, A139. DOI: `10.1051/0004-6361/201220271`. arXiv: `1208.5483 [astro-ph.GA]`.

— (Sept. 2016a). “Planck 2015 results. I. Overview of products and scientific results”. In: *AAP* 594, A1, A1. DOI: `10.1051/0004-6361/201527101`. arXiv: `1502.01582 [astro-ph.CO]`.

— (Sept. 2016b). “Planck 2015 results. XIII. Cosmological parameters”. In: *AAP* 594, A13, A13. DOI: `10.1051/0004-6361/201525830`. arXiv: `1502.01589 [astro-ph.CO]`.

Plummer, H. C. (Mar. 1911). “On the problem of distribution in globular star clusters”. In: *MNRAS* 71, pp. 460–470. DOI: `10.1093/mnras/71.5.460`.

Pohlen, M. and Trujillo, I. (Aug. 2006). “The structure of galactic disks. Studying late-type spiral galaxies using SDSS”. In: *AAP* 454.3, pp. 759–772. DOI: `10.1051/0004-6361:20064883`. arXiv: `astro-ph/0603682 [astro-ph]`.

Portail, M. et al. (Mar. 2015). “Made-to-measure models of the Galactic box/peanut bulge: stellar and total mass in the bulge region”. In: *MNRAS* 448.1, pp. 713–731. DOI: `10.1093/mnras/stv058`. arXiv: `1502.00633 [astro-ph.GA]`.

Portail, Matthieu et al. (Feb. 2017). “Dynamical modelling of the galactic bulge and bar: the Milky Way’s pattern speed, stellar and dark matter mass distribution”. In: *MNRAS* 465.2, pp. 1621–1644. DOI: `10.1093/mnras/stw2819`. arXiv: `1608.07954 [astro-ph.GA]`.

Potgieter, M. S. et al. (May 2013). “The long-term variability of cosmic ray protons in the heliosphere: A modeling approach”. In: *Journal of Advanced Research* 4.3, pp. 259–263. DOI: `10.1016/j.jare.2012.08.001`.

Predehl, P. et al. (Dec. 2020). “Detection of large-scale X-ray bubbles in the Milky Way halo”. In: *Nature* 588.7837, pp. 227–231. DOI: `10.1038/s41586-020-2979-0`. arXiv: `2012.05840 [astro-ph.GA]`.

Prouza, M. and Šmída, R. (Oct. 2003). “The Galactic magnetic field and propagation of ultra-high energy cosmic rays”. In: *AAP* 410, pp. 1–10. DOI: `10.1051/0004-6361:20031281`. arXiv: `astro-ph/0307165 [astro-ph]`.

Pshirkov, M. S. et al. (Sept. 2011). “Deriving the Global Structure of the Galactic Magnetic Field from Faraday Rotation Measures of Extragalactic Sources”. In: *APJ* 738.2, 192, p. 192. DOI: `10.1088/0004-637X/738/2/192`. arXiv: `1103.0814 [astro-ph.GA]`.

Ptuskin, Vladimir S. et al. (May 2006). “Dissipation of Magnetohydrodynamic Waves on Energetic Particles: Impact on Interstellar Turbulence and Cosmic-Ray Transport”. In: *APJ* 642.2, pp. 902–916. DOI: `10.1086/501117`. arXiv: `astro-ph/0510335 [astro-ph]`.

Ramesh, Rahul, Nelson, Dylan and Pillepich, Annalisa (Jan. 2023). “The circumgalactic medium of Milky Way-like galaxies in the TNG50 simulation - I: halo gas properties and the role of SMBH feedback”. In: *MNRAS* 518.4, pp. 5754–5777. DOI: 10.1093/mnras/stac3524. arXiv: 2211.00020 [astro-ph.GA].

Rao, Ramprasad et al. (Jan. 2014). “Detection of a Magnetized Disk around a Very Young Protostar”. In: *APJL* 780.1, L6, p. L6. DOI: 10.1088/2041-8205/780/1/L6. arXiv: 1311.6225 [astro-ph.GA].

Reich, P. and Reich, W. (Feb. 1986). “A radio continuum survey of the northern sky at 1420 MHz. II”. In: *AAPS* 63, p. 205.

Reich, P., Testori, J. C. and Reich, W. (Sept. 2001). “A radio continuum survey of the southern sky at 1420 MHz. The atlas of contour maps”. In: *AAP* 376, pp. 861–877. DOI: 10.1051/0004-6361:20011000.

Reich, W. (May 1982). “A radio continuum survey of the northen sky at 1420 MHz - Part I.” In: *AAPS* 48, pp. 219–297.

Reid, Mark J. (Jan. 1993). “The distance to the center of the Galaxy.” In: *ARAA* 31, pp. 345–372. DOI: 10.1146/annurev.aa.31.090193.002021.

— (Jan. 2009). “Is There a Supermassive Black Hole at the Center of the Milky Way?” In: *International Journal of Modern Physics D* 18.6, pp. 889–910. DOI: 10.1142/S0218271809014820. arXiv: 0808.2624 [astro-ph].

Reimer, A., Pohl, M. and Reimer, O. (June 2006). “Nonthermal High-Energy Emission from Colliding Winds of Massive Stars”. In: *APJ* 644.2, pp. 1118–1144. DOI: 10.1086/503598. arXiv: astro-ph/0510701 [astro-ph].

Reynolds, S. P. (Sept. 2008). “Supernova remnants at high energy.” In: *ARAA* 46, pp. 89–126. DOI: 10.1146/annurev.astro.46.060407.145237.

Robin, Annie C., Creze, Michel and Mohan, Vijay (Nov. 1994). “How Do the Stellar Disc and Thick Disc Stop ?” In: *arXiv e-prints*, astro-ph/9411095, astro–ph/9411095. DOI: 10.48550/arXiv.astro-ph/9411095. arXiv: astro-ph/9411095 [astro-ph].

Rodgers-Lee, D. et al. (Nov. 2017). “The ionizing effect of low-energy cosmic rays from a class II object on its protoplanetary disc”. In: *MNRAS* 472.1, pp. 26–38. DOI: 10.1093/mnras/stx1889. arXiv: 1707.07522 [astro-ph.SR].

Rodgers-Lee, D. et al. (Dec. 2020). “The Galactic cosmic ray intensity at the evolving Earth and young exoplanets”. In: *MNRAS* 499.2, pp. 2124–2137. DOI: 10.1093/mnras/staa2737. arXiv: 2009.02173 [astro-ph.SR].

Roy, S., Pramesh Rao, A. and Subrahmanyan, R. (Feb. 2008). “Magnetic field near the central region of the Galaxy: rotation measure of extragalactic sources”. In: *AAP* 478.2, pp. 435–442. DOI: 10.1051/0004-6361:20066470. arXiv: 0712.0269 [astro-ph].

Rubin, V. C., Ford W. K., Jr. and Thonnard, N. (June 1980). “Rotational properties of 21 SC galaxies with a large range of luminosities and radii, from NGC 4605 (R=4kpc) to UGC 2885 (R=122kpc).” In: *APJ* 238, pp. 471–487. DOI: 10.1086/158003.

Ruphy, S. et al. (Sept. 1996). “New determination of the disc scale length and the radial cutoff in the anticenter with DENIS data.” In: *AAP* 313, pp. L21–L24.

Ryans, R. S. I. et al. (Aug. 1997). “Optical and HI studies of high- and intermediate-velocity gas towards Complex A”. In: *MNRAS* 289.4, pp. 986–992. DOI: 10.1093/mnras/289.4.986.

Rybicki, George B. and Lightman, Alan P. (1979). *Radiative processes in astrophysics.*

Salem, Munier et al. (Dec. 2015). “Ram pressure stripping of the large magellanic cloud’s disk as a probe of the milky way’s circumgalactic medium”. English (US). In: *Astrophysical Journal* 815.1. Publisher Copyright: © 2015. The American Astronomical Society. All rights reserved. ISSN: 0004-637X. DOI: 10.1088/0004-637X/815/1/77.

Sanders, Jason L. and Binney, James (June 2015). “Extended distribution functions for our Galaxy”. In: *MNRAS* 449.4, pp. 3479–3502. DOI: 10.1093/mnras/stv578. arXiv: 1501.02227 [astro-ph.GA].

Sarkar, Kartick C. (Mar. 2024). “The Fermi/eROSITA Bubbles: A look into the nuclear outflow from the Milky Way”. In: *arXiv e-prints*, arXiv:2403.09824, arXiv:2403.09824. DOI: 10.48550/arXiv.2403.09824. arXiv: 2403.09824 [astro-ph.HE].

Sarkar, Kartick C., Nath, Biman B. and Sharma, Prateek (May 2017). “Clues to the origin of Fermi bubbles from O viii/O vii line ratio”. In: *MNRAS* 467.3, pp. 3544–3555. DOI: 10.1093/mnras/stx314. arXiv: 1610.00719 [astro-ph.GA].

Savage, Blair D. et al. (Oct. 2017). “Probing the Outflowing Multiphase Gas ∼1 kpc below the Galactic Center”. In: *APJS* 232.2, 25, p. 25. DOI: 10.3847/1538-4365/aa8f4c. arXiv: 1707.06942 [astro-ph.GA].

Schlickeiser, Reinhard (Jan. 1989). “Cosmic-Ray Transport and Acceleration. I. Derivation of the Kinetic Equation and Application to Cosmic Rays in Static Cold Media”. In: *APJ* 336, p. 243. DOI: 10.1086/167009.

Schmidt, M. (June 1956). “A model of the distribution of mass in the Galactic System”. In: *BAIN* 13, p. 15.

Schure, K. M. and Bell, A. R. (Oct. 2013). “Cosmic ray acceleration in young supernova remnants”. In: *MNRAS* 435.2, pp. 1174–1185. DOI: 10.1093/mnras/stt1371. arXiv: 1307.6575 [astro-ph.HE].

— (Jan. 2014). “From cosmic ray source to the Galactic pool”. In: *MNRAS* 437.3, pp. 2802–2805. DOI: 10.1093/mnras/stt2089. arXiv: 1310.7027 [astro-ph.HE].

Searle, L. and Zinn, R. (Oct. 1978). “Composition of halo clusters and the formation of the galactic halo.” In: *APJ* 225, pp. 357–379. DOI: 10.1086/156499.

Sembach, K. R. et al. (May 2003). “Highly Ionized High-Velocity Gas in the Vicinity of the Galaxy”. In: *APJS* 146.1, pp. 165–208. DOI: 10.1086/346231. arXiv: astro-ph/0207562 [astro-ph].

Shaw, Vasundhara, van Vliet, Arjen and Taylor, Andrew M. (Dec. 2022). “Galactic halo bubble magnetic fields and UHECR deflections”. In: *MNRAS* 517.2, pp. 2534–2545. DOI: 10.1093/mnras/stac2778. arXiv: 2202.06780 [astro-ph.HE].

Shen, Sijing et al. (Mar. 2013). “The Circumgalactic Medium of Massive Galaxies at z $\sim$3: A Test for Stellar Feedback, Galactic Outflows, and Cold Streams”. In: *APJ* 765.2, 89, p. 89. DOI: 10.1088/0004-637X/765/2/89. arXiv: 1205.0270 [astro-ph.CO].

Shu, F. H. (1992). *The physics of astrophysics. Volume II: Gas dynamics.*

Siebert, A. et al. (Apr. 2011). “Detection of a radial velocity gradient in the extended local disc with RAVE”. In: *MNRAS* 412.3, pp. 2026–2032. DOI: 10.1111/j.1365-2966.2010.18037.x. arXiv: 1011.4092 [astro-ph.GA].

Simard-Normandin, M. and Kronberg, P. P. (Nov. 1980). “Rotation measures and the galactic magnetic field.” In: *APJ* 242, pp. 74–94. DOI: 10.1086/158445.

Simpson, Christine M. et al. (Apr. 2023). “How cosmic rays mediate the evolution of the interstellar medium”. In: *MNRAS* 520.3, pp. 4621–4645. DOI: 10.1093/mnras/stac3601. arXiv: 2204.02410 [astro-ph.GA].

Skorodko, T. et al. (Mar. 2008). “Excitation of the Roper resonance in single- and double-pion production in nucleon-nucleon collisions*”. In: *European Physical Journal A* 35.3, pp. 317–319. DOI: 10.1140/epja/i2008-10569-6.

Sofue, Y. et al. (June 2016). “Galactic Centre hypershell model for the North Polar Spurs”. In: *MNRAS* 459.1, pp. 108–120. DOI: 10.1093/mnras/stw623. arXiv: 1603.02786 [astro-ph.GA].

Sofue, Yoshiaki (Aug. 2012). “Grand Rotation Curve and Dark Matter Halo in the Milky Way Galaxy”. In: *PASJ* 64, 75, p. 75. DOI: 10.1093/pasj/64.4.75. arXiv: 1110.4431 [astro-ph.GA].

— (Aug. 2022). “One-kiloparsec expanding cylinder of H I gas around the Galactic Center”. In: *PASJ* 74.4, pp. L23–L26. DOI: 10.1093/pasj/psac034. arXiv: 2205.02078 [astro-ph.GA].

Spitzer Lyman, Jr. (July 1956). “On a Possible Interstellar Galactic Corona.” In: *APJ* 124, p. 20. DOI: 10.1086/146200.

Stanimirović, Snežana et al. (Sept. 2002). “The Small-Scale Structure of the Magellanic Stream”. In: *APJ* 576.2, pp. 773–789. DOI: 10.1086/341892. arXiv: astro-ph/0109211 [astro-ph].

Stil, J. M., Taylor, A. R. and Sunstrum, C. (Jan. 2011). “Structure in the Rotation Measure Sky”. In: *APJ* 726.1, 4, p. 4. DOI: 10.1088/0004-637X/726/1/4. arXiv: 1010.5299 [astro-ph.GA].

Stinson, G. S. et al. (Sept. 2012). “MAGICC haloes: confronting simulations with observations of the circumgalactic medium at z=0”. In: *MNRAS* 425.2, pp. 1270–1277. DOI: 10.1111/j.1365-2966.2012.21522.x. arXiv: 1112.1698 [astro-ph.CO].

Strong, A. W. et al. (July 2009). “The GALPROP Cosmic-Ray Propagation Code”. In: *arXiv e-prints*, arXiv:0907.0559, arXiv:0907.0559. DOI: 10.48550/arXiv.0907.0559. arXiv: 0907.0559 [astro-ph.HE].

Strong, Andrew W., Moskalenko, Igor V. and Ptuskin, Vladimir S. (Nov. 2007). “Cosmic-Ray Propagation and Interactions in the Galaxy”. In: *Annual Review of Nuclear and Particle Science* 57.1, pp. 285–327. DOI: 10.1146/annurev.nucl.57.090506.123011. arXiv: astro-ph/0701517 [astro-ph].

Strong, Andrew W., Moskalenko, Igor V. and Reimer, Olaf (Oct. 2004). “Diffuse Galactic Continuum Gamma Rays: A Model Compatible with EGRET Data and Cosmic-Ray Measurements”. In: *APJ* 613.2, pp. 962–976. DOI: 10.1086/423193. arXiv: astro-ph/0406254 [astro-ph].

Su, Meng, Slatyer, Tracy R. and Finkbeiner, Douglas P. (Dec. 2010). “Giant Gamma-ray Bubbles from Fermi-LAT: Active Galactic Nucleus Activity or Bipolar Galactic Wind?” In: *APJ* 724.2, pp. 1044–1082. DOI: 10.1088/0004-637X/724/2/1044. arXiv: 1005.5480 [astro-ph.HE].

Sun, X. H. et al. (Jan. 2008). “Radio observational constraints on Galactic 3D-emission models”. In: *AAP* 477.2, pp. 573–592. DOI: 10.1051/0004-6361:20078671. arXiv: 0711.1572 [astro-ph].

Sun, X. H. et al. (Sept. 2015). "Faraday Tomography of the North Polar Spur: Constraints on the Distance to the Spur and on the Magnetic Field of the Galaxy". In: *APJ* 811.1, 40, p. 40. DOI: `10.1088/0004-637X/811/1/40`. arXiv: `1508.03889 [astro-ph.GA]`.

Suresh, Joshua et al. (Mar. 2017). "On the OVI abundance in the circumgalactic medium of low-redshift galaxies". In: *MNRAS* 465.3, pp. 2966–2982. DOI: `10.1093/mnras/stw2499`. arXiv: `1511.00687 [astro-ph.GA]`.

Tahara, M. et al. (Apr. 2015). "Suzaku X-Ray Observations of the Fermi Bubbles: Northernmost Cap and Southeast Claw Discovered With MAXI-SSC". In: *APJ* 802.2, 91, p. 91. DOI: `10.1088/0004-637X/802/2/91`. arXiv: `1501.04405 [astro-ph.HE]`.

Tatischeff, Vincent and Gabici, Stefano (Oct. 2018). "Particle Acceleration by Supernova Shocks and Spallogenic Nucleosynthesis of Light Elements". In: *Annual Review of Nuclear and Particle Science* 68.1, pp. 377–404. DOI: `10.1146/annurev-nucl-101917-021151`. arXiv: `1803.01794 [astro-ph.HE]`.

Taylor, A. R., Stil, J. M. and Sunstrum, C. (Sept. 2009). "A Rotation Measure Image of the Sky". In: *APJ* 702.2, pp. 1230–1236. DOI: `10.1088/0004-637X/702/2/1230`.

Taylor, Andrew M. and Giacinti, Gwenael (Jan. 2017). "Cosmic rays in a galactic breeze". In: *Phys Rev Lett* 95.2, 023001, p. 023001. DOI: `10.1103/PhysRevD.95.023001`. arXiv: `1607.08862 [astro-ph.HE]`.

Taylor, Corbin et al. (Oct. 2016). "The mass profile of the Milky Way to the virial radius from the Illustris simulation". In: *MRNAS* 461.4, pp. 3483–3493. DOI: `10.1093/mnras/stw1522`. arXiv: `1510.06409 [astro-ph.CO]`.

Tepper-Garcia, Thor, Bland-Hawthorn, Joss and Sutherland, Ralph S. (Nov. 2015). "The Magellanic Stream: Break-up and Accretion onto the Hot Galactic Corona". In: *APJ* 813.2, 94, p. 94. DOI: `10.1088/0004-637X/813/2/94`. arXiv: `1505.01587 [astro-ph.GA]`.

Terndrup, D. M. (Sept. 1988). "The Structure and Stellar Population of the Galactic Nuclear Bulge". In: *AJ* 96, p. 884. DOI: `10.1086/114855`.

The Magnetized Interstellar Medium (Feb. 2004).

Tourmente, Olivier, Rodgers-Lee, D. and Taylor, Andrew M. (Feb. 2023). "A galactic breeze origin for the Fermi bubbles emission". In: *MNRAS* 518.4, pp. 6083–6091. DOI: `10.1093/mnras/stac3517`. arXiv: `2207.09189 [astro-ph.HE]`.

Tress, Robin G. et al. (Dec. 2020). "Simulations of the Milky Way's central molecular zone - I. Gas dynamics". In: *MNRAS* 499.3, pp. 4455–4478. DOI: `10.1093/mnras/staa3120`. arXiv: `2004.06724 [astro-ph.GA]`.

Tumlinson, Jason, Peeples, Molly S. and Werk, Jessica K. (Aug. 2017). "The Circumgalactic Medium". In: *ARAA* 55.1, pp. 389–432. DOI: `10.1146/annurev-astro-091916-055240`. arXiv: `1709.09180 [astro-ph.GA]`.

Unger, Michael and Farrar, Glennys (Nov. 2023). "The Coherent Magnetic Field of the Milky Way". In: *arXiv e-prints*, arXiv:2311.12120, arXiv:2311.12120. DOI: `10.48550/arXiv.2311.12120`. arXiv: `2311.12120 [astro-ph.GA]`.

van der Marel, Roeland P. et al. (July 2012). "The M31 Velocity Vector. II. Radial Orbit toward the Milky Way and Implied Local Group Mass". In: *APJ* 753.1, 8, p. 8. DOI: `10.1088/0004-637X/753/1/8`. arXiv: `1205.6864 [astro-ph.GA]`.

Vidal, Matias et al. (Sept. 2015). “Polarized radio filaments outside the Galactic plane”. In: *MNRAS* 452.1, pp. 656–675. DOI: `10.1093/mnras/stv1328`. arXiv: `1410.4438 [astro-ph.GA]`.

Vivas, A. Katherina and Zinn, Robert (Aug. 2006). “The QUEST RR Lyrae Survey. II. The Halo Overdensities in the First Catalog”. In: *AJ* 132.2, pp. 714–728. DOI: `10.1086/505200`. arXiv: `astro-ph/0604359 [astro-ph]`.

Vladimirov, A. E. et al. (May 2011). “GALPROP WebRun: An internet-based service for calculating galactic cosmic ray propagation and associated photon emissions”. In: *Computer Physics Communications* 182.5, pp. 1156–1161. DOI: `10.1016/j.cpc.2011.01.017`. arXiv: `1008.3642 [astro-ph.HE]`.

Voelk, H. J. and Forman, M. (Feb. 1982). “Cosmic rays and gamma-rays from OB stars”. In: *APJ* 253, pp. 188–198. DOI: `10.1086/159623`.

Wakker, Bart P. et al. (Apr. 2012). “Characterizing Transition Temperature Gas in the Galactic Corona”. In: *APJ* 749.2, 157, p. 157. DOI: `10.1088/0004-637X/749/2/157`. arXiv: `1202.5973 [astro-ph.GA]`.

Wang, Q. Daniel and Yao, Yangsen (Nov. 2012). “Comments on “A huge reservoir of ionized gas around the Milky Way: accounting for the missing mass?” (2012 ApJL, 756, 8) and “The warm-hot gaseous halo of the Milky Way” (arXiv1211.3137)”. In: *arXiv e-prints*, arXiv:1211.4834, arXiv:1211.4834. DOI: `10.48550/arXiv.1211.4834`. arXiv: `1211.4834 [astro-ph.GA]`.

Watkins, Laura L., Evans, N. Wyn and An, Jin H. (July 2010). “The masses of the Milky Way and Andromeda galaxies”. In: *MNRAS* 406.1, pp. 264–278. DOI: `10.1111/j.1365-2966.2010.16708.x`. arXiv: `1002.4565 [astro-ph.GA]`.

Watkins, Laura L. et al. (Mar. 2019). “Evidence for an Intermediate-mass Milky Way from Gaia DR2 Halo Globular Cluster Motions”. In: *APJ* 873.2, 118, p. 118. DOI: `10.3847/1538-4357/ab089f`. arXiv: `1804.11348 [astro-ph.GA]`.

Wegg, Christopher and Gerhard, Ortwin (Nov. 2013). “Mapping the three-dimensional density of the Galactic bulge with VVV red clump stars”. In: *MNRAS* 435.3, pp. 1874–1887. DOI: `10.1093/mnras/stt1376`. arXiv: `1308.0593 [astro-ph.GA]`.

Weiland, J. L. et al. (Apr. 1994). “COBE Diffuse Background Experiment Observations of the Galactic Bulge”. In: *APJL* 425, p. L81. DOI: `10.1086/187315`.

Wilkinson, M. I. and Evans, N. W. (Dec. 1999). “The present and future mass of the Milky Way halo”. In: *MNRAS* 310.3, pp. 645–662. DOI: `10.1046/j.1365-8711.1999.02964.x`. arXiv: `astro-ph/9906197 [astro-ph]`.

Williams, Rik J. et al. (Oct. 2005). “Probing the Local Group Medium toward Markarian 421 with Chandra and the Far Ultraviolet Spectroscopic Explorer”. In: *APJ* 631.2, pp. 856–867. DOI: `10.1086/431343`. arXiv: `astro-ph/0504558 [astro-ph]`.

Xiao, L. et al. (May 2008). “Radio spectral properties and the magnetic field of the SNR S147”. In: *AAP* 482.3, pp. 783–792. DOI: `10.1051/0004-6361:20078461`. arXiv: `0801.4803 [astro-ph]`.

Xu, J. and Han, J. L. (Apr. 2024). “The huge magnetic toroids in the Milky Way halo”. In: *arXiv e-prints*, arXiv:2404.02038, arXiv:2404.02038. DOI: `10.48550/arXiv.2404.02038`. arXiv: `2404.02038 [astro-ph.GA]`.

Xu, Jun and Han, Jin-Lin (Aug. 2014). “A compiled catalog of rotation measures of radio point sources”. In: *Research in Astronomy and Astrophysics* 14.8, 942-

958, pp. 942–958. DOI: 10.1088/1674-4527/14/8/005. arXiv: 1405.1920 [astro-ph.GA].

Xue, X. X. et al. (Sept. 2008). “The Milky Way’s Circular Velocity Curve to 60 kpc and an Estimate of the Dark Matter Halo Mass from the Kinematics of ~2400 SDSS Blue Horizontal-Branch Stars”. In: *APJ* 684.2, pp. 1143–1158. DOI: 10.1086/589500. arXiv: 0801.1232 [astro-ph].

Xue, Xiang-Xiang et al. (Apr. 2014). “The SEGUE K Giant Survey. II. A Catalog of Distance Determinations for the SEGUE K Giants in the Galactic Halo”. In: *APJ* 784.2, 170, p. 170. DOI: 10.1088/0004-637X/784/2/170. arXiv: 1211.0549 [astro-ph.GA].

Xue, Xiang-Xiang et al. (Aug. 2015). “The Radial Profile and Flattening of the Milky Way’s Stellar Halo to 80 kpc from the SEGUE K-giant Survey”. In: *APJ* 809.2, 144, p. 144. DOI: 10.1088/0004-637X/809/2/144. arXiv: 1506.06144 [astro-ph.GA].

Yang, H. -Y. K. and Ruszkowski, M. (Nov. 2017). “The Spatially Uniform Spectrum of the Fermi Bubbles: The Leptonic Active Galactic Nucleus Jet Scenario”. In: *APJ* 850.1, 2, p. 2. DOI: 10.3847/1538-4357/aa9434. arXiv: 1706.05025 [astro-ph.HE].

Yang, H. -Y. K. et al. (Dec. 2012). “The Fermi Bubbles: Supersonic Active Galactic Nucleus Jets with Anisotropic Cosmic-Ray Diffusion”. In: *APJ* 761.2, 185, p. 185. DOI: 10.1088/0004-637X/761/2/185. arXiv: 1207.4185 [astro-ph.GA].

Yang, H. -Y. Karen, Ruszkowski, M. and Zweibel, E. (Dec. 2013). “The Fermi bubbles: gamma-ray, microwave and polarization signatures of leptonic AGN jets”. In: *MNRAS* 436.3, pp. 2734–2746. DOI: 10.1093/mnras/stt1772. arXiv: 1307.3551 [astro-ph.GA].

Yang, Lili and Razzaque, Soebur (Apr. 2019). “Constraints on very high energy gamma-ray emission from the Fermi bubbles with future ground-based experiments”. In: *Phys Rev D* 99.8, 083007, p. 083007. DOI: 10.1103/PhysRevD.99.083007. arXiv: 1811.10970 [astro-ph.HE].

Yasui, Chikako et al. (Mar. 2008). “Star Formation in the Extreme Outer Galaxy: Digel Cloud 2 Clusters”. In: *APJ* 675.1, pp. 443–453. DOI: 10.1086/524356. arXiv: 0711.0257 [astro-ph].

Yusef-Zadeh, F., Hewitt, J. W. and Cotton, W. (Dec. 2004). “A 20 Centimeter Survey of the Galactic Center Region. I. Detection of Numerous Linear Filaments”. In: *APJS* 155.2, pp. 421–550. DOI: 10.1086/425257. arXiv: astro-ph/0409292 [astro-ph].

Yusef-Zadeh, F., Morris, M. and Chance, D. (Aug. 1984). “Large, highly organized radio structures near the galactic centre”. In: *Nature* 310.5978, pp. 557–561. DOI: 10.1038/310557a0.

Yusef-Zadeh, F. et al. (Jan. 2013). “Interacting Cosmic Rays with Molecular Clouds: A Bremsstrahlung Origin of Diffuse High-energy Emission from the Inner 2°×1° of the Galactic Center”. In: *APJ* 762.1, 33, p. 33. DOI: 10.1088/0004-637X/762/1/33. arXiv: 1206.6882 [astro-ph.HE].

Zech, William F. et al. (May 2008). “The High-Velocity Gas toward Messier 5: Tracing Feedback Flows in the Inner Galaxy”. In: *APJ* 679.1, pp. 460–480. DOI: 10.1086/587135. arXiv: 0802.0286 [astro-ph].